Dynamics of turbulent western boundary currents at low latitudes, a numerical study

Cataria Quam Cyrille Akuetevi

THÈSE

Pour obtenir le grade de

DOCTEUR DE L'UNIVERSITÉ DE GRENOBLE

Spécialité : **Physique appliquée à l'océan**

Arrêté ministériel :

Présentée par

Cataria Quam Cyrille AKUETEVI

Thèse dirigée par **Achim Wirth**
et codirigée par **Bernard Barnier**

préparée au sein **Laboratoire des Ecoulements Géophysiques et Industriels (UMR 5519) / Laboratoire de Glaciologie et de Géophysique de l'environnement (UMR 5183)**
et de **l'école doctorale Terre Univers et Environnement**

Dynamics of turbulent western boundary currents at low latitude, a numerical study

Thèse soutenue publiquement le **20/02/2014**,
devant le jury composé de :

Mme, Chantal Staquet
Pr, UJF Grenoble, Présidente
Mme, Alessandra Lanotte
CR, ISAC (Italie), Rapporteur
Mr, Yves Morel
DR, Directeur LEGOS, Rapporteur
Mr, Guillaume Roullet
MC, Univ Brest, Examinateur
Mr, Nickolas Hall
Pr, UPS, Univ Toulouse, Examinateur
Mr, Achim Wirth
CR1, LEGI, Directeur de thèse
Mr, Bernard Barnier
DR1, LGGE, Co-Directeur de thèse

Acknowledgments/Remerciements

Contents

III   Discussion and Conclusions   133

8 Reduced Gravity Shallow Water Model   135

9 Application to Somali Current via NEMO (Drakkar)   139

10 Synergies and Future Directions of Research   145

References   148

IV   Appendix   159

11 Article   161

12 CDFTOOLS   199

V   MINUTES   221

Abstract

Strong western boundary currents are a dominant feature of the worlds oceans, also at low latitudes. They are called the North Brazil Current in the Atlantic and the Somali Current in the Indian Ocean. They exhibit a turbulent dynamics and their region is a source of strong kinetic energy production and internal variability of the worlds oceans. Several places exists where the western boundary currents retroflect (i.e separation from the coast) and generate coherent structures as anticyclonic eddies and dipoles.

The dynamics of oceanic western boundary currents has so far not been extensively studied in the viewpoint of turbulent boundary-layer theory. The approach followed in this thesis is to use a fine resolution reduced-gravity shallow water model to understand the turbulent boundary-layer processes and then apply these results to the Ocean General Circulation Model NEMO in the Drakkar configuration. The case of the Somali Current is considered for this application.

The first part of this doctoral thesis is directed towards the study of the turbulent western boundary-layer through the determination of the turbulent structures, fluxes, balances of low latitude turbulent western boundary currents.

The dynamics of low latitude turbulent western boundary currents, subject to two different types of idealized wind forcing, Monsoon Winds and Trade Winds, is considered using numerical results from integrations of a dedicated fine resolution (2.5km) reduced gravity shallow-water model. For viscosity values of $1000\text{m}^2{\cdot}\text{s}^{-1}$ and above, the boundary-layer dynamics compares well to the analytical solutions of the Munk-layer and the inertial-layer, derived from quasi-geostrophic theory. Modifications due to variations in the layer thickness (vortex stretching) are only important a few kilometers from the boundary. When the viscosity is reduced the boundary-layer becomes turbulent and coherent structures in form of anticyclonic eddies, *bursts* (violent detachments of *the viscous sub-layer*) and dipoles appear. Three distinct boundary-layers emerge, the *viscous sub-layer*, the *advective boundary-layer* and the *extended boundary-layer*. The first is characterized by a dominant vorticity balance between the viscous transport and the advective transport of vorticity. The second, by a balance between the advection of planetary vorticity and the advective transport of relative vorticity. The extended boundary-layer is the area to which turbulent motion from the boundary extends.

The scaling of the three boundary-layer thicknesses with viscosity is evaluated. This scaling is used to revisit the validity of the laminar Munk-layer theory for the high Reynolds number turbulent western boundary currents. It is shown that small westward velocities have a stabilizing effect (inertial effect) on the boundary current and alter the vorticity balance near the boundary. This inertial effect must be taken into account in the parameterization of the small scale turbulence of turbulent western boundary currents. The consequences for the grid resolution, refinement and the complexity of the numerical modelling of western boundary currents are discussed.

A pragmatic approach to determine the eddy viscosity for coarse resolution numerical models based on the Munk formula, the scale of the anticyclones and Prandtl's formula

is proposed.

The second part of this thesis transposes the findings of the reduced-gravity shallow water model to the Ocean General Circulation Model NEMO in the Drakkar configurations. The case of the Somali Current is considered which reverses due to the Monsoon Winds. Ten years model data of three simulations ORCA025.L75-MJM95 (1/4º), ORCA12.L46-MAL84 (1/12º) and ORCA12.L46-MAL95 (1/12º) with different wind stress forcings and different boundary conditions are used. Qualitative validation of the Arabian Sea upper-layer circulation of the three configurations is done which confirms the feedback dynamics of the previous southwest monsoon on the next southwest monsoon circulation put forward in recent studies [see *e.g.* Beal & Donohue (2013); Beal et al. (2013); McCreary et al. (1993)]. The initiation of a northward flow precursor of the early Great Whirl in March/April at 6ºN is a consequence of the arrival of the annual Rossby wave at the Somali Coast, one or two months before the southwest Monsoon starts.

An upgraded schematic diagram of the Somali Current upper-layer flow patterns over the course of the year is proposed.

The formation process of the Somali eddies is entangled. The feature known as coalescence of the Southern Gyre and the Great Whirl based on the coalescence of the two cold wedges, most frequently appears to be an elastic collision between the two eddies in which the GW becomes the Socotra Eddy. This elucidates the formation process of the Socotra Eddy, which seems to be nothing else than the relocation of the Great Whirl after the elastic collision between the Great Whirl and the Southern Gyre at the end of July or at the beginning of August.

The influence of the numerical resolution and the bi-harmonic viscosity coefficient on the coherent structures, and the scale of motion are discussed.

Acronyms

ABL: Advective Boundary-Layer
ADCP: Acoustic Doppler Current Profiler
AEBL: Arabian Extended Boundary Layer
AVISO: Archiving, Validation and Interpretation of Satellite Oceanographic Data
BBL: Bottom Boundary-Layer
CFL: Courant, Friedrichs and Lewy condition
CNRS: Centre National de Recherche Scientifique
EACC: East African Coast Current
EBL: Extended Boundary-Layer
ECMWF: European Center for Medium-Range Weather Forecasts
EICC: East Indian Coast Current
EUC: Equatorial Undercurrent
FRIC: Frictional terms
GW: Great Whirl
JC: South Java Current
LADCP: Lowered Acoustic Doppler Current Profiler
LEGI: Laboratoire des Ecoulements Géophysiques et Industriels
LC: Leeuwin Current
LH: Laccadive High
LL: Laccadive Low
MW: Monsoon Winds
NCEP: National Centers for Environmental Prediction
NEMO: Nucleus for European Modeling of the Ocean
NEMC: Northeast Madagascar Current
NERC: National Environment Research Council
NMC: Northeast Monsoon Current
nSC: northward Somali Current
OGCM: Ocean General Circulation Model
OPA: Ocean PArallélisé
PSU: Practical Salinity Unit
PV: Potential Vorticity
PVA: Potential Vorticity Advection
RGSWM: Reduced Gravity Shallow Water Model
RHJ: Ras al Hadd Jet
RVA: Relative Vorticity Advection
SBEL: Somali Extended Boundary Layer
SMC: Southwest Monsoon Current
sSC: southward Somali Current
SC: Somali Current
SE: Socotra Eddy

SG: Southern Gyre
SEC: South Equatorial Current
SECC: South Equatorial Counter-Current
SEMC: Southeast Madagascar Current
STR: Stretching terms
SWE: Shallow Water Equations
SWOT: Sea Water Ocean Topography
TKE: Turbulent Kinetic Energy
TRVA: Turbulent Relative Vorticity Advection
TW: Trade Winds
VSL: Viscous Sub-Layer
WBC: Western Boundary Current
WBL: Western Boundary-Layer
WICC: West Indian Coast Current
WOCE: World Ocean Circulation Experiment

Chapter 1

Introduction

The world's oceans play an important role in the global climate system by transporting heat from the tropical zone towards high latitudes, where it is exchanged with the atmosphere and strongly influences the worlds weather patterns. Most of this net poleward heat transport is carried by the western boundary currents (WBCs hereafter). Strong WBCs are dominant features and the most energetic regions of the world's oceans. The near western boundary region is the origin of a substantial part of turbulent kinetic energy production in the ocean. It is an area of intense upwelling [Schott & McCreary Jr (2001); Wirth et al. (2002)], with intermittent detachments [see Robinson (1991); Arnéodo et al. (2008)] which enhance the biological production [Kawamiya & Oschlies (2003)].

The WBCs are also present at low latitudes. Examples are the North Brazil Current (NBC hereafter) in the Atlantic and the Somali Current (SC hereafter) in the Indian Ocean. In both cases strong anticyclonic eddies are observed [Richardson et al. (1994); Schott & McCreary Jr (2001); Wirth et al. (2002)]. There are however substantial differences between the two cases. One is the forcing by the wind stress field. In the equatorial Atlantic the Trade Winds are the major force. Whereas in the Indian Ocean the seasonally reversing Monsoon Winds dominate. Another difference is the latitudinal inclination of the coast line, it is westward in the Atlantic Ocean and eastward in the Indian Ocean.

There is a large number of analytical work and also numerical work with a realistic coastline and topography on the dynamics of the SC and the NBC. Some important results are summarized below.

1.1 Analytical results

A considerable number of analytical calculations have attempted to answer the classical question of why WBCs at low latitude retroflect (*i.e.*, make an anticyclonic turn of more than 90). The traditional view is that the WBC separates from the wall, turns offshore, and forms an eddy. In the pioneer work "The retroflection paradox" of Nof & Pichevin (1996) in the frame work of the NBC they stipulate that: "integration of the steady inviscid momentum equation along the boundary gives the longshore momentum flux (or flow force) and shows that such a scenario leads to a paradox. To resolve the

paradox the separated current must constantly shed anticyclones, which propagate to the northwest due to β-effect (the latitudinal variation of the Coriolis parameter) and an interaction with the boundary. This new eddy shedding mechanism, which is not related to the traditional instability of a zonal jet, may explain why the NBC must produce rings". In a series of papers [*e.g.*, Nof & Pichevin (1996), hereafter NP] state that under a rather restricted set of conditions, this is a necessity arising from a momentum imbalance for a steady frictionless retroflecting current [Pichevin & Nof (1996, 1997); Nof & Pichevin (1999); Pichevin et al. (1999); see also Nof et al. (2004) for an interesting review]. By integrating the zonal momentum equation in a reduced gravity model of the ocean over a suitable area, Van Leeuwen & de Ruijter (2009) show that the derivation as proposed by NP is valid only for currents that satisfy very specific outflow conditions. They treat all possible configurations that retroflecting currents can have and also discuss the retroflecting currents with friction. They state that "in a basin-wide view of these separating current systems, a scaling analysis reveals that steady separation is impossible when the interior flow is non-dissipative (*e.g.*, linear Sverdrup-like). These findings point to the possibility that a large part of the variability in the world's oceans is due to the separation process rather than to instability of a free jet."

After giving a succinct synopsis of the analytical approaches to explain the retroflection and the eddy shedding, it is necessary to consider numerical approaches for further investigation.

There is today no analytical solution of the eddy shedding boundary current and numerical simulations of varying complexity are necessary to understand its dynamics.

1.2   Realistic models: the Somali Current

A considerable number of modelling studies (with a realistic coast line and topography) have (over more than 30 years) simulated the WBCs. Most of them treat the mid-latitude WBCs rather than the low latitude WBCs. The low latitudes WBCs namely the North Brazil Current (NBC hereafter) and the Somali Current (SC hereafter) are the center of interest of this thesis. To proceed it is necessary to give some background on which this work is based.

The Somali Current is chosen in this section and this choice is motivated by its strong variability subject to the varying Monsoon winds (see chapter 5 for more detail), whereas the NBC is driven by the Trade Winds which are less variable.

Observations from recent WOCE measurements and TOPEX/Poseidon satellite altimetry show that the Northern Somali Current retroflects during the summer monsoons to form a large anticyclonic eddy the 'Great Whirl' in the 4-10ºN latitude range and two anticyclonic gyres: the 'Southern Gyre' localized south of 4ºN and the 'Socotra Eddy' close to the Socotra Island (see section 5.2 for more detail). Most of the modeling studies have attempted to simulate the Northern Somali Current response to the summer monsoon and to understand the processes that cause it. Both local and remote forcing mechanisms have been proposed to explain its appearance. Local forcing is defined here

to be directly driving by the alongshore component of the coastal winds. Remote forcing includes offshore wind fields that excite baroclinic Rossby waves that subsequently propagate to the African coast. Several categories of such waves have been considered: i) equatorially trapped Rossby waves; ii) Rossby waves that radiate off the Indian coast; and iii) Rossby waves generated by the wind curl offshore from the Somali Coast. A prominent example of the latter is the region of very strong negative wind curl along the eastern side of the *Findlater Jet*[1]; it is expected to drive an anticyclonic circulation, and several studies have suggested that the Great Whirl may be a directly forced response to this curl [Schott & Quadfasel (1982); Luther & O'Brien (1985)]. Another possible remote forcing mechanism is the inertial overshoot of the northward-flowing Somali Current across the equator. Collectively, the studies indicate that local forcing is the primary forcing mechanism of the summertime Somali Current [see *e.g.* Hurlburt & Thompson (1976); Philander & Pacanowski (1981); Lin & Hurlburt (1981); Cox (1979, 1981); Philander & Delecluse (1983); McCreary & Kundu (1988)], but that remote effects as i) equatorial waves [see *e.g.* Lighthill (1969); Cane & Gent (1984); Visbeck & Schott (1992)] and ii) inertial overshoot [Anderson & Moore (1979); Knox & Anderson (1985)] are also important, and in some cases significantly alter the boundary flows.

Although realistic models permit to represent the observed features of the world's oceans, it is difficult to learn about isolated processes because all the phenomena take part simultaneously in the dynamics and interact non-linearly. The only way to guarantee our understanding of the oceanic dynamics is to decompose it in processes. This is the origin of the idea of idealized modelling.

1.3 Idealized models: western boundary currents at low latitudes

Idealized models are a powerful tools to entangle the dynamics of a complex system as the ocean. Idealization is the process by which scientific models assume facts about the phenomenon being modeled that are close to the reality and make models easier to understand or solve. The first stage is then to identify the important processes of the system. The second stage is the choice of one or several physical models wherein the process in question is (quasi-) isolated. The physical model represents a laboratory experiment or a real or hypothetical physical situation. This model should be sufficiently complete and realistic to include the salient features of the process but quite simple to allow an understanding at human scale. The choice of the physical model is the decisive stage in scientific research, requesting scientific intuition and experience. The intrinsic work on the model, then, is often systematic.

There is a large number of idealized numerical work that simulates the SC and the NBC with a realistic coast line and topography but there are very little works with an idealized coast line, to entangle the dynamics of low latitude WBCs.

---

1. The Findlater jet: The atmospheric equivalent of an oceanic western boundary current, a narrow low-level, atmospheric jet, develops during the Southwest monsoon, and blows diagonally across the Indian Ocean, parallel to the coasts of Somali and Oman

In a series of numerical experiments (with varying Reynold number) on the tropical deep WBC in a rectangular domain forced by a localized, Northern Hemisphere mass source and a distributed sink that require a net, cross-equatorial mass flux, Edwards & Pedlosky (1998a) investigated how potential vorticity changes sign as fluid crosses the equator and thus established that the eddy field is an essential mechanism for the potential vorticity transformation in nonlinear cross-equatorial flow. They discovered that the vorticity dynamics associated with cross-equatorial flow is different from those in the mid-latitude studies. Their second work [Edwards & Pedlosky (1998b)] focuses on the stability of the deep WBC and permits to predict successfully the time and length scales for the growth of the instability, the critical Reynold number at which time-dependent motion appears and its tendency to form near the equator as found in a β-plane numerical model. Their findings suggest that the latitudinal dependence of the instability reflects the meridional variation of the internal deformation radius. Fox-Kemper & Pedlosky (2004) discusses the dynamics of a single wind-driven gyre in a barotropic constant depth β-plane model, by focusing on vorticity fluxes and the inertial effects on the boundary by controlling non-locally thin regions near the boundaries with a locally enhanced viscosity. In their work the circulation strength appears to be unrealistic.

The above mentioned research was directed towards a detailed determination of the vorticity balances, fluxes and stability of the WBC.

Flowing along the western boundaries, the turbulent dynamics of WBCs which is the subject of my thesis remains poorly studied in the viewpoint of boundary-layer theory. To the best of our knowledge there is so far no description or theory of near wall turbulence in the WBC, that goes beyond the synoptic anticyclonic eddies. Even for oceanic WBCs in general the quantitative description is mainly based on laminar Munk-layer, inertial-layer theories and the analysis of their stability [see *e.g.* Edwards & Pedlosky (1998b); Ierley & Young (1991)]. This is in stark contrast to engineering fluid dynamics, where the turbulent boundary-layer theory is the leading domain since its birth in the beginning of the 20th century by *Prandtl (1904)* [Prandtl (1944)]. Indeed, numerical evidence from idealized experiments with a turbulent boundary-layer is scant. I here investigate other subjects such as coherent structures and multiple boundary-layers and their characteristic length scales. My research is clearly inspired by the recent (since 1990s) research on boundary-layers in the engineering community, which today focuses mostly on the role of coherent structures, length scales and intermittency, after average quantities and fluxes have been determined prior to this date. I also like to point out that the present study of the WBC from another viewpoint (boundary-layer theory viewpoint) is important for the community of ocean modelers as the scales considered in this study are those of the transition form today's coarse to fine resolution models and idealized research on the qualitative and quantitative transition in the dynamics at these scales is valuable to the community.

1.4 Outline of the thesis

The first part of this thesis examines the dynamics of two types of turbulent WBCs at low latitudes: the first is obtained by an idealized Monsoon Winds forcing and the resulting boundary current crosses the equator. The second is subject to an idealized Trade Winds forcing leading to two gyres, one north and another south of the equator. To study the dynamics I use a $1\frac{1}{2}$-layer shallow water model in a rectangular domain and in an equatorial β-plane geometry. The aim is to study the low latitude turbulent WBCs, determine their structure and their dependence on the Reynolds number, by varying the viscosity between experiments. The experimental set-up comprises essential prerequisites such as a fine resolution throughout the domain and long-time integrations to obtain statistically converged results. The physical situation considered, the mathematical model to study the dynamics and its numerical implementation are discussed in the chapter 2. Results on the taxonomy of the coherent structures, the turbulent fluxes, their parameterization and the vorticity balance are given in the chapter 4 and discussed in the chapter 8

The second part of this thesis is to apply the findings of the idealized reduced-gravity shallow water model to the realistic simulations of the OGCM NEMO in the DRAKKAR configurations. The Indian Ocean and its exceptional WBC namely of the Somali Current is considered. The chapter 5 reviews briefly observations and gives a general overview of the wind-stress fields. It discusses the Indian Ocean general circulation and more specifically the Arabia Sea circulation with an upgraded schematic diagram of the Somali Current flow patterns over the course of the year. The NEMO model, the Drakkar configurations, the three simulations ORCA025.L75-MJM95 (1/4º), ORCA12.L46-MAL84 (1/12º) and ORCA12.L46-MAL95 (1/12º) used and the diagnostic tools are described in the chapter 6. The validation of the Arabian Sea circulation and the dynamics of the planetary waves driven circulation and their influence on the Somali Current, the formation processes of Somali eddies and their scale of motion are given in the chapter 7 and discussed in chapter 9.

Part I

Dynamics of Turbulent Western Boundary Currents at Low Latitude in a Reduced Gravity Shallow Water Model

Chapter 2

Reduced Gravity Shallow Water Model

Contents

In fluid dynamics, the modelling of free surface flows is an extensive domain of research which plays an important role in many geophysical and engineering applications such as the ocean circulation, coastal exploitation, man-made structures in rivers or lakes or the study of atmosphere for instance. It is usual to describe this kind of flow in a classical fluid mechanics framework using the three dimensional Navier-Stokes equations, assuming the fluid to be Newtonian, viscous and incompressible. Computationally, the complete resolution of the Navier-Stokes equations for a free surface flow is known to be dramatically onerous and the three dimensional framework often entails numerical complexity in the meshing procedure and the implementation of the discretization method. For these reasons, and when the fluid domain can be regarded as a thin layer of fluid (when the ratio between the vertical and the horizontal scales is small enough), it is usual to consider the shallow water equations rather than the Navier-Stokes equations.

More generally, the shallow water equations (SWE hereafter) model the dynamics of a shallow, rotating layer of homogeneous incompressible and inviscid fluid and are typically used to describe vertically averaged flows in three dimensional domains, in terms of horizontal velocity and layer thickness variation.

Numerical solutions of hydrodynamic problems offer the possibility of predicting the behavior of the relevant variables in practical situations. Computational models of the SW are well-established tools in many research fields involving free surface flows, like for instance hydraulics, ocean circulation or coastal engineering.

The SW is widely used in simulation of oceanic dynamics. They are also used for idealized studies [see for instance Morel & McWilliams (1997); Thierry & Morel (1999); Vandermeirsch et al. (2001), and references therein].

This set of SWE is particularly well-suited for the study and the numerical simulations of the present considered dynamics of WBCs.

Before continuing it is essential to recall the basis of the SW model.

2.1 From the Navier-Stokes equations to the shallow water equations

I briefly introduce the classical set of three dimensional Navier-Stokes equations which are the basis of the following analysis. Incompressible homogeneous fluid dynamics in 3D is described by the Navier-Stokes equations in Cartesian coordinates:

$$\partial_t u + u\partial_x u + v\partial_y u + w\partial_z u + \frac{1}{\rho_0}\partial_x P \;\; = \;\; \nu\nabla^2 u + F_x, \tag{2.1}$$

$$\partial_t v + u\partial_x v + v\partial_y v + w\partial_z v + \frac{1}{\rho_0}\partial_y P \;\; = \;\; \nu\nabla^2 v + F_y, \tag{2.2}$$

$$\partial_t w + u\partial_x w + v\partial_y w + w\partial_z w + \frac{1}{\rho_0}\partial_z P \;\; = \;\; -g\frac{\rho}{\rho_o} + \nu\nabla^2 w + F_z, \tag{2.3}$$

$$\partial_x u + \partial_y v + \partial_z w \;\; = \;\; 0, \tag{2.4}$$

$$+ \text{ boundary conditions}, \tag{2.5}$$

where u is the zonal, v the meridional and w the vertical (positive upward even in oceanography) velocity component, P the pressure, ρ density, ρ_o the average density, ν viscosity of seawater, g gravity, $\nabla^2 = \partial_{xx} + \partial_{yy} + \partial_{zz}$ is the Laplace operator, F represent forces other than the intrinsic fluid forces. For homogeneous and incompressible fluid motions, the condition of mass conservation reduces to the incompressibility condition (Eq.(2.4)).

In the ocean the depth of the fluid varies in space. The average thickness H of the oceans is around 4km whereas their horizontal characteristic value is about 4000km. So the ratio of the vertical scale to the horizontal one, the so-called aspect ratio, is about $\frac{1}{1000}$. In this context, I would assume that the vertical movements and variations are very small compared to the horizontal ones. The continuity equation allows in the same way to estimate the ratio of the vertical and horizontal velocity scales, respectively W and V:

$$\frac{W}{V} \approx \frac{H}{L} \approx \frac{1}{1000}, \tag{2.6}$$

where H, L, W, V, are respectively the characteristic scales for the vertical and the horizontal dimensions of the ocean domain of interest and for the vertical and horizontal velocities. By focusing attention on single scale motions only, that is, by characterizing the motion by single scale for velocity and length, the nearly horizontal character of the fluid trajectories makes the vertical velocity w so small compared to the horizontal ones that it can to first order be neglected ($w \ll u, v$). This reduces the Eq.(2.3) to:

$$\partial_z P = -g\rho, \tag{2.7}$$

which is called the *hydrostatic approximation* as the vertical pressure gradient is now independent of the velocity in the fluid.

Another important aspect is the smallness density differences $\frac{\Delta\rho}{\rho} \approx 3 \cdot 10^{-3}$ of sea water which permits the incompressibility assumption, that is $\rho = \rho_0$ is a constant and $\Delta\rho = 0$. Using the homogeneity $\Delta\rho = 0$ further suggest that:

$$\partial_{xz} P = \partial_{yz} P = 0. \tag{2.8}$$

Deriving Eq.(2.1) and Eq.(2.2) with respect to the vertical direction one can see that if $\partial_z u = \partial_z v = 0$ at some time this property will be conserved such that u and v do not vary with depth. Putting all this together, for an incompressible fluid, the three-dimensional momentum Navier-Stokes equations, can be simplified to:

$$\partial_t u + u\partial_x u + v\partial_y u + \frac{1}{\rho}\partial_x P = \nu\nabla^2 u + F_x, \tag{2.9}$$

$$\partial_t v + u\partial_x v + v\partial_y v + \frac{1}{\rho}\partial_y P = \nu\nabla^2 v + F_y, \tag{2.10}$$

$$\partial_x u + \partial_y v + \partial_z w = 0, \tag{2.11}$$

$$\text{with } \partial_z u = \partial_z v = \partial_{zz} w = 0, \tag{2.12}$$

$$+ \text{ boundary conditions.} \tag{2.13}$$
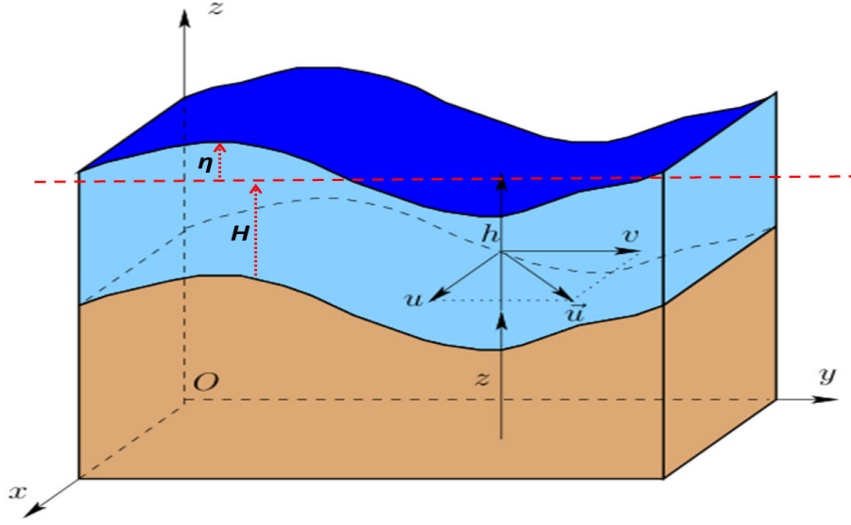
Figure 2.1 – *Schematically illustration of shallow water configuration.*

The next step is to find the form of the horizontal pressure gradient force acting on the shallow, incompressible fluid. Supposed in the ocean there exists a "free" surface of constant or nearly constant pressure, which is also a material surface in the sense that no mass crosses it. Let η be the height variation. As mentioned above, it is assumed that no fluid crosses the free surface. If follows that the height of a parcel embedded in the free surface satisfies

$$\frac{D\eta}{Dt} = w(\eta), \tag{2.14}$$

where $\frac{D}{Dt} = \partial_t + u\partial_x + v\partial_y$ is the horizontal Lagrangian derivative.

Similarly, no fluid can cross the lower-layer, so the fluid motion must follow the two layers inter-facial topography:

$$\frac{D\eta}{Dt} = (H + \eta)\partial_z w, \tag{2.15}$$

or

$$\partial_t\eta + u\partial_x\eta + v\partial_y\eta - (H + \eta)\partial_z w = 0, \tag{2.16}$$

or

$$\partial_t\eta + u\partial_x(H + \eta) + v\partial_y(H + \eta) + (H + \eta)(\partial_x u + \partial_y v) = 0. \tag{2.17}$$

Using the assumption that the density is constant with depth and the hydrostatic approximation, the pressure at a depth d from the unperturbed free surface is given by: $P = g\rho(\eta + d))$, and the horizontal pressure gradient is related to the horizontal gradient of the free surface by:

$$\partial_x P = g\rho\partial_x\eta \quad \text{and} \quad \partial_y P = g\rho\partial_y\eta. \tag{2.18}$$

Substituting Eq. (2.18) in the Navier-Stokes equations leads to the shallow water equations:

$$\partial_t u + u\partial_x u + v\partial_y u + g\partial_x \eta \;=\; \nu\nabla^2 u + F_x, \tag{2.19}$$

$$\partial_t v + u\partial_x v + v\partial_y v + g\partial_y \eta \;=\; \nu\nabla^2 v + F_y, \tag{2.20}$$

$$\partial_t \eta + \partial_x[(H+\eta)u] + \partial_y[(H+\eta)v] \;=\; 0, \tag{2.21}$$

$$+ \text{ boundary conditions.} \tag{2.22}$$

All variables appearing in Eq. (2.19), (2.20) and (2.21) are independent of the z-coordinate! In the rotating fluid, the Coriolis force is added to the shallow water equations:

$$\partial_t u + u\partial_x u + v\partial_y u - fv + g\partial_x \eta \;=\; \nu\nabla^2 u + F_x, \tag{2.23}$$

$$\partial_t v + u\partial_x v + v\partial_y v + fu + g\partial_y \eta \;=\; \nu\nabla^2 v + F_y, \tag{2.24}$$

$$\partial_t \eta + \partial_x[(H+\eta)u] + \partial_y[(H+\eta)v] \;=\; 0, \tag{2.25}$$

$$+ \text{ boundary conditions,} \tag{2.26}$$

where $f = 2\Omega \sin\theta$ ($\Omega = 2\pi/T$ represents the planetary angular velocity with T the rotation period of the earth, θ the latitude).
At low-latitude, the dependence of f is close to linear. The linear approximation:

$$f = \beta y, \tag{2.27}$$

is called the *equatorial β-plane*. In this β-plane approximation the horizontal coordinate system is supposed to be Cartesian, that is the convergence of the meridians with latitude is neglected.

The shallow water configuration is represented schematically in Fig. 2.1. After formulating the shallow water equations, let's go to the most widely used example of shallow water equations in the study of the upper oceanic circulation simulation.

2.2 From the shallow water equations to the reduced gravity model

The simplest way to simulate the upper ocean circulation is to assume that the ocean is homogeneous in density. Such a model has no vertical structure. However, there is a prominent main thermocline in the oceans, so a more precise way of simulating the upper ocean circulation is to incorporate the main thermocline as a step function in density. In this way, the stratification in the ocean is simplified as a two-layer fluid. Fluid below the main thermocline moves typically much slower than that above the main thermocline. As a good approximation, one can assume that fluid in the thicker lower-layer is near stagnant. Such a model has one active layer only, and it is called a *reduced gravity SW model*. The advantage of a reduced gravity model is its ability to approximate the first baroclinic mode of the circulation and the structure of the main thermocline.

The essence in constructing up a reduced gravity model is to treat the main thermocline (or the pycnocline) in the oceans as a step function in density, so density in the upper layer is equal to a constant $\rho_1 = \rho$ and the density in the lower layer is $\rho_2 = \rho + \Delta\rho$. Furthermore, the lower layer is assumed infinitely deep and at rest, so pressure gradient in the lower layer is infinitely small. This implies that the lower layer is always in equilibrium. The lower layer is passive, does not act on the upper layer but adapts to its dynamics, so that:

$$\eta_1 = \frac{\rho_1 - \rho_2}{\rho_1}\eta_2 = \frac{\Delta\rho}{\rho}\eta_2. \tag{2.28}$$

The total layer thickness variation is $\eta = \eta_1 - \eta_2$ which is also given by

$$\eta = \frac{\rho}{\Delta\rho}\eta_1. \tag{2.29}$$

The dynamics is described by the same SWE (2.23), (2.24) and (2.25), with gravity g replaced by the *reduced gravity*

$$g' = \frac{\Delta\rho}{\rho}g. \tag{2.30}$$

The momentum and continuity equations for a reduced gravity model are:

$$\partial_t u + u\partial_x u + v\partial_y u - fv + g'\partial_x \eta = \nu\nabla^2 u + F_x, \tag{2.31}$$
$$\partial_t v + u\partial_x v + v\partial_y v + fu + g'\partial_y \eta = \nu\nabla^2 v + F_y, \tag{2.32}$$
$$\partial_t \eta + \partial_x[(H+\eta)u] + \partial_y[(H+\eta)v] = 0, \tag{2.33}$$
$$+ \text{ boundary conditions}. \tag{2.34}$$

It is noteworthy to mention the absence of inter-facial friction terms in the above reduced-gravity equations. The friction between two superposed layers, separated by a density gradient is small as turbulent fluxes, of tracers and momentum, across the interface are inhibited by the stratification. This reduced gravity model is used for the sequel of the first part to entangle the dynamics of turbulent western boundary current. This choice of the reduced gravity model is justified by the horizontal scale of the coherent structures and boundary-layers which is always larger than 10km. The layer height is $H = 200$m, using the scaling analysis as in Eq. (2.6)

$$\frac{H}{\lambda_2} \approx 2 \cdot 10^{-2}, \tag{2.35}$$

where λ_2 is the smallest scales in the vortical dynamics (see section 4.6) shows that the layer is indeed shallow.

Chapter 3

Application to Low Latitudes Upper Circulation

Contents

As said in the introduction, at low latitudes of the Atlantic and Indian oceans occur the NBC and the SC, respectively with their system of eddies. The Atlantic Ocean is dominated by the Trade Winds. In the Indian Ocean exist also a weak Trade Winds but the wind stress is dominated by the Monsoon Winds [Schott & McCreary Jr (2001)].

The reduced gravity model is used to investigate the response of the western boundary region of a tropical ocean subject to winds typical of the Trade Winds and Monsoon Winds. The central problem is similar to that of mid-latitude gyres in which the vorticity budget of a strongly nonlinear system is considered.

Two types of the WBC are considered: cross-equatorial flows and non-cross-equatorial flows obtained by applying the two types of idealized wind stress forcing in a highly idealized shallow model. In those studies, the vorticity input by the wind forcing must be dissipated through the boundary-layer dynamics. A term-by-term evaluation of the vorticity balance in the boundary region where eddies occur is used to analyze the balance. To simplify the study several idealizations have been adopted. The model is configured in a highly idealized basin, with horizontal boundaries that coincide with lines of longitudes and latitudes. The longitudes and the latitudes are supposed to form a Cartesian grid, neglecting the sphericity of the earth, such geometry is referred to as the β-plane. However, I believe that these simplifications do not alter the fundamental dynamics described here: that strongly nonlinear, cross-equatorial and non-cross-equatorial flow requires the turbulent exchange of vorticity between frictional and inertial regions of the boundary current.

3.1   The physical problem considered

The model geometry is extremely simple, in accord with the desire to perform the simplest possible experiment which might represent the cross and non-cross equatorial WBCs in attempt to simulate the Tropical Atlantic and Indian Ocean WBCs. A rectangular basin that straddles the equator is chosen. The formulation considers an active layer of fluid above an infinite resting layer as introduced above. The choice of the average thickness $H = 200$m is dictated by the tropical thermocline depth size and the desire to have the model's Rossby wave propagation speed similar to the baroclinic speed observed in the tropical ocean. The reduced gravity $g' = \frac{\Delta \rho}{\rho} g = 0.03$m $\cdot$ s^{-2} is chosen according to the density difference of the tropical ocean. Regarding the similarity of the tropical Atlantic and the tropical Indian ocean, the dynamic processes studied here are similar for both oceans. The basin has the size of the Indian Ocean (Fig. 3.1), but please note that this size does not affect substantially the system's non-linear dynamics, since the non-linear term itself is almost negligible outside the boundary current regions.

Idealized models are mostly used to study the mid-latitude oceans. Indeed the model used in the present study was validated by reproducing a mid-latitude gyre (not shown). In the experiments presented here, the model is forced by wind stress. Note that the amplitude of the fluid motion and hence the strength of the system's nonlinearity are influenced by the magnitude of the wind stress and the lateral viscosity. Thus, nonlinear

advection effects of WBC can be studied varying this two parameters [Jiang et al. (1995)]. The results obtained can be compared to the coherent vortex structures observed by satellite which often take on the appearance of eddies and dipoles. It can also be compared to results from laboratory experiments in rotating tanks [Stern & Whitehead (1990); Lichter et al. (1992)].

3.2   The mathematical model

The $1\frac{1}{2}$-layer reduced gravity shallow water equations are integrated in tropical latitude rectangular basin on the β-plane, given by $0 \leq \mathrm{x} \leq L_x$ and $0 \leq \mathrm{y} \leq L_y$. The dynamic is governed by the reduced-gravity shallow water equations:

$$\partial_t u + u\partial_x u + v\partial_y u - fv + g'\partial_x \eta \; = \; \nu\nabla^2 u + \frac{C_1\tau_x}{\rho(H+\eta)}, \tag{3.1}$$

$$\partial_t v + u\partial_x v + v\partial_y v + fu + g'\partial_y \eta \; = \; \nu\nabla^2 v + \frac{C_2\tau_y}{\rho(H+\eta)}, \tag{3.2}$$

$$\partial_t \eta + \partial_x[(H+\eta)u] + \partial_y[(H+\eta)v] = 0; \tag{3.3}$$

recall, u and v represent, respectively, the zonal and meridional velocities. The Coriolis parameter $f = \beta y$ is a linear function of latitude, $g' = \frac{\Delta\rho}{\rho}g$ is the reduced gravity, and τ_x, τ_y represent, respectively, the zonal and meridional wind-stress that drives the upper ocean. The system is subject to wind-stress forcing τ_x, τ_y and to the Laplacian lateral diffusion with an eddy viscosity ν. It is necessary to impose the no-slip boundary conditions and its role is also to prevent the accumulation of energy/enstrophy at the smallest scales that are resolved numerically. Please see Frisch et al. (2008), for a detailed discussion of this bottleneck phenomena.

Considering the partial derivative by x of the Eq. (3.2) minus the partial derivative by y of the Eq. (3.1) and introducing the relative vorticity $\xi = \partial_x v - \partial_y u$ lead to the associated vorticity equation:

$$\partial_t \xi + u\partial_x \xi + v\partial_y \xi + \beta v + (\xi + f)(\partial_x u + \partial_y v) - \nu\nabla^2 \xi = S, \tag{3.4}$$

or in conservative form:

$$\partial_t \xi + \partial_x[u(\xi + f)] + \partial_y[v(\xi + f)] - \nu\nabla^2 \xi = S, \tag{3.5}$$

where S is the curl of the forcing.

The region which has been considered in this study is shown in Fig. 3.1, superimposed on a map of the Indian Ocean for reference. The basin is a rectangular box spanning from 1000km south of the equator to 3000km north of it ($L_x = 4000\mathrm{km}$) and it extends $L_y = 6000\mathrm{km}$ in the latitudinal direction. In Fig. 3.1, the inner, red bold rectangle describes the boundary for the numerical experiments discussed. The southern boundary of the model basin does not correspond to any real boundary of the Indian Ocean.
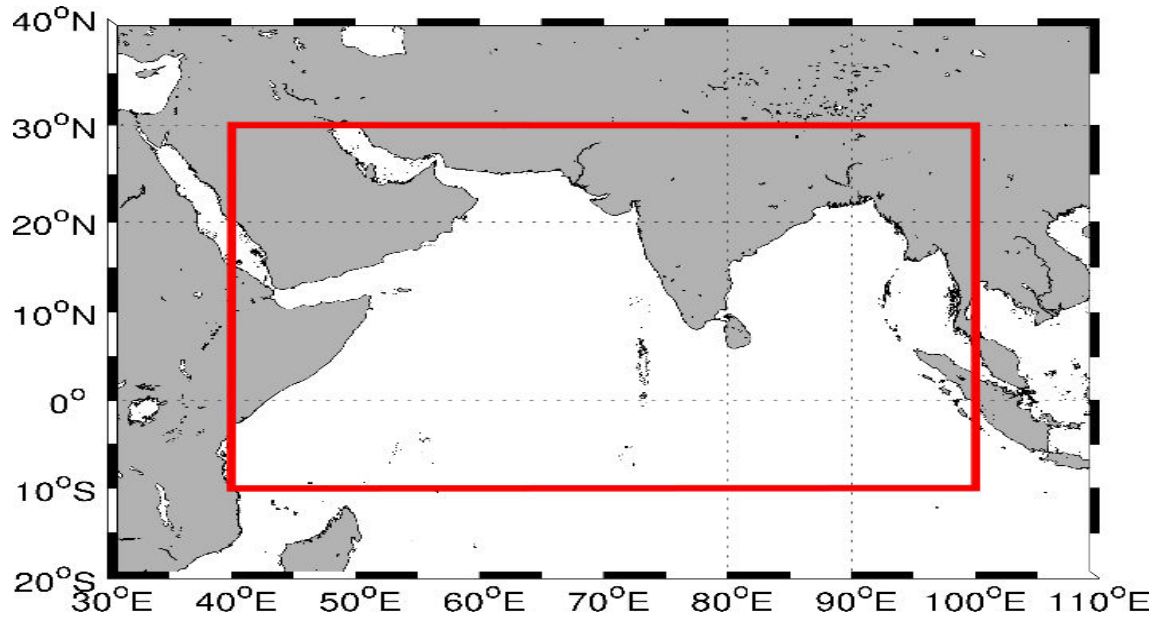
Figure 3.1 – *Regions of solution (red line), superimposed on a map of the Indian Ocean for reference.*

parameter	Value
β, rate of change of Coriolis parameter	$2 \cdot 10^{-11} \mathrm{m}^{-1} \cdot \mathrm{s}^{-1}$
τ_0, wind-stress amplitude	$0.1 \mathrm{N} \cdot \mathrm{m}^{-2}$
ν, eddy viscosity coefficient	$1000 \mathrm{m}^2 \cdot \mathrm{s}^{-1}$
H, upper-layer thickness	200m
ρ, upper-layer density	$1000 \mathrm{kg} \cdot \mathrm{m}^{-3}$
L_x, east-west extend	6000km
L_y, north-south extend	4000km
$g\prime$, reduced gravity	$0.03 \mathrm{m} \cdot \mathrm{s}^{-2}$

Table 3.1 – *Model parameters*

3.3   The numerical implementation

The numerical method used to solve the SW equations is a centered, second-order finite difference scheme in space. A second-order *Runge-Kutta* scheme is used for time stepping.

The numerical grid has a square geometry, no grid refinement is used. Grid refinement on the boundary leads to highly anisotropic grids, this is adapted for laminar boundary-layers which vary in the vicinity of the boundary. In non-linear dynamics, small scale structures are torn away from the boundary rotated and transported towards the interior, such process can only be well represented by fine isotropic grids extending far from the boundary. A fine numerical resolution of square geometry ($\Delta x = \Delta y = 2.5$km) is employed throughout the entire domain. This uncommon choice, of not using grid refinement at the boundary, is justified by the results in the section 4.5, where it is clearly seen that for high Reynolds number flows, parts of the viscous boundary-layer are torn of the wall and transported away from it by the surrounding turbulent flow. Such kind of process can only be represented when there is fine resolution in both horizontal directions throughout the extended boundary-layer (to be defined in the sub-section 4.6). Please note that the resolution is well below the Munk scale $\delta_{\mathrm{M}} = (\nu/\beta)^{1/3}$ (detailed in section 4.3), the smallest scale in the boundary-layer, which is around 18km in the lowest viscosity run. Fine resolution in time and space is favored rather than high-order schemes.

The time-step is $\Delta t = 90$s, which is almost ten times shorter than the CFL time-step imposed by the speed of the gravity waves. In the non-linear boundary-layer the high vorticity in the boundary-layer is intermittently torn of the boundary. This process is the equivalent of bursts in 3D boundary-layers [see *e.g.* Robinson (1991)]. It is this process and its non-linear evolution that asks for a short time step.

3.3.1   Discretization: finite difference approximations

In general, a *finite difference* approximates the value of some derivative of a scalar function $A(x)$ at a point x_o in its domain, say $A'(x_o)$ or $A''(x_o)$, relies on a suitable combination of sampled function values at nearby points. The underlying formalism used to construct these approximation formulae is known as the *calculus of finite differences*. Its development has a long and influential history, dating back to *Newton*.

The simplest finite difference approximation is the ordinary difference quotient

$$\frac{A(x+h) - A(x)}{h} \approx A'(x), \tag{3.6}$$

that appears in the original calculus definition of the derivative. Indeed, if A is differentiable at x, then $A'(x)$ is, by definition, the limit as $h \to 0$ of the finite difference quotients. Geometrically, the difference quotient measures the slope of the secant line through the two points $(x, A(x))$ and $(x + h, A(x + h))$ on its graph. For small enough h, this is a reasonably good approximation to the slope of the tangent line, $A'(x)$, as illustrated in the first picture in Fig. 3.2. Throughout the discussion, h, the *step size*, which may be

either positive or negative, is assumed to be small in order to have a good approximation. When $h > 0$, Eq. (3.6) is referred to as a *forward difference*, while $h < 0$ yields a *backward difference*.
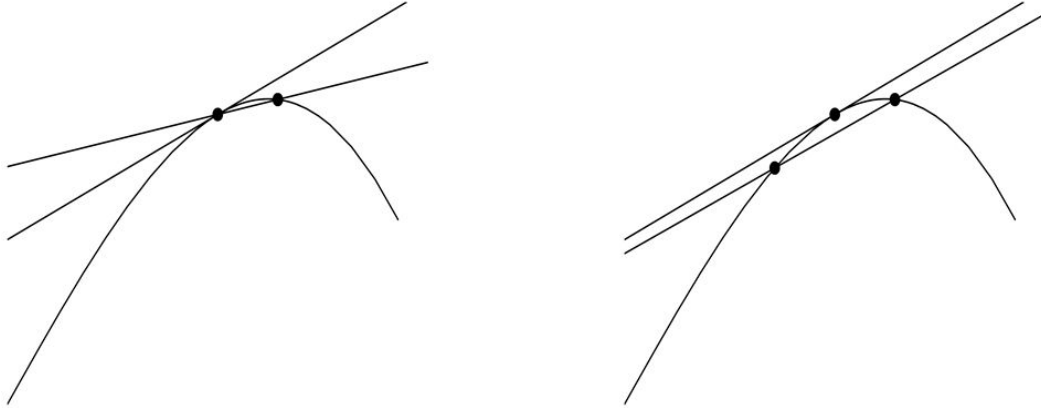
Figure 3.2 – *Finite difference approximation. Forward difference (a) and central difference (b)*

How good an approximation is the difference quotient? To answer this question, assuming that $A(x)$ is at least twice continuously differentiable, let's now examine its Taylor expansion to first order

$$A(x + h) = A(x) + A'(x)h + \frac{1}{2}A''(\alpha)h^2, \tag{3.7}$$

at the point x. The point α, which depends on both x and h, is lying between x and $x+h$. Rearranging Eq. (3.7) leads to:

$$\frac{A(x + h) - A(x)}{h} - A'(x) = \frac{1}{2}A''(\alpha)h. \tag{3.8}$$

Thus, the error in the finite difference approximation Eq. (3.6) can be bounded by a multiple of the step size:

$$\left| \frac{A(x + h) - A(x)}{h} - A'(x) \right| \leq C|h|, \tag{3.9}$$

where $C = max \left[\frac{1}{2}|A''(\alpha)| \right]$ depends on the magnitude of the second derivative of the function over the interval in question. Since the error is proportional to the first power of h, the finite difference quotient Eq. (3.6) is a *first order* approximation to the derivative $A'(x)$. When the precise formula for the error is not so important, I will write:

$$A'(x) = \frac{A(x + h) - A(x)}{h} + O(h). \tag{3.10}$$

The "big O" notation $O(h)$ refers to a term that is proportional to h, or, more precisely, whose absolute value is bounded by a constant multiple of $|h|$ as $h \to 0$.

To approximate higher order derivatives, I need to evaluate the function at more than two points. In general, an approximation to the nth order derivative $A^{(n)}(x)$ requires at least $n+1$ distinct sample points.

For example, let us try to approximate $A''(x)$ by sampling A at the particular points x, $x+h$, and $x-h$. Which combination of the function values $A(x-h)$, $A(x)$, $A(x+h)$ should be used? The answer is found by consideration of the Taylor expansions [1]

$$A(x+h) = A(x) + A'(x)h + A''(x)\frac{h^2}{2} + A'''(x)\frac{h^3}{6} + O(h^4), \quad (3.11)$$

$$A(x-h) = A(x) - A'(x)h + A''(x)\frac{h^2}{2} - A'''(x)\frac{h^3}{6} + O(h^4), \quad (3.12)$$

where the remaining terms are proportional to h^4. Adding the two formulae together gives

$$A(x+h) + A(x-h) = 2A(x) + A''(x)h^2 + O(h^4). \quad (3.13)$$

Dividing by h^2 and rearranging terms, permits to arrive at the *centered finite difference approximation* to the second derivative of a function:

$$A''(x) = \frac{A(x+h) - 2A(x) + A(x-h)}{h^2} + O(h^2). \quad (3.14)$$

Since the error is proportional to h^2, this forms a second order approximation.

To further improve the order of accuracy of finite difference approximation it is necessary to employ more sample points. For instance, if the first order approximation Eq. (3.14) to $A'(x)$ based on the two points x and $x+h$ is not sufficiently accurate, one can try combining the function values at three points, say x, $x+h$, and $x-h$. To find the appropriate combination of function values $A(x-h)$, $A(x)$, $A(x+h)$, let us return to the *Taylor* expansions Eq. (3.11). To solve for $A'(x)$, I subtract [2] the two formulae, and so

$$A(x+h) - A(x-h) = 2A'(x)h + A'''(x)\frac{h^3}{3} + O(h^4). \quad (3.15)$$

Rearranging the terms, It is led to the well-know *centered difference formula*

$$A'(x) = \frac{A(x+h) - A(x-h)}{2h} + O(h^2), \quad (3.16)$$

which is a second order approximation to the first derivative. Geometrically, the centered difference quotient represents the slope of the secant line passing through the two points $(x-h, A(x-h))$ and $(x+h, A(x+h))$ on the graph of A centered symmetrically about the point x. Fig. 3.2 illustrates the two approximations, and the advantage of the centered

---

[1]. Throughout, the function A(x) is assumed to be sufficiently smooth in order that the derivatives that appear are well defined and the expansion formula is valid.

[2]. *Important*: The terms $O(h^4)$ do *not* cancel, since they represent potentially different multiples of h^4

difference version is graphically evident. High order approximations can be found by evaluating the function at yet more sample points, say, $x + 2h$, $x - 2h$, etc.

The centered second order finite difference scheme is used to solve the SW equations. The example of the Eq. (3.1) is detailed here and it is the same manner for the other equations. After discretization the Eq. (3.1) becomes:

$$\frac{u^{n+1}(i,j) - u^n(i,j)}{\Delta t} + u^n(i,j) \cdot \frac{u^n(i+1,j) - u^n(i-1,j)}{2 \cdot \Delta x} + v^n(i,j) \cdot \frac{u^n(i,j+1) - u^n(i,j-1)}{2 \cdot \Delta y} - f(i,j) \cdot v^n(i,j) + g' \cdot \frac{\eta^n(i+1,j) - \eta^n(i-1,j)}{2 \cdot \Delta x}$$

$$= -\nu \left[\frac{u^n(i+1,j) - 2u^n(i,j) + u^n(i-1,j)}{\Delta x^2} + \frac{u^n(i,j+1) - 2u^n(i,j) + u^n(i,j-1)}{\Delta y^2} \right] + \frac{C_1 \cdot \tau_x(i,j)}{\rho[H + \eta^n(i,j)]}, \quad (3.17)$$

where the superscripts n and $n+1$ represent the time stepping. Knowing that the system evolving from the rest $(u^0(i,j) = v^0(i,j) = \eta^0(i,j) = 0$ and by deduction $\xi^0(i,j) = 0)$, and the value of the forcing and the other parameters, the state of system after Δt time must be obtain easily by:

$$u^{n+1}(i,j) \quad = \quad u^n(i,j) \quad - \quad \Delta t \quad \cdot \quad \left\{ u^n(i,j) \cdot \frac{u^n(i+1,j) - u^n(i-1,j)}{2 \cdot \Delta x} + \quad \cdot \quad \cdot \quad \cdot \quad \cdot \quad \cdot \quad \cdot \quad \cdot \quad \cdot \quad \cdot \quad \cdot \quad - \frac{C_1 \cdot \tau_x(i,j)}{\rho[H + \eta^n(i,j)]} \right\}. \quad (3.18)$$

By iteration the state of the system at future times can be obtained.

3.3.2 Runge-Kutta methods

The German mathematicians *Carl Runge* and *Martin Kutta* were the first to systematically studied a general class of numerical schemes for ordinary differential equations in the late nineteenth century. *Runge-Kutta* methods are by far the most popular and powerful general-purpose numerical methods for integrating ordinary differential equations. While not appropriate in all possible situations, *Runge-Kutta* schemes are surprisingly robust, performing efficiently and accurately in a wide variety of problems. They are the method of choice in many applications. They comprise the engine that powers most computer software for solving general initial value problems for systems of ordinary differential equations.

The most general Runge-Kutta Methods takes the form

$$A_{k+1} = A_k + h \sum_{i=1}^{m} c_i F(t_{i,k}, A_{i,k}), \tag{3.19}$$

where m counts the number of terms in the method. Each $t_{i,k}$ denotes a point in the kth mesh interval, so $t_k \leq t_{i,k} \leq t_{k+1}$. The second argument $A_{i,k} \approx A(t_{i,k})$ can be viewed as an approximation to the solution at the point $t_{i,k}$, and so is computed by a similar, but simpler formula of the same type. There is a lot of flexibility in the design of the method, through choosing the coefficients c_i, the times $t_{i,k}$, as well as the scheme (and all parameters therein) used to compute each of the intermediate approximations $A_{i,k}$. As always, the order of the method is fixed by the power of h to which the Taylor expansions of the numerical method Eq. (3.19) and the *Taylor expansion* Eq. (3.11) agree. Clearly, the more terms I include in the *Runge-Kutta* formula Eq. (3.19), the more free parameters are

available to match terms in the solution's *Taylor series*, and so the higher the potential order of the method. Thus, the goal is to arrange the parameters so that the method has a high order of accuracy, while, simultaneously, avoiding unduly complicated, and hence computationally costly, formulae.

To describe the design of my method, let us retake the precedent example Eq. (3.18), I choose the intermediate approximation to the solution $A_{i,k} = u_r^n(i,j)$ at the point $t_{i,k} = \frac{\Delta t}{2}$:

$$u_r^{n+1}(i,j) \quad = \quad u^n(i,j) \quad - \quad \frac{\Delta t}{2} \quad \cdot \quad \left\{ u^n(i,j) \cdot \frac{u^n(i+1,j) - u^n(i-1,j)}{2 \cdot \Delta x} + \quad \cdot \quad \cdot \quad \cdot \quad \cdot \quad \cdot \quad \cdot \quad \cdot \quad \cdot \quad \cdot \quad - \frac{C_1 \cdot \tau_x(i,j)}{\rho[H + \eta^n(i,j)]} \right\}. \quad (3.20)$$

The intermediate approximation to the solution $u_r^n(i,j)$ and the other intermediate approximation to the solutions $u_r^n(i,j)$ and $v_r^n(i,j)$ at the point $\frac{\Delta t}{2}$ are used to have the more accurately solution:

$$u^{n+1}(i,j) \quad = \quad u^n(i,j) \quad - \quad \Delta t \quad \cdot \quad \left\{ u_r^n(i,j) \cdot \frac{u_r^n(i+1,j) - u_r^n(i-1,j)}{2 \cdot \Delta x} + \quad \cdot \quad \cdot \quad \cdot \quad \cdot \quad \cdot \quad \cdot \quad \cdot \quad \cdot \quad \cdot \quad - \frac{C_1 \cdot \tau_x(i,j)}{\rho[H + \eta^n(i,j)]} \right\}. \quad (3.21)$$

Replacing the intermediate approximation to the solution in the Eq. (3.21) gives:

$$u^{n+1}(i,j) = u^n(i,j) - \frac{\Delta t^2}{2} \cdot \left\{ u^n(i,j) \quad \cdot \quad \cdot \quad \cdot \quad \cdot \quad \cdot \quad \cdot \quad - \frac{C_1 \cdot \tau_x(i,j)}{\rho[H + \eta^n(i,j)]} \right\}, \quad (3.22)$$

compared to the Eq. (3.19), this leads to $c_i \sim \frac{1}{2}$ and $h \sim \Delta t^2$. Since the power of h is 2, this forms a second-order *Runge-Kutta* scheme.

3.3.3 Courant-Friedrichs-Lewy condition

In 1967 *Richard Courant*, *Kurt Friedrichs*, and *Hans Lewy*, of the University of Göttingen in Germany, published a famous paper entitled "On the partial difference equations of mathematical physics" [Courant et al. (1967)]. This paper was written before the invention of the digital computers, and its purpose in investigating finite difference approximations was to apply them to prove existence of solutions to partial differential equations. But the "*CFL*" paper laid the theoretical foundations for the practical finite difference computations, too, and in particular, it identified a fundamental necessary condition for convergence of any numerical scheme that has subsequently come to be known as the **CFL condition**. As a consequence, the time step must be less than a certain time in many explicit time-marching computer simulations, otherwise the simulation will produce incorrect results. Thus, the time step needs to be restricted in such a way that no interaction is possible between waves from different cells during each time step. This restriction can result in expensive computations. *Courant, Friedrichs* and *Lewy* defined a stability criterion for fully explicit schemes given by $CFL < 1$ where CFL is known as the *Courant number*. Different authors propose different definitions for this number, leading to different time restrictions. I choose here to define the time step as follows:

$$\Delta t \leq CFL \frac{\min(\Delta x, \Delta y)}{\max_{i,j}(|\mathbf{u}_{i,j}| + c_{i,j})}, \quad (3.23)$$

where $\mathbf{u}_{i,j}$ is the magnitude of the velocity and $\Delta x, \Delta y$ are the grid-size in the (x, y)-directions, Δt remains the time step, $c = \sqrt{g'H}$ the speed of gravity waves.

The value of CFL depends on the method used to solve the discretized equation. In the present study, according to the uniformity of the grid-size ($\Delta x = \Delta y = 2.5$km) and the speed of the gravity waves $c = \sqrt{g'H}$, the Courant number is:

$$CFL_{\max} = \frac{\Delta x}{\sqrt{g'H}} = \frac{2500\text{m}}{\sqrt{0.03\text{ms}^{-2} \cdot 200\text{m}}} = 1020.6s. \tag{3.24}$$

The CFL condition is satisfy and as said previously the time-step $\Delta t = 90s$ is over ten times shorter than the CFL time-step imposed by the speed of the gravity waves.

3.3.4 Implementation of the numerical scheme

The experiments was performed with no-slip boundary conditions, a second-order Runge-Kutta scheme for time stepping and a spacial centered second-order finite difference scheme. Fortran 90 is used for the code. Model outputs are done as 1-day snapshots. One run of 5000days took around 5 months on the computer. The runs are computed on LEGI machines:

– **Calcul3 :** is a Xeon cluster of 12 nodes each with 12 CPU and 48GB of RAM (4GB RAM/CPU),
– **Calcul9 :** is hybrid machine composed by a symmetric multiprocessing (SMP) machine of 28 CPU Itanium (Calcul9-ita) and a Xeon cluster of 6 nodes.

Data was analyzed using Matlab.

Chapter 4

Results

Contents

4.1 Experiments performed

The dynamics is governed by the reduced gravity shallow water Eqs. (3.1), (3.2) and (3.3) and the no-slip boundary conditions. The system's behavior is mainly determined by C_1, C_2 and ν, the three parameters that control the strength of external wind forcing and the lateral viscosity, respectively. The spatio-temporal complexity of the system's behavior increases with increasing C_1 and C_2, and decreasing ν. The other model parameters are kept constant and are given in Tab. 3.2. As in McCreary & Kundu (1988) the wind-stress forcing fields used in the experiments are composed of one or more patches of the form:

$$\left(\begin{array}{c} C_1 \cdot \tau_x \\ C_2 \cdot \tau_y \end{array} \right) s(t),$$

where x and y are the zonal and meridional coordinates. To avoid an initial shock, the wind stress increases from zero as: $s(t) = 1 - exp(\frac{-t}{t_c})$ with spin-up time $t_c = 180$days. The offshore and alongshore structures, $X(x)$ and $Y(y)$, are given in Eqs. (4.1) and (4.2) and are illustrated schematically in Fig. 4.1. They are chosen in such a way that I have two kinds of winds, the Trade Winds and the Monsoon Winds leading to non-cross-equatorial and cross-equatorial WBCs respectively. In intention to have the same velocity for the two WBCs the experiment with $\nu = 1000$m$^2 \cdot$s^{-1} (linear solution) was chosen to adjust C_1 and C_2. The above leads to the implemented wind-stress in Eqs. 3.1 and 3.2 which is discriminated into a Trade Winds -forcing (C_1, C_2)=(4,0) (hereafter TW) and a Monsoon Winds -forcing (C_1, C_2)=(0,3.5)(hereafter MW) .

$$\tau_x = 0.1\frac{\text{N}}{\text{m}^2}[1 - exp(\frac{x}{L_x})][exp(-4 * (\frac{y}{L_y} - 0.25)^2)][1 - exp(\frac{-t}{t_c})], \qquad (4.1)$$

$$\tau_y = 0.1\frac{\text{N}}{\text{m}^2}[exp(-4 * (\frac{x}{L_x})^2 - 0.2)][1 - exp(\frac{-t}{t_c})]. \qquad (4.2)$$

The TW is reduced towards the eastern part of the domain as the observed TW weakness near the eastern part of the Atlantic and Indian Ocean. The TW and MW are represent schematically in Fig. 4.1.

For both types of wind forcing (TW and MW), experiments for different values of the viscosity were performed. Experiments are referred by the type of forcing followed by the viscosity value: for example MW1000 is an experiment with MW forcing and a viscosity $\nu = 1000$m$^2 \cdot$s^{-1}. The highest viscosity experiments with $\nu = 1000$m$^2 \cdot$s^{-1}, MW1000 and TW1000 converge towards a stationary dynamics before 2000days of integration. The corresponding Reynolds number based on the maximal average meridional velocity in the boundary current and the Munk-layer thickness at y = +1500km is $Re = v_o \delta_\text{M}/\nu = 31$ and 42 for TW1000 and MW1000 respectively. The numerical resolution and scheme allowed to perform calculations with viscosities down to $\nu = 125$m$^2 \cdot$s^{-1} for the TW, for the MW the lowest viscosity was $\nu = 300$m$^2 \cdot$s^{-1}. The reason for the more stable TW experiments lies in the existence of inertial effects that prevent the boundary to decrease below the value imposed by the inertial layer, it will be discussed in the sections 4.3.2 and 8.1. The

set of numerical experiments in this study examine a variety of viscosities ν summarized in Tab. 4.1.

As said above, in the high viscosity experiments the dynamics converges towards a stationary state before 2000days of the integration, while the lower viscosity experiments with time-dependent eddying flows converge to a statistically stationary state in about 3000 days. To ensure the significance of the statistics, experiments were performed for 5000days of the dynamics and time averages were calculated over the last 2000days and represented by the symbol "$\langle\rangle$".
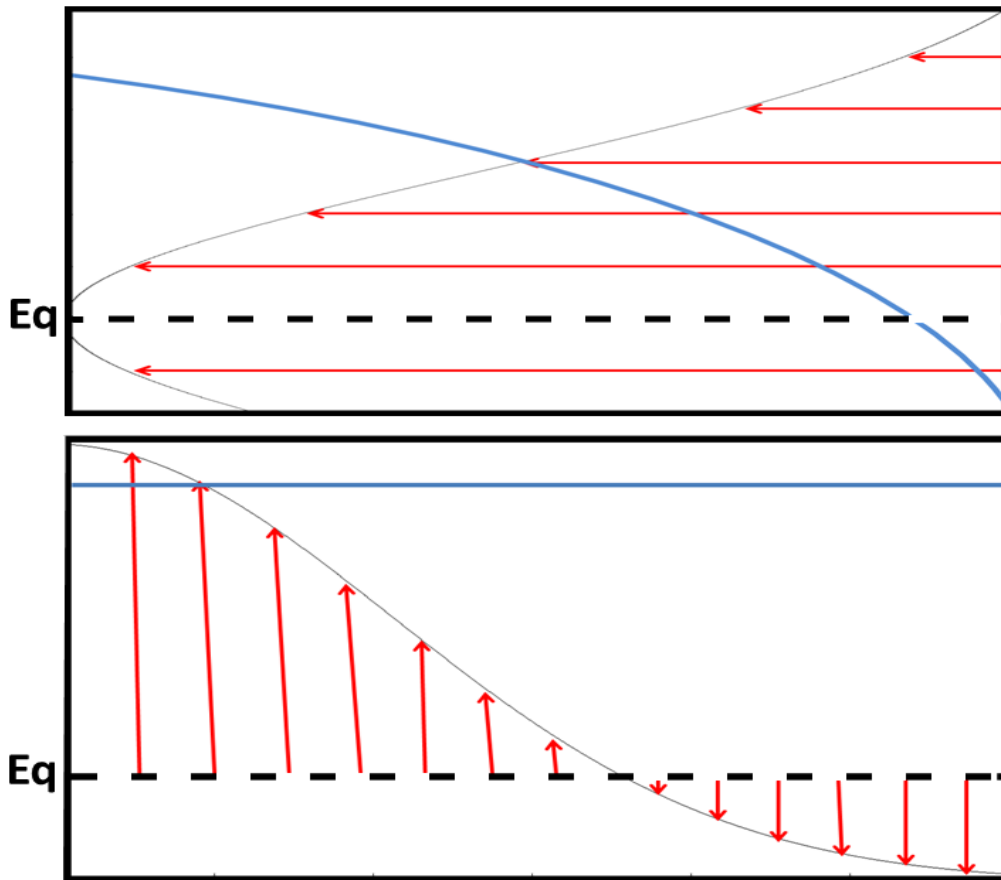

Figure 4.1 – *Schematically illustrations of the offshore and alongshore structures for TW-forcing (top) and MW-forcing (bottom). The eastward decrease of magnitude of the TW-forcing is represented in blue line (top) as described in the Eq. (4.1). The magnitude of MW-forcing is kept constant with longitude, it is represented in blue line (bottom) as described in the Eq. (4.2).*

runs	C_1	C_2	$\nu(\mathrm{m}^2 \cdot \mathrm{s}^{-1})$	$\delta_{\mathrm{M}}(\mathrm{km})$	$\mathrm{V}_{eddy}(\mathrm{cm} \cdot \mathrm{s}^{-1})$
TW1000	4	0	1000	36.84	–
TW500	4	0	500	29.24	–
TW400	4	0	400	27.14	–
TW300	4	0	300	24.66	–
TW250	4	0	250	23.20	–
TW150	4	0	150	19.57	–
TW125	4	0	125	18.42	–
MW1000	0	3.5	1000	36.84	21.1
MW500	0	3.5	500	29.24	9.1
MW400	0	3.5	400	27.14	8.7
MW300	0	3.5	300	24.66	6.8

Table 4.1 – *Table of numerical experiments. In the TW experiments, no northward migration are observed so no V_{eddy}.*

4.2   Munk-layer theory and the inertial-layer theory

To start it is useful to remind briefly the foundations for a modern theory of ocean circulation and the western boundary-layers (WBL hereafter). There are two principal theories concerning laminar oceanic boundary-layers, the Munk-layer theory [Munk (1950)] and the inertial-layer theory [Charney (1955)] which form the basis of the theories developed in this thesis.

Sverdrup (1947) showed that the circulation in the upper-layer away from the boundary is directly related to the curl of the wind stress. Stommel (1948) used the same equations by Sverdrup but added a simple bottom friction and showed that the circulation in oceanic gyres is asymmetric because the Coriolis force varies with latitude (see Fig. 4.2). Finally, Munk (1950) built upon this wind-driven circulation foundation, replacing the bottom friction by a lateral no-slip boundary condition and lateral eddy viscosity which dissipates the vorticity input by the wind stress and permits to fix the boundary current width. He obtained a boundary-layer comparable to the flow observed in the Gulf Stream and the Kuroshio. Together the three oceanographers laid the foundations for a modern (quasi-geostrophic) theory of ocean circulation.

Despite this notable advances in the understanding of the ocean circulation, the detailed structure of the WBC remained, however, essentially unexplained which lead Charney (1955) to state "In order to account for the observed width of the current, Munk was forced to postulate an eddy viscosity so large that the eddy sizes were themselves comparable to the width" (see also eddy viscosity estimation sub-section 4.11). In an analysis of wind-driven circulations, Charney (1955) found that the entering of fluid in the western boundary-layer has an inertial effect in the vicinity of the western boundary-layer. Pedlosky (1987, chap. 5) gives a very useful, succinct, and mathematically clear description of the various theories for the WBC.

To continue let me recall the two principal theories concerning laminar oceanic boundary-
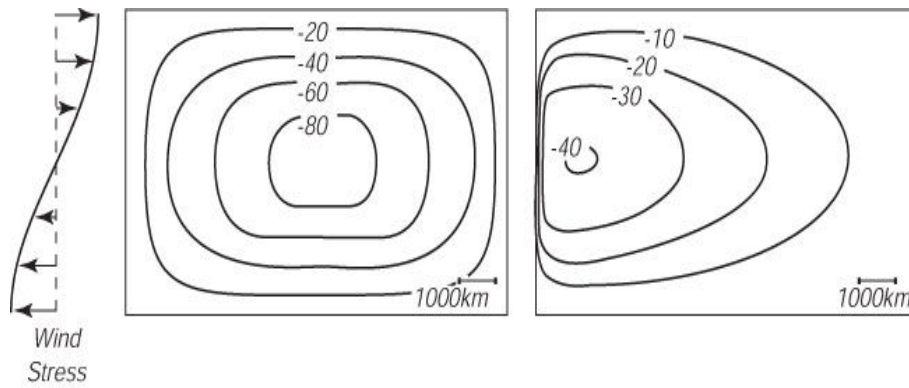
Figure 4.2 – *Stream function for flow in a basin as calculated by Stommel (1948). Left: Flow for non-rotating basin or flow for a basin with constant Coriolis force. Right: Flow when Coriolis force varies with latitude [After Stommel (1948)].*

layers, the Munk-layer theory [Munk (1950)] and the inertial-layer theory [Charney (1955); Pedlosky (1979); Vallis (2006)] in the framework of the reduced gravity shallow-water equations. Both theories were derived using the quasi-geostrophic equations on the β-plane.

Munk's lateral boundary-layer theory does not consider the bottom/inter-facial friction used by Stommel because it is negligible across the pycnocline as explained in section 2.2. Considering Munk's wind-driven barotropic gyre, the western boundary-layer exists as a balance between the meridional transport of planetary vorticity and the lateral diffusion of relative vorticity into the western wall. As a fluid element moves northward a distance Δy_* in the boundary-layer, its planetary vorticity is increased by an amount $\beta\Delta y_*$ and in the absence of friction would suffer a change in relative vorticity ζ_* by the opposite amount $-\beta\Delta y_*$, due to the conservation of total vorticity. In a stationary state, friction forces must compensate this relative vorticity in the fluid element and diffuse it in/out the boundary.

In a stationary state, the vorticity Eq. (3.4) can be written as

$$\cancel{\partial_t \xi} + u\partial_x \xi + v\partial_y \xi + \beta v + (\xi + f)(\partial_x u + \partial_y v) - \nu\nabla^2\xi = S. \qquad (4.3)$$

In the linear limit when the viscosity is large, the non-linear terms $u\partial_x \xi + v\partial_y \xi$ are negligible. In the vicinity of the western boundary-layer the forcing is weak, the term F can be neglected. The western boundary layer closure is that described by Munk (1950) in quasi-geostrophic approximation (no explicit stretching terms $(\xi + f)(\partial_x u + \partial_y v)$). The averaged Eq. (4.3) becomes:

$$\cancel{\partial_t \xi} + \cancel{u\partial_x \xi} + \cancel{v\partial_y \xi} + \beta v + \cancel{(\xi + f)(\partial_x u + \partial_y v)} - \nu\nabla^2\xi = \cancel{S}. \qquad (4.4)$$

The vorticity balance is assumed by the planetary vorticity advection and the viscous

dissipation. According to the western boundary-layer closure

$$u \ll v, \quad \partial_x \gg \partial_y, \tag{4.5}$$

the vorticity is

$$\xi = \partial_x v - \partial_y u \approx \partial_x v. \tag{4.6}$$

The Eq. (4.4) becomes:

$$\beta v - \nu \partial_{xxx} v \approx 0. \tag{4.7}$$

Munk's vorticity balance Eq. (4.7) and the lateral no-slip boundary conditions lead to Munk's analytic solution:

$$v_{\mathrm{M}}(x) = v_{\mathrm{M}}^0 \exp\left(-\frac{x}{2\delta_{\mathrm{M}}}\right) \sin\left(\frac{\sqrt{3}}{2}\frac{x}{\delta_{\mathrm{M}}}\right), \tag{4.8}$$

where v_{M}^0 is the amplitude and

$$\delta_{\mathrm{M}} = \left(\frac{\nu}{\beta}\right)^{\frac{1}{3}} \tag{4.9}$$

is the *Munk-layer width*. After its passage through the boundary-layer, the fluid elements can smoothly rejoin the Sverdrup interior. For lower viscosity values the Munk-layer is thinner as can be seen from Eq. (4.9).

Fluid entering the western boundary-layer can lead to an inertial boundary-layer [Charney (1955); see also Pedlosky (1979); Vallis (2006)]. In this case the dominant balance is between the non-linear advection of relative vorticity and the meridional transport of planetary vorticity. In this limit the friction term $\nu \nabla^2 \xi$ can be neglected and in the western boundary-layer the forcing (S) is sub-dominant. The inertial-layer theory in the quasi-geostrophic approximation (no stretching terms $(\xi + f)(\partial_x u + \partial_y v)$) was described first by Charney (1955) [see also Pedlosky (1979); Vallis (2006)].
In a stationary state and the vorticity Eq. (3.4) can be written as

$$\cancel{\partial_t \xi} + u\partial_x \xi + v\partial_y \xi + \beta v + \cancel{(\xi + f)(\partial_x u + \partial_y v)} - \cancel{\nu \nabla^2 \xi} = \cancel{S}. \tag{4.10}$$

In the inertial boundary-layer, the relative meridional vorticity advection $v\partial_y \xi$ can be neglected as the dominant relative vorticity transport is in the zonal direction ($u\partial_x \xi \gg v\partial_y \xi$). Eq. (4.10) becomes:

$$\cancel{\partial_t \xi} + u\partial_x \xi + \cancel{v\partial_y \xi} + \beta v + \cancel{(\xi + f)(\partial_x u + \partial_y v)} - \cancel{\nu \nabla^2 \xi} = \cancel{S}. \tag{4.11}$$

In the western boundary-layer

$$u \ll v, \quad \partial_x \gg \partial_y, \tag{4.12}$$

and the vorticity is

$$\xi = \partial_x v - \partial_y u \approx \partial_x v. \tag{4.13}$$

The Eq. (4.11) further simplifies to:

$$u\partial_{xx}v + \beta v \approx 0, \tag{4.14}$$

which leads to the inertial-layer theory analytic solution:

$$v_{\mathrm{I}}(x) = v_{\mathrm{I}}^0 \exp\left(-\frac{x}{\delta_{\mathrm{I}}}\right), \tag{4.15}$$

where v_{I}^0 is the amplitude and

$$\delta_{\mathrm{I}} = \left[\frac{-U_{\mathrm{I}}(y)}{\beta}\right]^{\frac{1}{2}} \tag{4.16}$$

is the *inertial-layer thickness*, also called *Charney scale*, found by Charney (1955) and Morgan (1956). Here $U_{\mathrm{I}}(y)$ is the maximum speed of the westward Sverdrup flow impinging on the boundary-layer hence the minus sign in the formula (4.16).

It is noteworthy to mention that the inertial-layer theory is valid only for the outer part of the WBC in the westward-flowing area. As can be seen from solution (4.15), the inertial boundary-layer does not respect the no-slip boundary condition. It needs to be supplemented by a frictional sub-layer which is located between the boundary and the inertial-layer.

When $\delta_{\mathrm{M}} > \delta_{\mathrm{I}}$, friction is important throughout the boundary-layer and the inertial-layer is suppressed.

The analytic solutions of these two theories will be used in the sub-section 4.3.2 to fit the numerical results of laminar experiments.

It is demonstrated with no doubt that these two laminar theories give a good description of laminar flows but a pertinent question subsists, is it true for the turbulent flows? For the case of turbulent flows which are in a statistically stationary state, the vorticity Eq. 3.4 can be averaged in time leading to:

$$\cancel{\langle\partial_t\xi\rangle} + \langle u\partial_x\xi\rangle + \langle v\partial_y\xi\rangle + \langle\beta v\rangle + \langle(\xi + f)(\partial_x u + \partial_y v)\rangle - \langle\nu\nabla^2\xi\rangle = \langle S\rangle. \tag{4.17}$$

The Munk-layer and inertial-layer theories can now be applied to the averaged terms and it is interesting to ask if these theories survive in some averaged sense. The answer will discuss in the sub-section 4.9.2.

4.3   Laminar solution

4.3.1   General circulation

Shown in Fig. 4.3a and Fig. 4.3b are layer thickness variation (η) contours and horizontal velocity arrows from the laminar experiments MW1000 and TW1000, after the

spin-up time, at t = 2000days. Velocity vectors are plotted every 20 x 50 grid points in the x and y directions. These figures show the classic Sverdrup interior solution with a Munk or inertial boundary-layer. The velocity vectors are small in regions where the flow is weak and difficult to distinguish in the figures. In these regions, the sense of the geostrophic flow must be inferred from the η-field. For both types of wind forcing, strong

Figure 4.3 – *Instantaneous velocity arrows superimposed on layer thickness variation η field at time t = 2000days for MW1000 (a) and TW1000 (b) experiments.*

WBCs with a recirculation in the rest of domain were observed. The TW exhibits two poleward WBCs one in each hemisphere. The southern WBC is less strong due to the domain extending only 1000km to the south but 3000km to north. The northern WBC will be the center of interest. The TW is characterized by two anticyclonic gyres in each hemisphere. Along the northern and southern boundaries of the basin are eastward currents. At the interior exists a weak westward flow along the equator and finally the gyres
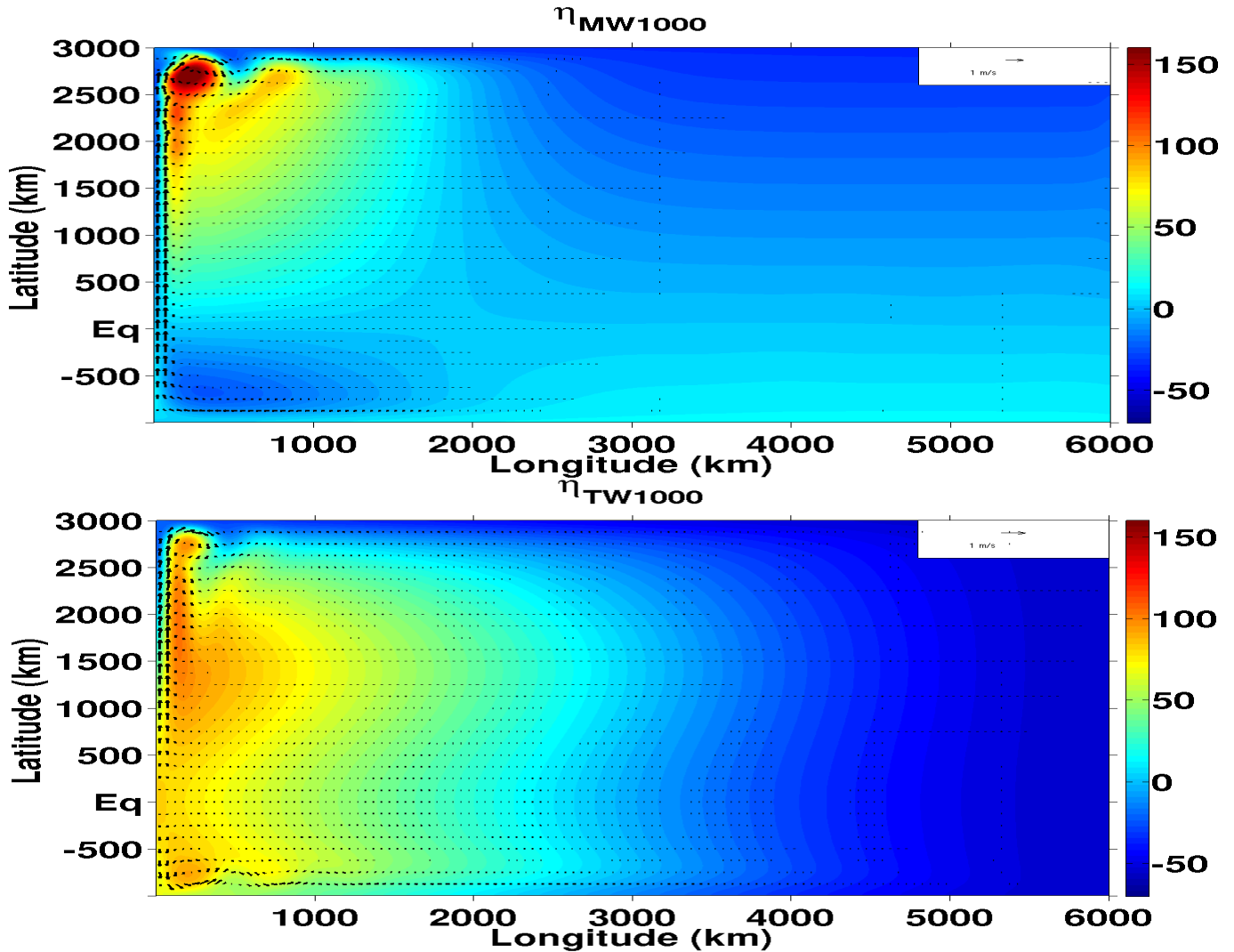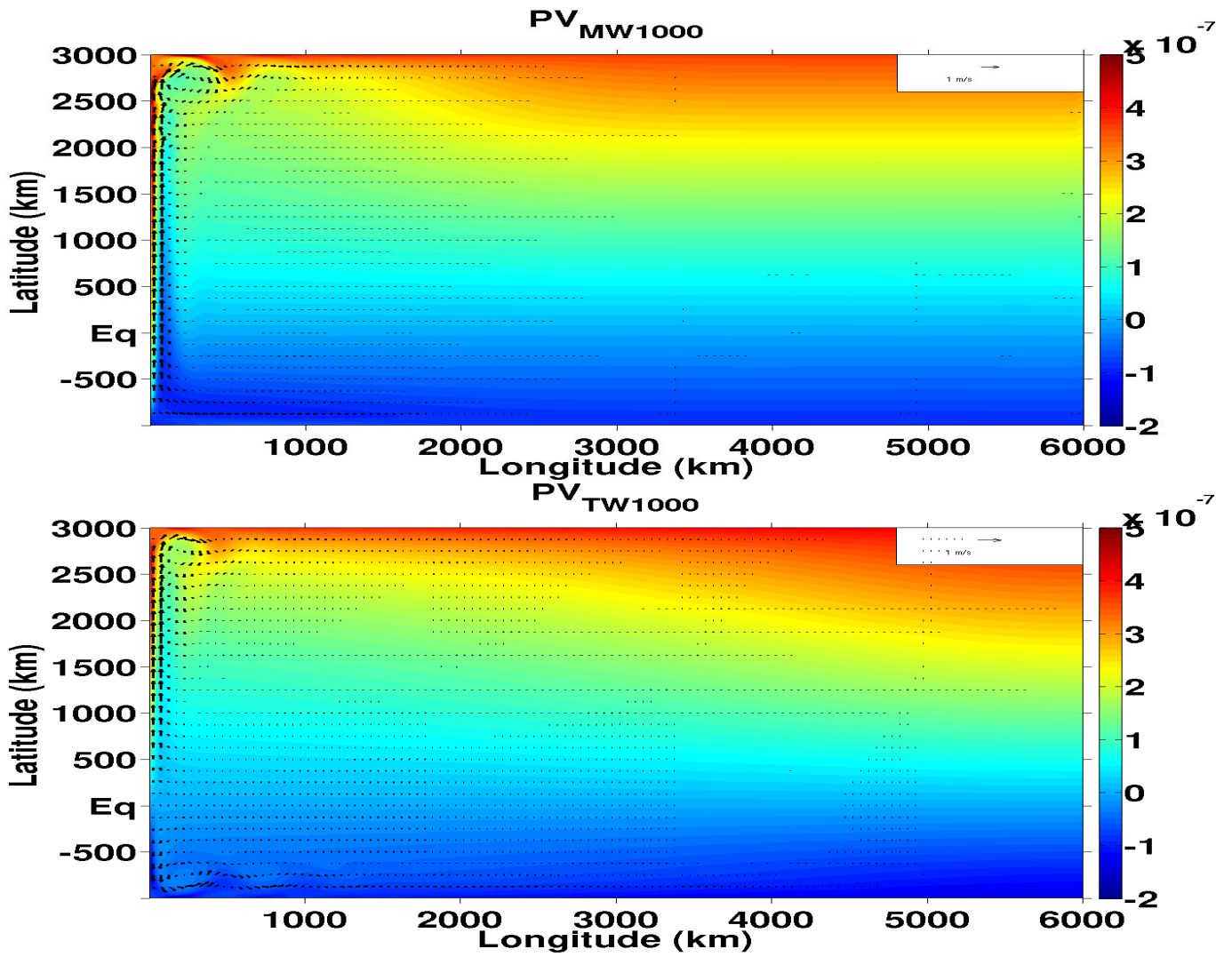
Figure 4.4 – *Instantaneous velocity arrows superimposed on the potential vorticity field at time t = 2000days for MW1000 (a) and TW1000 (b) experiments.*

are completed by strong poleward WBCs in both hemispheres.

The MW circulation is dominated by one intense WBC that transports fluid northward across the equator. At the northern and southern boundary of the basin exists eastward and westward currents, respectively. Finally the gyre is completed by a weak southward interior flow cross the equator outside the WBC.

Another important difference between the circulation resulting from MW and TW forcing, is that for the former the boundary current is in the northern direction and the zonal velocity vanishes almost completely except in the far southern and the northern part of the domain (Fig. 4.3a). While in the latter the zonal velocity is westward at low latitudes up to about y = +1300km and eastward above (Fig. 4.3b). In this linear limit, the potential vorticity contours associated with the flow simply follow roughly the lines of latitudes for the MW (Fig. 4.4a) but the TW (Fig. 4.4b) exhibits an westward splitting of potential vorticity contours along the equator. I will show in the sequel that these relative small zonal velocities, associated to the potential vorticity contours parallelism to the latitudes have an important impact on the stability and nature of the boundary current system.

4.3.2 Comparison with laminar Munk-layer and inertial-layer theories

Before proceeding to the more complicated non-linear solutions, it is useful to review the familiar, linear solution which can be determined from a combination of *Sverdrup theory* [Sverdrup (1947)] and *Stommel theory* [Stommel (1948)] with a *Munk-layer theory* [Munk (1950)] and *inertial-layer theory* [Charney (1955)]. It provides a useful baseline to compare the more complicated non-linear flows for the two sets of experiments. This section compares the laminar solutions of reduced gravity shallow water model to these two theories.

So according to the Munk-layer theory [Munk (1950); Pedlosky (1987)], the vorticity balance is assumed by meridional transport of the planetary vorticity and the friction dissipation as mentioned above in the Eq. (4.7).

The analytic solution of Munk for the meridional velocity near the western boundary is:

$$v_{\mathrm{M}}(x) = v_{\mathrm{M}}^0 \exp\left(-\frac{x}{2\delta_{\mathrm{M}}}\right) \sin\left(\frac{\sqrt{3}}{2}\frac{x}{\delta_{\mathrm{M}}}\right), \tag{4.18}$$

where v_{M}^0 is the velocity scale, $\delta_{\mathrm{M}} = (\frac{\nu}{\beta})^{\frac{1}{3}}$ is the characteristic boundary-layer thickness of Munk-layer as mentioned above in the Eq. (4.9).

The natural definition of the WBC width noted x_{M} is given analytically by the point where $\sin\left(\frac{\sqrt{3}}{2}\frac{x}{\delta_M}\right)$ has its first non-trivial zero, that is:

$$x_{\mathrm{M}} = \frac{2\pi}{\sqrt{3}}\delta_M = \frac{2\pi}{\sqrt{3}}\left(\frac{\nu}{\beta}\right)^{\frac{1}{3}}. \tag{4.19}$$
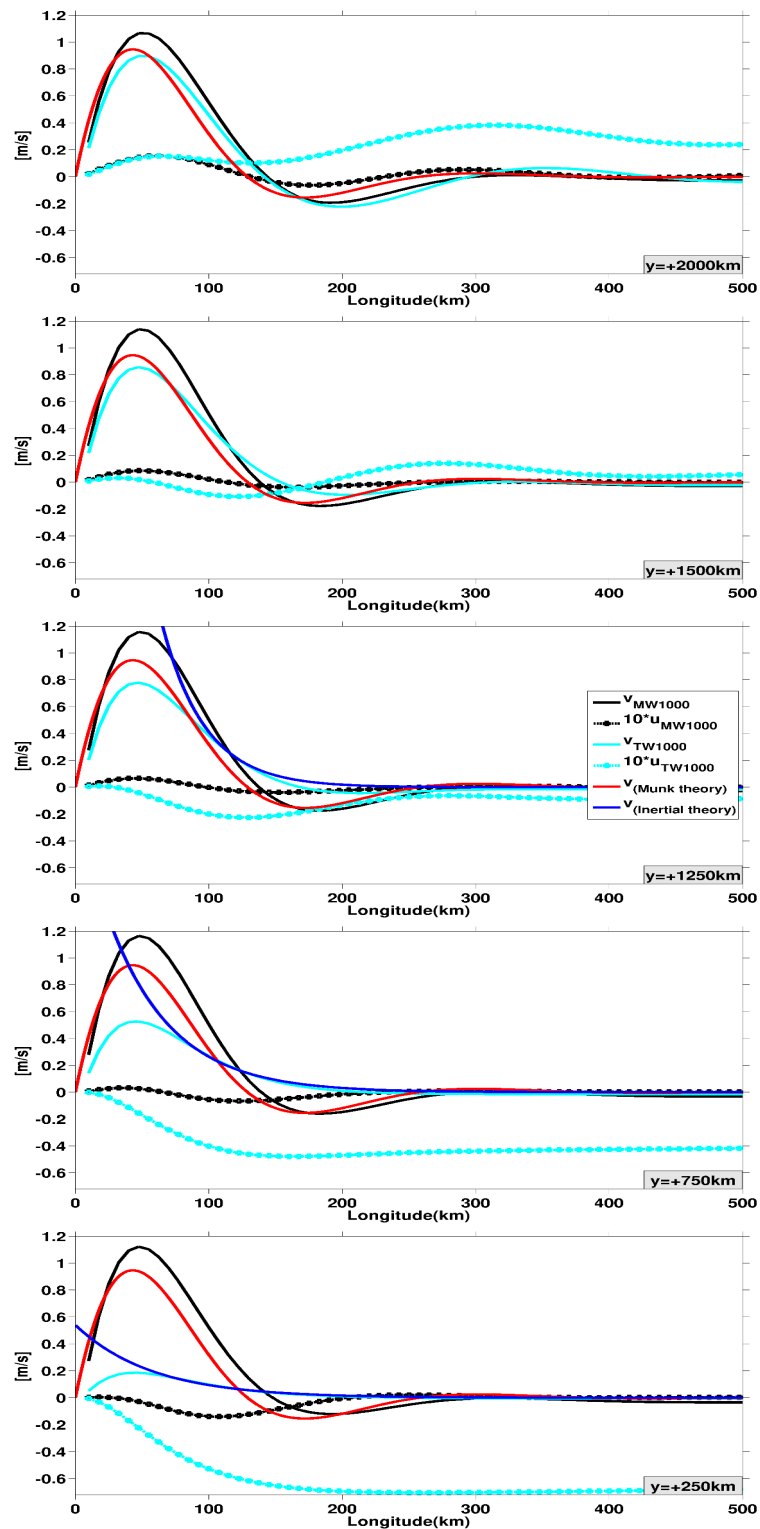
Figure 4.5 – *Zonal profiles of u and v components for MW1000 and TW1000 at five latitudes.* **From the top to the bottom:** *(a) y = +2000, (b) y = +1500,(c) y = +1250, (d) y = +750 and (e) y = +250km; superimposed by the zonal profile of the analytical solution of Munk theory [Munk (1950); Pedlosky (1987)] (red curve) with arbitrary amplitude but with the true nontrivial zero $x_M = \frac{2\pi}{\sqrt{3}}\delta_M = 133km$ and the analytical inertial solution (blue curve) with $\delta_I = \sqrt{\frac{-u}{\beta}}$ and arbitrary amplitude to match it with model solutions.*

Using the values $\nu = 1000\text{m}^2\cdot\text{s}^{-1}$ and $\beta = 2\cdot 10^{-11}\text{m}^{-1}\cdot\text{s}^{-1}$ for the linear experiments yields x_M=133km.

Munk-layer theory is based on quasi-geostrophy and neglects variations in the layer thickness, which can be important in the reduced gravity model (see section 4.9). I will show later in section 4.8 that the vortex stretching term (fifth term in Eq. (3.4)) which is not in the Munk-layer theory contributes to the vorticity balance. It is found to be important very close to the boundary but decreases rapidly before the meridional velocity reaches its maximum. It does not lead to substantial deviations from the Munk-layer and inertial-layer solutions as can be verified in Fig. 4.5. The zonal profiles of meridional component v and zonal component u are plotted at different latitudes for the experiments MW1000 and TW1000 to deduce the width of WBC represented Fig. 4.5. Additionally these profiles are fitted to the Munk analytic solution of meridional velocity with arbitrary amplitude v_M^0 as red curve with respect of $x_\text{M} = 133$km. There is a fair agreement between Munk-layer theory and the numerical results for the MW1000 and TW1000 experiments at higher latitude, where inertial effects vanish (where the zonal velocity is positive or equal to zero), as can be seen in Fig. 4.5a, b. At low latitudes there is also a fair agreement for the MW1000 experiment with Munk's analytic solution, while the TW1000 circulation is significantly marked by westward velocity (inertial effects) which alters completely the boundary-layer structure, leading to an inertial boundary-layer [Charney (1955); see also Pedlosky (1979); Vallis (2006)]. The outer part of the boundary-layer is now much better fitted (as can be seen in Fig. 4.5c, d and e) by the analytic solution of the inertial boundary theory:

$$v_\text{I}(x) = v_\text{I}^0 \exp\left(-\frac{x}{\delta_\text{I}}\right), \tag{4.20}$$

where $\delta_\text{I} = \sqrt{\frac{-u_\text{I}(y)}{\beta}}$ is the characteristic boundary-layer thickness (as mentioned above in Eq. (4.16)) of the inertial boundary-layer and v_I^0 is a velocity scale. Note, that the inertial solution for the meridional velocity has no zero-crossing. The analytic solution of inertial boundary-layer is plotted with arbitrary amplitude v_I^0 as a red dashed curve and fitted to the inertial part of the TW1000 zonal profiles at low latitudes.

The MW1000 WBC width is around 150km all along the boundary. In contrast, the TW1000 WBC width is around 250km at y $= +250$km and narrows to be approximately 150km at y $= +1700$km, this variation of the WBC width is explained by the inertial effect, more negative values of the zonal velocity in the TW1000 experiment at low latitudes.

There are zonal westward flows, which means that there is inertial effect at the north of the equator until approximately y $= +1300$km, where the flows return eastward up to the northern part of domain.

At the boundary the inertial solution is modified by the viscous dissipation, which is necessary to satisfy the no-slip boundary condition. Such viscous dissipation is also necessary for the basin wide vorticity balance as discussed in section 4.9. Note, that the inertial scale δ_I, also called the *Charney scale*, is a result of the large scale dynamics due to the wind-forcing. It depends only weakly on the viscosity. Whereas the Munk-layer scale δ_M depends only on external parameters, it can be calculated independently

of the circulation. When $\delta_\mathrm{I} > \delta_\mathrm{M}$ inertial effects govern the outer part of the boundary-layer, prevent it from becoming thinner and stabilize it [see Ierley & Young (1991)]. This explains the increased stability of the equatorward part of the boundary-layer in the TW circulation. Please note, that an eastward velocity here called *"counter-inertial effect"* has no such stabilizing effect. Indeed in the TW experiment there is an eastward average velocity in the northern part of the domain, the *Charney scale* becomes complex value and a tendency to spatial and temporal oscillations is observed (section 4.9 in Fig. 4.24c).

All this proves that the inertial effect is the cause of the difference between the structures of both WBCs and so the difference between the dynamics subject to the two forcings.

Considering the area where the inertial effect vanishes, in other words at higher latitudes, the width of WBC are equal for MW1000 and TW1000, it appears clearly that there are small but significant differences very close to the boundary around $\Delta x_\mathrm{M} = 17 km$ between the numerical results and the analytic prediction of the Munk layer. The analytic Munk-layer solution is based on quasi-geostrophic theory (as explained above), where the variations of layer-thickness is neglected. In the present solutions of the reduced gravity model the variation of layer thickness along the streamlines are considerable in the boundary-layer as can be seen in Fig. 4.3. These variations of layer-thickness also lead to a "topographic" beta-effect which adds to the planetary beta value, it will be discussed in detail in the sub-section 4.11.

4.4 Transition to instability and strongly nonlinear flow

Knowing that the interior flow field is quite similar to that predicted by Sverdrup theory, independent of viscosity to leading order, this section focuses on the qualitative description of western boundary features for all experiments. It is the dynamics of the western boundary current that is strongly dependent on the viscosity parameter.

4.4.1 Trade Winds experiments

This sub-section describes solutions that are forced by TW-forcing. As said above, the TW experiment exhibit two poleward WBCs one in each hemisphere. Only the northern WBC is described here. Zooms of snapshots of potential vorticity in the western boundary region are shown Fig. 4.6 for different experiments. From the left to the right TW1000 (a), TW500 (b), TW250 (c), TW150 (d) and TW125 (e), and at different times from the top to the bottom at t = 60, 100, 300, 1000 and 2500days are shown. After only 60days, the coastal current is strong enough for the effects of the non-linear terms to be apparent in the lower viscosity experiments. During the spin-up phase, except for the purely linear experiment TW1000, solutions show the signature of two or three eddies which move northward rapidly and weaken, at t = 280days. They have decayed to negligible strength upon reaching the northwestern wedge of the basin. As the eddies propagate northward,

new ones develop north of the equator. The current overshoots the latitude of the strongest eastward interior flow, bends offshore to form an anticyclonic eddy, returns southward in a coastal counter-current, and finally returns again northward creating thus a semi-closed cyclonic eddy, before joining the eastward interior current. The latitude is different according to the experiment, but is approximately y = +2500km when the experiment has reached a statistically converged state. The system of eddies propagates slowly northward and reaches the northern wedge. The experiment TW500 reaches a quasi-steady state by ∼ 700days.

As the viscosity decreases, the steady linear solution becomes deformed by the influence of non-linearity in the dynamics. The interior remains largely linear in its balance, but inertial effects become important in the vicinity of the boundary current just north of the equator until the latitude y = +1300km. This explains the preference of eddies to be formed north of this latitude.

For even smaller viscosities, the influence of non-linearity increases. The system of eddies wedged in the northwestern part of the domain grows more intense and strongly deforms the mean potential vorticity contours. The circulation near the western boundary is turbulent except in the region where the zonal westward velocity is non-negligible. In other words, where inertial effects are important. The area of turbulent motion extends zonally over a broader portion of the basin, as shown in Fig. 4.6, for lower viscosity experiments. It is noteworthy that several stochastic intermittent detachments of positive potential vorticity in the vicinity of the boundary in the WBC just northward of the eddy center are observed at the boundary and followed by dipole formation. This phenomena will be discussed in detail in the section 4.5.

4.4.2 Monsoon Winds experiments

This sub-section describes solutions that are forced by MW-forcing. As said above the MW is dominated by one intense WBC that transports fluid northward across the equator. Zooms of the western boundary region of snapshots of potential vorticity are shown in Fig. 4.7 for different viscosity experiments from the left to the right MW1000 (a), MW500 (b), MW400 (c) and MW300 (d), and from the top to the bottom at t = 60, 100, 200, 300, 1000 and 2500days. The structures of the WBCs differ markedly from those of the TW experiments. For the different values of viscosity, the MW experiments exhibit four distinct phases:

(i) Like in the TW forcing, after t = 60days, the coastal current is strong enough for the effects of the non-linear terms to be apparent for all the experiments. At the beginning, all the four experiments show similar features as in the lower viscosity TW experiments with a temporal discrepancy according to the experiments. Two or three eddies are shed at days 60 to 250, they migrated northward slowly and weakly, collapsed in the northwestern wedge of the basin.

(ii) As the eddies propagate northward, new ones develop south of y ≈ +1100km like the pair of eddies in the TW-forcing case and the pair migrates rapidly northward to attain the northwestern wedge roughly at day 400.

Figure 4.6 – *Zoom near the western boundary of snapshots of potential vorticity for different viscosity experiments from the left to the right TW1000 (a), TW500 (b), TW250 (c), TW150 (d), and TW125 (e), and from the top to the bottom at t = 60, 100, 200, 300, 1000, 2500days.*
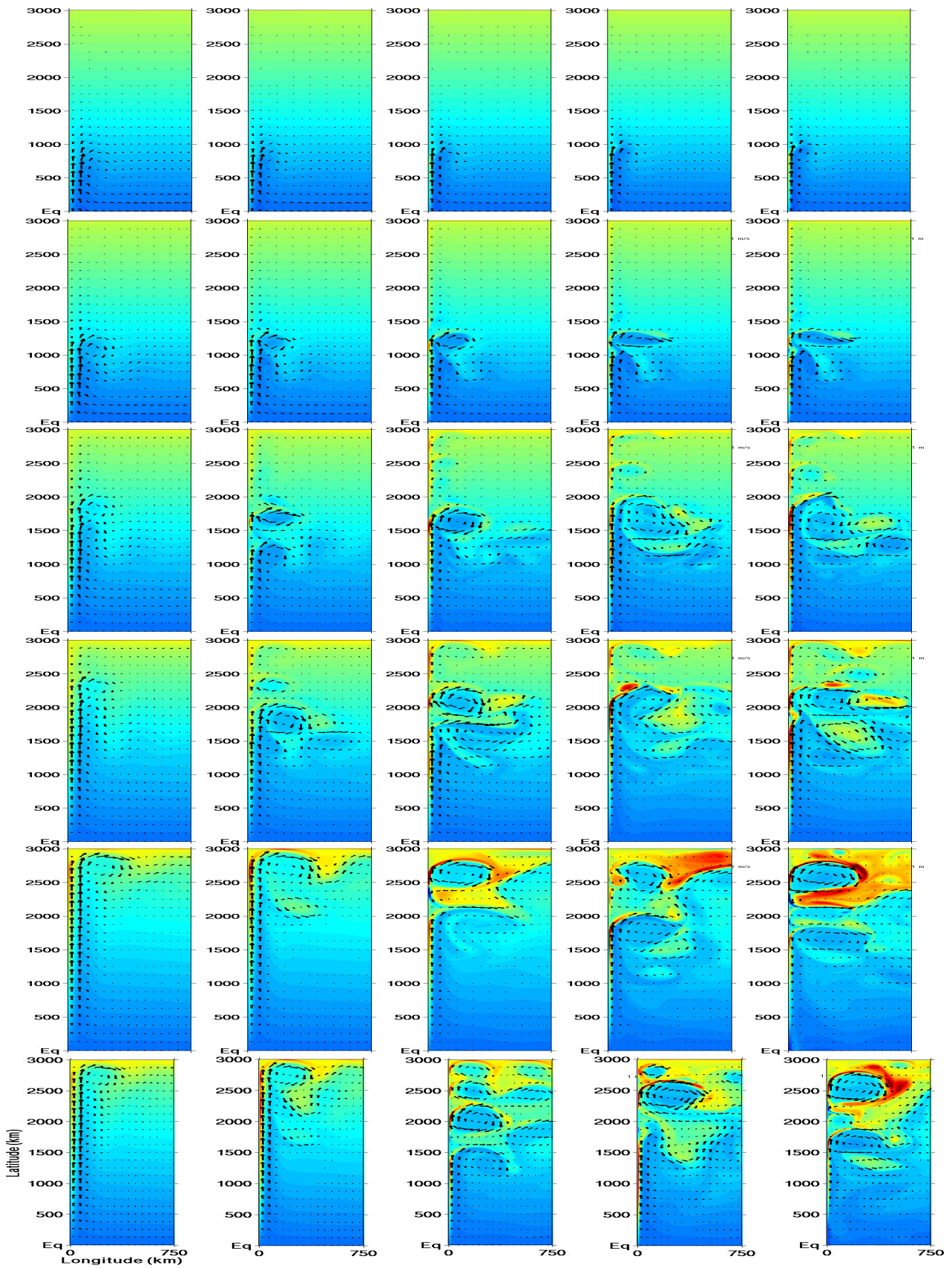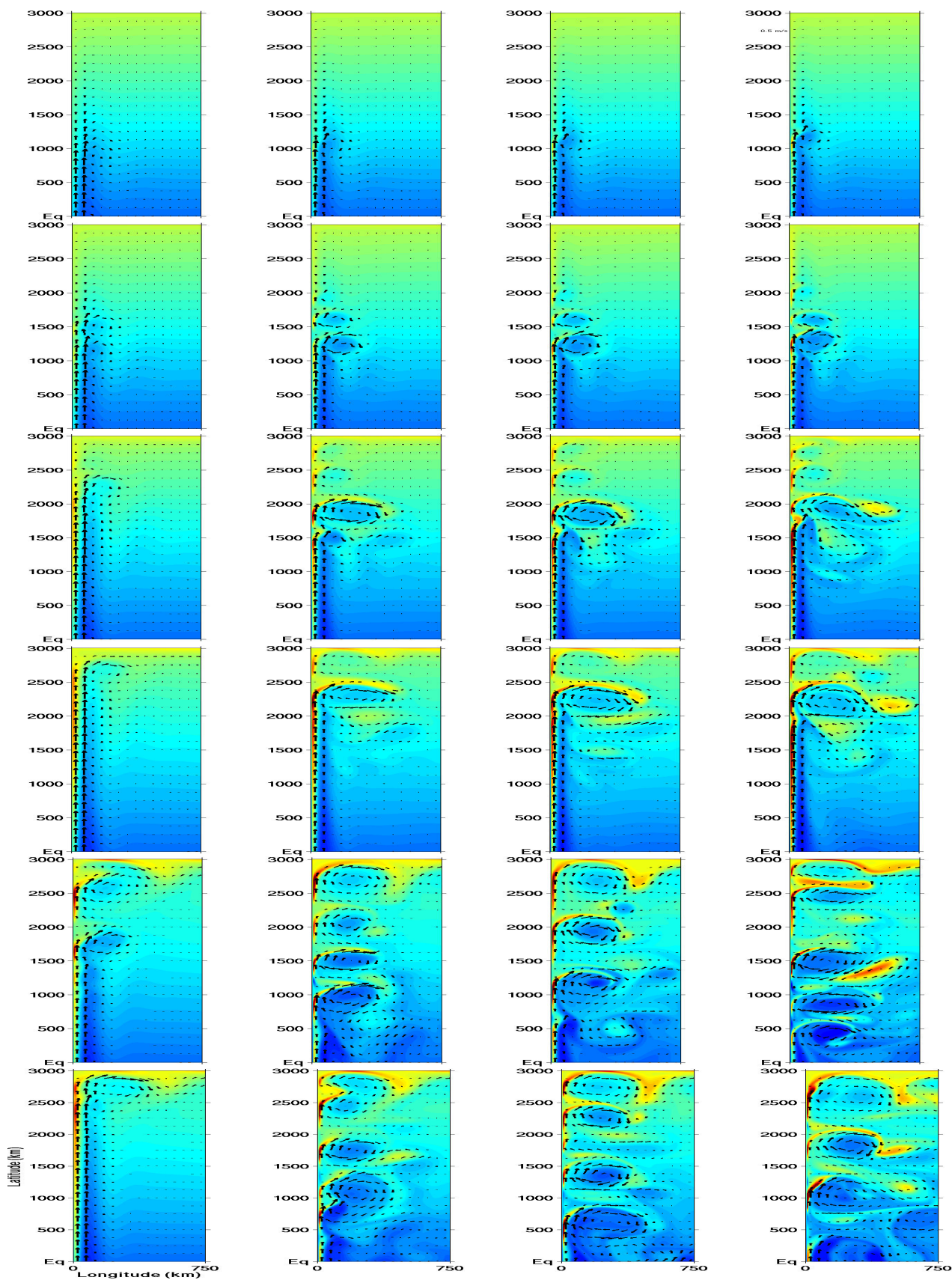
Figure 4.7 – *Zoom near the western boundary of snapshots of potential vorticity for different viscosity experiments from the left to the right MW1000 (a), MW500 (b), MW400 (c) and MW300 (d), and from the top to the bottom at t = 60, 100, 200, 300, 1000, 2500days.*

(iii) Intermittent detachments and discontinuations of WBC are observed, they are begin approximately by day 380 slightly north of y = +2000km for the experiment MW300. Thus the WBC is separated from the boundary into a pair of eddies locate in northwestern wedge retroflects and shed a weak dipole. After the first detachment follows a series of similar events at latitudes further southward, during the northward migration of eddies along the western boundary. These intermittent detachments are called *bursts*, they will be detailed in the sub-section 4.5.2.

(iiii) After day 1700, the WBC of the experiment MW1000 becomes laminar. Development of coherent eddies is observed in the experiment MW500 along the western boundary during the entire experiment. The experiments MW400 and MW300 show a turbulent eddy field with many eddy coalescences during their migration. Formed north of the equator, these eddies are always anticyclonic, moving northward with velocities V_{eddy} given in the Tab. 4.1.

4.4.3   Non-Importance of the equator

Two types of non-linear WBCs are investigated: in the MW-forcing experiment the WBC crosses the equator and in the TW-forcing experiment the WBC circulates only north of the equator. In each experiment the WBC retroflects and an eddy-shedding state with different degree of instability is observed. It appears clearly that the retroflection of the WBC and formation of eddies is not due to the inertial overshoot of the equator by the current but only due to the vorticity dynamics which will be discussed in the sections 4.8 and 4.9.

4.5   Coherent structures

Turbulence plays an important role in the ocean dynamics by transferring energy through a cascading process from large scales to small scales [see *e.g.* Klein et al. (2011)], at which the turbulence can be dissipated. Coherent structures are features of the turbulence flow field. They are flow patterns that can be recognized atop the more disorderly motions. It associates a concrete form to the "eddy". For coherent structure dynamics, the potential vorticity (PV) is usually a useful quantity of the evolution [Morel & McWilliams (1997)].

4.5.1   Anticyclone

Vortex

The most conspicuous coherent structures are the anticyclonic eddies along the western boundary. In the MW simulations they start to appear at viscosity values of around $\nu = 1000\text{m}^2\cdot\text{s}^{-1}$ (MW1000) as poleward traveling waves in the boundary-layer. They travel northward along the boundary at speeds of $V_{eddy} \approx 2.3 \cdot 10^{-1}\text{m}\cdot\text{s}^{-1}$. This speed is faster than the fastest Rossby wave meaning that they do not radiate Rossby waves [Ierley & Young (1991)]. In the MW1000 experiment, they are a transient phenomena and disappear
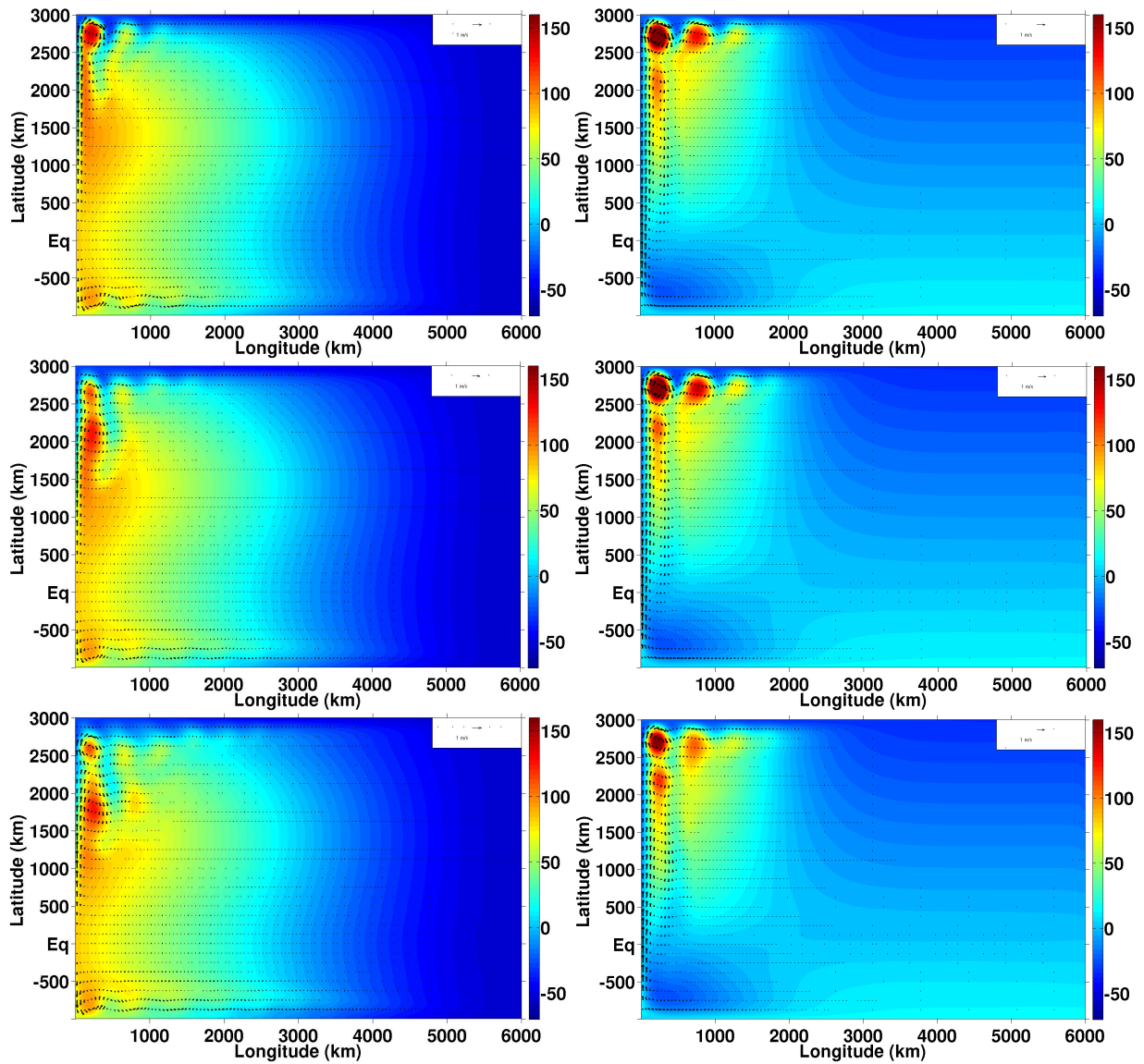
Figure 4.8 – *Time-averaged fields of velocity arrows superimposed on the time-averaged layer thickness $\langle\eta\rangle$ for different experiments. TW experiments (Left panels), from top to bottom: TW500, TW250 and TW125. MW experiments (right panels), from top to bottom: MW500, MW400 and MW300.*

after the spin-up. The eddy size increases with a decreasing viscosity. At viscosities of $\nu \approx 500\text{m}^2\cdot\text{s}^{-1}$ (MW500), they are coherent regular vortices. Their diameter is then around the equatorial Rossby radius of deformation $L_\beta = \sqrt{\sqrt{g'H}/\beta} = 350\text{km}$, a size that compares well to the size of the eddies in the Somali Current [Schott & McCreary Jr (2001); Wirth et al. (2002)] and to the eddies of the North Brazil current [Richardson et al. (1994)]. When inspecting the potential vorticity (PV) they appear as negative PV anomalies that move northward with an average speed of $V_{eddy} \approx 1 \cdot 10^{-1}\text{m}\cdot\text{s}^{-1}$, while the fluid velocity in their interior reaches speed of $v_{eddy} = 2\text{m}\cdot\text{s}^{-1}$.

With decreasing viscosity their shape and northward displacement exhibit a random-like behavior as can be seen in the snapshots of Figs. 4.6 and 4.7 indicating a chaotic dynamics. For the lower viscosity values the eddy dynamics becomes more chaotic, some of the eddies migrate into the interior of the basin, merge with other eddies or are disintegrated in a 2D turbulent eddy dynamics. At the lowest viscosity value of $\nu = 300\text{m}^2\cdot\text{s}^{-1}$ (MW300), the average northward displacement velocity is around $V_{eddy} \approx 6 \cdot 10^{-2}\text{m}\cdot\text{s}^{-1}$, while the fluid velocity in their interior reaches speeds of $v_{eddy} = 2\text{m}\cdot\text{s}^{-1}$.

The boundary-layer of the TW experiment is stabilized at lower latitudes, by the inertial effect as discussed in section 4.3.2 above. There are no eddies south of y = +1000km, the latitudes at which the time averaged zonal velocity is negative. At higher latitudes, for higher viscosities in TW experiments, a single traveling wave is created that migrates northward to the northwest corner of the domain, where it disappears. An eddy dynamics appears for the viscosities below $\nu = 400\text{m}^2\cdot\text{s}^{-1}$. A pair of eddies is formed and migrates slowly northward. After the migration the pair of eddies is wedged in the northwestern part of the domain. For the lower viscosity experiments the formation and the northward migration of the pair of eddies are chaotic and meandered. In the northwestern wedge, the eddies fluid velocities reach locally up to $v_{eddy} = 2.4\text{m}\cdot\text{s}^{-1}$.

Turbulence persists only at latitudes where the average zonal velocity outside the boundary-layer is eastward, that is, where no inertial effect is present. No continuous systematic eddy migration is depicted, so the Hovmöller diagrams are not plotted for the TW experiments.

Eddy versus Ring / Eddy versus Solitonic Wave

The anticyclonic eddies are the dominant coherent structures and they are seen in all variables u,v,η, q and the fluid speed U. In order to know that if the coherent vortices formed are rings (that is an annular structure of high velocity surrounding an almost motionless kernel) or an eddy in solid body rotation, a closer inspection of the variation of layer thickness, the PV and the fluid velocity U within the eddy are shown in Fig. 4.9. One has to mention that in the literature "*eddy*" or "*ring*" are often used interchangeably to denote the same object. The closer inspection shows vortices in almost perfect solid body rotation and not vortex rings, with an almost motionless core (eye). The eddies fluid velocity shows no low speed plateau in the center of the eddies and the velocity is greater near the western boundary branch than at the offshore branch. The zonal section of the PV shows a rough plateau throughout the eddies. As the PV is a variable conserved by
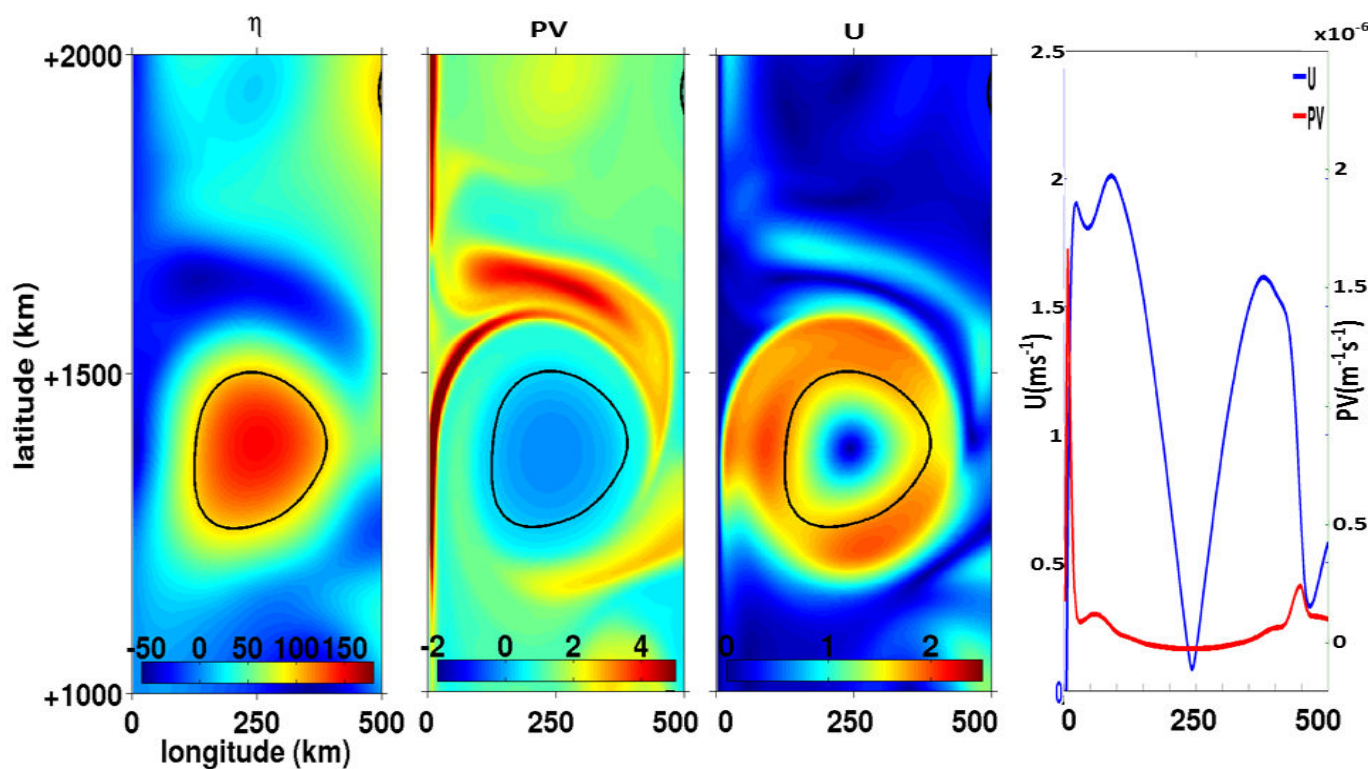
Figure 4.9 – *Snapshots of zoom on vortice at t = 1237 day for the variables: layer thickness variation (a), potential vorticity (b), speed (c) and zonal section through the eddy center of speed and potential vorticity (d). Arbitrary black contour of layer thickness variation $\eta = 100m$ is plotted to distinguish the eddy.*

the Lagrangian dynamics, this shows that water masses are captured by the eddies and transported with them. It mean that eddies are not solitonic waves.

Eddy tracking

The anticyclonic eddies appear during the spin-up time in all experiments as northward traveling waves for the viscosity of $\nu = 1000\text{m}^2\cdot\text{s}^{-1}$, and as coherent structures for the lower viscosity. The anticyclonic eddies are the dominant features at the western boundary
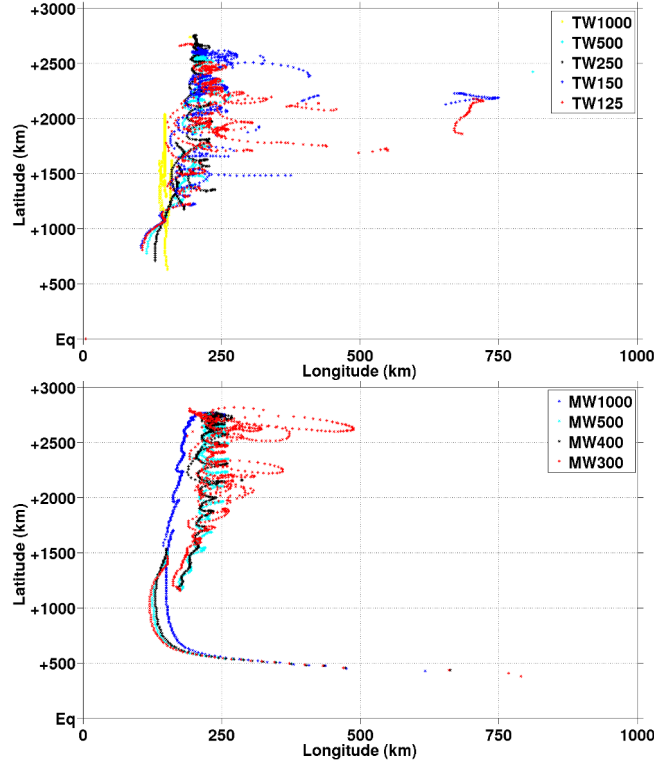
Figure 4.10 – *Location of the eddies determined by the maximum value of layer thickness variation $\eta_{\max}$ during the first 800 days of integration for the TW (a) and MW (b) experiments.*

and have a positive layer thickness anomaly. Assuming that the maximum value of the layer thickness anomaly $\eta_{\max}$ coincide with the eddy center, the idea is to localize the eddy by this local maximum. The eddies are tracked during the first 800 days of integration and are plotted in the Fig. 4.10.

For the TW experiments (Fig. 4.10a), the eddy centers begin to appear north of the latitude y = +500km between approximately the longitudes x = 110km and x = 180km. The trajectories sketched by the $\eta_{\max}$ prove that, during their northward migration, the eddies bend offshore up to approximately x = 700km for the lower viscosities. But the trajectory of TW1000 eddies is parallel to the boundary meaning that the $\eta_{\max}$ values in this experiment are just the signature of poleward traveling structures.

For the MW experiments (Fig. 4.10b), the maximum value of layer thickness anomaly η_{max} begin along the equator. They are the signature of westward equatorial trapped waves which propagate boundary-ward and further northward along the boundary. In the lower viscosity experiments (all except MW1000) they are only captured by the analysis during the initial phase, when no strong eddies are present. Once the eddies have developed, their signal dominates the signal of the waves and the analysis only captures the eddy dynamics.

This confirms that there are only wavelike features in the MW1000 experiment. For the lower viscosities the signature of η_{max} corresponding to the eddy location with maximum η_{max} appears at latitude y = +1300km and longitude x = 180km. Eddies are generated further south and the magnitude of the layer thickness anomaly increases during their northward migration. They are only visible in the analysis when their signature is stronger than that of the waves.

During the northward migration, the trajectories of the η_{max} show that the eddies bend offshore up to approximately x = 480km for the lower viscosity experiment MW300 and around x = 250km for the experiments MW400 and MW500.

I will show in section 4.6 that the coherent structures can move further into the interior of the basin after the first 800 days of integration. The coherent eddies are very important for the offshore mixing of upwelled and nutrient-rich water masses sustaining biological production. However the tracked layer thickness anomaly maximum η_{max} analysis are not exhaustive for tracking all the eddies formed but just the one eddy with the value of η_{max} per day. During the spin-up time Rossby waves dominate the first η_{max} values detected before the appearance of the non-linear effect which allows the formation of the coherent anticyclonic structures.

4.5.2   Burst

For the experiments with the lower values of the viscosity, intermittent detachments of the viscous sub-layer just northward of the eddy center are observed at the boundary (see Fig. 4.11). The viscous sub-layer is the thin layer of a few tenths of kilometers thickness, at the boundary where the vorticity has large positive values. It is discussed in detail in sub-section 4.9.1. These detachments are the most violent phenomena in the experiments with the strongest velocity and vorticity gradients.

When the sheet of positive vorticity along the western boundary in the Munk-layer breaks due to the action of an anticyclone, the southward part detaches, is torn of the boundary by the anticyclone and accelerates away from the boundary (see Fig. 4.11). North of the detachment the vorticity anomaly vanishes. In the detachment, the meridional velocity vanishes or inverses. The separation of the boundary-layer plays a key role in boundary-layer dynamics since the work of Prandtl (1944) [see also Schlichting & Gersten (2000)]. These events are the analog to *bursts* or ejections in the classical boundary-layer [Robinson (1991)] and are thus given the same name here. They are strong spatially localized and temporally intermittent ejections of fluid with positive vorticity, away from the wall initiated by the large anticyclonic eddies.

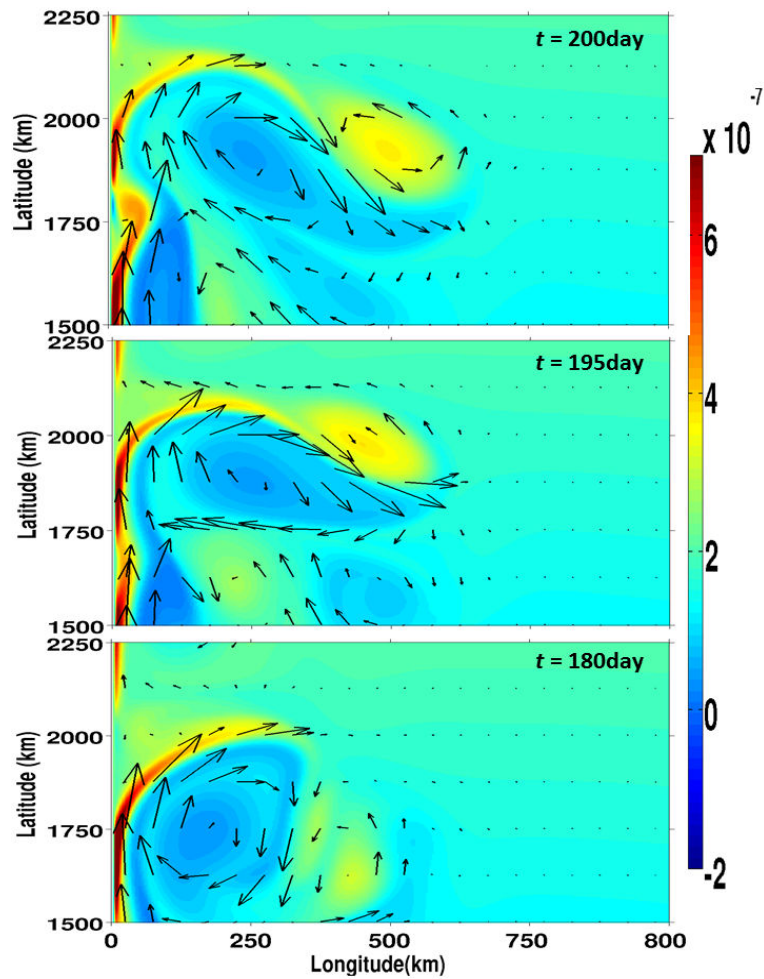Figure 4.11 – *Sequence of potential vorticity snapshots showing bursts and its subsequent development into dipoles for MW300. The snapshots were taken at days 180 (c), 195 (b) and 200 (a).*
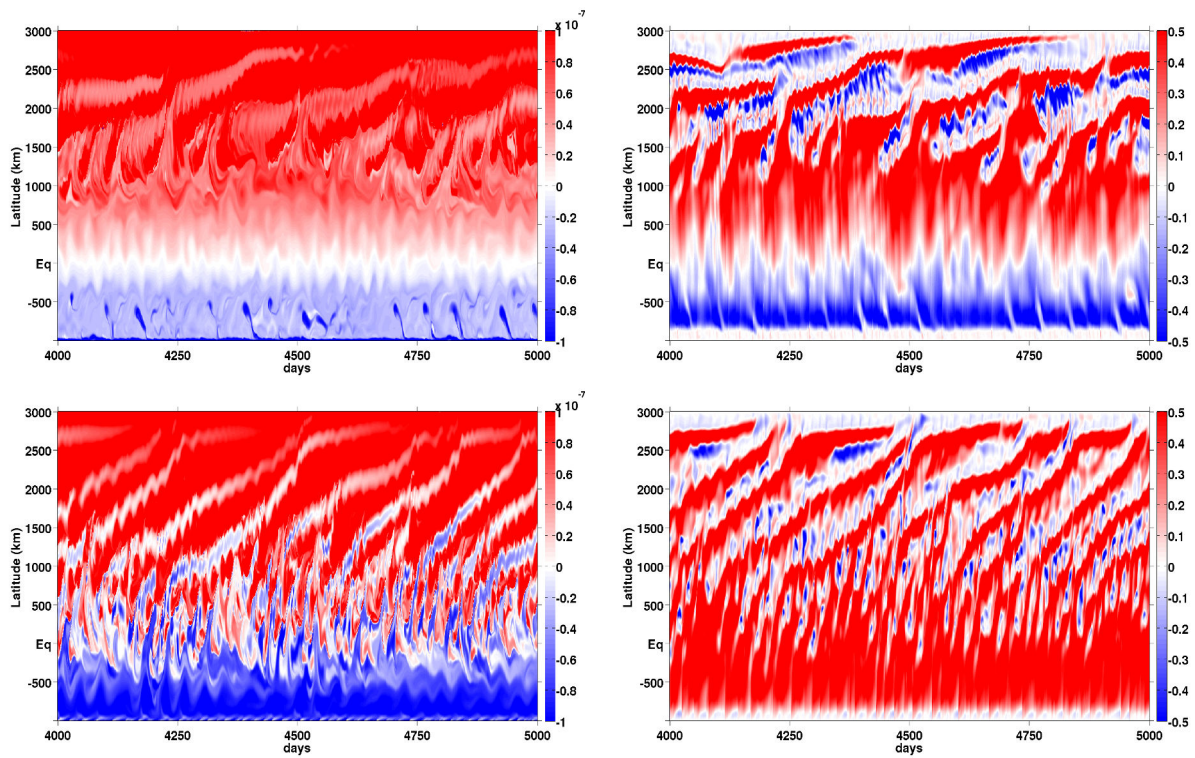
Figure 4.12 – **Left panels:** *Hovmöller diagrams of the potential vorticity at the center of eddies (lower viscosity experiments).* **Right panels:** *Near wall meridional velocity v in the viscous sub-layer. TW125 (top) and MW300 (bottom).*

The ejection of the boundary-layer and its offshore transport, asks for fine numerical resolution in both horizontal directions not only in the vicinity of the boundary-layer but also in areas to which the boundary-layer fragment is transported.

In the analysis, bursts are identified as events when the meridional velocity in the viscous sub-layer is negative, that is a velocity inversions in the viscous sub-layer. Please note that velocity inversions are also a common feature in viscous sub-layers of wall bounded flows in engineering applications [Schlichting & Gersten (2000)].

The Hovmöller diagrams of meridional velocity in the viscous sub-layer is plotted in the right panels of Fig. 4.12 (b and d) for the experiments TW125 and MW300 from t = 4000days to 5000days. The corresponding potential vorticity Hovmöller diagrams are plotted in the left of Fig. 4.12 (a and c). For the lower viscosity experiments, meridional velocity inversions are observed (Fig. 4.12b and d) associated to the passage of the anti-cyclone as can be seen in the Hovmöller diagrams of potential vorticity (Fig. 4.12a and c). The comparison of the two diagrams shows that despite the fact that bursts are created by the anticyclone, they have their one life-cycle. Burst detachments appear to be faster than the dynamics of the anticyclone in the interior.

To quantify the occurrence of burst, the percentage in time of the meridional velocity inversion at y = +1000km is given by the T1 and the average over time and y $\in$[+125, +2250km] by T2 in Tab. 4.2. In the lower viscosity MW-experiments the percentage of the meridional velocity inversion is similar at y = +1000km than those of the range of latitude between y $\in$[+125km, +2250km] showing that there is only a feeble dependence on latitude as can be seen in the Fig. 4.12d for MW300-experiment. In the lower viscosity TW-experiments almost no bursts occur south of y = +1000km in the TW-experiments as there are no eddies (Fig. 4.12c). For viscosities $\nu = 1000\text{m}^2\cdot\text{s}^{-1}$ or larger there are no bursts (Fig. 4.12b,d) as there are no eddies (Fig. 4.12a,c). Bursts are observed for $\nu = 500\text{m}^2\cdot\text{s}^{-1}$ and lower in the MW-experiments; and for $\nu = 400\text{m}^2\cdot\text{s}^{-1}$ and lower in the TW-experiments. The percentage of bursts strictly increases with decreasing viscosity in all the experiments performed and reaches values of around 20% (Tab. 4.2) for the lowest values of the viscosity, showing that they are a dominant feature of low viscosity boundary currents.

In the case of the high viscosity experiments, signatures of almost bursts are observed during the northward propagation of the wave-like features. The signatures appear as zero-vorticity sheets in the Hovmöller diagram of potential vorticity for the MW1000-experiment between latitudes y = +1000km and y = +2300km (not shown). The onset bursts are not able to detached the viscous sub-layer, so pairs of positive and negative vorticity are observed in the viscous sub-layer which slip rapidly along the boundary (not shown). This explains the high northward velocity propagation in the MW1000-experiment of the wave-like features.

Note that the slipping pairs of positive and negative vorticity gradually change into bursts with the decreasing of the viscosity and lead to the formation of dipoles for the lower viscosity experiments.

Nowadays, even if the eddy-permitting/resolving ocean models are able to entangle the large-scale patterns of the western boundary currents, as the retroflections and large-

Experiments	TW125	TW150	TW250	TW300	TW400	TW500	TW1000
T1(%)	0.93	0.8	0	0	0	0	0
T2(%)	15.57	11.62	4.81	2.63	0.52	0	0
Experiments				MW300	MW400	MW500	MW1000
T1(%)				21.67	17.5	13.57	0
T2(%)				19.07	14.36	10.38	0

Table 4.2 – *Percentage in time of the meridional velocity inversion in the viscous sub-layer at y = +1000km (T1) and for y ∈[+125, +2250km] (T2).*

scale eddies, they are not adapted to represent the fine-scale structures as the bursts and dipoles. The dynamics of bursts is indispensable for upwelling and mixing at small scale. Processes which are important for bio-geochemical evolution. The findings show that today's eddy-permitting/resolving ocean models resolution is far from being sufficient to entangle such non-linear small-scale processes.

4.5.3 Dipole

A sequence of three zoom snapshots of velocity vectors superimposed on potential vorticity (Fig. 4.11), shows the typical appearance of the flow during separation, the creation of the bursts, the dipole formation and the subsequent propagation.

In Fig. 4.11c, at day 180, the current remains adjacent to the boundary up to y = +1750km. At that location the viscous sub-layer then separates from the boundary and positive vorticity is pulled away from the boundary to the interior: the burst. At day 195 (Fig. 4.11b) the positive vorticity spins cyclonicly close to the larger anticyclonic eddy, the thus formed dipolar structure moves away from the boundary at day 200 (Fig. 4.11a). Additionally, to the left a new burst begins its formation (Fig. 4.11a).

In many instances the positive vorticity anomalies, ejected from the boundary during the bursts, pair with negative vortex anomalies from within the anticyclones and form dipoles which then travel ballisticaly (at almost constant velocity) over distances of several eddy diameters. Or, they return boundary-ward, to collide with the boundary current and perturb it. The size of the dipoles measured by the distance of the vorticity minimum and maximum spans between the thickness of the viscous boundary-layer δ_ν and the size of the coherent anticyclones (see next section). Many bursts are created by an anticyclonic eddy during its northward migration. Bursts create dipoles which interact with the eddy and perturb it. The bursts are responsible for the fact that at lower viscosity the anticyclonic eddies are less coherent.

4.6 Scales of motion

As an example let us consider the velocity field $u(y) = A\sin(y/L + \omega t)$ which has the vorticity $\zeta(y) = A\cos(y/L + \omega t)/L$.

Using the formula

$$\sqrt{\frac{\langle u^2 \rangle}{\langle \zeta^2 \rangle}}, \tag{4.21}$$

gives L, the scale of the velocity field. The following analysis is based on this formula.

For the understanding of the dynamics it is essential to determine the spatial scales of the turbulent motion. Two key quantities are considered, based on the above definition:

$$\lambda_1 = \sqrt{\frac{K(t)}{Q(t)}}, \qquad \lambda_2 = \sqrt{\frac{Q(t)}{P(t)}}, \tag{4.22}$$

where

$$K(t) = \frac{1}{2}\langle \mathbf{u}^2(x,t) \rangle \tag{4.23}$$

is the averaged kinetic energy of fluid motion,

$$Q(t) = \frac{1}{2}\langle \zeta^2(x,t) \rangle \tag{4.24}$$

is the averaged enstrophy, and

$$P(t) = \frac{1}{2}\langle (\bigtriangledown \zeta)^2(x,t) \rangle \tag{4.25}$$

the averaged palinstrophy.

in 3D turbulence λ_1 is the Taylor-scale divided by $\sqrt{5}$ [Frisch (1995)]. This length scale characterizes the size of the velocity gradients and represents the large-scale eddies.

λ_2 is characteristic of the viscous dissipation length-scale in the enstrophy cascade [Boffetta & Ecke (2012)], the smallest scales in the vortical dynamics and represents small scale eddies like coherent dipoles and bursts. The separation of these scales gives an idea of the scale range over which turbulence is active. These scales are instructive in a turbulent environment but in the boundary-layer dominated by viscosity their significance is limited. At the boundary $\lambda_1 = 0$ as energy vanishes, which does not mean that there are infinitely small scales. The smallest scale is given by the Munk scale δ_{M} even when the analytic solutions for the laminar Munk-layer are (with $x' = \sqrt{3}x/(2\delta_{\mathrm{M}})$):

$$\lambda_1 = \delta_{\mathrm{M}}\sqrt{\left(\frac{2\sin(x')}{\sin(x') - \sqrt{3}\cos(x')}\right)^2} \quad \text{and} \quad \lambda_2 = \delta_{\mathrm{M}}\sqrt{\left(\frac{\sin(x') - \sqrt{3}\cos(x')}{\sin(x') + \sqrt{3}\cos(x')}\right)^2}, \tag{4.26}$$

which oscillate between zero and infinity. This shows that the above scales are not useful for analyzing time-independent flow and therefore are not useful for high viscosity experiments. Note, that traces of these oscillations remain in the low viscosity MW experiments.
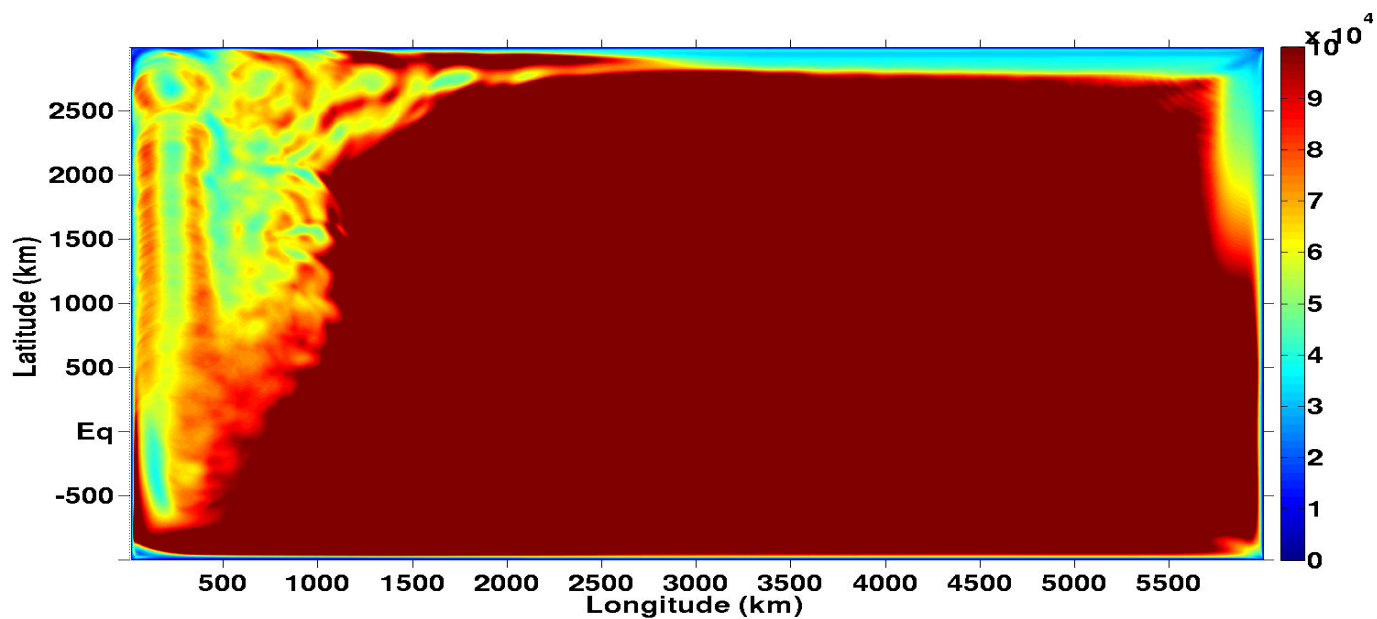
Figure 4.13 – *Taylor scale $\lambda_1(m)$ for MW300. Note that the color-bar is fixed at 100km to bring out the large-scale eddies*
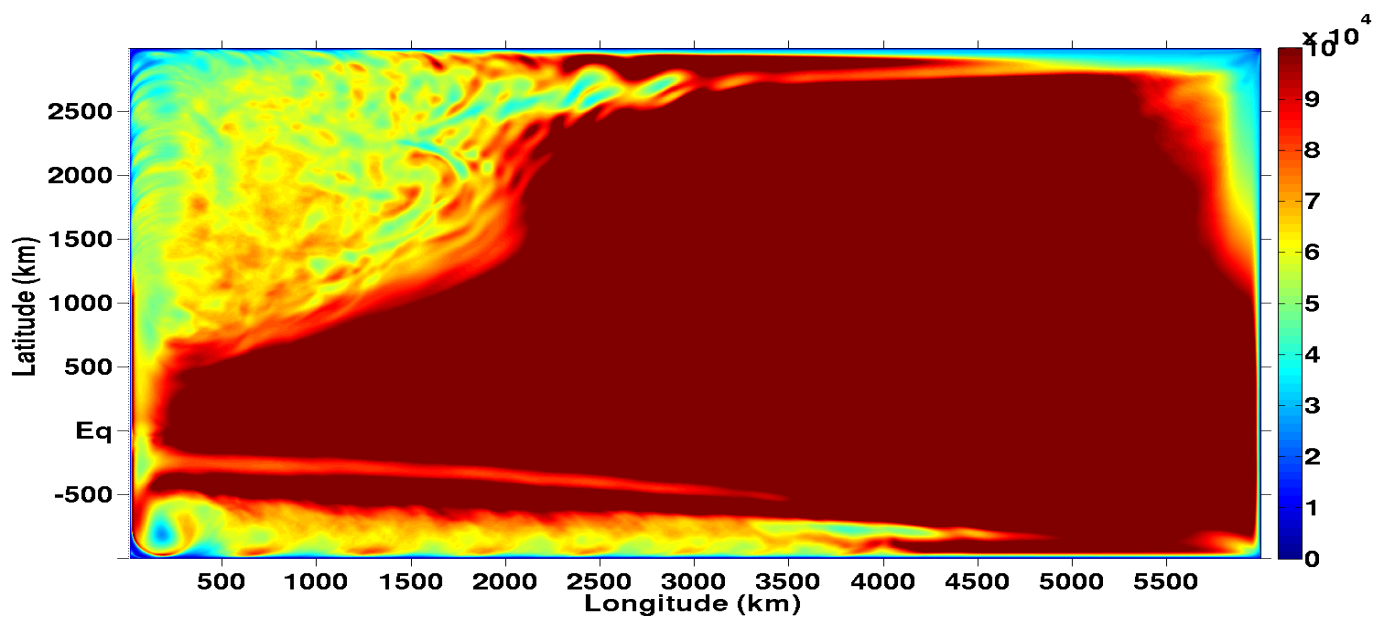
Figure 4.14 – *Taylor scale $\lambda_1(m)$ for TW125. Note that the color-bar is fixed at 100km to bring out the large-scale eddies*
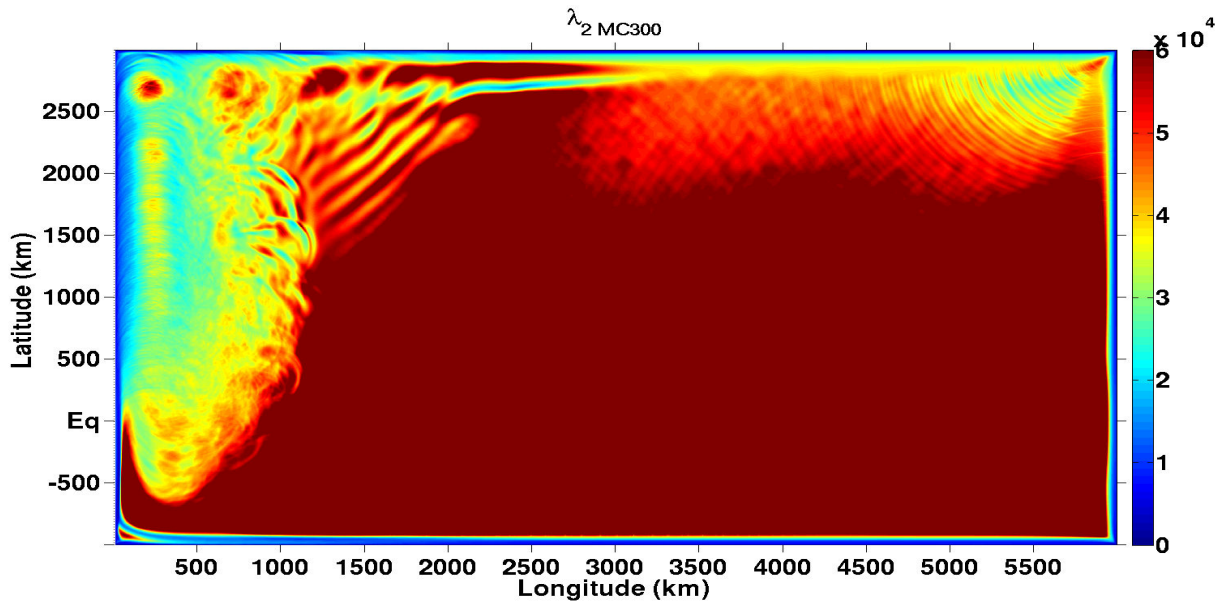
Figure 4.15 – $\lambda_2(m)$ for MW300. Note that the colorbar is fixed at 60km to bring out the small-scale eddies
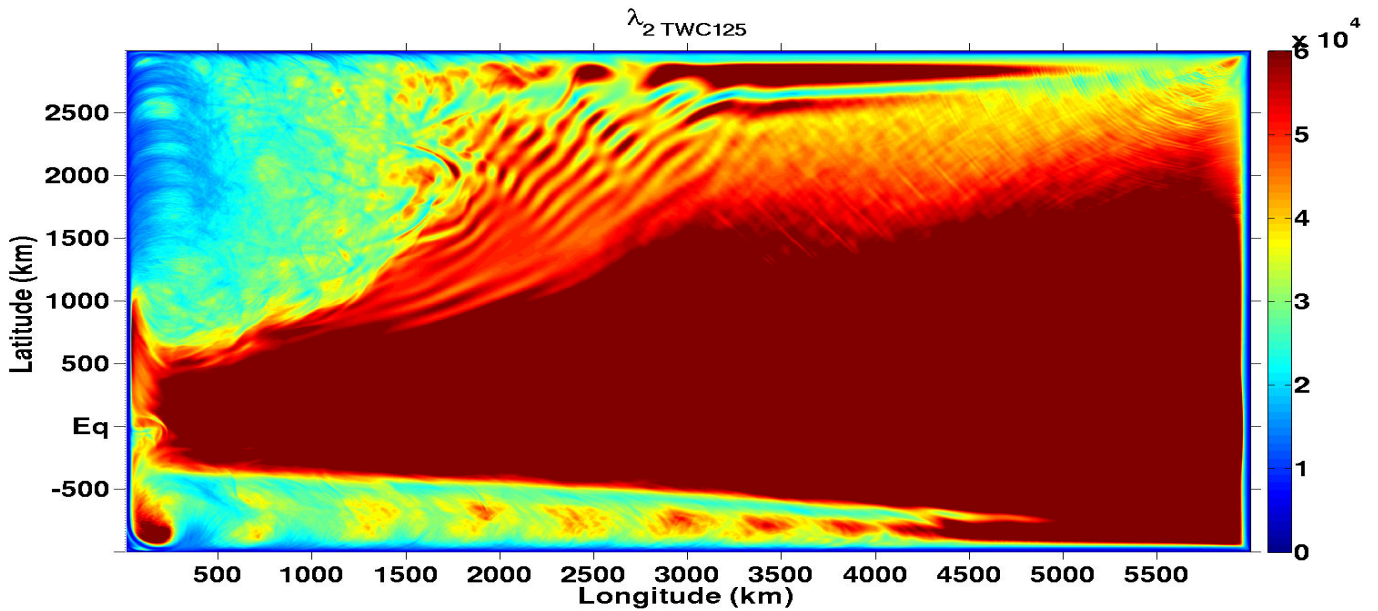
Figure 4.16 – $\lambda_2(m)$ for TW125. Note that the color-bar is fixed at 60km to bring out the small-scale eddies
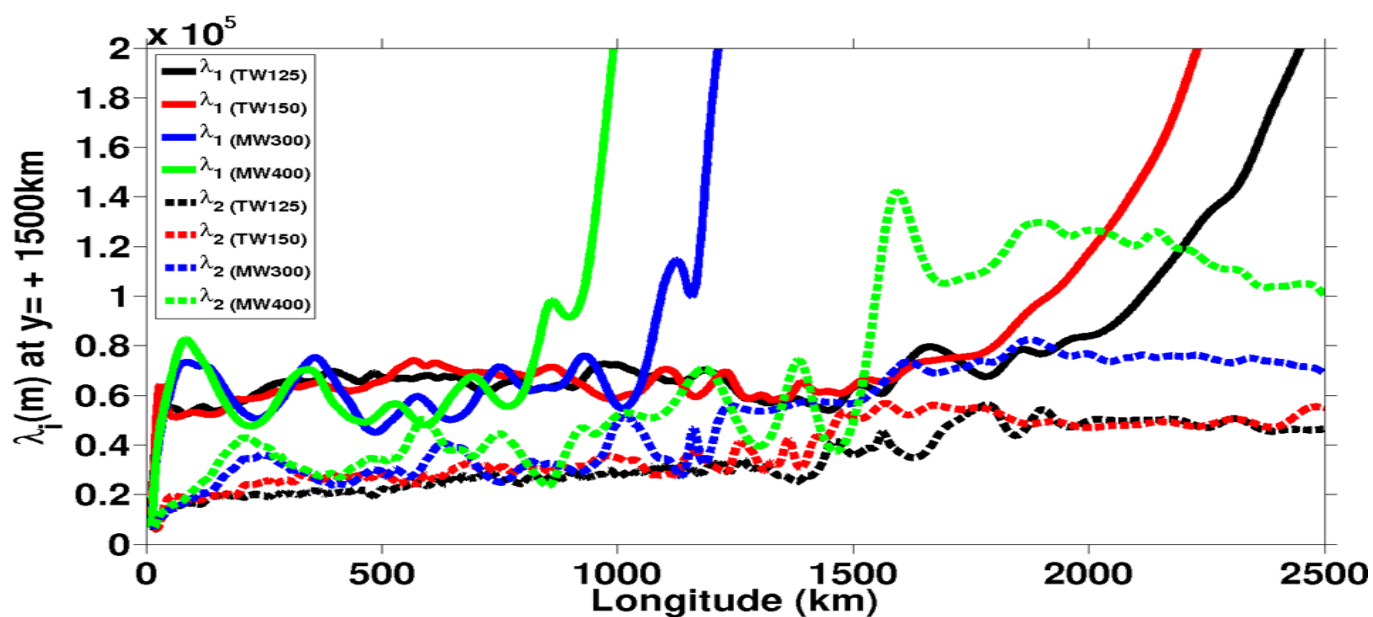
Figure 4.17 – *Zoom of zonal profiles of Taylor scale λ_1 and the viscous dissipation length-scale λ_2 at $y = +1500km$ for TW125, TW250, MW300 and MW400.*
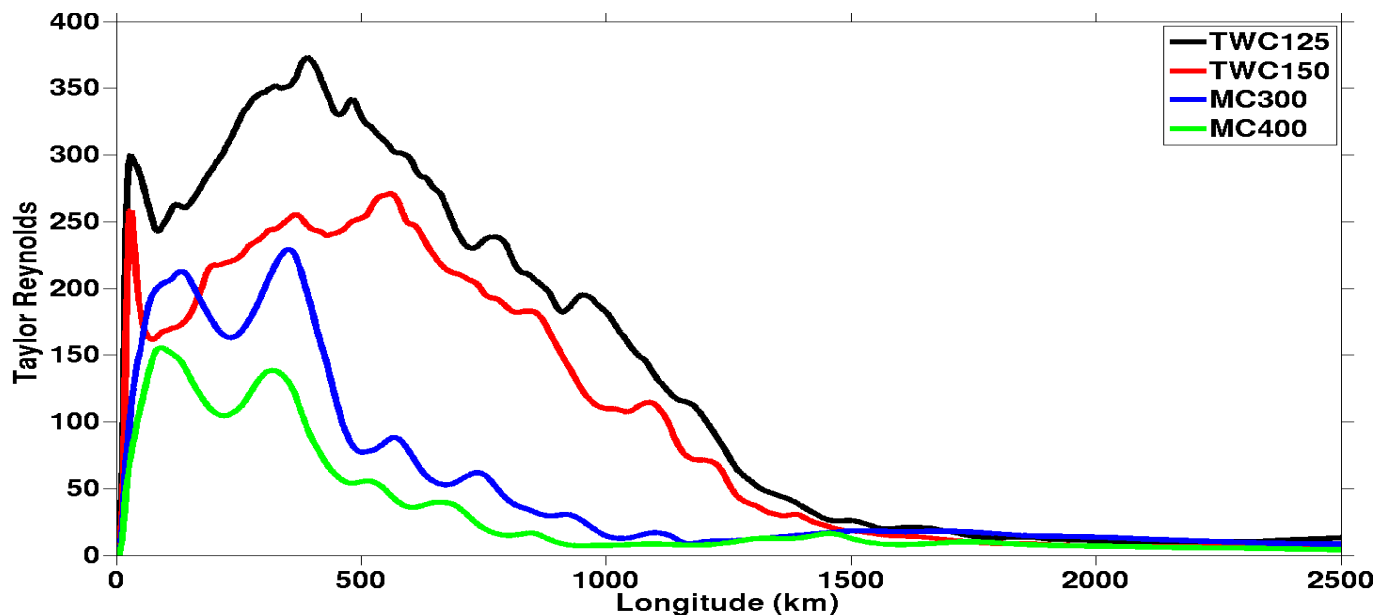
Figure 4.18 – *Zoom of zonal profiles of Taylor Reynolds number R_{e_λ} associated to λ_1, at $y = +1500km$ for TW125, TW250, MW300 and MW400.*

The Fig. 4.13 and Fig. 4.14 show the spatial distribution of the Taylor scale in the highest Reynolds number (or lower viscosity) experiments for the MW and TW case, respectively. A striking feature is the wide extension of the low-size scale values into the interior of the domain in both cases, the feeble variation within this domain and the sudden jump to high values at its clearly defined boundary. A clear plateau at around a scale of 60km is observed which extends of up to 2000km into the interior of the domain for the TW125 experiment. This area of the plateau is called the *extended boundary-layer* (EBL hereafter) and their width is δ_{ext}. The differences observed in the δ_{ext} for the TW and MW experiments reside in the intense inertial effects at low latitude in the TW experiment and the intense counter-inertial effects at the high latitude in the TW experiment. The MW experiment has no inertial effect as explained in the section 4.3.2. The scale of 60km is easily explained by the eddy size of 400km $\approx 2\pi$60km.

A clear plateau at around of a scale of 20km is also observed in the spatial distribution of the dissipation length scale λ_2 for the lower viscosities (Fig. 4.15 and Fig. 4.16) which confirmed the extented boundary-layer existence.

For a deeper understanding, the zonal profiles at latitude y $= +1500$km (where inertial effects vanish in the TW experiment) are shown for different experiments with low viscosity values (Fig. 4.17). The profiles show that the zonal extension δ_{ext} of the EBL is increasing with decreasing viscosity. The scale λ_2 is almost equal to the Munk-scale δ_{M} near the boundary and increases slowly thereafter, approaching the Taylor scale λ_1. When λ_2 reaches the eddy scale λ_1, the velocity gradients are dissipated and turbulence disappears. The behavior of both scales, λ_1 being constant and λ_2 increasing by barely a factor of two through the EBL, shows that grid refinement near the boundary might be useful in laminar, low Reynolds number simulations, but is not adapted for the fully turbulent case where small scale structures dominate even far from the boundary.

As mentioned above, the zonal extension of the EBL increases with a decreasing viscosity as I demonstrate in Fig. 4.25 . A striking feature is that, although the extension of the extended boundary-layer depends on viscosity, the scales within it appear almost independent of it, once the viscosity is low enough to allow for turbulent motion. Turbulent motion is likely to include the scales from λ_1 down to λ_2.

It is important to notice that in my calculations, λ_2 is always more than 5 times the grid size showing that the dynamics is numerically well resolved in my calculations.

The spatial distribution of the Taylor Reynolds number

$$Re_\lambda = \frac{u'\lambda_1}{\nu} \tag{4.27}$$

is calculated. Their zonal profiles for lower viscosity experiments (Fig. 4.18) show the rapid increase of R_λ reaching the maximum value near the boundary. This means that the turbulence is created in this area and transported into the interior. This shows again that grid refinement is not adapted for the fully turbulent case where small scale structures dominate, not only at the boundary but are transported into the interior.

4.7 Moments of the velocity field

After having discussed the time averages of the velocity components, I focus now on higher order moments of the fluctuations of these components. The spatial distribution of these moments for lower viscosity value experiments are calculated for the MW experiments, their zonal structure in the WBL depends only weakly on latitude. The example of MW300 experiment is given at the latitude y = +1500km in the Fig. 4.19a. To better understand the origin of these fluctuations, let's examine the moments of the velocity field of an eddy. To proceed let's assume first that the coherent structure, the eddy, is a perfect circle of radius R in anticyclonic solid-body rotation. An orthonormal coordinate system is at the circle's center. The circle equation is $x^2 + y^2 = R^2$. The water-mass in the eddy is moved around circularly. The fluctuating velocity can be expressed in the orthonormal
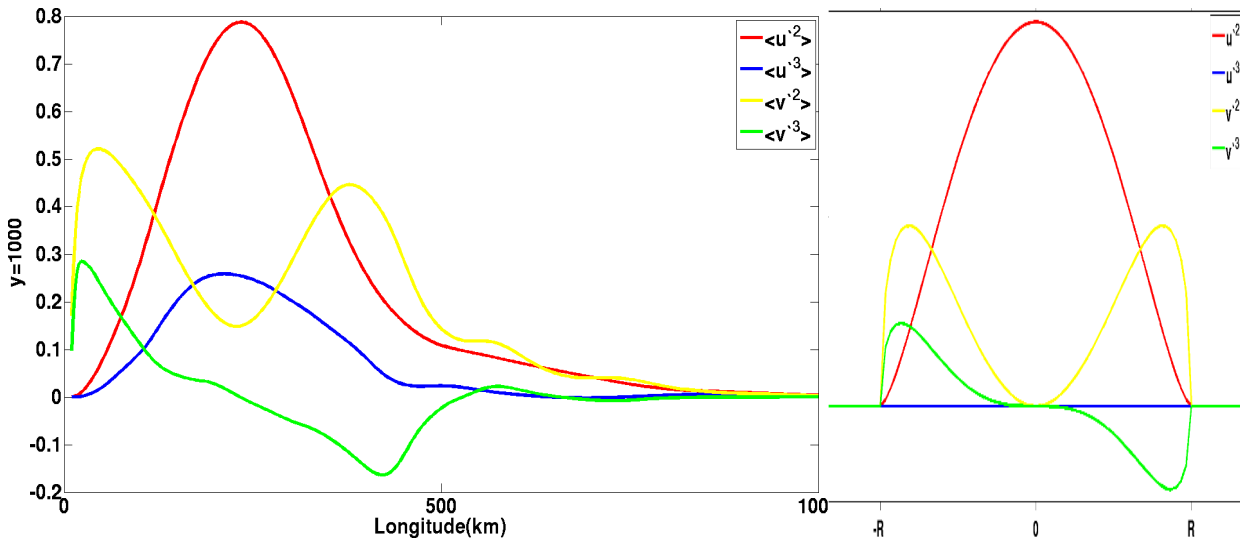
Figure 4.19 – *Zonal profiles of second and third moments of the velocity components from MW300 at y = +1500km (a) versus the analytic solutions of integration of the velocities from the idealize perfect circle eddy of equation $x^2 + y^2 = R^2$ (b).*

coordinate system as:

$$u' = y \qquad v' = -x \qquad for \qquad x^2 + y^2 > R^2. \tag{4.28}$$

Let's integrate/average the velocities field along the y-axis. The meridional integration of the disc is equivalent to taking time averages at one y-location of a disc (or a succession of disks) moving in the y-direction at constant velocity. The meridional integration between

$y_1 = \sqrt{R^2 - x^2}$ and $y_2 = -\sqrt{R^2 - x^2}$ gives:

$$
\begin{aligned}
\tilde{u} &= \int_{y_2}^{y_1} y \, \mathrm{d}y = \left[\frac{y^2}{2}\right]_{y_2}^{y_1} = 0, \\
\tilde{v} &= -\int_{y_2}^{y_1} x \, \mathrm{d}y = [-xy]_{y_2}^{y_1} = -2x\sqrt{R^2 - x^2}, \\
\tilde{u'^2} &= \int_{y_2}^{y_1} y^2 \, \mathrm{d}y = \left[\frac{y^3}{3}\right]_{y_2}^{y_1} = \frac{1}{3}\left(R^2 - x^2\right)^{\frac{3}{2}}, \\
\tilde{v'^2} &= \int_{y_2}^{y_1} x^2 \, \mathrm{d}y = \left[x^2 y\right]_{y_2}^{y_1} = 2x^2\sqrt{R^2 - x^2}, \\
\tilde{u'^3} &= \int_{y_2}^{y_1} y^3 \, \mathrm{d}y = \left[\frac{y^4}{4}\right]_{y_2}^{y_1} = 0, \\
\tilde{v'^3} &= -\int_{y_2}^{y_1} x^3 \, \mathrm{d}y = \left[x^3 y\right]_{y_2}^{y_1} = -2x^3\sqrt{R^2 - x^2}.
\end{aligned}
$$

The analytic solutions of the integration are plotted in Fig. 4.19b. The comparison between Figs. 4.19a and 4.19b shows that major aspects of the turbulent fluxes can be, to a good accuracy, explained by the anticyclonic discs. The positive value of $\langle u'^3 \rangle$ can not be explained by the disc model, which leads to a vanishing third order moment. It means, that bursts of fluid, away from the boundary are stronger and spatially more localized than the recirculation towards the boundary. This agrees the findings of anisotropic burst and dipole dynamics in section 4.5. The positive value of $\langle u'^3 \rangle$ is therefore the signature of the bursts and dipoles.

4.8   Vorticity balance of the western boundary current

By averaging the vorticity equation Eq. (3.4), over time-scales that are long compared to the time-scales of fluctuations in the system, a steady-state vorticity balance is obtained. The steady-state vorticity equation becomes:

$$
\langle u\partial_x\xi \rangle + \langle v\partial_y\xi \rangle + \langle \beta v \rangle + \langle (\xi + f)(\partial_x u + \partial_y v) \rangle - \langle \nu\nabla^2\xi \rangle = \langle S \rangle. \tag{4.29}
$$

In the Munk-layer, planetary vorticity advection is balanced by vorticity diffusion. As the system becomes nonlinear, the boundary-layer structure is not obvious, but can be diagnosed from the model. This section examines the structure of the boundary-layer as a function of latitude and longitude. The purpose is to determine the time-mean structure of the WBC. Reconsidering the time-averaged vorticity equation, the different terms in the l.h.s. of Eq. (3.4) correspond to terms 1-2: relative vorticity advection (RVA), term 3: planetary vorticity advection (PVA), term 4: stretching (STR) and term 5: the friction (FRIC).

4.8.1 Laminar experiments MW1000 and TW1000

In the laminar experiments the system divides into multiple regions with different dominances of terms presiding in the MW and TW experiments. The different components of the time-averaged vorticity equation for a sub-domain near the western boundary are shown in Figs. 4.20 and 4.21. Like predicted by the Munk-layer theory the local vorticity balance in the boundary-layer is, to leading order, between the FRIC (Figs. 4.20d and 4.21d) and the PVA (Figs. 4.20b and 4.21b). Munk-layer theory is base on quasi-geostrophy and neglects vortex stretching, which is important in the reduced-gravity model used at high latitude. The STR found to be important very close to the boundary at high latitude but decreases rapidly before the PVA (or meridional velocity) reaches its maximum.

As STR, the RVA also appears to be important in the balance very close to the boundary . It is negative at high latitudes for the MW and TW but positive at low latitude for TW and seen to be the dominant positive term near the equator where inertial effect were present. This dominance appears in the MW experiment in southern hemisphere. All of this suggest the RVA to be dominant very close the boundary in the area of the southern westward branch of the anticyclonic gyre and the STR to be dominant in the area of northern eastward branch of the anticyclonic gyre according to the global circulation.

4.8.2 Turbulent experiments MW300 and TW125

After having discussed the high viscosity experiments, I now consider the lower viscosity experiments.

Experiment MW300

The different terms of the time-averaged vorticity equation for a sub-domain of experiment MW300 near the WBC are shown in Fig. 4.22.

Frictional dissipation (Fig. 4.22d) occurs in the intense viscous boundary layer that resides immediately adjacent to the western boundary. Its magnitude and, to some extent, zonal scale decrease with latitude. The PVA (Fig. 4.22b) is proportional to $\langle v \rangle$ and therefore reveals the zonal width of the advective boundary-layer. The boundary current in this non-linear experiment is relatively narrow in the southern portion of the sub-domain, but widens northward considerably with latitude . The RVA (Fig. 4.22a) is characterized by an intense layer adjacent to the western boundary compensating the FRIC contribution at the boundary. The effect of stretching is important (Fig. 4.22c) only very close the western boundary.

Experiment TW125

For the lower viscosity TW experiments, the system is also divided into multiple regions with different dominances presiding. The different terms of the time-averaged
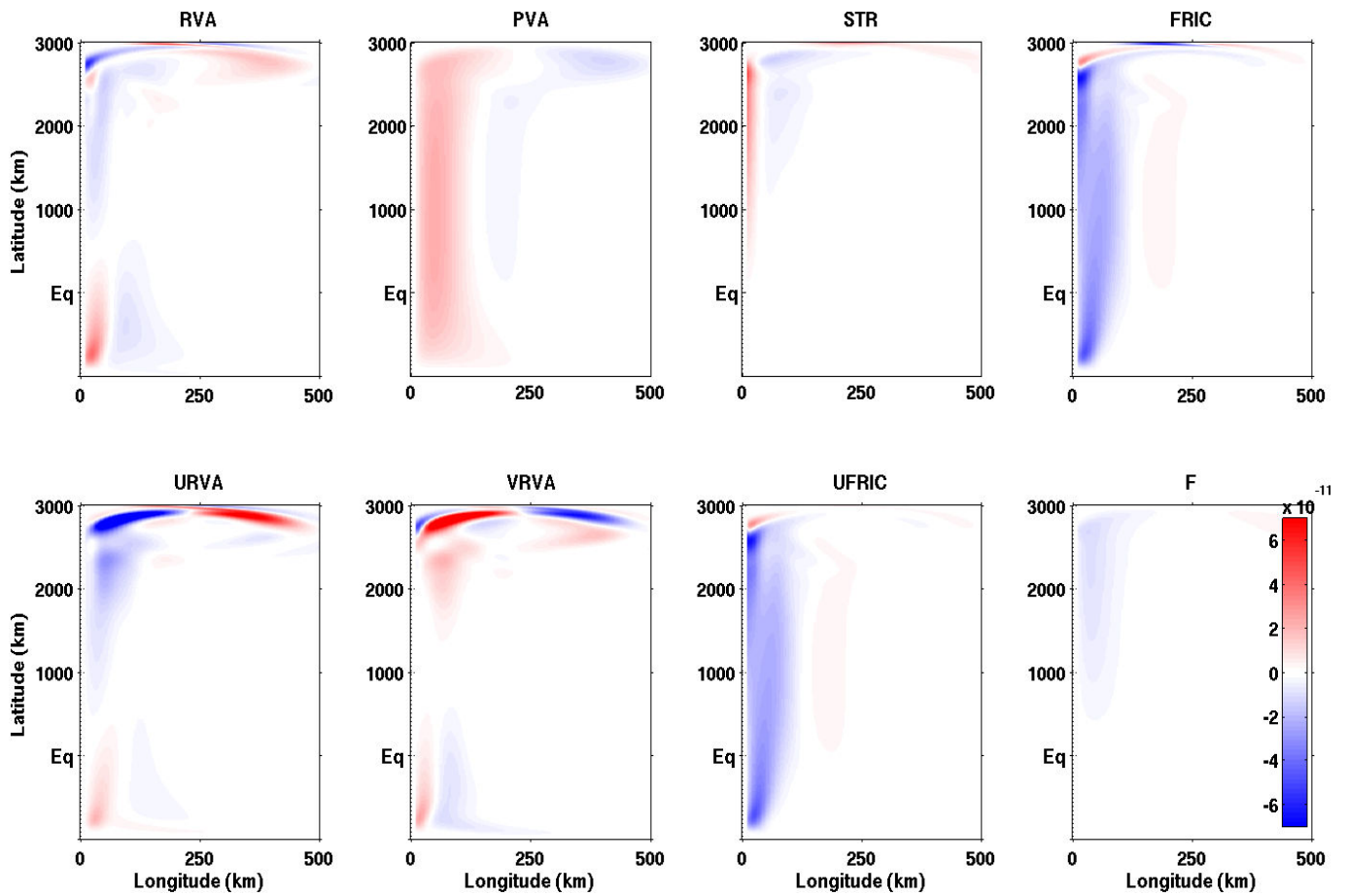
Figure 4.20 – *MW1000: plan view of the averaged vorticity equation terms (Eq. (3.4)) in a WBC sub-domain. Top panels, to the left to the right: RVA (relative vorticity advection), PVA (planetary vorticity advection), STR (the stretching) and FRIC (the friction). Bottom panels, to the left to the right: URVA (zonal component of RVA), VRVA ((meridional component of RVA), UFRIC (zonal component of the FRIC) and F (comprise the curl of the forcing and residual time dependence).*
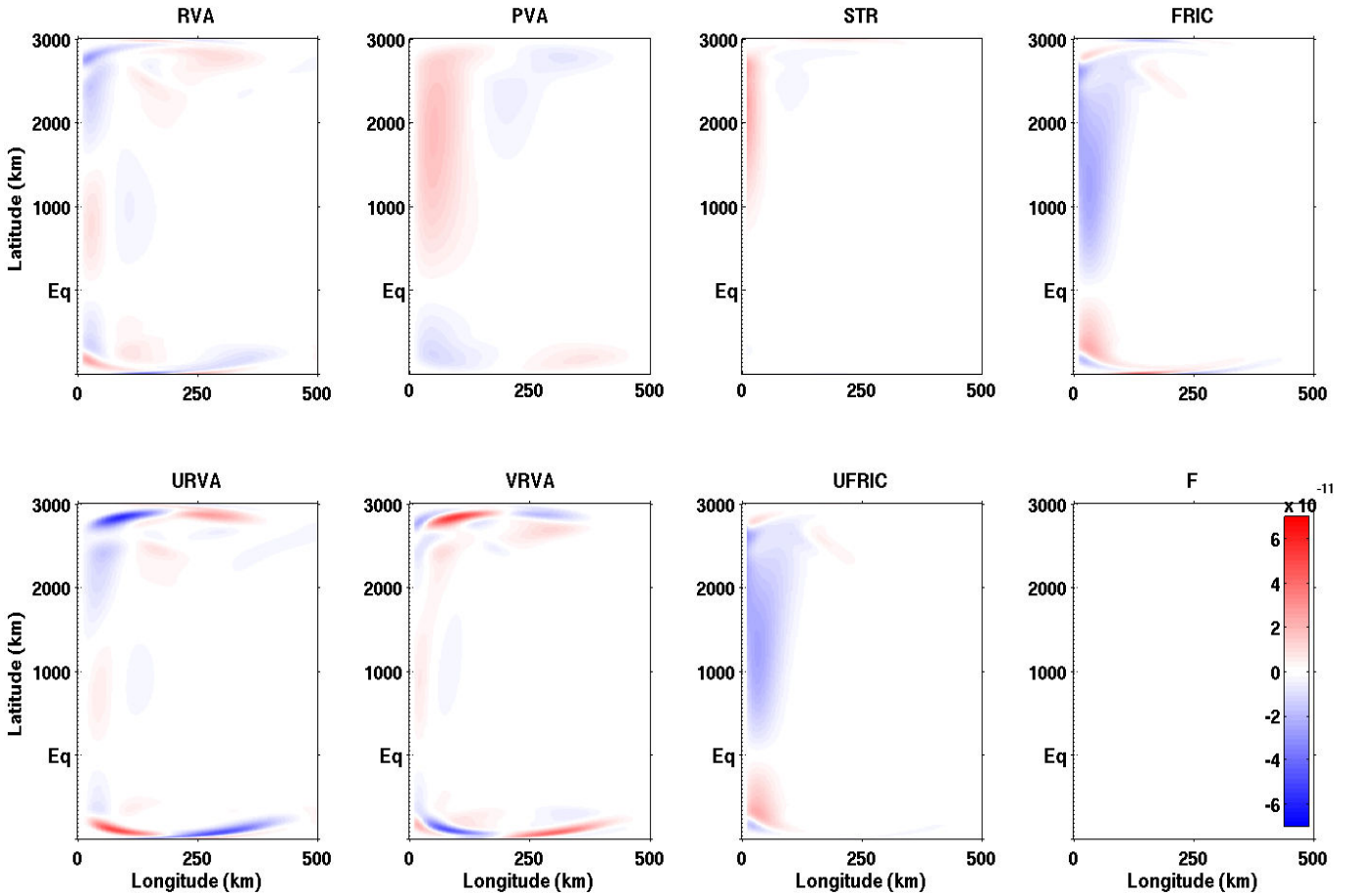
Figure 4.21 – *As in Fig. 4.20, but for TW1000 experiment.*

vorticity equation (Eq. (3.4)) in a WBC sub-domain of experiment TW125 are shown in
Fig. 4.23.

According to the poleward direction of the WBC in both hemispheres the magnitude
of the terms are similar to those of the experiment MW300 but of opposite sign in both
hemisphere. The analysis here focuses on the northern hemisphere of the sub-domain. The
frictional dissipation (Fig. 4.23d) occurs entirely in the intense frictional boundary-layer
that resides immediately adjacent to the western boundary. The PVA (Fig. 4.23b) reveals
the zonal width of the advective boundary-layer; the northward WBC circulates north of
the equator and widens considerably northward. The RVA (Fig. 4.23a) is characterized by
an intense layer adjacent to the western boundary; but the weaker contribution with an
oppositely signed to its east is located north of the latitude y = +1000km. In the advective
layer the RVA balances the PVA. The effect of stretching (Fig. 4.23c) is also small but
widens slightly northern of y = +1000km. The terms have the similar magnitude in the
southern hemisphere with an opposite sign excepted the STR.

I also plotted the meridional/zonal components of the relative vorticity advection sep-
arately in all experiments (laminar and turbulent), there are strong cancellations between
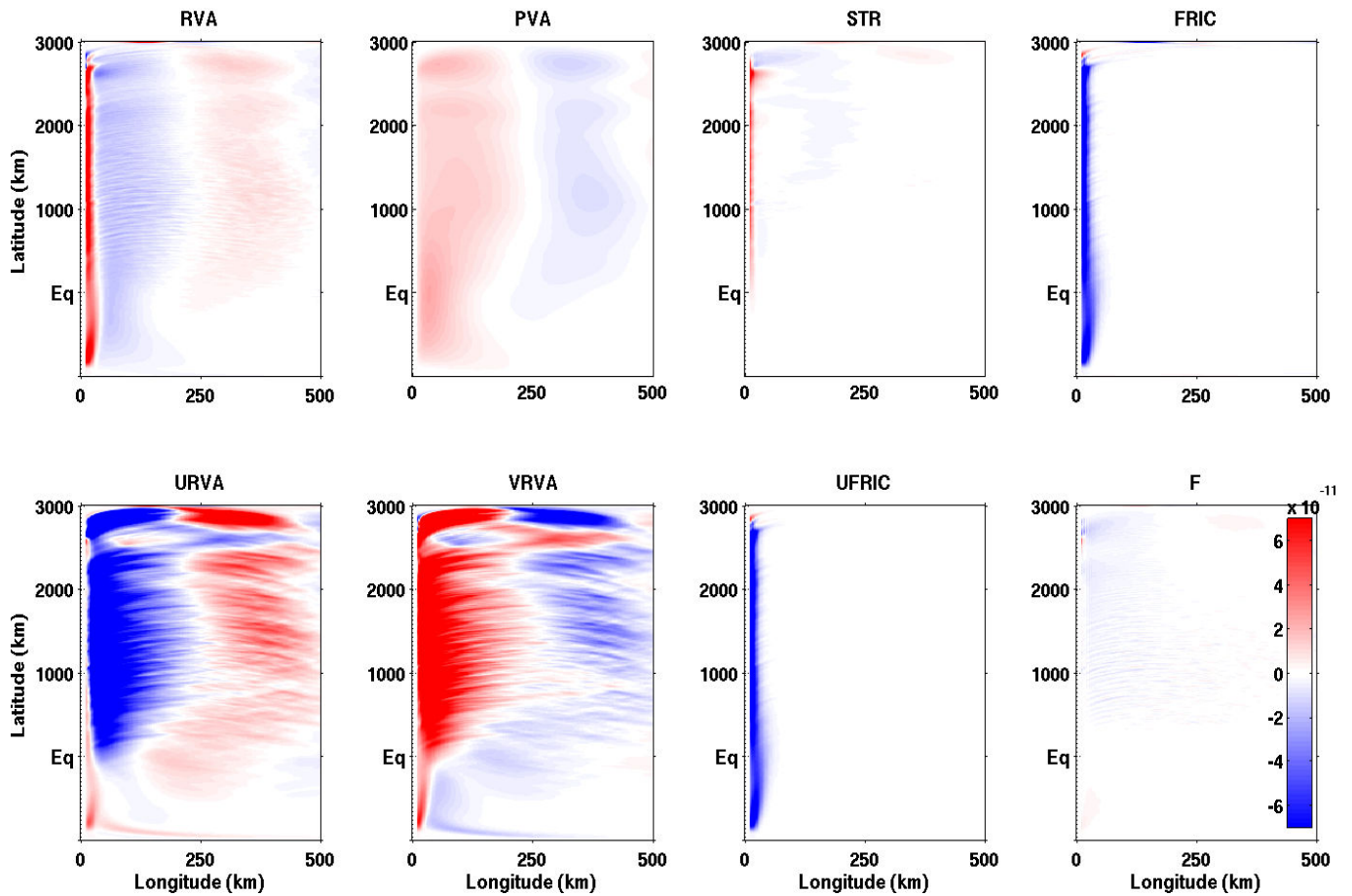
Figure 4.22 – *As in Fig. 4.20, but for MW300 experiment.*

the two components. This shows that their contribution should not be considered separately. While the plot of the meridional/zonal components of the frictional terms (FRIC) in all experiments (laminar and turbulent) show the meridional component to be negligible, only the zonal component of the frictional term contribute to the vorticity balance.

4.9   Turbulent Vorticity Fluxes

After having separated the non-linear vorticity fluxes in an advective part and a stretching part in the previous section, I now separate it in an averaged part and turbulent part.

4.9.1   Viscous sub-layer and advective boundary-layer

The vorticity balance in the laminar, time independent boundary-layer is described in sub-section 4.8.1. In the unstable boundary-layer the vorticity balance changes. To entangle the behavior of the vorticity balance, the dynamics is supposed to be in a statistically

Figure 4.23 – *As in Fig. 4.20, but for TW125 experiment.*

stationary state and the variables are separated into a time average and a perturbation that is: $a = \langle a \rangle + a'$. The Eq. (3.5) for the average vorticity balance then reads:

$$\partial_x \left[\langle u \rangle \langle \xi \rangle \right] + \partial_y \left[\langle v \rangle \langle \xi \rangle \right] + \partial_x \langle u' \xi' \rangle + \partial_y \langle v' \xi' \rangle + \beta \langle v \rangle$$
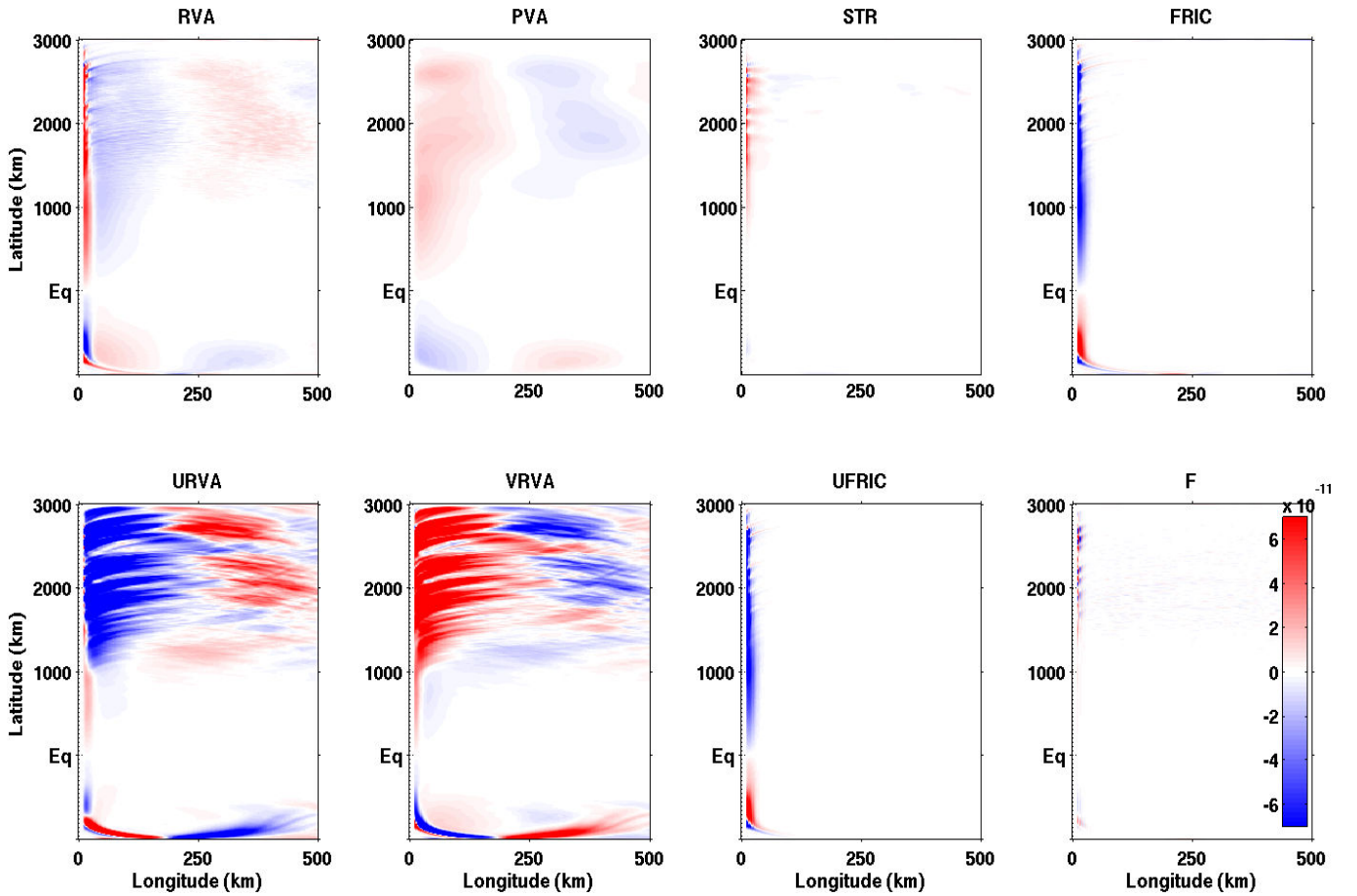$$+ f \left[\partial_x \langle u \rangle + \partial_y \langle v \rangle \right] - \nu \nabla^2 \langle \xi \rangle = \langle S \rangle. \tag{4.30}$$

An integration of the advection of vorticity over a closed basin vanishes and the integral balance is between the forcing (r.h.s of Eq. (4.30)) and the viscous vorticity flux through the boundary (last term on the l.h.s. of Eq. (4.30)). Within the basin the advection of vorticity (relative, terms 1-4, and planetary term 5) can connect the (basin-wide) source to the sink. From another angle like in the above section, the different terms in the l.h.s of Eq. (4.30) correspond in order to terms 1-2:relative vorticity advection (RVA), terms 3-4 turbulent relative vorticity advection (TRVA), term 5: planetary vorticity advection (PVA) and term 6: friction (FRIC). For high viscosities the local vorticity balance in the boundary-layer is, to leading order, between the PVA and the FRIC, leading to a Munk-layer as discussed in the section 4.3.2. When the viscosity is reduced the RVA and TRVA play an increasing role in the vorticity balance. The RVA spatially connects the
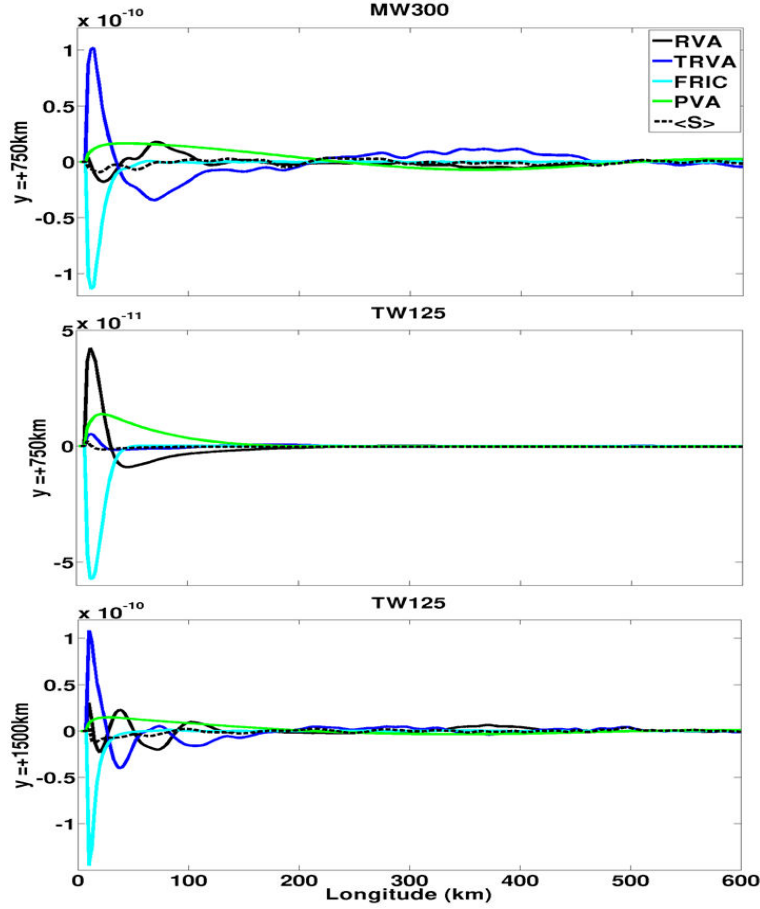
Figure 4.24 – *Vorticity balance terms of Eq. (4.30) are plotted for the MW forcing at y = +750km (upper figure) and for the TW forcing at y = +750km (middle figure) and y = +1500km (bottom figure). ⟨S⟩ comprises curl of forcing, stretching and residual time dependence*

PVA and the viscous dissipation (FRIC) and both can exhibit a different zonal length scale. This is clearly visible in Fig. 4.24: the FRIC dominates in a narrow region near the boundary, whereas the PVA happens, on average, on a wider region. The advection of relative vorticity can be decomposed into the advection of the average vorticity by the average velocity field (RVA), which I call inertial contribution, and the turbulent transport of vorticity (TRVA). The difference between the TW and the MW circulation at low latitudes is that, for the former the inertial terms are important while for the later the turbulent terms transport the vorticity. This explains the laminar boundary-layer of the TW circulation at low latitudes and the turbulence of the MW boundary-layer. Please note that the inertial boundary-layer in the TW circulation stays laminar even for the smallest viscosity used, if it becomes turbulent at even lower viscosities, is an open question. This behavior is clearly depicted in Fig. 4.24, where at low latitudes of the TW circulation the inertial part connects the planetary vorticity advection to the viscous dissipation, whereas

at higher latitudes and for the MW circulation it is the turbulent advection. The area of the viscous dissipation is called the *viscous sub-layer* (VSL hereafter) while the expression "*advective boundary-layer*" (ABL hereafter) is chosen for the wider area of large average meridional velocity. The thickness of the former is denoted by δ_ν while the thickness of the later is denoted by δ_V, in the Munk-layer they both coincide $\delta_\nu = \delta_V = \delta_M$.

4.9.2 Scaling of the width of the boundary-layers

Let's recall the question ask in the section 4.2 namely, "It is demonstrated with no doubt that these two laminar theories give a good description of laminar flows but a pertinent question subsists is it true for the turbulent flows?" To answer this substantial question the scalings of the width of the three boundary-layers identified previously (advective boundary-layer, extended boundary-layer and viscous sub-layer) are used.

The thickness δ_ν of the viscous sub-layer is estimated by the distance from the boundary at which the value of the Laplacian of the average vorticity has reduced to a third of its maximal value. The same criterion was applied to the average meridional velocity to obtain δ_V. Results for the corresponding boundary-layer scales for the two types of forcing, different viscosities and at different latitudes are assembled in Fig. 4.25. For the viscous sub-layer, results show that its thickness drops well below the Munk-scale for low viscosities, while the thickness of the advective boundary-layer is always above. Please note that Ierley & Young (1991) propose a scaling of $\delta_\nu \sim \nu^{1/6}$ for the boundary-layer with an inertial component based on laminar boundary-layer theory and an ansatz for the shape of the boundary-layer.
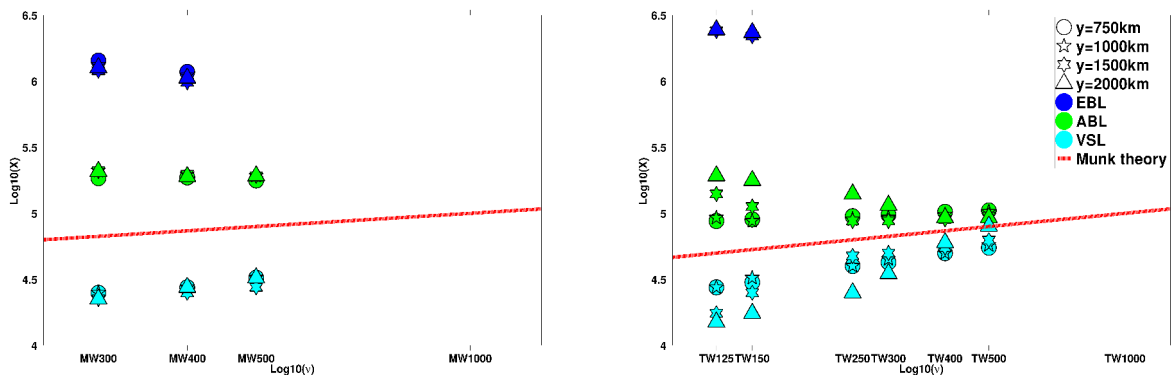
Figure 4.25 – *Thickness of viscous sub-layer (VSL), advective boundary-layer (ABL) and extended boundary-layer (EBL) for MW-forcing (a) and TW-forcing (b) at different latitudes y.*

I analyzed the scalings of the turbulent boundary-layer thickness by just considering values obtained from turbulent boundary-layers. The presnt results for the inertial boundary-layer, see Tab. 4.3, show a much steeper scaling of $\frac{1}{2}$ at low latitudes. This exponent suggests that the dominant vorticity advection near the boundary does not depend on the viscosity and has to be balanced at the boundary by viscous dissipation. At

	MW			TW		
y(km)	VSL	ABL	EBL	VSL	ABL	EBL
+750	0.50	-0.07	-0.68	0.50	0.13	–
+1000	0.50	-0.17	-0.63	0.50	0.08	–
+1500	0.39	-0.17	-0.71	0.89	-0.27	-0.48
+2000	0.71	-0.15	-0.62	1.20	-0.57	-0.25

Table 4.3 – *Scaling of the sub-layers at different latitudes y*

higher latitudes the scaling is higher for the TW forcing, showing that the boundary-layer thickness decreases even faster with decreasing viscosity, when "inverse inertial" effects are present. In all calculations with a turbulent boundary-layer, the thickness of the viscous sub-layer is well below the Munk-layer thickness. In Fig. 4.24 the inertial part shows an oscillatory behavior at high latitudes for the TW-forcing, where the zonal velocity is positive, which leads to an inertial boundary layer scale that is complex valued which explains the oscillations.

The scaling of the advective boundary-layer thickness δ_V for the MW case shows a slight increase with decreasing viscosity (see Tab. 4.3) and a possible saturation around 200km. For the TW case δ_V shows a slight decrease with decreasing viscosity at low latitudes and a saturation at the value corresponding to the inertial boundary-layer. At higher latitudes the δ_V increases with decreasing viscosity. At higher latitudes, where no inertial boundary-layer is present, the thickness of the advective boundary-layer still increases with decreasing viscosity.

4.10   Eddy viscosity

Reconsidering the conservative form of the vorticity equation Eq. (3.5), in a statistically stationary state, the averaged equation reads: :

$$\langle \partial_x(u(\zeta + f))\rangle + \langle \partial_y(v(\zeta + f))\rangle = \nu(\partial_{xx} + \partial_{yy})\langle \zeta \rangle + \langle F \rangle, \tag{4.31}$$

which is equal to:

$$\partial_x\langle u(\zeta + f)\rangle + \partial_y\langle v(\zeta + f)\rangle = \nu(\partial_{xx} + \partial_{yy})\langle \zeta \rangle + \langle F \rangle. \tag{4.32}$$

Writing all variables as the mean part and the fluctuating part $a = \langle a \rangle + a'$, Eq. (4.32) becomes:

$$\partial_x\left[\langle u \rangle(\langle \zeta \rangle + f)\right] + \partial_y\left[\langle v \rangle(\langle \zeta \rangle + f)\right]$$
$$+\partial_x\langle u'\zeta'\rangle + \partial_y\langle v'\zeta'\rangle$$
$$= \nu(\partial_{xx} + \partial_{yy})\langle \zeta \rangle + \langle F \rangle. \tag{4.33}$$

The first line of Eq. (4.33) is the transport of the average vorticity due to the average velocity field, it is equal to:

$$\langle u \rangle\partial_x\langle \zeta \rangle + \langle v \rangle\partial_y\langle \zeta \rangle + \beta\langle v \rangle + (\langle \zeta \rangle + f)(\partial_x\langle u \rangle + \partial_y\langle v \rangle). \tag{4.34}$$

The second line of Eq. (4.33) are the turbulent fluxes, they are equal to :

$$\partial_x(\langle u'\zeta'\rangle) + \partial_y(\langle v'\zeta'\rangle).$$ (4.35)

Defining two turbulent viscosities in each direction:

$$\nu_{\text{eddy}}^x = -\frac{\langle u'\zeta'\rangle}{\partial_x\langle\zeta\rangle},$$ (4.36)

$$\nu_{\text{eddy}}^y = -\frac{\langle v'\zeta'\rangle}{\partial_y\langle\zeta\rangle}.$$ (4.37)

The Eq. (4.33) can be written with these two turbulent quantities:

$$\partial_x\left[\langle u\rangle(\langle\zeta\rangle + f)\right] + \partial_y\left[\langle v\rangle(\langle\zeta\rangle + f)\right]$$
$$= \partial_x\left[(\nu + \nu_{\text{eddy}}^x)\partial_x\langle\zeta\rangle\right] + \partial_y\left[(\nu + \nu_{\text{eddy}}^y)\partial_y\langle\zeta\rangle\right] + \langle F\rangle.$$ (4.38)

Assuming that $\nu_{\text{eddy}}^x = \nu_{\text{eddy}}^y = Cte = \nu'_{\text{eddy}}$, the Eq. (4.38) becomes:

$$\partial_x\left[\langle u\rangle(\langle\zeta\rangle + f)\right] + \partial_y\left[\langle v\rangle(\langle\zeta\rangle + f)\right]$$
$$= (\nu + \nu'_{\text{eddy}})(\partial_{xx} + \partial_{yy})\langle\zeta\rangle + \langle F\rangle.$$ (4.39)

This means that when the above applies the turbulent fluctuations act as a turbulent eddy viscosity on the mean flow with:

$$\nu'_{\text{eddy}} = \nu_{\text{eddy}} - \nu.$$ (4.40)

The following sub-sections are focused on different methods to estimate this turbulent eddy viscosity which will call hereafter eddy viscosity for reason of simplicity.

4.11 Estimation of eddy viscosity via Munk formula

This sub-section proposes a simple pragmatic approach to determine the eddy viscosity via the Munk-layer formula of the viscous boundary-layer. The approach is based on the assumption that the inertial effect and stretching terms do not depend on viscosity to leading order, and so the beta-effective β_{eff} (to be defined below) does not depend on viscosity.

To proceed, let's define and estimate the beta-effective (β_{eff}) before the estimation of eddy viscosity.

4.11.1 Estimation of the effective beta value (β_{eff})

The potential vorticity formula on the β-plane is:

$$q = \frac{\zeta + f_o + \beta y}{H + \eta}.$$ (4.41)

According to the variation of the layer-thickness with the latitude y, the layer-thickness can be approximated to first order by

$$\eta = \alpha y, \tag{4.42}$$

where α is a constant.

The potential vorticity becomes:

$$q = \frac{\zeta + f_o + \beta y}{H + \alpha y}, \tag{4.43}$$

which can be written as

$$q = \frac{\zeta + f_o + \beta y}{H} \cdot \frac{1}{1 + \frac{\alpha}{H} y}, \tag{4.44}$$

where $\frac{\alpha}{H} y$ is small. Neglecting the relative vorticity and considering the first order approximation in $\frac{\alpha}{H} y$ of the planetary vorticity, I obtain:

$$q \approx \frac{f_o + \beta y}{H} (1 - \frac{\alpha}{H} y). \tag{4.45}$$

The Eq. (4.45) is equal in the first order in y to:

$$q \approx \frac{f_o + (\beta - \frac{\alpha}{H} f_o) y}{H}. \tag{4.46}$$

The comparison with the exact vorticity formula (Eq. (4.41)) leads to an effective β term:

$$\beta_{\mathrm{eff}} = \beta - \frac{\alpha}{H} f_o, \tag{4.47}$$

where I added, the exact beta and the topographic-beta:

$$\beta_{\mathrm{topo}} = -\frac{\alpha}{H} f_o. \tag{4.48}$$

Reconsidering the first non-trivial zero (Eq. (4.19)) of the analytic solution of Munk-layer theory, I obtain:

$$x_{\mathrm{M}} = \frac{2\pi}{\sqrt{3}} \left(\frac{\nu}{\beta} \right)^{\frac{1}{3}} \quad \Leftrightarrow \quad x_{\mathrm{M}} \left(\frac{\beta}{\nu} \right)^{\frac{1}{3}} = \frac{2\pi}{\sqrt{3}}, \tag{4.49}$$

which means that the quantity $x_{\mathrm{M}} \left(\frac{\beta}{\nu} \right)^{\frac{1}{3}}$ is constant and equal to $\frac{2\pi}{\sqrt{3}}$. As shown in section 4.3.2 the profile of the meridional velocity v in the boundary-layer is close to the shape of the analytic solution of Munk-layer theory, when inertial effects are absent for the stationary experiments of viscosity $1000 \mathrm{m}^2 \cdot \mathrm{s}^{-1}$. Using the theoretical first non-trivial zero x_{M} and the experimental first non-trivial zero x_0 lead to:

$$x_{\mathrm{M}} \left(\frac{\beta}{\nu} \right)^{\frac{1}{3}} = x_0 \left(\frac{\beta_{\mathrm{eff}}}{\nu} \right)^{\frac{1}{3}} = \frac{2\pi}{\sqrt{3}}, \tag{4.50}$$

which allows to calculate the beta-effective value by the formula:

$$\beta_{\text{eff}} = \beta \left(\frac{x_{\text{M}}}{x_0} \right)^3. \tag{4.51}$$

The topographic beta formula Eq. (4.48) is given by:

$$\beta_{\text{topo}} = \beta_{\text{eff}} - \beta = \beta \left[\left(\frac{x_{\text{M}}}{x_0} \right)^3 - 1 \right]. \tag{4.52}$$

As determined previously in the section 4.3.2, using the values $\nu = 1000\text{m}^2 \cdot \text{s}^{-1}$ and $\beta = 2 \cdot 10^{-11}\text{m}^{-1} \cdot \text{s}^{-1}$ gives $x_{\text{M}} = 133\text{km}$ and the numerical results give $x_0 = 145\text{km}$ where inertial effects vanished (high latitudes). At these higher latitudes the beta-effective is around $\beta_{\text{eff}} = 1.5434 \cdot 10^{-11}\text{m}^{-1} \cdot \text{s}^{-1}$ and the beta-topographic is around $\beta_{\text{topo}} = 0.4566 \cdot 10^{-11}\text{m}^{-1} \cdot \text{s}^{-1}$.

Indeed the gradients of layer-thickness along the y-axis in the boundary-layer vary and the corresponding first order topographic beta values agree with the above ansatz for the planetary beta-effective.

4.11.2   Estimation of the eddy viscosity

It is shown in the section 4.3.2 and Fig. 4.5 that the profile of the meridional velocity v in the stationary boundary-layer is close to the shape of the analytic solution of Munk-layer theory, where the inertial effects are absent. For the lower viscosity experiments when turbulence occurs, the shape of the time averaged meridional velocity still somehow resembles the Munk-layer solution with a meridional velocity which has a first non-trivial zero at a distance x_0 from the boundary. For the Munk-layer this distance is equal to $(2\pi/\sqrt{3})\delta_{\text{M}}$. The meridional gradient in layer thickness α (given above) imposed by the large scale circulation adds a topographic $-\frac{\alpha}{H}f_o$ to the planetary value as discussed above. The idea is now to calculate an eddy viscosity ν_{eddy} using the same method to estimate the beta-effective based on the distance $x_{0_{\text{stat}}}$ (first non-trivial zero of the stationary experiments of viscosity $1000\text{m}^2 \cdot \text{s}^{-1}$) and the distance x_0 (first non-trivial zero of the averaged meridional velocity in an unstable and turbulent experiment), which is given by

$$\nu_{\text{eddy}} = \left(\frac{x_0}{x_{0_{\text{stat}}}} \right)^3 \nu_{\text{stat}}, \tag{4.53}$$

where $\nu_{stat} = 1000\text{m}^2 \cdot \text{s}^{-1}$ is a viscosity for which the flow is stationary. Such method can not be applied to the inertial boundary-layer where the average meridional velocity decays exponentially away from the boundary and does not vanish (see section 4.3.2).

A clear scaling for $\nu_{eddy} - \nu$ as a function of the maximum r.m.s. velocity u' is shown in Fig. 4.26, for data from the MW- and TW-forcing at higher latitudes. The scatter plot is well fit by an affine regression line of equation

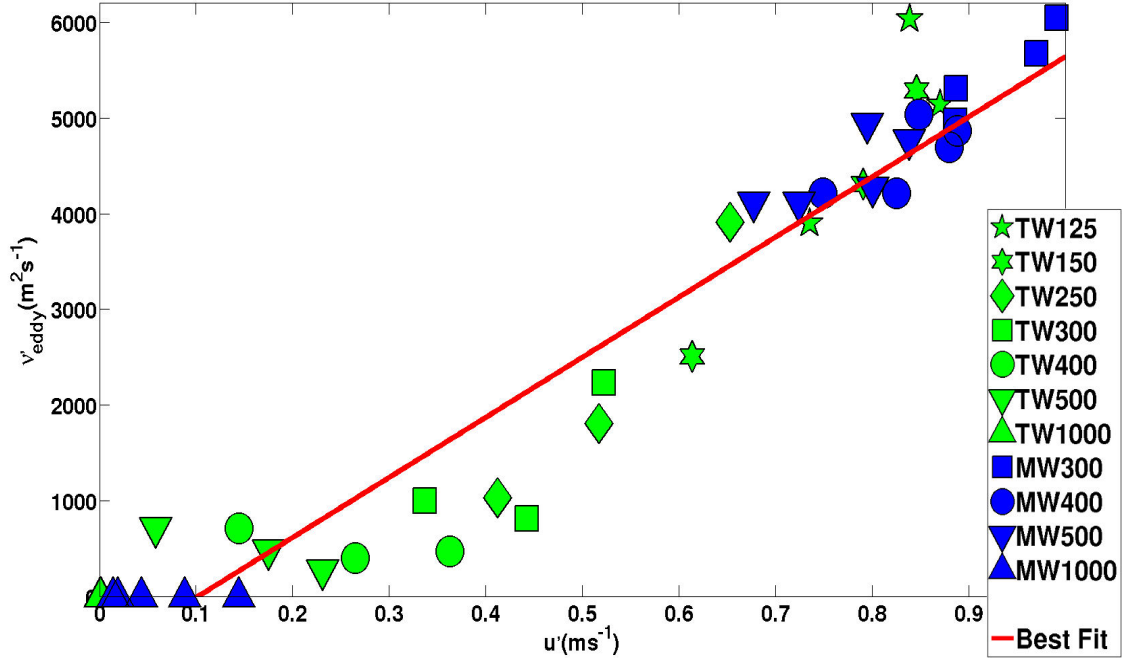$$\nu_{\text{eddy}} - \nu = u' \cdot 6283.3m - 639.3\frac{m^2}{s}, \tag{4.54}$$

Figure 4.26 – *Scatter plot diagram of eddy viscosity computed from the outputs using the Munk formula neglecting the variation of β_{eff}, as function of the maximum fluctuating velocity for all experiments at latitudes $y = +1500km$, $y = +1750km$ and $y = +2000km$. The green plots correspond to the TW experiments, the blue plots those of MW experiments and the red line is the best fit linear regression.*

which means that whatever the forcing and the viscosity, there is a correlation between the eddy viscosity and the fluctuating velocity. The correlation of the best fit linear regression is R = 0.9701. The finding that for small values of u' there is no turbulent contribution to the eddy viscosity is explained by the fact, that the small perturbations have a wave-like structure which do not lead to turbulent fluxes.

The simplest way to estimate an eddy viscosity proposed by *Prandtl's* Mischungsweg (mixing length) λ and the fluctuating velocity u' [Prandtl (1925)] is:

$$\nu_{\text{eddy}} - \nu = \alpha \lambda u'. \tag{4.55}$$

The results of the non-linear experiments confirm this proportionality. The numerical result for large scale eddy (Taylor-scale) $\lambda = L_{\text{eddy}}/(2\pi) = 60km$ calculated previously within the extended boundary leads to $\alpha \approx 0.1$. Supposing that the eddy viscosity is due to the anticyclones, this value of α is within the range proposed by Smagorinsky (1993). The values of λ and u' can not be obtained from external parameters but are a result from the numerical experiment. In concrete cases, they can often be obtained from observation or fine resolution numerical simulations.

Using $\alpha = 0.1$ and the typical values for the Somali Current of $L_{\text{eddy}} = 400km$ and $u' = 1\text{m·s}^{-1}$ leads to $\nu_{\text{eddy}} \approx 6000\text{m}^2\text{·s}^{-1}$ and a $\delta_{\text{Munk}} \approx 120km$. A consequence of this is

that even a non-eddy permitting ocean model should have a grid size not exceeding 50km to capture the boundary-layer dynamics and the associated heat transport at least in an average sense and no value of the eddy viscosity larger than $6000 \text{m}^2 \cdot \text{s}^{-1}$ should be used.

   This pragmatic approach leads to a viscosity and a boundary-layer thickness that compares well to average values in the turbulent boundary current. This approach is of course questionable as the eddy size is larger than the mean current, that is the scale separation is smaller than unity and the eddy viscosity approach asks for large scale separations. This problematic was already noticed by Charney (1955) who states: "In order to account for the observed width of the current, Munk was forced to postulate an eddy viscosity so large that the eddy sizes were themselves comparable to the width"

   An estimation of the eddy viscosity based on the average meridional velocity was given and I have shown, that it can be connected via Prandtl's formula to the velocity fluctuations. This is however not a parameterization as the turbulent fluxes themselves are not obtained from the large-scale dynamics.

4.12   Further attempts of the estimation of the eddy viscosity

   In this section, I discuss further attempts for the determination of the eddy viscosity and show how they fail.

4.12.1   Estimation of the eddy viscosity via eddy fluxes

   Reconsidering the Eq. (4.38):

$$\partial_x \left[\langle u \rangle (\langle \zeta \rangle + f) \right] + \partial_y \left[\langle v \rangle (\langle \zeta \rangle + f) \right]$$
$$= \partial_x \left[(\nu + \nu_{\text{eddy}}^x) \partial_x \langle \zeta \rangle \right] + \partial_y \left[(\nu + \nu_{\text{eddy}}^y) \partial_y \langle \zeta \rangle \right] + \langle F \rangle.$$

Rather than decomposing the eddy viscosity into x and y components, which is rather arbitrary, It can also be decomposed into a component in the direction of the large scale vorticity gradient $\nu_{\text{eddy}}^{\parallel}$. Writing in vector notation:

$$\begin{pmatrix} \nu_{\text{eddy}}^x \partial_x \langle \zeta \rangle \\ \nu_{\text{eddy}}^y \partial_y \langle \zeta \rangle \end{pmatrix} = - \begin{pmatrix} \langle u' \zeta' \rangle \\ \langle v' \zeta' \rangle \end{pmatrix}, \tag{4.56}$$

and multiplying it by the mean vorticity gradient $(\partial_x \langle \zeta \rangle, \partial_y \langle \zeta \rangle)$ on both sides gives:

$$\nu_{\text{eddy}}^x (\partial_x \langle \zeta \rangle)^2 + \nu_{\text{eddy}}^y (\partial_y \langle \zeta \rangle)^2 = -\langle u' \zeta' \rangle \, \partial_x \langle \zeta \rangle - \langle v' \zeta' \rangle \, \partial_y \langle \zeta \rangle, \tag{4.57}$$

which leads to

$$\nu_{\text{eddy}}^{\parallel} = -\frac{\langle u' \zeta' \rangle \, \partial_x \langle \zeta \rangle + \langle v' \zeta' \rangle \, \partial_y \langle \zeta \rangle}{(\partial_x \langle \zeta \rangle)^2 + (\partial_y \langle \zeta \rangle)^2}, \tag{4.58}$$

clearly if $\nu_{\text{eddy}}^x = \nu_{\text{eddy}}^y$ then $\nu_{\text{eddy}}^{\parallel} = \nu_{\text{eddy}}^x = \nu_{\text{eddy}}^y$. The quantity $\nu_{\text{eddy}}^{\parallel}$ is easier to calculate as it is less likely that the denominator vanishes as it is the sum of two positive quantities. If $\nu_{\text{eddy}}^{\parallel}$ is well behaved, it would mean that indeed relative vorticity diffusion is due to small scale motion. In my simulations (not shown) it however varies largely and takes values of both signs.

In the case that the turbulent fluxes do not diffuse relative vorticity but total vorticity $\langle \partial_y \zeta \rangle + \beta$ or potential vorticity $q = \frac{\zeta + f}{\eta + H}$, then I obtain:

$$\nu_{\text{eddy}}^{\parallel,\beta} = -\frac{\langle u'\zeta' \rangle \, \partial_x \langle \zeta \rangle + \langle v'\zeta' \rangle \, (\partial_y \langle \zeta \rangle + \beta)}{(\partial_x \langle \zeta \rangle)^2 + (\partial_y \langle \zeta \rangle + \beta)^2}, \tag{4.59}$$

$$\nu_{\text{eddy}}^{\parallel,q} = -\frac{\langle u'q' \rangle \, \partial_x \langle q \rangle + \langle v'q' \rangle \, \partial_y \langle q \rangle}{(\partial_x \langle q \rangle)^2 + (\partial_y \langle q \rangle)^2}. \tag{4.60}$$
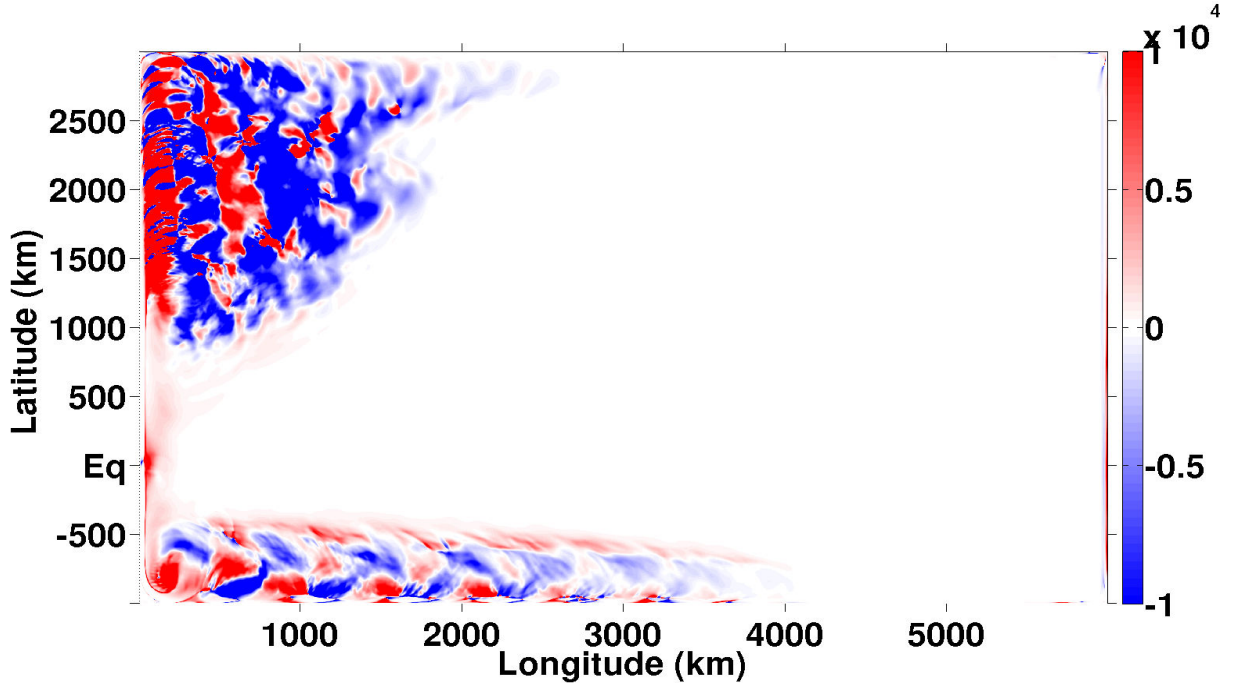

Figure 4.27 – $\nu_{\text{eddy}}^{\parallel,q}$ *computed for TW125*

The spatial distribution of the quantities $\nu_{\text{eddy}}^{\parallel}$ and $\nu_{\text{eddy}}^{\parallel,\beta}$ (not shown) are found to present bands of very high positive and very low negative values of eddy viscosity. Proving that neither relative vorticity transport nor the potential vorticity transport follows a diffusive law. Indeed the plots of $\nu_{\text{eddy}}^{\parallel,q}$ (Figs. 4.27 and 4.28) show four alternating bands of high positive and low negative eddy viscosity along the boundary located within the extended boundary-layer (EBL). The TW125 bands are wider than the MW300 bands. The existence of negative turbulent viscosity means that the flux of potential vorticity
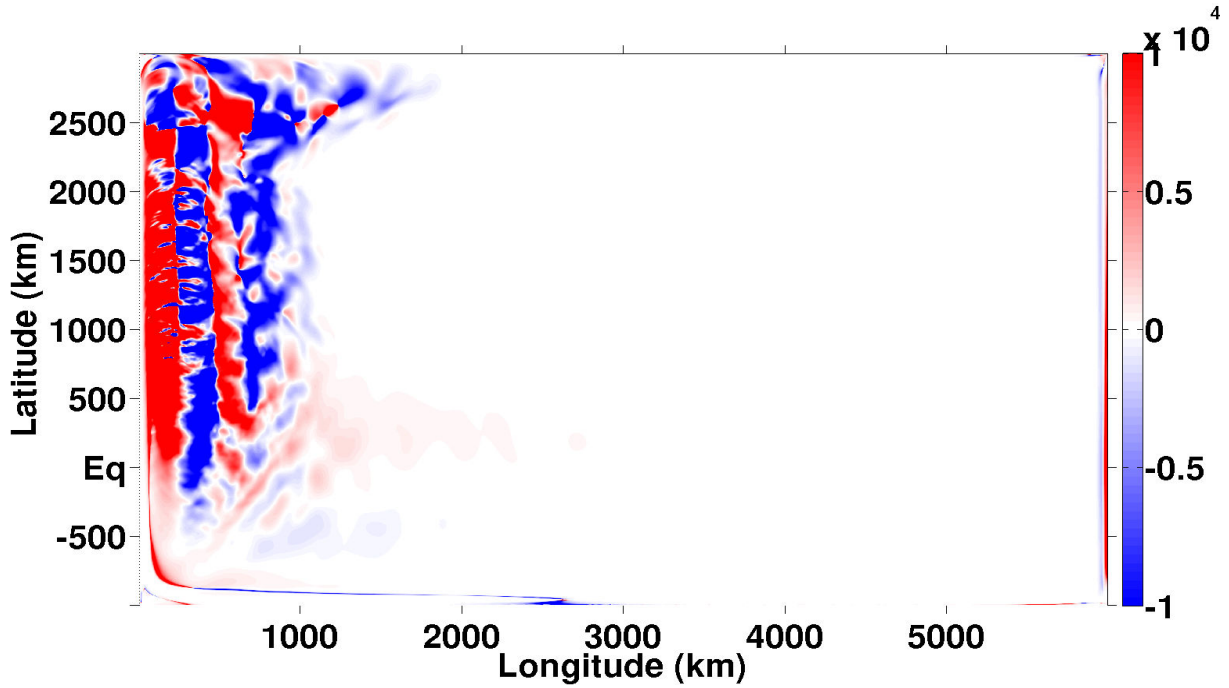
Figure 4.28 – $\nu_{\text{eddy}}^{\|,\text{q}}$ computed for MW300

is up the gradient of the mean potential vorticity profile. The mean potential vorticity gradient and the flux change sign at different longitudes introducing regions in the EBL where they have the same sign. This is in contrast with the common view in first order turbulent closure that the turbulent diffusion is down-gradient. The negative turbulent viscosity is nothing other than a "*counter-gradient transport*" or a "*nonlocal transport*", well known in the turbulence closure problem for convective boundary-layers [see *e.g.* Zilitinkevich et al. (1999)]. It appears clearly that the pure eddy viscosity approach cannot account for these turbulent fluxes. A nonlocal transport term must be added to account for these turbulent fluxes.

4.12.2   Estimation of the eddy viscosity and nonlocal transport via eddy fluxes

In order to describe the turbulent transport in the regions where occurs a counter-gradient flux, Ertel (1942) and Deardorff (1966) proposed to modify the usually applied flux-gradient relationship in K-theory by incorporating the counter-gradient correction terms γ_x and γ_y, on the l.h.s.:

$$\begin{pmatrix} \nu_{\text{eddy}}^x(\partial_x\langle\zeta\rangle + \gamma_x) \\ \nu_{\text{eddy}}^y(\partial_y\langle\zeta\rangle + \gamma_y) \end{pmatrix} = - \begin{pmatrix} \langle u'\zeta'\rangle \\ \langle v'\zeta'\rangle \end{pmatrix}. \tag{4.61}$$

I did not find a convincing parameterization, that allows to express the four free parameters in terms of quantities of the large-scale circulation. The simple and pragmatic

approach based on the Munk formula explained in the section 4.11 seems to be the best approach to deal with the problem of parameterizing the small-scale fluxes in coarse resolution models.

Part II

Application to the Somali Current via NEMO (Drakkar)

We are in a time of paradigm change in the numerical modelling of the global ocean dynamics, from coarse resolution models which give non chaotic response to the forcing field applied, to fine resolution models that allow for meso-scale eddies and their turbulent interaction. This part of the thesis focuses on the realistic ocean models used for climate studies and ocean forecasting. The results from part I obtained through an idealized reduced gravity shallow water model, inspired by the boundary-layer theory of engineering fluid mechanics are used to entangle the dynamics of low latitudes western boundary current in the ocean general circulation model NEMO in the Drakkar configurations (1/4º and 1/12º). The aim is to confirm the legitimacy and the importance of the need to study the ocean western boundary-layers via the viewpoint of turbulent boundary-layer theory. The turbulent nature of the western boundary currents has been largely established by observations. In the first part of this thesis, highly idealized model of two types of low latitudes turbulent western boundary currents have been studied, one corresponding to the North Brazil Current in the Atlantic Ocean and the other to the Somali Current in the Indian Ocean. The case of the Indian Ocean is considered in this applied study. The dynamics of the Indian Ocean is quite fascinating, due to the reversal of the Monsoon Winds. A realistic high resolution model is a useful framework for understanding the complex and unique Indian western boundary circulation. To proceed it is useful to briefly recall the observed circulation and dynamics of the Indian Ocean, which I do in the chapter 5. The description of the model NEMO, the Drakkar configurations (ORCA025, ORCA12) and the simulations used in this applied study are presented in the chapter 6. Validation of the Indian Ocean general circulation simulated with the Drakkar configurations, the formation processes of the Somali eddies, their scale of motion, the turbulent fluxes, and the influence of boundary conditions on the circulation are given in chapter 7 and discussed in chapter 9.

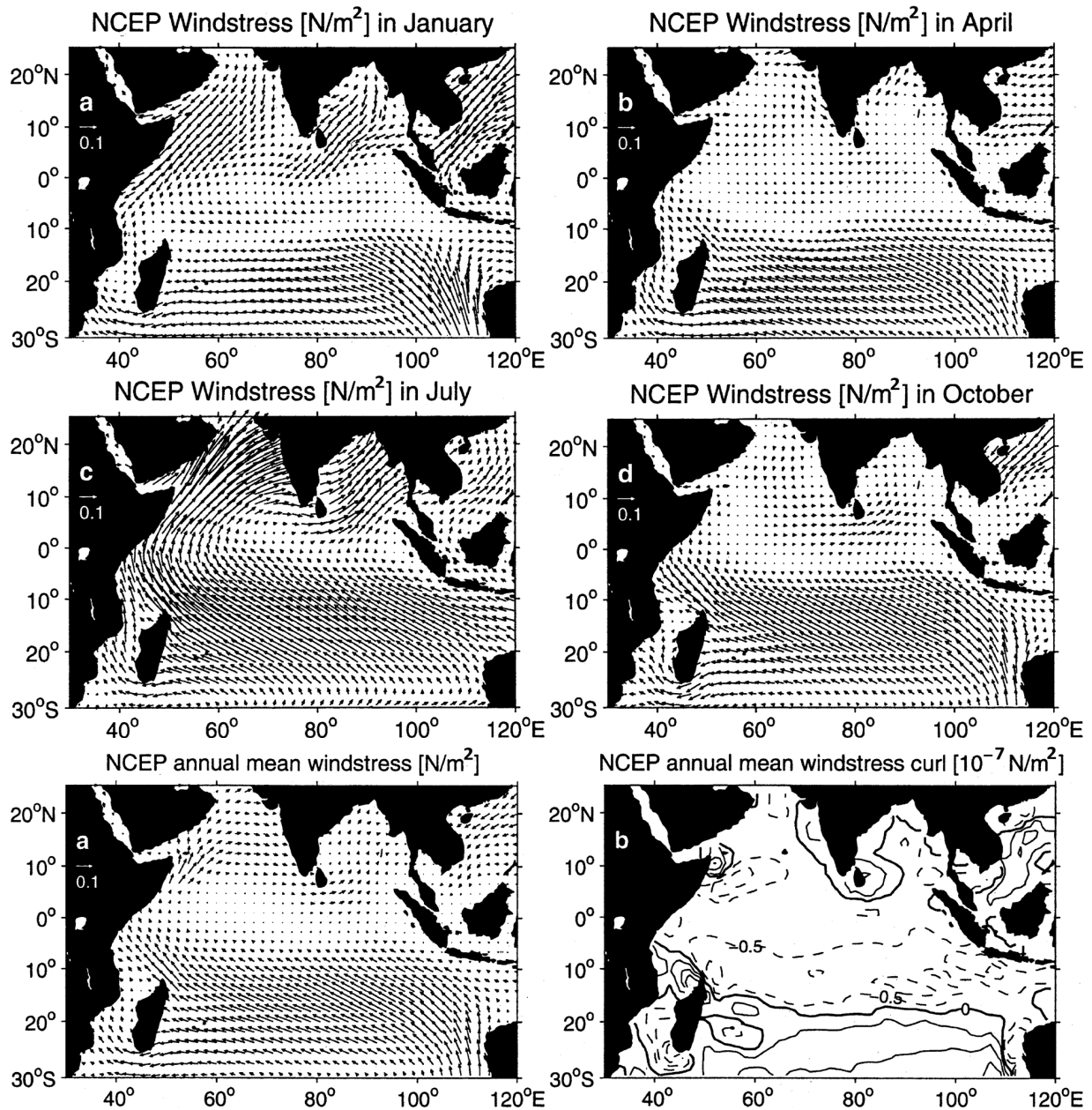# Chapter 5

Observations

Contents

5.1   Winds

Figure 5.1 – *Monsoon Winds stress fields from the NCEP climatology for January (a), April (b), July (c), November (d), annual-mean fields of wind stress (e) and wind stress curl (f) [After Schott & McCreary Jr (2001)].*

The Indian Ocean is unique among the three tropical ocean basins in that it is blocked at 25°N by the Asian continent and therefore cannot export northward the heat gained at tropical latitudes. The Indian ocean climate system is affected by the dramatic reversal of

the surface winds propelled by seasonally varying land-ocean temperature contrast (*i.e.* the Monsoon). In this section a brief overview of the Indian Ocean wind climatologies from NCEP [After Schott & McCreary Jr (2001)] wind stresses is used to discuss overall patterns of wind variability.

The Monsoon cycle is described here (Fig. 5.1a – d) based on the NCEP wind stress climatology for January, April, July and October.

During winter, in the northern hemisphere, Monsoon Winds are directed away from the Asian continent, producing northeasterly wind stresses over the Arabian Sea and the Bay of Bengal (Fig. 5.1a). Inversely during the summer Monsoon, winds are southwesterly and thus directed toward the Asian continent over both basins (Fig. 5.1c). Contrary to the winter situation, there is now a continuation of the southern-hemisphere Trade Winds into the Arabian Sea in the form of a narrow atmospheric jet, the *Findlater Jet* [Findlater (1971)]. A unique wind forcing pattern occurs over the Indian Ocean, which is different than the pattern found in other equatorial oceans. It involves the occurrence of semi-annual eastward winds over the equator, from April to June and from October to November (Fig. 5.1b,d). These winds generate an annual-mean equatorial zonal wind stress that is eastward and so the mean sea surface temperature (SST) along the equator is warm, in marked contrast to the situation in the other tropical oceans where the equatorial upwelling prevails.

From April to May, weak alongshore winds occur off Somali (Fig. 5.1b). The subsequent onset of the Monsoon over the Arabian Sea has been found to occur in several different ways [Fieux & Stommel (1977)]. The onset can be an abrupt change from the weak pre-monsoonal winds into the fully developed Southwest Monsoon in early to mid-June. Alternatively the onset may be gradual, extending over several weeks, or there may be multiple onsets during which the monsoon dies down again for interim phases after the first onset. The Southwest Monsoon becomes most strongly developed in late July but may then undergo phases of breaks, which may be associated with the 40-60days oscillations or other large-scale intra-seasonal signals [Madden & Julian (1972)].

The Southeast trades appear to prevail south of 10ºS in the annual signal (Fig. 5.1e). The Southeast trades reach their seasonal maximum and most northerly extent during southern winter. The summer Monsoon Winds dominate the winds in other seasons in the northern hemisphere in the annual mean, and the mean stress in the Arabian Sea is therefore anticyclonic. The mean curl is anticyclonic over the Indian Ocean north of about 15ºS, with the exception of small areas around Madagascar and India (Fig. 5.1f)

5.2 Indian Ocean general circulation

This section provides a brief overview of the Indian general circulation following the prominent review of Schott & McCreary Jr (2001). The surface currents during both monsoon seasons are schematically illustrated in Figs. 5.2 and 5.3 by Schott & McCreary Jr (2001), as observed from ship-drift climatologies [Cutler & Swallow (1984)] and from drifters [Molinari et al. (1990); Shenoi et al. (1999)]. Transport values, estimated at some
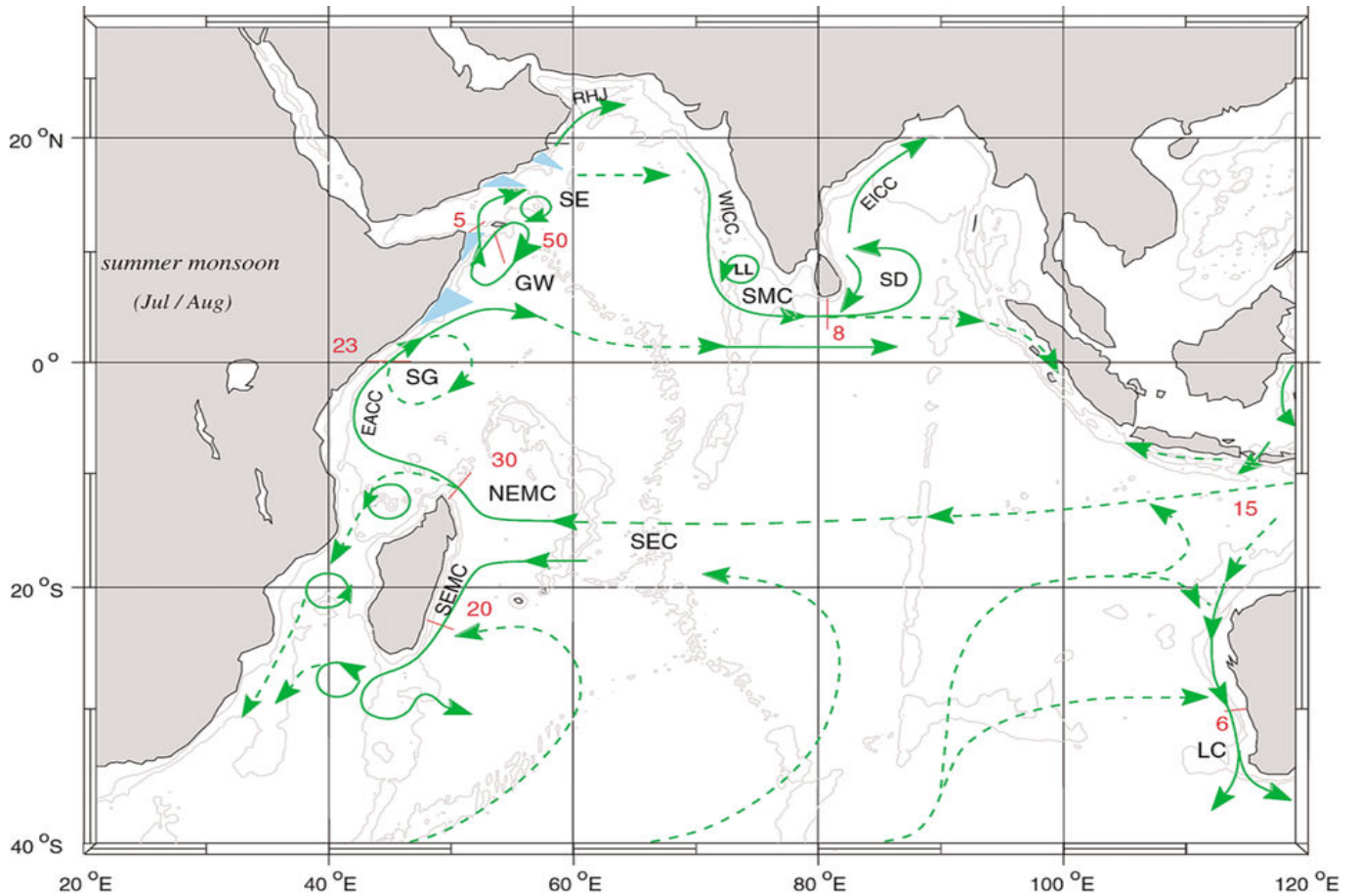
Figure 5.2 – *A schematic representation of identified current branches during the South-west Monsoon, including some choke point transport numbers (Sv=10^{6}m^3·s^{-1}). Currents branches indicated (see also Fig 5.3) are the South Equatorial Current (SEC),South Equatorial Counter-current (SECC), Northeast and Southeast Madagascar current (NEMC and SEMC), East African Coast Current (EACC), Somali Current (SC), Southern Gyre (SG) and the Great Whirl (GW) and associated upwelling wedges, Socotra Eddy (SE), Ras al Hadd Jet (RHJ) and upwelling wedges off Oman, West Indian Coast Current (WICC), Laccadive High and Low (LH and LL), East Indian Coast Current (EICC), Southwest and Northeast Monsoon Current (SMC and NMC), South Java Current (JC) and Leeuwin Current (LC). See text for details [After Schott & McCreary Jr (2001)].*
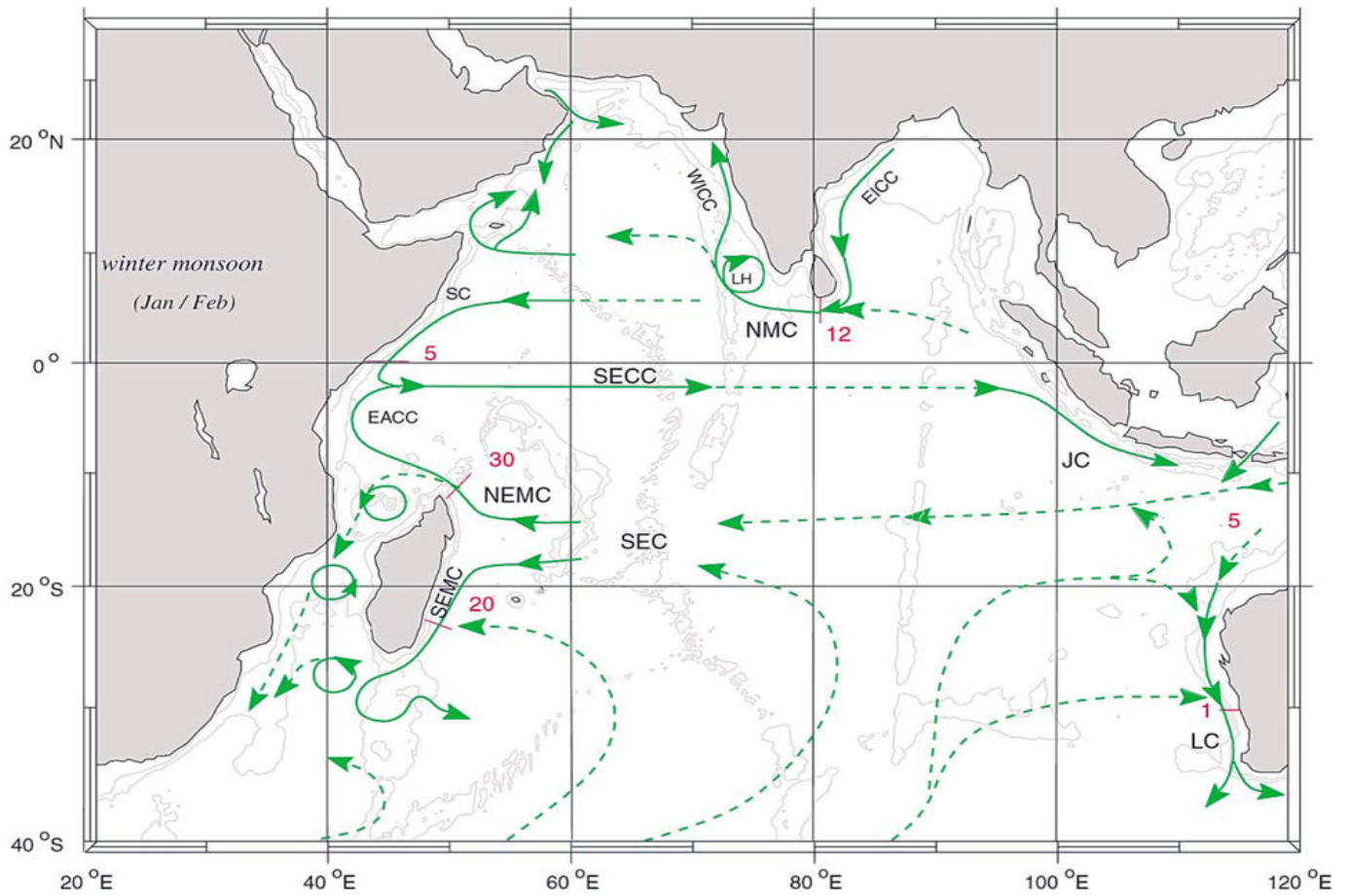
Figure 5.3 – *As in Fig. 5.2, but for the Northeast Monsoon [After Schott & McCreary Jr (2001)].*

key sections from moored current meter arrays measurements, are also indicated in the schematic maps.

Southern hemisphere

Similar to the situation in other oceans, there is a broad zonal inflow by the South Equatorial Current (SEC), driven by the Southeast Trades (see Fig. 5.1) which feeds the Northeast and Southeast Madagascar Currents (NEMC and SEMC) within the latitude range 12º-25ºS (Fig. 5.2). The NEMC flows past the northern tip of Madagascar at Cape Amber and feeds into the East African Coastal Current (EACC). Available observational data from the western boundary circulation south of the area influenced by the Monsoon regime, *i.e.*, south of about 10ºS, do not reveal much seasonal variability [Swallow et al. (1988)]. Therefore, the schematic representations in Figs. 5.2 and 5.3 show identical circulation branches in the SEC regime during both seasons.

Southwest Monsoon (Summer)

The typical situation when the southwest Monsoon is fully developed is shown in Fig. 5.2. During the Southwest Monsoon, the SEC and EACC supply the northward flowing Somali Current (nSC hereafter).

As described by Schott & McCreary Jr (2001), after crossing the equator, one part of the nSC turns offshore at about 4ºN, forming a cold upwelling wedge on its left side; the other part recirculates across the equator as the *Southern Gyre* (SG). In the north, a second gyre is formed, the *Great Whirl* (GW). A third eddy, the *Socotra Eddy* (SE) is often (not always) seen during the late phase of the summer monsoons, northeast of Socotra Island (Fig. 5.2). A recent drifter climatology study of the Arabian Sea by Beal et al. (2013) suggests that the SG is a retroflection of an extension of EACC and not a recirculation of the nSC across the equator. The recent drifter climatology improvement over the Arabian Sea confronted with the present schematic currents (Figs. 5.2 and 5.3) will be discussed in detail in section 5.3.

The Southwest Monsoon Current (SMC) at south of Sri Lanka flows eastward during this season. Most of the SMC connection to the Somali Current outflow appears to be at low latitudes, but part of its source waters originates from the southward-flowing West Indian Coastal Current (WICC), involving the Laccadive Low (LL). During this season, the East Indian Coastal Current (EICC) bifurcates in the Bay of Bengal, fed by the inflow from the south, partially by the flow out of the SMC around a cyclonic dome to the east of Sri Lanka.

Northeast Monsoon (Winter)

During the northeast Monsoon, the EACC meets the southward Somali Current (sSC hereafter) in a confluence zone at $2 - 4$ºS, then supplies the eastward flowing South Equatorial Counter-current (SECC, Fig. 5.3). At the eastern end of the SECC, a boundary current, the South Java Current (JC) flows southeastward. There is an inflow across the Arabian Sea from the east into the sSC, which seems to occur in several branches (it will be detailed in the following section). South of Sri Lanka and India, the Northeast Mon-

soon Current (NMC) flows and curves up to the north around 70ºE to feed the WICC. A major anticyclone, the Laccadive High (LH) [Bruce et al. (1994)] or the Lakshadweep eddy [Shetye (1998)] appears inshore of this current, off the western tip of India. A second westward branch flowing south of Socotra may also receive waters from the WICC. The schematic currents of Fig. 5.3 do not show the exact connection between the sSC and the NMC.

In the Bay of Bengal, the EICC reverses direction twice a year. It flows northeastward from February until September with a strong peak in March-April and southwestward from October to January with strongest flow in November. The surface circulation in the interior of the Bay of Bengal is best organized from February to May, when the EICC forms the western boundary current of a basin-wide anticyclonic gyre. This gyre disappears during the summer monsoon, when the boundary current splits at the 10ºN confluence. In the interior, the circulation then seems to consist of several rings. During winter, there seems to be a cyclonic gyre in the interior of the Bay of Bengal which is coupled to the southward flow of the EICC.

Equatorial regime

A particular phenomenon, singular to the Indian Ocean owing to the semi-annual eastward winds along the equator (Fig. 5.1), is the occurrence of strong eastward surface jets [Wyrtki (1973)] during the transition seasons between the monsoons, *i.e.*, April to June and October to December (not shown in the schematic figures). Their effect is to carry warm upper-layer waters eastward, lowering the sea level and decreasing the mixed-layer thickness in the west, but increasing them in the east [Rao et al. (1989)] thereby causing an eastern temperature maximum (not shown). These eastward flowing, upper-layer, current anomalies propagate poleward along the eastern boundary of the basin. The lack of sustained westward equatorial winds is the reason for another Indian Ocean peculiarity, indeed an eastward Equatorial Undercurrent (EUC) occurs only during part of the year, typically February to June. It can appear in other seasons as well, when anomalous easterlies occur.

The schematic identified currents by Schott & McCreary Jr (2001) provide a good description on the main general circulation but uncertainty subsists in the connection of some currents. Piracy has prevented further ship measurements off the Somali Coast, but recent improvement in satellite and drifter data, together with numerical simulations, provide a robust means to go beyond the static schematics currents and examine the seasonally evolving surface circulation. The case of Arabian Sea is described in the following section.

5.3   Arabian Sea

A recent study of the absolute near-surface currents of the Arabian Sea derived from the global array of satellite-tracked drifting buoys provides some corrections to the
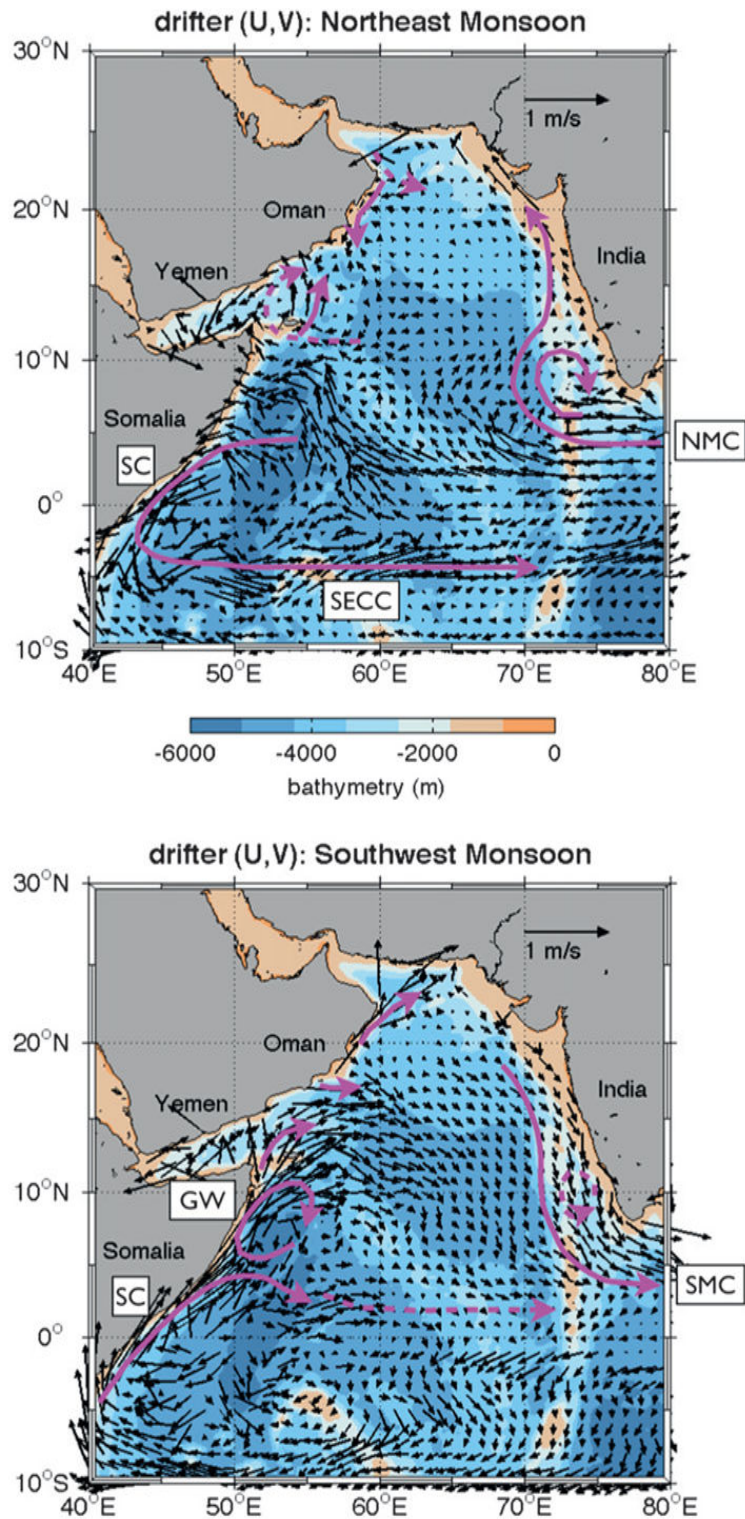
Figure 5.4 – *The circulation of the Arabian Sea (vectors) during the (top) northeast and (bottom) southwest Monsoons, from the surface drifter climatology. The northeast (southwest) Monsoon is depicted as the currents averaged over the months of December – February (June – August). Magenta arrows are the schematics of identified currents after Schott & McCreary Jr (2001). Where the drifter climatology does not reflect the schematic, arrows are dashed. Color shading is bathymetry from 1–min gridded topography for the world (ETOPO1). Landmasses are shaded gray [After Beal et al. (2013)].*
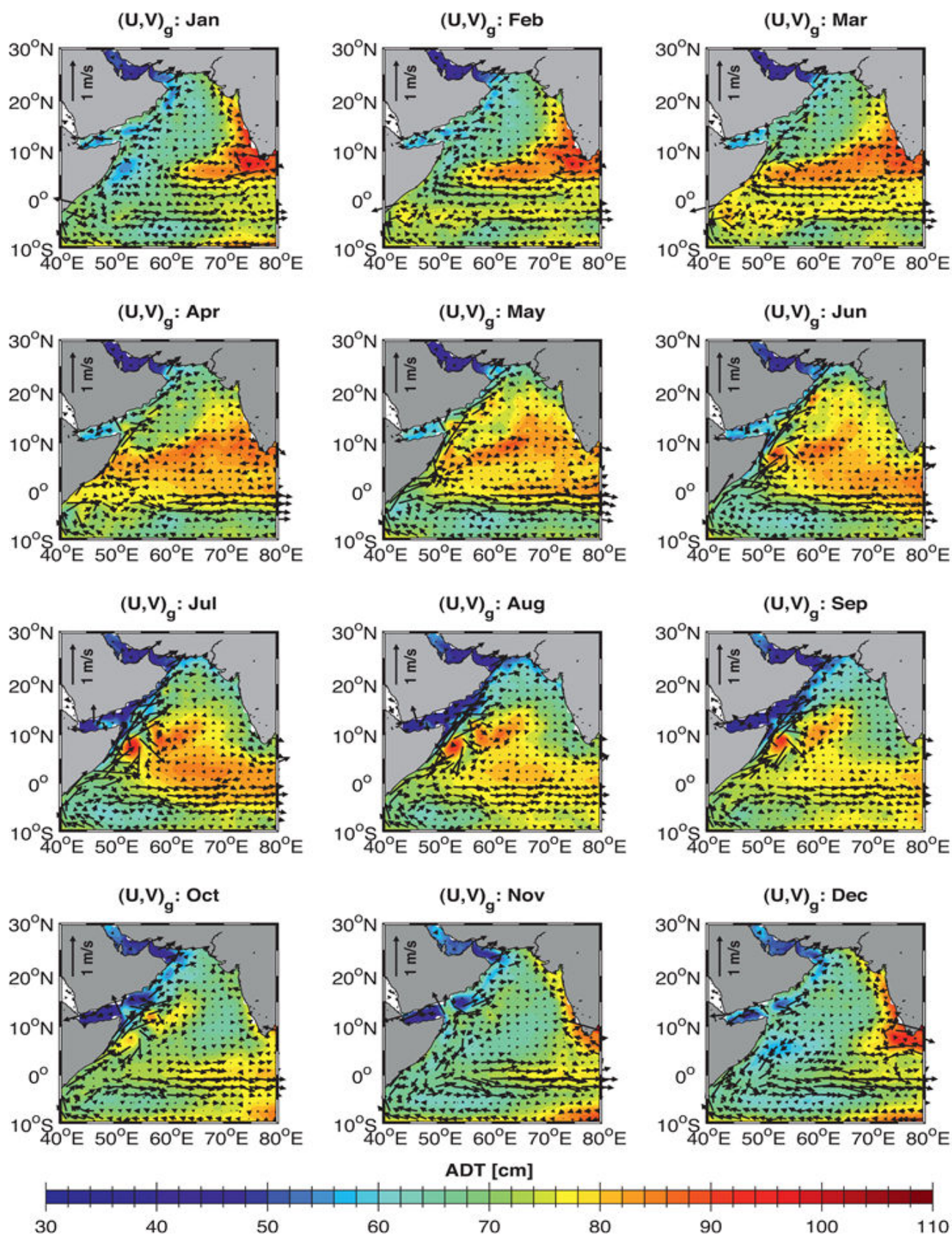
Figure 5.5 – *Monthly-mean geostrophic surface currents (vectors) from the drifter-altimeter synthesis, and absolute dynamic topography (ADT; color shading) from Archiving, Validation, and Interpretation of Satellite Oceanographic data (AVISO). Note the early appearance of the GW, or its precursor, in March, and the year-round SECC. Land-masses are shaded gray [After Beal et al. (2013)].*

schematic currents (shown in Figs. 5.2 and 5.3) proposed by Schott & McCreary Jr (2001). The schematic currents are magenta arrows superimposed on the drifter climatology in Fig. 5.4. Where the drifter climatology does not reflect the schematic, arrows are dashed [Beal et al. (2013)].

Southwest Monsoon (Summer)
During the southwest Monsoon, the Arabian Sea circulation is predominantly anticyclonic and considerably stronger than during the northeast Monsoon (Fig. 5.4b), hence the southwest Monsoon prevails in the annual-mean circulation (Fig. 5.1d) [Schott & McCreary Jr (2001)]. As said above the Schott & McCreary Jr (2001) schematic currents show the nSC branching into an eastward current at about 2º/3ºN: this is not supported by the drifter data (Fig. 5.4b). Instead Beal et al. (2013) found that this branch is nothing else than the EACC which extends across the equator, retroflects at 3ºN and loops back across the equator to feed into the SECC. Hence, this feature previously known as the SG appears to be a retroflection of the EACC and not a recirculation of the EACC. They argue that the boundary flow along the Somali Coast during the southwest Monsoon should be considered as an extension, or overshoot of the EACC up to 3ºN, and only north of here it is truly the nSC. In the later phase of southwest Monsoon, when the EACC and the nSC are connected, it will be shown in the section 7.1, that the distinction of each current will prove to be impossible. Farther north, the nSC extends across the mouth of the Gulf of Aden and may be connected to northward flow along the Oman coast. The rest of circulation is confirmed by the drifter climatology except the LL.

Northeast Monsoon (Winter)
During the northeast Monsoon excepted the westward flow which curves to the north to cross the mouth of Gulf of Aden, and the southeastward flow from the Gulf of Oman (dashed magenta arrows in Fig. 5.4a), the drifter climatology confirms the near-surface circulation identified by Schott & McCreary Jr (2001). However near the Somali Coast, between 5º and 10ºN, there is a super-mesoscale cyclonic circulation (Fig. 5.5, December – January) not previously identified [Beal et al. (2013)]. It appears to be fed by waters from the NMC, which then exit into the sSC.

The effect of annual Rossby waves on the circulation
Recent studies point out the initiation of the northward flowing nSC along the length of the western boundary as early as March/April, together with a weak anticyclone at 6ºN, a precursor to the GW. The early arrival of the GW was recently noted by Beal & Donohue (2013) in a regional study of SSH data and by Beal et al. (2013). The monthly-mean geostrophic currents of this latest study (Fig. 5.5) provide evidence for the initiation of the northward flowing nSC which challenges the concept that the nSC is established after an adjustment of the circulation to the southwest Monsoon winds stress curl [see *e.g.* Lighthill (1969)]. The Fig. 5.5 shows the appearance of the nSC in April to be coincident with the arrival of an annual high in absolute dynamic topography, centered along 8ºN.

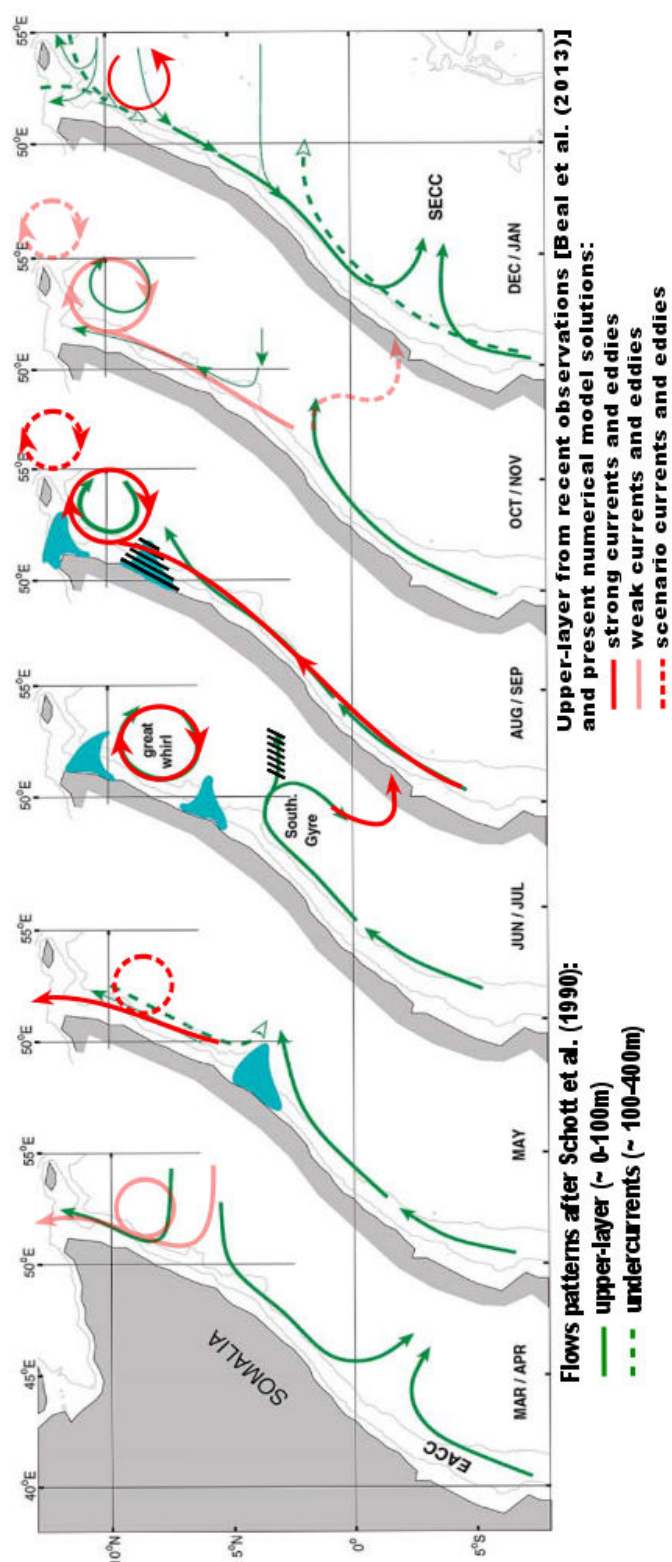This signal is due to first- and second-mode annual Rossby waves [Brandt et al. (2002)].

Figure 5.6 – *Schematic diagram of the Somali Current upper-layer flow patterns over the course of the year from Schott & McCreary Jr (2001) (green), updated by recent study from Beal et al. (2013) and simulated circulations of this thesis (red arrows). Discordant circulation patterns are hatched in black. The simulated circulations are discussed in detail in sections 7.1 and 7.2.*

Shetye (1998) theorizes that the process starts during the previous southwest Monsoon, when strong negative wind stress curl triggers a chain of planetary waves which feed back on the initiating region. Indeed this process begins with the generation of westward, down-welling Rossby waves from the wind curl region of the Somali Coast. At this southwest monsoonal period, the system formed by the WBCs (nSC, EACC) and the eddies (SG and GW) prevents the westward propagation of these downwelling Rossby waves. The Rossby waves are constrained to turn into "coastal" Kelvin waves and propagate equator-ward adjacent to the system formed by the WBCs and the eddies. At the equator, these "coastal" Kelvin waves are trapped and are turned into equatorial Kelvin waves. It will be shown in the sub-section 7.1.2 that these equatorial Kelvin waves are originated from about 50 – 60ºE. The equatorial Kelvin waves propagated eastward, hit the Sumatra Coast, bifurcated and propagated as two poleward coastally-trapped Kelvin waves. The northern branches propagated along the coastal waveguide of the rim of the Bay of Bengal [Subrahmanyam et al. (2001); Shankar & Shetye (1997)]. After reaching the southern tip of India, these northern branches of coastally-trapped Kelvin waves turn into Rossby waves which propagate back into the Arabian Sea. The latest Rossby waves reach the Somali Coast during March/April. This implies that the forcing from the previous southwest Monsoon feeds back on the circulation in the Arabian sea two months ahead of the next Monsoon. Shetye (1998) theorizes a predicted time scale of approximately 300days for the process. This planetary waves process will be detailed in the sub-section 7.1.2. (Note that, there are northern branch of the coastally-trapped Kelvin wave which propagates along the east coast of the Arabian Sea. This coastally-trapped Kelvin wave does not reach the west coast of the Arabian Sea itself, as a result of its rapidly diminishing lateral scale with latitude and the gap in the coastal boundary at the Gulf of Oman (Fig. 5.5, November – March)).

This is not to say that the Monsoon Winds and wind stress curl do not play the dominant role in the forcing of the nSC once the southwest Monsoon sets in, but that the initial nSC precursor to the earlier GW in April, two months before the onset of the southwest Monsoon Winds, is clearly the result of the propagation of Rossby and Kelvin waves around the northern Indian Ocean waveguide, which in turn were initiated in the Arabian Sea by strong downwelling wind curl during the previous southwest Monsoon. These mechanics need further study and will be investigated in the OGCM NEMO in the Drakkar configurations.

After this succinct description of the general circulation of the Indian Ocean, I now focus on the WBCs, namely SC and EACC and their vortex system.

5.4   Somali Current

Historically, describing and understanding the remarkable annual cycle of the SC system with its reversal of the entire current system has been one of the greatest challenges for the Indian Ocean oceanographic community. This section is devoted to this topic. The seasonal development of the Somali Current system was first described by Schott

et al. (1990). Recent observations allow to update here the Schott et al. (1990) schematic diagram of the SC which is illustrated schematically (red arrows) in Fig. 5.6.

April – May
Before the onset of the southwest monsoon the sSC crosses the equator to meet the EACC in a confluence zone at 2 – 4ºS. According to the year the reversal of the sSC may occur in March/April [Beal et al. (2013)] due to the arrival of the Rossby waves as said above.

These Rossby waves, associated to a weak basin-wide anticyclonic circulation (with the NMC at its south flank), reach the Somali Coast where the energy is transfered to the northward flow, precursor to the nSC and a weak GW appears [Beal et al. (2013)]. The importance of this forcing mechanism is supported in several examples of remotely forced circulations in $2\frac{1}{2}$-layer numerical model by McCreary et al. (1993). The appearance of the onset of the weak GW to be a response of this mechanism needs further study. The Schott et al. (1990) schematic and the drifter climatology of Beal et al. (2013) suggest that from the weakening of the northeast Monsoon until the onset of southwest Monsoon, the nSC and sSC coexist.

June – July
Once the southwest Monsoon Winds set in, the influence of the Rossby waves remote forcing on the surface currents is no longer significant. The EACC cancels the sSC, it flows northward across the equator owing to strong local winds [Beal et al. (2013)] up to about 3º – 4ºN; there, it retroflects offshore [Beal et al. (2013)] to form the feature previously known as the SG, and a cold wedge develops along its shore-ward side [Schott et al. (1990)].

While the nSC which is part of the reversing monsoon circulation, flows north of 3ºN and becomes stronger. The Great Whirl develops between 4 – 10ºN, and a second cold wedge appears at the latitude where it turns offshore (10 – 12ºN). At this time, there is a net upper-layer outflow from the Somali Current system into the Gulf of Aden through the passage between Socotra and the Horn of Africa. A cut through the GW for the mean currents of the southwest Monsoon, determined from moored stations south of Socotra, shows that the GW reaches down to almost 1000m with speeds of 10cm·s^{-1}, and that the eddy structure remains visible even at greater depths [Schott & McCreary Jr (2001)].

September – October
In the late phase of the southwest Monsoon the GW has become an almost closed circulation cell (Fig. 5.7 and 5.5) with very little exchange between its offshore recirculation branch and the interior Arabian Sea, as is apparent from the differences in surface salinities between the GW and the region to the east of it (Fig. 5.7). To the north, another anticyclonic feature, the SE (Fig. 5.7), develops in some years and its signature is observed in monthly-mean geostrophic surface currents (Fig. 5.5, [Beal et al. (2013)]) during October.

Strong upwelling exists where the nSC turns offshore as observed by *Swallow* and *Bruce* in 1964 along approximately 12ºN [Swallow & Bruce (1966)] during a particularly
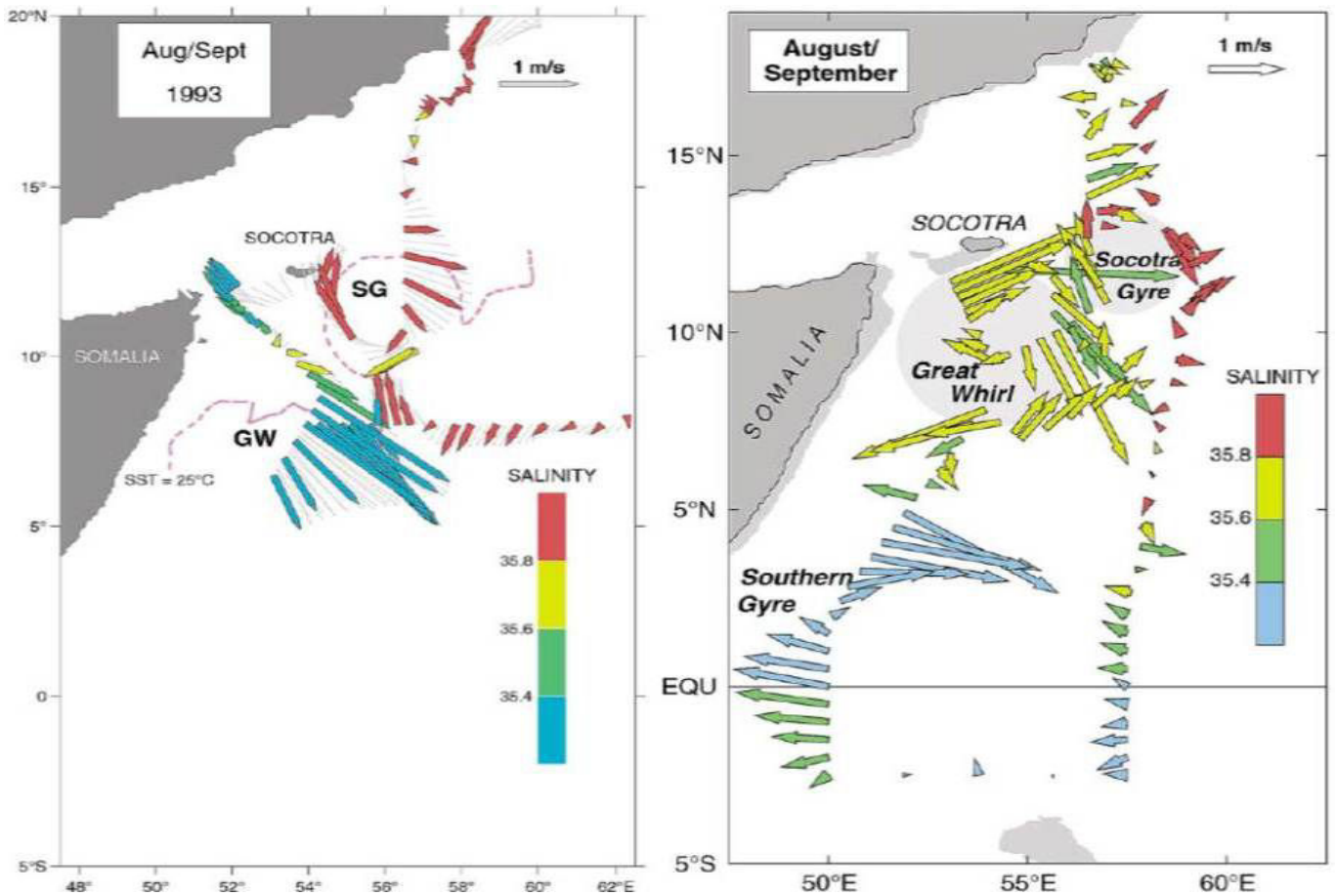
Figure 5.7 – *Somali Current flow patterns during the late summer monsoon phases of a) 1993 [after Fischer et al. (1996)] and b) 1995 [after Schott et al. (1997)]. Marked are the Southern Gyre, Great Whirl and Socotra Gyre or Socotra Eddy. Near-surface salinities (color-coded on the current vectors) indicate that lower-salinity waters originating from the southwestern and upwelling regions recirculate in the Great Whirl and do not leave the Somali Current zone toward the east in the 4º-12ºN latitude belt. Instead, outflow from the northern Somali Current during the summer monsoon occurs through the Socotra passage. Note also that the GW in 1995 was located much more northerly, against the banks of southern Socotra, than in 1993.*

strong upwelling episode with upwelled waters colder than 17ºC while typical upwelling temperatures are in the 19 – 23ºC range. Some observations have suggested that the two-gyre system may at times collapse, when satellite SST images [Evans & Brown (1981)] have indicated a rapid ($\sim$1 m·s^{-1}) northward propagation of the southern cold wedge. This interpretation has been supported by ship-survey measurements suggesting that low salinity southern waters were present in the wake of the migrating southern cold wedge [Schott (1983); Swallow et al. (1983)]. In some cases, the southern wedge merged with the northern one, suggesting that the SG and GW have coalesced, as sketched in Fig. 5.6. It has to be noted, though, that such a breakdown was not documented in the 1995 – 96 WOCE observations [e.g. Schott et al. (1997)]. Apart this interpretation, the collapse of the two eddies is still unresolved. This phenomena will be discussed in detail in the sub-section 7.2.2. Its occurrence may be a rare event, and in that respect, August/September schematic may not represent the typical seasonal cycle; rather, the typical case may be a continuation of the July situation throughout the southwest Monsoon.

November
When the Southwest Monsoon dies down, the EACC retroflects offshore again at 3ºN, while the GW continues to spin in its original position (Fig. 5.6). The GW is even discernible underneath the developing Northeast Monsoon circulation well toward the end of the year [Bruce et al. (1981)]. The monthly-mean (Fig. 5.5) shows that the GW's end of life most probably occurs from October till November.

December – March
At this period, the northeast Monsoon is well established and triggers the reversal of nSC. The nSC hands over to the southward flowing sSC. The sSC gradually pushes EACC more and more to the south into the southern hemisphere, setting their confluence at about 2 – 4ºS.

Inter-annual variability
Significant inter-annual differences in the system of cold upwelling wedges off Somali and their movements during the course of the Southwest Monsoon had already been reported [Evans & Brown (1981); Schott (1983)]. Analysis of the location and intensity of the GW based on the WOCE moored and shipboard observations during 1993 – 1996, shows a strong inter-annual variability the GW. The GW were seem to become disorganized in August 1996 [Schott et al. (1997)]. These observations could not be explained in any obvious way by the forcing field variability.

These succinct descriptions of the Indian Ocean near-surface circulation, of course, are more complicated, particularly at the equatorial region where exist the system form by the WBCs (EACC, sSC and nSC) and the eddies (SG, GW, SE). To entangle this dynamics, the OGCM NEMO in the Drakkar configurations is used. The next chapters describe the global model, the configurations and the simulations used to entangle the identified features which deserve further study in the Indian ocean.

Chapter 6

NEMO Model and Drakkar Configuration

Contents

6.1   Introduction

This chapter presents a succinct description of the ocean general circulation model (OGCM) NEMO on which the DRAKKAR configurations are based (please see http://www.nemo-ocean.eu/ for more detailed informations).

6.2   NEMO modelling system

NEMO (Nucleus for European Modeling of the Ocean, [Madec (2008)] is an ocean modeling system which regroups three components:

– **the oceanic circulation component** [Madec (2008)], on which it is possible to couple two other components:
– **the sea ice component** which is carried by the LIM model (Louvain-la-Neuve sea ice model, [Fichefet & Maqueda (1997)])
– **the oceanic passive tracers component** TOP which includes notably the marine bio-geochemistry model PISCES (pelagic Interaction Scheme for Carbon and Ecosystem Studies [Aumont & Bopp (2006)]).

The development of the NEMO system is organized by a European consortium between the CNRS[1],MERCATOR Ocean, UKMO[2], the NERC[3] and the CMCC. NEMO is used by a large community of scientists at both European and international level with 240 projects inventoried for 2008 in 27 countries (with 14 European countries). The main objectives of these projects are:

– the oceanographic research which regroups most of the NEMO studies.
– operational oceanography Mercator Ocean, Fisheries and oceans Canada, The Met Office Hadley Center
– seasonal and climate forecasting (ECMWF[4], Météo France, EC-EARTH[5] and the climate projection in the IPCC experiments framework (IPSL[6]).

The entire description of the oceanic code is given by Madec (2008). The following sections present a brief description of the oceanic circulation component. This description, far from being exhaustive, has the principal aim to introduce the OGCM that produced the simulations of the Indian Ocean used here.

The physics of the model

Primitive equations

NEMO model resolves the fundamental equations governing a rotating fluid motion on a sphere. These equations, derived from the fluid mechanics, are:

---

1. Centre National de la Recherche Scientifique.
2. United Kingdom Meteorological Office.
3. National Environment Research Council.
4. European Center for Medium-Range Weather Forecasts.
5. consortium for the development of European earth system model based on the ECMWF modeling system.
6. Institut Pierre-Simon Laplace

- Momentum equations or *Navier-Stokes* equations, derived from the principle of momentum conservation
- Continuity equation, derived from the principle of mass conservation
- Heat conservation equation, derived from the principle of energy conservation
- Salt conservation equation, derived from the dissolved substances conservation law
- Sea water equation of state which links the temperature, the salinity and the density.

Considering the geophysical characteristic scales and the properties of the ocean, a series of simplifying assumptions are made:

- *spherical earth approximation :*
  the geopotential surfaces are assumed to be spheres so that gravity (local vertical) is parallel to the earth's radius
- *thin-shell approximation :*
  the ocean depth ($\approx$ 3.8km) is small compared to the earth's radius (6400km)
- *Boussinesq hypothesis :*
  according to the feeble variations of the density of the sea water compared to the reference value $\rho_0 = 1020$ kg·m^3, the density variations are neglected except in their contribution to the buoyancy force
- *incompressibility hypothesis :*
  the density is considered as quasi-constant, the mass conservation equation implies the non divergence of the velocity fields which is assumed to be zero ($\nabla \cdot \vec{u} = 0$)
- *Hydrostatic hypothesis :*
  the vertical momentum equation is reduced to a balance between the vertical pressure gradient and the buoyancy force (this removes convective processes from the initial Navier-Stokes equations and so convective processes must be parameterized instead)
- *turbulent closure hypothesis :*
  the turbulent fluxes (which represent the effect of small scale processes on the large-scale) are expressed in terms of large-scale features

Note that the model used the free surface formulation [Roullet & Madec (2000)]. These assumptions allow to obtain the system of equations called "primitive equations":

$$\partial_t \vec{u}_h = -\left[(\nabla \times \vec{u}) \times \vec{u} + \frac{1}{2}\nabla(\vec{u}^2)\right]_h - f\vec{k} \times \vec{u}_h - \frac{1}{\rho_0}\nabla_h p + gT_c\nabla_h\partial_t\eta + \vec{D}^u \quad (6.1)$$

$$\partial_z p = -\rho g, \quad (6.2)$$

$$\nabla \cdot \vec{u} = 0, \quad (6.3)$$

$$\partial_t T = -\nabla \cdot (\vec{u}T) + D^T, \quad (6.4)$$

$$\partial_t S = -\nabla \cdot (\vec{u}S) + D^S, \quad (6.5)$$

$$\rho = \rho(T, S, p), \quad (6.6)$$

$$\partial_t \eta = \nabla \cdot [(H + \eta)u_h] + P - E, \quad (6.7)$$

where $\vec{u} = \vec{u}_h + \vec{w} = (u, v, w)$ is the velocity vector (m·s^{-1}), T the potential temperature (^{o}C), S the salinity (PSU), ρ is the *in situ* density given by the equation of state, g is the gravitational acceleration, f is the Coriolis parameter function of the latitude ϕ

($f = 2\Omega\sin\phi$). $\vec{D}^u$, $\vec{D}^T$ and $\vec{D}^S$ are the parameterizations of small-scale associated to the non-resolved processes expressed in form of a diffusion, respectively applied to the momentum, the temperature and the salinity. $P - E$ represents the precipitation minus evaporation budget.

The spatio-temporal discretization

The numerical method used to solve the primitive equations in this model are based on the traditional, centered second-order finite difference scheme in space. The vertical discretization is in z-level with partial step representation of the bathymetry (the thickness of the level at the ocean bottom is adjusted to the true ocean depth. The arrangement of variables is the same in all directions. It consists of cells centered on scalar points (T, S, p, ρ) with vector points (u, v, w) defined in the center of each face of the cells (Fig. 6.1). This is the three dimensions "C" grid in *Arakawa*'s classification [Mesinger et al. (1976)].

For the temporal discretization, a Leapfrog scheme (Eq. 6.8) is used. This temporal scheme is known to produce a numerical mode where odd and even time-steps diverge. To prevent this divergence, the leap-frog scheme is used in association with *Asselin* time filter [Asselin (1972)] that mixes odd and even time-steps (Eq. 6.9).

$$x^{t+\Delta t} = x^{t-\Delta t} + 2\Delta t\ \mathbf{RHS}_x^{t-\Delta t, t, t+\Delta t} \tag{6.8}$$

$$x_f^t = x^t + \gamma\left(x_f^{t-\Delta t} - 2x^t + x^{t+\Delta t}\right) \tag{6.9}$$

where x stands for u, v, T or S; **RHS** is the Right-Hand- Side of the corresponding time evolution equation; Δt is the time step; and the superscripts indicate the time at which a quantity is evaluated. The subscript f denotes filtered values and γ is the Asselin coefficient.
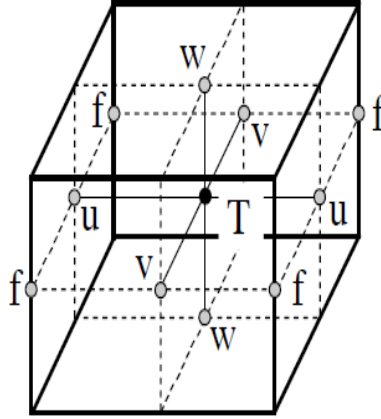

Figure 6.1 – *Arrangement of variables, T indicates scalar points where temperature, salinity, density, pressure and horizontal divergence are defined. (u,v,w) indicates vector points, and f indicates vorticity points where both relative and planetary vorticities are defined [After Madec (2008)].*

Parameterizations

Some physical processes have spatial and/or temporal scales smaller than respectively the mesh grid size or the time step. Such processes, generally called sub-grid scale processes can not be explicitly resolved by the primitive equations according to the spatio-temporal discretization used. Besides, some processes are wrongly or simply not accounted for, because of the assumptions made to derive the primitive equations (*e.g.* the non-hydrostatic processes such as deep convection or gravity currents). In either conditions, a parameterization proves to be necessary to represent these processes [See Madec (2008) for more information]. I briefly discuss here the subgrid-scale parameterizations because they have an impact on the side wall boundary-layer.

Lateral parameterization: For the momentum, the lateral dissipation (viscosity) is executed according to a bilaplacian operator applied along geopotential surfaces with a coefficient which is dependent on the cubic local grid-size. For the tracers, the lateral diffusion is executed according to a laplacian operator applied along isopycnal surfaces with a coefficient which is dependent on the local grid-size.

Vertical parameterization: For momentum and tracers, the vertical mixing is parameterized in a diffusive form by analogy with molecular diffusion. The fluxes depend thus linearly on local vertical gradients of variables at large scale :

$$\vec{D}^{vX} = \frac{\partial}{\partial z}(A^{vX}\frac{\partial X}{\partial z}) \quad \text{where} \quad X = \vec{U}, \theta, S \tag{6.10}$$

The dissipation and the diffusive turbulent vertical coefficients A^{vX} used in this formulation are calculated according to the turbulence closure model TKE (Turbulent Kinetic Energy, [Blanke & Delecluse (1993)]).

Bottom boundary-layer parameterization: A major consequence of the hydrostatic approximation is the inadequate representation of gravity driven downslope flows or dense water, particularly the overestimation of the vertical mixing. This problem of representation of dense water appeared to be most crucial in geopotential coordinate model [Winton et al. (1998); Lee et al. (2002)]. A Bottom boundary-layer (BBL) parameterization, first introduced by Beckmann & Döscher (1997), and adapted to the C-grid and the partial steps by Hervieux (2007), improves (but only slightly) the representation of the overflow by allowing the advection and the diffusion of tracers and the momentum in the bottom layer.

Boundary conditions: The ocean is delimited by the atmosphere and the sea ice at surface, and by the bathymetry and the coasts. The existence of these boundaries implies exchanges between oceanic, cryospheric, atmospheric and terrestrial systems. Some of these exchanges can be considered as minor comparing to the timescale of the processes studied and so negligible in the model. Other exchanges appear essential for the good representation of the processes scale and then are resolved directly or parameterized in the couple systems (it is the case of the ocean and the sea ice) or prescribed in the forced system (here is the case of the ocean which is forced by the atmosphere).

Boundary conditions at the coast: The discrete representation of a domain with complex boundaries (coastlines and bottom topography) leads to arrays that include large

portions where a computation is not required as the model variables remain at zero.

The boundary condition on the normal velocity (no flux through solid boundaries) can thus be easily implemented using the mask system. The boundary condition on the tangential velocity requires a more specific treatment. This boundary condition influences the relative vorticity and momentum diffusive trends, and is required in order to compute the vorticity at the coast. Four different types of lateral boundary condition are available, controlled by particular value of the mask$_f$ array along the coastline. Only two types are used in this study,these are:

    – **free-slip boundary condition**: the tangential velocity at the coastline is equal to the offshore velocity, *i.e.* the normal derivative of the tangential velocity is zero at the coast, so the vorticity : mask$_f$ array is set to zero inside the land and just at the coast;

    – **partial free-slip boundary condition**: the tangential velocity at the coastline is smaller than the offshore velocity, *i.e.* there is a lateral friction but not strong enough to make the tangential velocity at the coast vanish. This can be selected by providing a value of mask$_f$ strictly between 0 and 2.

6.2.1 Drakkar configuration and simulations

Drakkar [7] is not an acronym. The Drakkar consortium uses the NEMO model described above.

This section provides a succinct description of the global ocean and sea ice realistic configurations implemented by the Drakkar consortium, and the simulations used in this second part of the thesis. (please see http://www.drakkar-ocean.eu/ for more detailed informations).

ORCA025.L75 configuration and ORCA025.L75-MJM95 simulation

This sub-section addresses in a few words the ORCA025.L75 configuration [Barnier et al. (2006)] and the ORCA025.L75-MJM95 simulation which is used for the applications in this thesis. The simulation is performed in the frame of MyOcean project with some adaptations included in the Drakkar version of the code. Without data assimilation, the run is free, originally served as reference run for the reanalysis runs. The vertical grid has 75 levels, with a resolution of 1m near the surface and 200m in the deep ocean. The horizontal-grid is the standard ORCA25 tri-polar grid (1440 x 1021 grid-points). The 1/4 degree resolution corresponds to the equator. Resolution increases poleward (The grid-size is scaled by the cosine of the latitude, except in the Arctic).

The ERAinterim reanalysis products are used for the atmospheric forcing with specific customizations such as relaxation to surface salinity. The run started on January, 1, 1989 and ended December, 31, 2009, corresponding to the available ERA-interim forcing field. The bi-harmonic viscosity coefficient was changed during the integration in order

---

7. It is French name for the Viking ships, chosen because, the scientific interests were initially focused on the Northern sub-polar Atlantic basins.

to fix numerical instability. A bi-harmonic viscosity of $-1.8 \cdot 10^{11}$ $m^4 \cdot s^{-1}$ is used. The experiment was performed with version 3.2.1 of NEMO. I used only last 10 years in this thesis (2000-2009). Model outputs are done as 5-day averages. Then monthly-means are computed in the post-processing using the *CDFTOOLS* (see section 6.2.2). The validation of ORCA025.L75-MJM95 is done, please see http://www.drakkar-ocean.eu/ for more information.

ORCA12.L46 configuration and ORCA12.L46-MAL84/MAL95 simulations

This sub-section describes in a few word the ORCA12.L46 simulations ($1/12^o$ of resolution) performed in the frame of the Drakkar project.

The ORCA12 is used by a large scientists community but I describe here in particular the configurations used in this thesis. The simulations are computed at MEOM (LEGI, CNRS).

The mesh is an ORCA tri-polar grid $1/12^o$ at the equator (north-pole folding condition). The horizontal resolution is 4322 x 3059 grid-points, the grid-spacing is from 10km at the equator down to 3km at high latitudes. The vertical grid is constituted by 46 levels Drakkar type, with a resolution of 6m near the surface and 250m in the deep ocean. The code is based on version NEMO 3.2.2. Please see http://www.drakkar-ocean.eu/ for more detailed informations.

MAL84
The ORCA12.L46-MAL84 simulation started from rest in 1978, with initial climatology temperatures salinities. The forcing is DFS4.1 relative wind with free slip boundary condition. Only the last 10 years (1983-1992) outputs are used.

MAL95
The ORCA12.L46-MAL95 simulation started from a restart file from Kiel run ORCA12.L46-K001 (started in 1978 from Levitus and forced by CORE2 forcing fields) simulation in 1989, January 1st. During the entire run performed at MEOM-LEGI (1989-2007), the time-step of 360s is used. The forcing used is ERA-interim relative wind. The boundary condition is partial slip. The last 10 years outputs are used. A bi-harmonic viscosity of $-1.25 \cdot 10^{10}$ $m^4 \cdot s^{-1}$ is used. Note that in the ORCA12 configuration, the viscosity is reduced by a factor 14 compared to ORCA025 configuration.

These two simulations are used not only for their high resolution compared to the MJM95 but especially to entangle the effects of the free slip and the partial slip on the boundary layers and the effects of the bi-harmonic coefficient used. Of course the different wind-stress forcings are discussed too.

6.2.2 CDFTOOLS

The model outputs are done as 5-day averages. To analyze the 10 year data set for each simulation, I used existing CDFTOOLS programs and I wrote new ones. CDFTOOLS is a Fortran 90 package of programs and libraries used as diagnostic tools for NEMO-OPA9 model output. It has been initialized in the frame of the Drakkar project. This package

is open (see http://www-meom.legi.grenoble-inp.fr/Web/ for more information). I wrote two CDFTOOLS programs (see appendix 12) to calculate the Taylor-scale and viscous dissipation scale quantities.

Chapter 7

Results

Contents

7.1   Validation of the upper-layer circulation

7.1.1   Monthly evolution of the upper-layer circulation

This section compares the model solutions to the existing observations. With the aim of doing a better comparison and of validating the upper-layer circulation of the model solutions in relation to the recent study of upper-layer circulation by Beal et al. (2013) from drifter-altimeter synthesis, the monthly-mean of the model solutions are calculated as in the Fig. 5.5 from Beal et al. (2013). The simulated currents at 100m depth (where the Ekman effects are negligible), are chosen to fit the observed monthly-mean geostrophic surface currents from Beal et al. (2013). In the following the monthly-mean evolution of the upper-layer circulation and the SSH is described for the three experiments.

ORCA025.L75-MJM95 simulation (Fig. 7.1)

Northeast Monsoon (December – February)
During the winter or the northeast Monsoon, the sSC flows along the Somali Coast, crosses the equator to be in confluence with the EACC in December, feeding into the eastward SECC. The confluence latitude appears to be located between 1ºN – 1ºS during this period. Flowing along the equator, the SECC appears to be wider in the southern hemisphere between about 1ºN and 5ºS while the observed SECC flows only in the southern hemisphere between 0º and 5ºS year-round [Beal et al. (2013)]. The SECC gradually strengthens and extends eastward across the basin from December to April. From December to February, next to the boundary between 5º and 10ºN there is a super-mesoscale cyclonic circulation as recently identified by Beal et al. (2013) associated with low SSH. The NMC flows westward into the basin south of India and curves to the north around 70ºE (in December) to feed the WICC. The NMC gradually extends westward across the basin from December to March on the south flank of the SSH high which is the Rossby wave high [Beal et al. (2013)]. It does not connect with the super-mesoscale cyclone in the west, because the cyclone is gone by the time the NMC reaches the western boundary. In the north of the basin, there is a southward flow along the Oman and Yemen coasts which recirculates cyclonicly adjacent to an anticyclonic velocity field with a relative SSH high around the Socotra Island. Differently the drifter-altimeter monthly-mean geostrophic currents show a broad, northward geostrophic flow which occurs year-round off the coast of Yemen and Oman.

March – May
The Rossby wave high centered at 7º30N, associated to the NMC at 5ºN on its south flank reaches the western boundary. This arrival yields the formation of northward flow nSC north of the latitude 5º30N at the place of sSC. South of 5ºN the NMC feeds the remaining part of sSC. The April-mean shows a relative SSH high associated to a weakly anticyclone between about 5º and 8ºN which is the signature of the early GW occurred in April as said above in the section 5.3. This confirmed the dynamics of the annual Rossby waves, precursor to the GW which occurs in April, two months before the onset of the
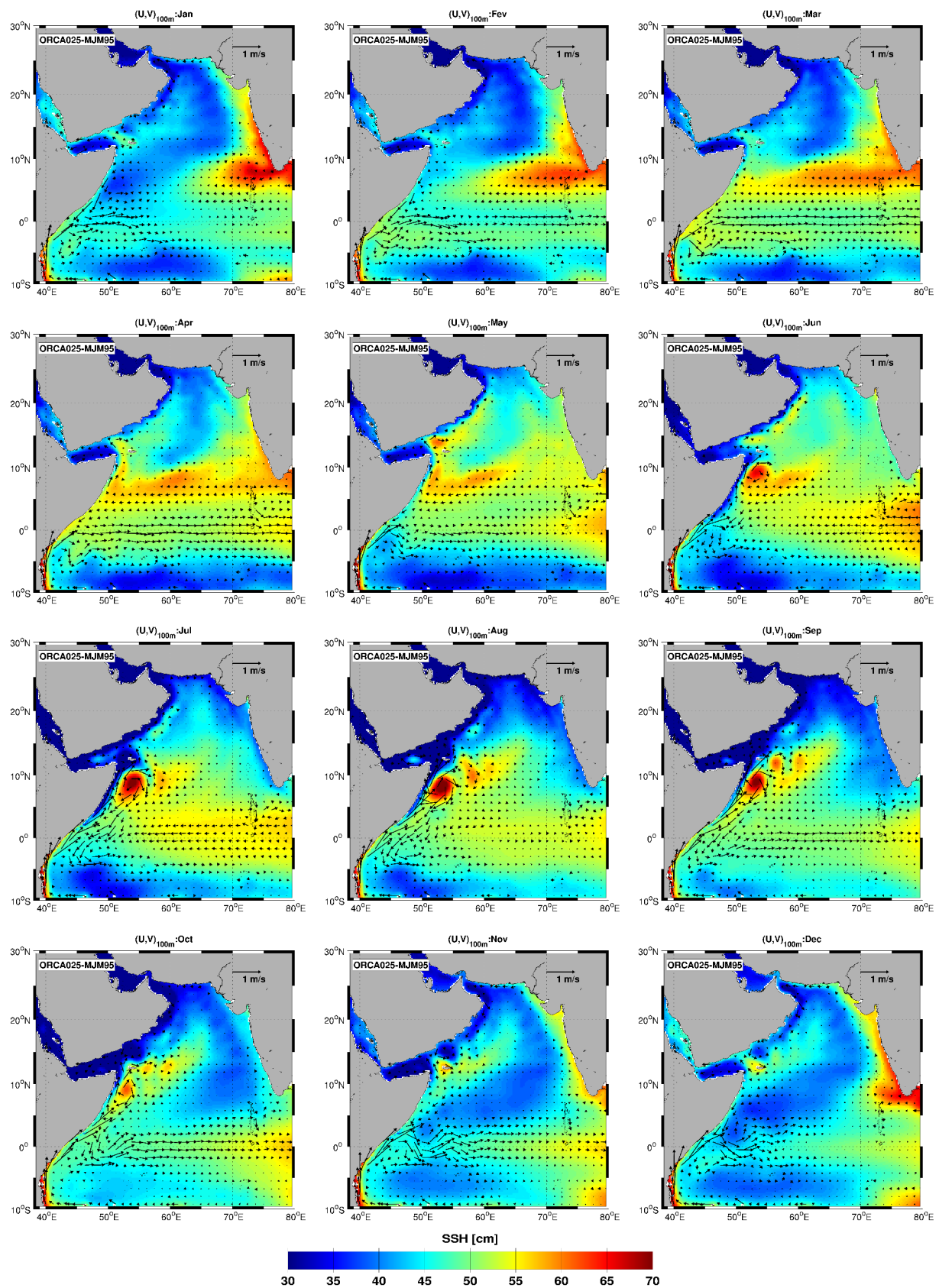
Figure 7.1 – *Monthly-mean currents (vectors; $m \cdot s^{-1}$) at z = 100m and sea surface height (SSH; color shading; cm) from ORCA025.L75-MJM95. Landmasses are shaded gray.*
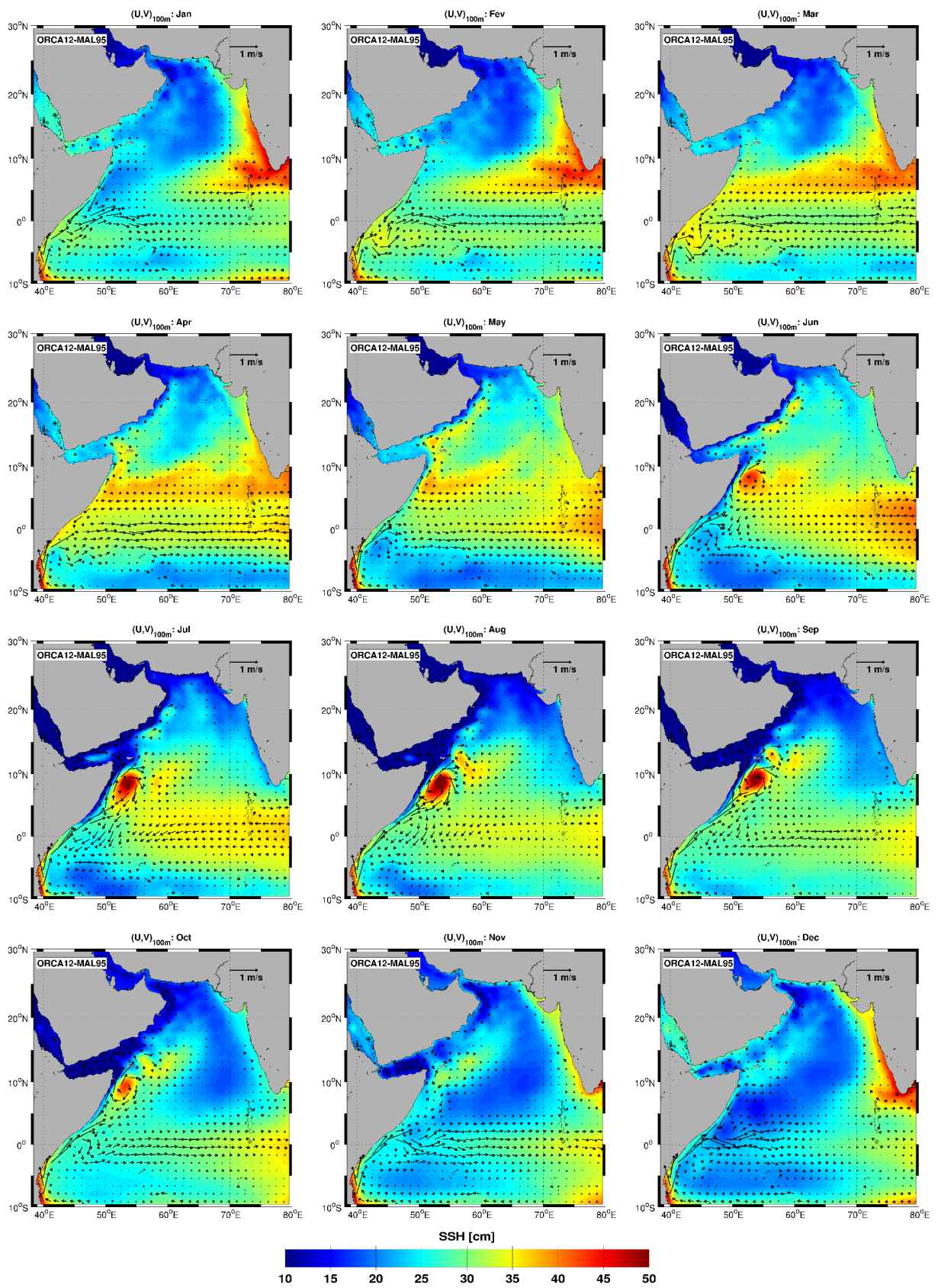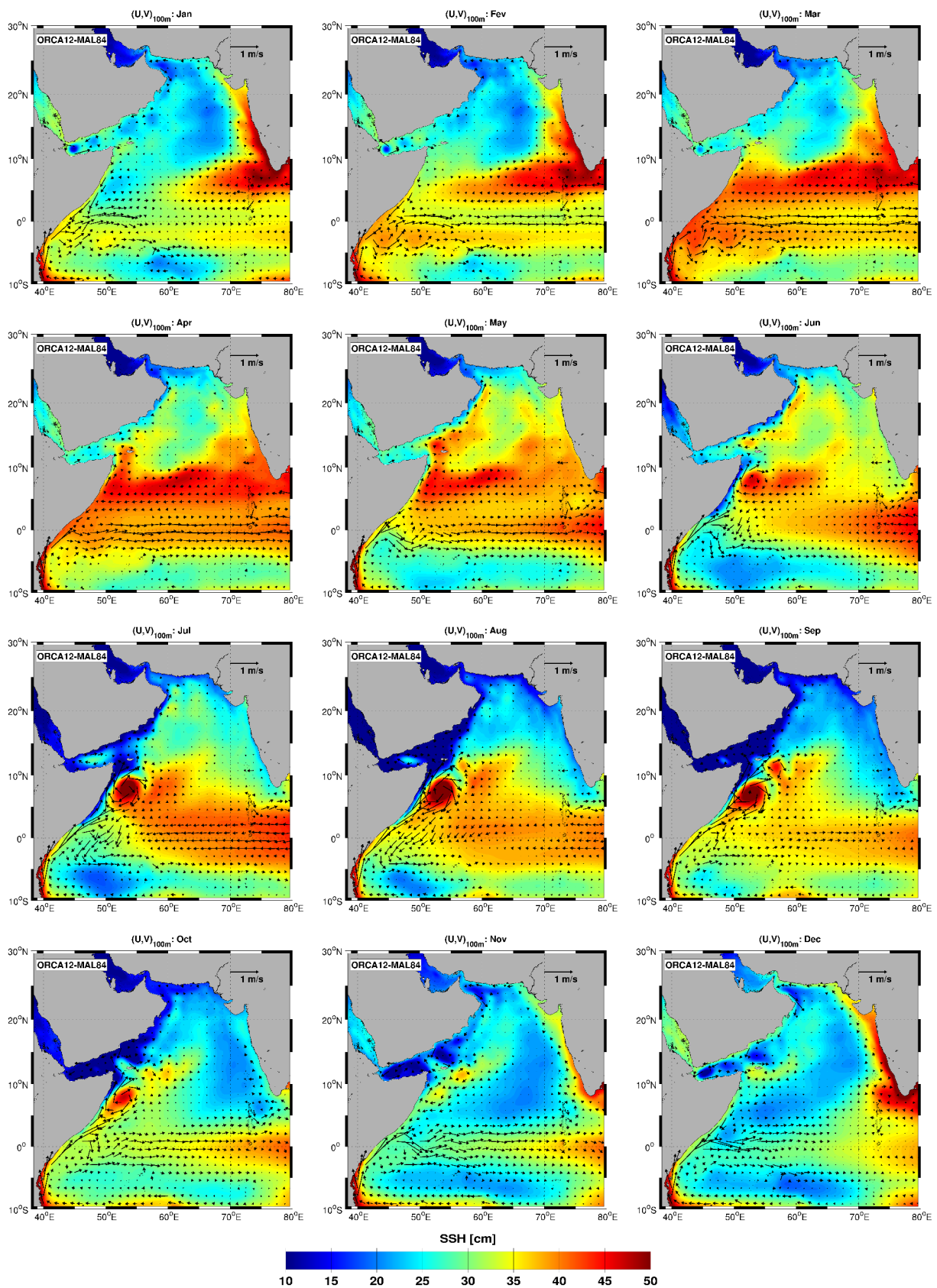
Figure 7.2 – *Monthly-mean currents (vectors; m·s⁻¹) at z = 100m and sea surface height (SSH; color shading; cm) from ORCA12.L46-MAL95. Landmasses are shaded gray.*

Figure 7.3 – *Monthly-mean currents (vectors; $m \cdot s^{-1}$) at $z = 100m$ and sea surface height (SSH; color shading; cm) from ORCA12.L46-MAL84. Landmasses are shaded gray.*

southwest Monsoon Winds [Shetye (1998); Rao et al. (2010); Beal et al. (2013)]. This early GW persists until the southwest Monsoon sets in, but the initial nSC appears clearly to be established by the reflection of short, coastally trapped Rossby wave after the arrival of the elevation of propagated SSH anomaly as postulated before by McCreary et al. (1993) and as observed in drifter-altimeter by Beal et al. (2013). This is corroborated by the model solutions. In the north of the basin, the southward flow along the Oman and Yemen coasts cancels in March, and changes direction to flow northward from April to August.

Southwest Monsoon (June – August)

During the summer or southwest Monsoon, only the northward flowing part of the SC exists between about 3º – 12ºN. The nSC speed reaches 1m·s^{-1}. The nSC retroflects to forms an intense GW between about 6º and 11ºN. The mean-flow shows a southward recirculation next to the nSC across the equator until about 4ºS, before feeding the SECC at this latitude. This southward mean-flow is an artefact of the southward branch of the retroflection of the EACC. Indeed the EACC retroflects to form the SG which migrates northward. The SG collapses/collides with the GW (discussed in sub-section 7.2.2). In the later phase of the southwest Monsoon after the northward migration of the SG, the EACC is continuous with the nSC, so it is not possible to distinguish between each current. There is a relative maximum of SSH associated with an anticyclonic flow east of the GW. Another anticyclonic relative high of SSH is located northeast of the GW (east of the Socotra Island), the Socotra Eddy (SE) in July. During this season, the southward flow SMC appeared weak along the Indian coast. In the mid-basin, a westward flow appear associated with a high SSH anomaly along the equator, formed in June and July which propagates eastward (equatorial Kelvin wave).

September – November

In September, the SE is fully developed and continues to spin until October at the east of the Socotra Island. During this period, the intensity of the GW and the SE decrease and they disappear completely in November. The nSC intensity decrease also during this period. Only a relative high of SSH persists around the Socotra Island until February. The eastward propagation of the equatorial Kelvin waves gives rise to westward Rossby wave which reaches the Somali coast in December to reverse the northward flow nSC into southward flow sSC in December.

ORCA12.L46-MAL95 simulation (Fig. 7.2)

Northeast Monsoon (December – February)

During the winter or the northeast Monsoon, the general circulation and the SSH monthly-mean pattern are similar as in MJM95 experiment, but another local small scale structures appear. Cyclonic recirculation eddies that propagate eastward in the Gulf of Aden are discernible in the December-mean SSH and velocity fields. From January to March, anticyclonic eddies of comparable scale pair with the latest cyclonic recirculation eddies

move westward together in the Gulf of Aden as observed by Fratantoni et al. (2006) in their satellite-derived study. The Rossby wave appears less ordered than in the MJM95 experiment and propagates around the latitude 7°N. The zonal flows appear more intense than in the MJM95 experiment. The southward flow along the Oman and Yemen coasts is weaker than in the MJM95 experiment. It appears to shut down in February, one month before the observed shout down in the MJM95 experiment.

March – May

In March the Oman and Yemen coastal flow reverse to flow northward. The other large circulation patterns during this period are similar to those of the MJM95 experiment.

Southwest Monsoon (June – August) and September – November

With the exception of small scale structures appearance, some spacial and temporal lag, the large circulation patterns and the dynamics during this period are similar to those of the MJM95 experiment. This comes as no surprise, since the two experiments are forced by the same ERA-interim wind field.

ORCA12.L46-MAL84 simulation (Fig. 7.3)

Northeast Monsoon (December – February)

During this season as in the previous experiments the large circulation patterns are similar but the flows appear stronger than in the MJM95 experiment. After the retroflection, the EACC appears to recirculation anticyclonic with two relative SSH high before feeding the SECC. There is a relative high of SSH south of the Socotra Island which appears to be located around the Socotra Island in the MJM95 experiment from December to February. Note that the propagated SSH high is ordered as in the MJM95 experiment.

March – May:

in March when the Rossby wave reaches the Somali Coast, the reflected short wave doesn't penetrate in the Gulf of Aden.

With the exception of small scale structures appearance, some spacial and temporal lag, the large circulation patterns and the dynamics are similar to those of the MJM95 experiment.

7.1.2 The effect of annual Rossby waves on the circulation

The Monthly-mean currents at 100m depth of the three experiments MJM95 (Fig. 7.1), MAL84 (Fig. 7.3) and MAL95 (Fig. 7.2), revealed that the nSC appears north of 5°N as early as March/April, together with a weak anticyclone at 7°N, a precursor to the GW. As said above this early arrival of the GW was recently observed by Beal & Donohue (2013) and Beal et al. (2013) (Fig. 5.5) at 6°N in a regional study of SSH data. These observations combined with the present experiment solutions challenge the concept that the nSC flow is established after an adjustment of the circulation to the southwest Monsoon wind stress
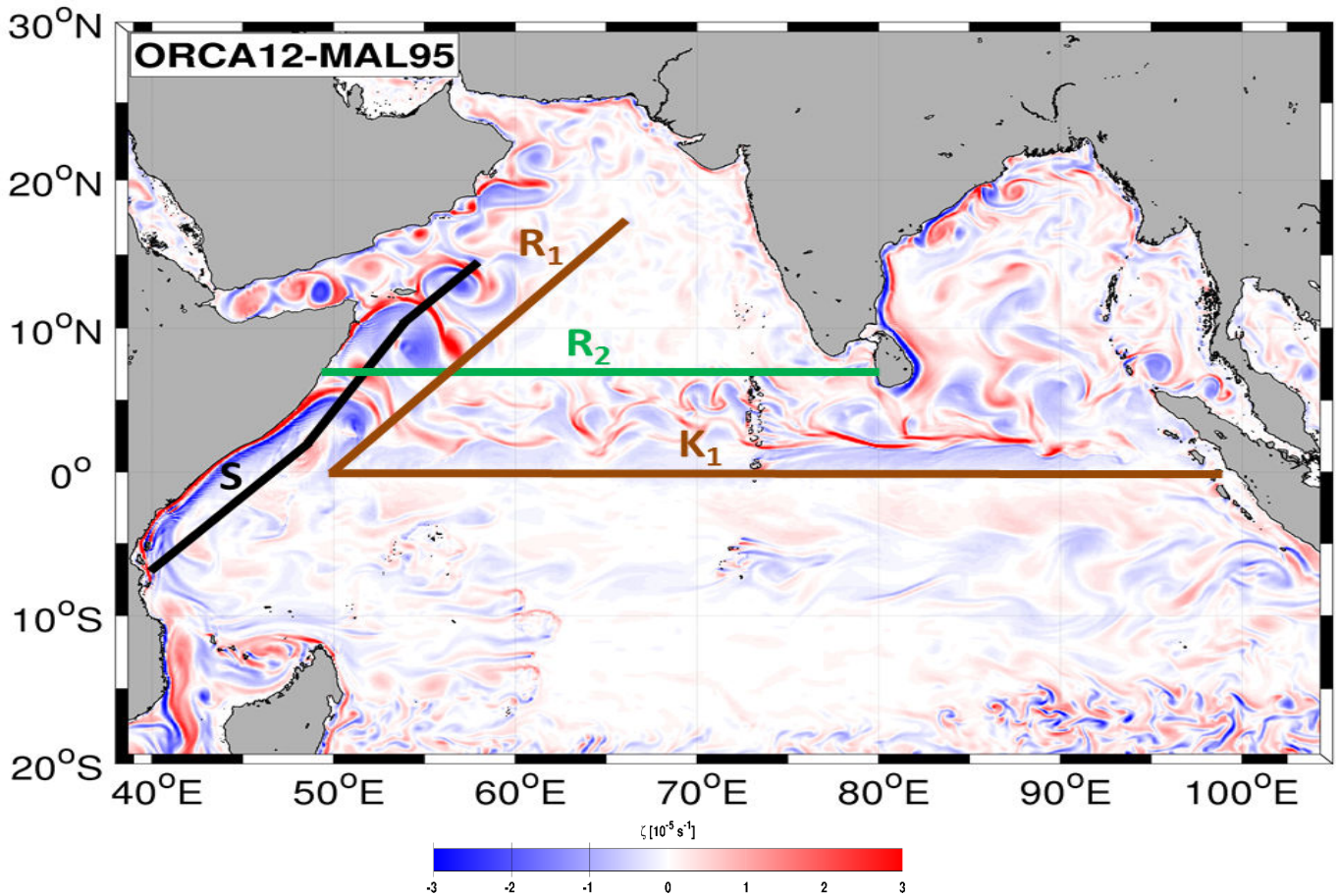
Figure 7.4 – *Snapshot of relative vorticity (October, 17, 1998) at surface with lines showing the location of Hovmöller sections: S section along the Somali Coast across the Somali eddies (black line), R_1 section across the Rossby waves (green line) initiated by the negative wind stress curl, K_1 equatorial section across the Kelvin waves which appear to be created between longitudes 50 and 60^oE, and R_2 section across the Arabian Sea at $7/7^o30N$ through the annual Rossby wave.*

curl [see *e.g.* Lighthill (1969)]. In this case, a minimum lag on the order of one month between the onset of the wind curl in May/June (not shown) and the appearance of the nSC would be expected. This is the time scale, according to linear theory, for Rossby waves to propagate from the region of wind curl forcing (the center of the north Arabian Sea) to the western boundary near the equator [see *e.g.* Lighthill (1969)]. Hence, these observations combined with the present experiment solutions point to a different forcing for the initiation of the nSC. This is not to say that Monsoon Winds and wind stress curl do not play the dominant role in forcing the nSC once the southwest Monsoon sets in, but the initial northward flow is clearly established by a different process.

Looking again at Fig. 7.1, Fig. 7.2 and Fig. 7.3 and Fig. 5.5, the appearance of northward flow along the boundary in March/April (April) is coincident with the arrival of the annual SSH high centered along 7°30N for MJM95, 7°N for MAL experiments (8°N in the observations). This signal is due to first- and second-mode annual Rossby waves [Brandt et al. (2002)], which follow the pathway defined by the waveguide around the northern Indian Ocean. This process begins with a westward, downwelling Rossby wave from the wind curl region to the Somali Coast, continues with equatorial Kelvin waves which appear to be created between about 50 and 60°E. According to the pathway of the Rossby waves and the Kelvin waves, Hovmöller diagrams are done (as sketched in the sections R_1K_1 and R_2 in Fig. 7.4) and shown in Figs. 7.5, 7.6 and 7.7. Year-round, there are two pairs of upwelling (SSH low in sections R_1K_1) and downwelling (SSH high in sections R_1K_1) equatorial Kelvin waves which propagate eastward.

[(not shown) After hitting the Sumatra coast, they bifurcate and propagate as two poleward coastally-trapped Kelvin waves which can be observed in the Hovmöller diagrams as SSH low/high around 99°E. After about one month, the northern branches propagate over varied distances along the coastal waveguide of the Bay of Bengal. In the Bay of Bengal, the first upwelling (downwelling) Kelvin wave occurs during January-March (May-August) and the second upwelling (downwelling) Kelvin wave occurs during August-September (October-December). These four Kelvin waves are discernible in the Hovmöller diagrams (as SSH low/high around 99°E) with about one month lag before, noised by inter-annual variability. All four Kelvin waves show distinct life cycles limited to the coastal wave guide of the Bay of Bengal, the only exception being the second downwelling Kelvin wave. The first upwelling Kelvin wave while propagating along the waveguide weakens off the western rim of the Bay of Bengal and terminates off the southeast coast of India. This suggest that this first upwelling Kelvin wave has a limited role in remotely triggering coastal upwelling observed off the southwest coast of India as early as February/March. The propagation of the first downwelling Kelvin wave also terminates mid-way in the coastal waveguide of the head of the Bay of Bengal. Among the two, the pairs of upwelling and downwelling Kelvin waves, the second downwelling Kelvin wave is the more pronounced].

It propagates all through the coastal waveguide around the rim of the Bay of Bengal, and radiates a Rossby wave back into the Arabian Sea from the southern tip of India at 80°E in October/November centered around the latitudes 7°30N for MJM95, 7°N for MAL experiments and propagates westward as said above and shown in Figs. 7.5a, 7.6a

7N30

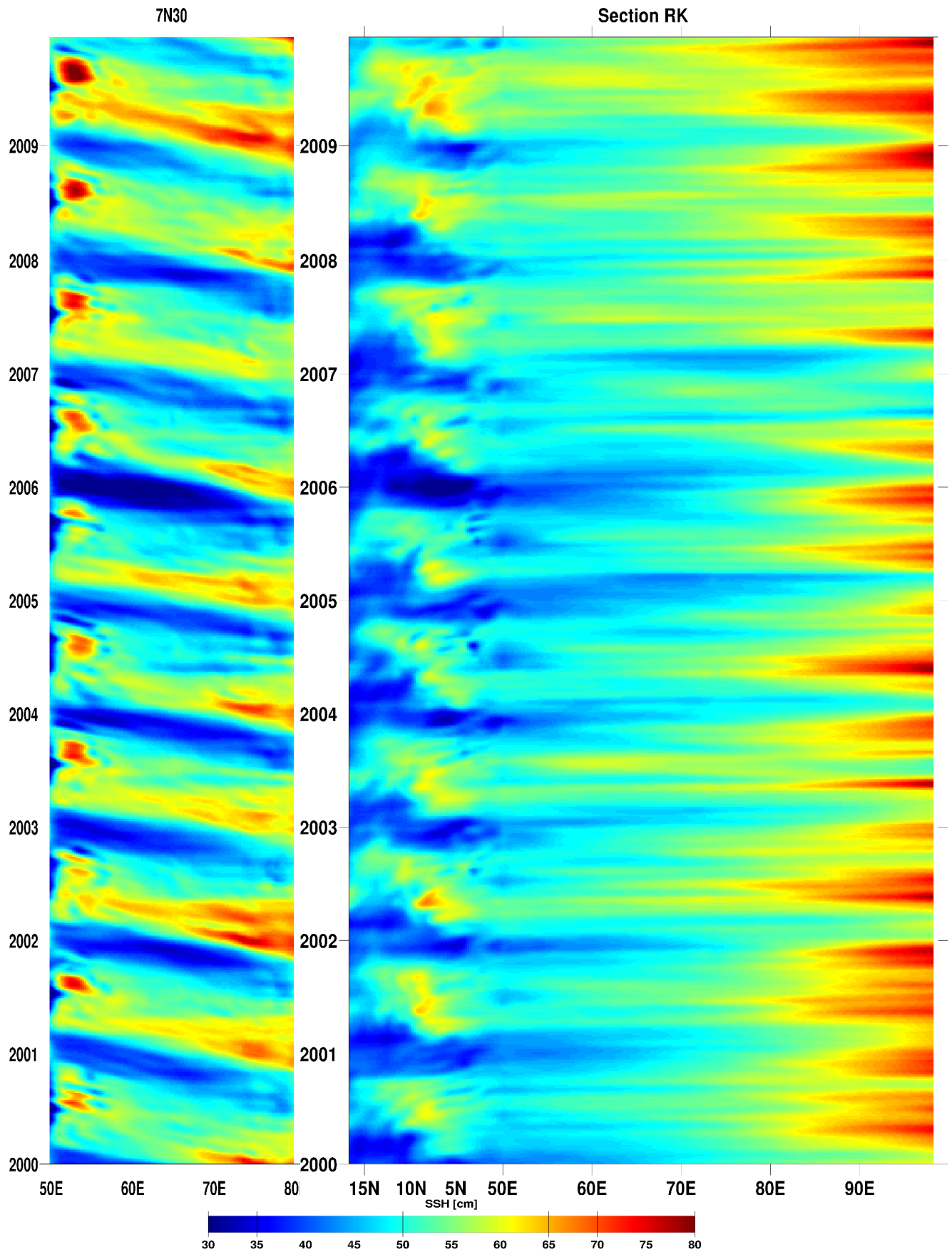**Section RK**

SSH [cm]

30 35 40 45 50 55 60 65 70 75 80

Figure 7.5 – *Longitude-time section along 7°30N (section R_2) and latitude/longitude time section (section R_1K_1) of SSH for the MJM95 experiment.*
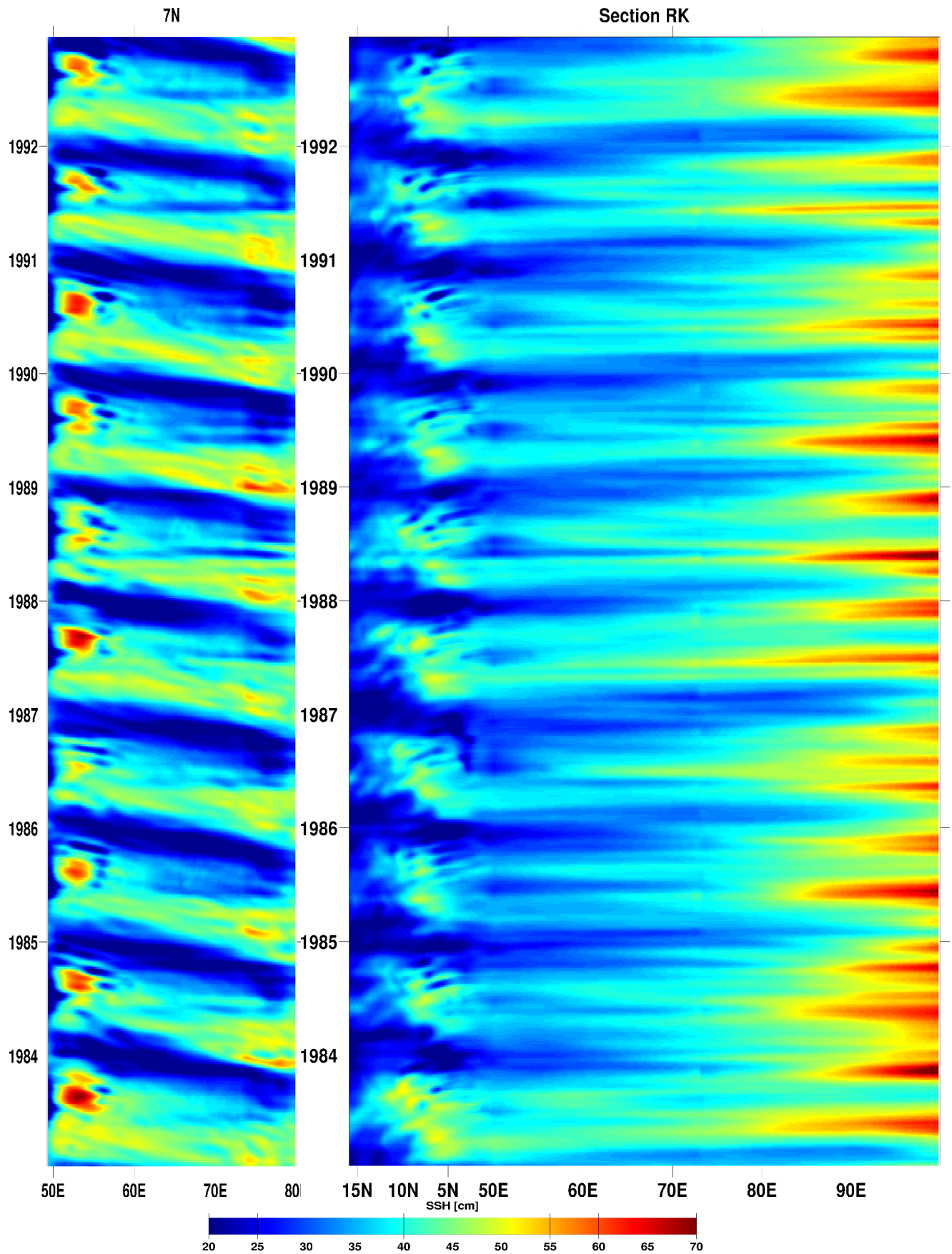
Figure 7.6 – *Longitude-time section along 7°N (section R_2) and latitude/longitude time section (section R_1K_1) of SSH for the MAL84 experiment.*

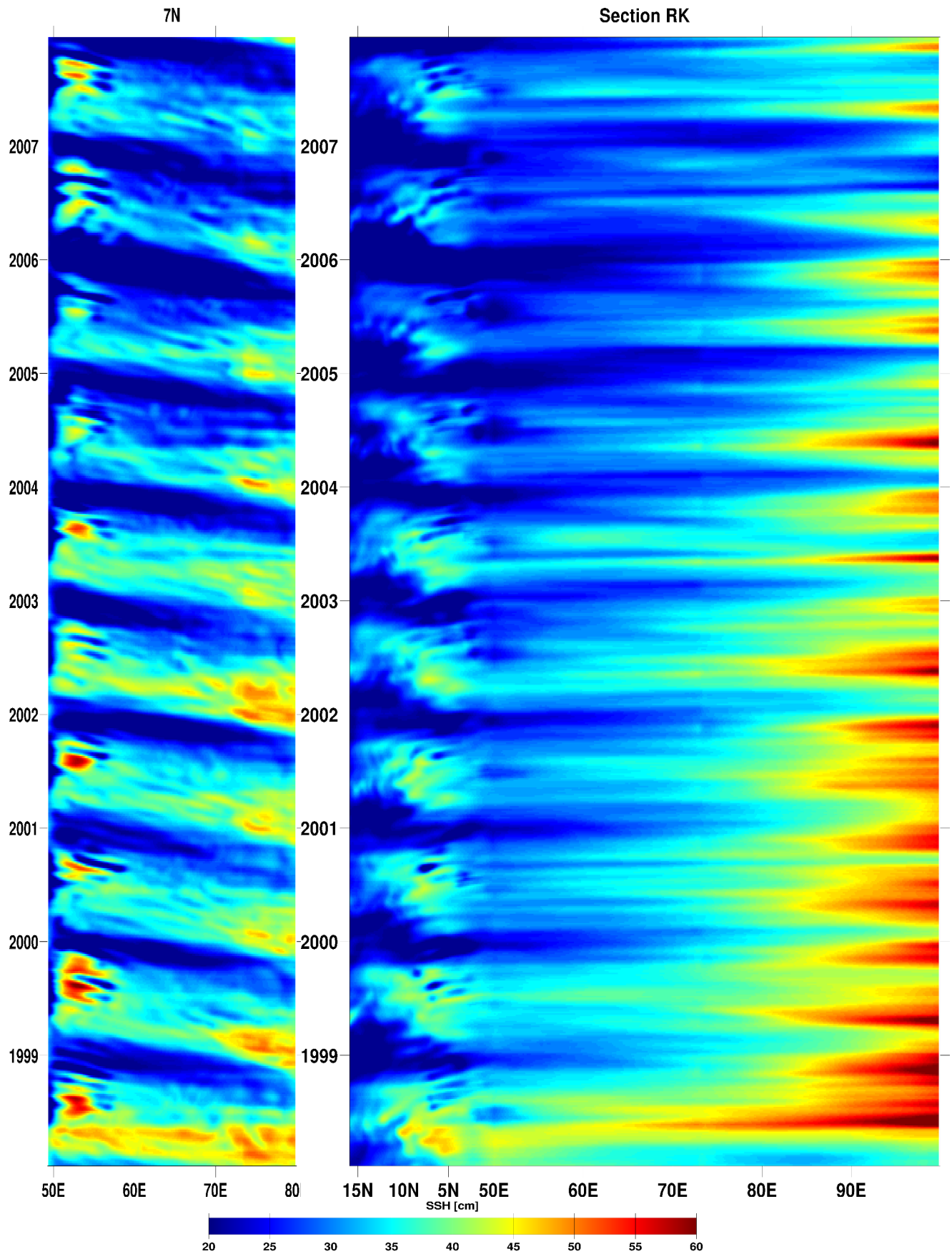Figure 7.7 – *Longitude-time section along 7°N (section R_2) and latitude/longitude time section (section R_1K_1) of SSH for the MAL95 experiment.*

and 7.7a. This Rossby wave was recently observed at the same period but centered at the latitude 8ºN (see Fig. 5.5) in the altimeter data study by Beal et al. (2013). The leading edge of Rossby reaches the west coast in March-April as can be observed in Fig. 7.5a, 7.6a and 7.7a (April for the observation as shown in Fig. 5.5), so that the offshore gradient of SSH changes sign and the coastal current switches from southward (sSC) to northward (nSC) north of 5ºN and then the two currents coexist until the establishment of the southwestern Monsoon. This confirms the suggestion by Beal & Donohue (2013) that the elevation of the propagated SSH anomaly once it reaches the coast in April (the precursor of the GW) could result from the reflection of short, coastally trapped Rossby waves.

This process confirms the Shetye theory [Shetye (1998)] which stipulates that the forcing originates during the previous southwest Monsoon, when strong, negative wind stress curl triggers a chain of planetary waves which feed back on the initiating region in a predicted time scale of approximately 300days.

It is noteworthy to mention that the second branch of coastal downwelling Kelvin wave which propagates along the eastern coast of the Arabian Sea does not make the same waveguide propagation around to the west coast of the Arabian Sea itself, as a result of its rapidly diminishing lateral scale with latitude and the gap in the coastal boundary at the Gulf of Oman.

The monthly-mean climatology differences in the three experiments are to be expected because of:

- the model resolution used, which allowed part of the sub-grid structures of the MJM95 experiment to be resolved by the MAL84 and MAL95 experiments,
- the chaotic dynamics of the models, the model forcing and the initial conditions which amplify in areas where the nonlinearity in the governing equations plays a key role, hence some spacial and temporal lags in the solutions.

Even so the three experiments show very few difference in the general circulation: simulated currents are in good agreement with the observed climatologies, except the Indian global-mean SSH values which are smaller than the observed absolute dynamic topography. However the SSH fields permitted to confirm the suggestion of Beal et al. (2013) that the southwest Monsoon circulation can precondition the next through the dynamics of the effect of annual Rossby waves on the circulation.

7.1.3   Qualitative validation of the SSH field

The model's ability to reproduce the Monsoon characteristics and simulating SSH field for the three experiments have been compared to the monthly-mean absolute dynamic topography from AVISO [Beal et al. (2013)]. In general the experiments represent the same areas of low/high monthly-mean SSH as seen from the observed AVISO monthly-mean absolute dynamic topography (Fig. 5.5). The arrival of this Rossby wave at the Somali Coast is seen in March/April. Thus the experiments simulate well the dynamics of the Rossby waves. The early northward flowing nSC in March/April is corroborated also by *in situ* observations. Indeed during March/April 1979, Leetmaa et al. (1982) reported in

the ship-drift observations that the SC was flowing northward into the northeast Monsoon associated the arrival of the Rossby wave.

The differences between simulated and observed SSH is seen in the annual Rossby waveguide axis of which seen to be centered at 8ºN in the observed absolute dynamic topography while the experiments show the waveguide axis to be centered at about 7º30N (for MJM95 experiment) and 7ºN (for MAL84 and MAL95 experiments). The global-mean sea level differs between the models solutions and between the models solutions and AVISO observations. Indeed there is no constraint on the model fresh water forcing (evaporation/precipitation budget) to fit the observed sea level. Consequently each model simulation has a mean sea level set by its own fresh water budget. All these allow to validate the upper layer circulation of the Arabian Sea.

For detailed validation of the global simulations ORCA025.L75-MJM95, ORCA12.L46-MAL84 and ORCA12.L46-MAL95 of which the regional extractions are done, the reader is referred to Barnier et al. (2011); Lecointre et al. (2011a,b).

7.2   Coherent structures

Describing the monsoon driven ocean circulation is challenging because large amounts of data are required in both space and time to resolve the evolution of the flow in a region with no steady circulation. Above I used monthly-mean satellite observations to validate the model solutions, but the dynamics of Somali eddies evolves at a much faster time scale. The available satellite observations together with *in situ* measurements as described in the section 5.4 do not provide a sufficient space and time resolution necessary to study the fast dynamics of Somali eddies.

To the best of our knowledge the nature of the interaction between the SG and the GW on the one hand, and the mechanism formation of the SE on the other hand, are still unresolved. In view of this lack of high frequency observations, model solutions can provide the high frequency information about the formation and the evolution of the Somali eddies. This section describes the formation processes of the Somali eddies.

7.2.1   Anticyclone

For simplicity and clarity in the description of the complicated formation process of the Somali eddies, I distinguish the eddies as this description will progress.

The northward flowing nSC in March/April appears to be a precursor of the formation of the weak *early* GW, hereafter called the *e*GW.

Regularly at the beginning of June, when the southwest Monsoon is well established, the GW is a *fully* developed GW, hereafter called the *f*GW.

March – June
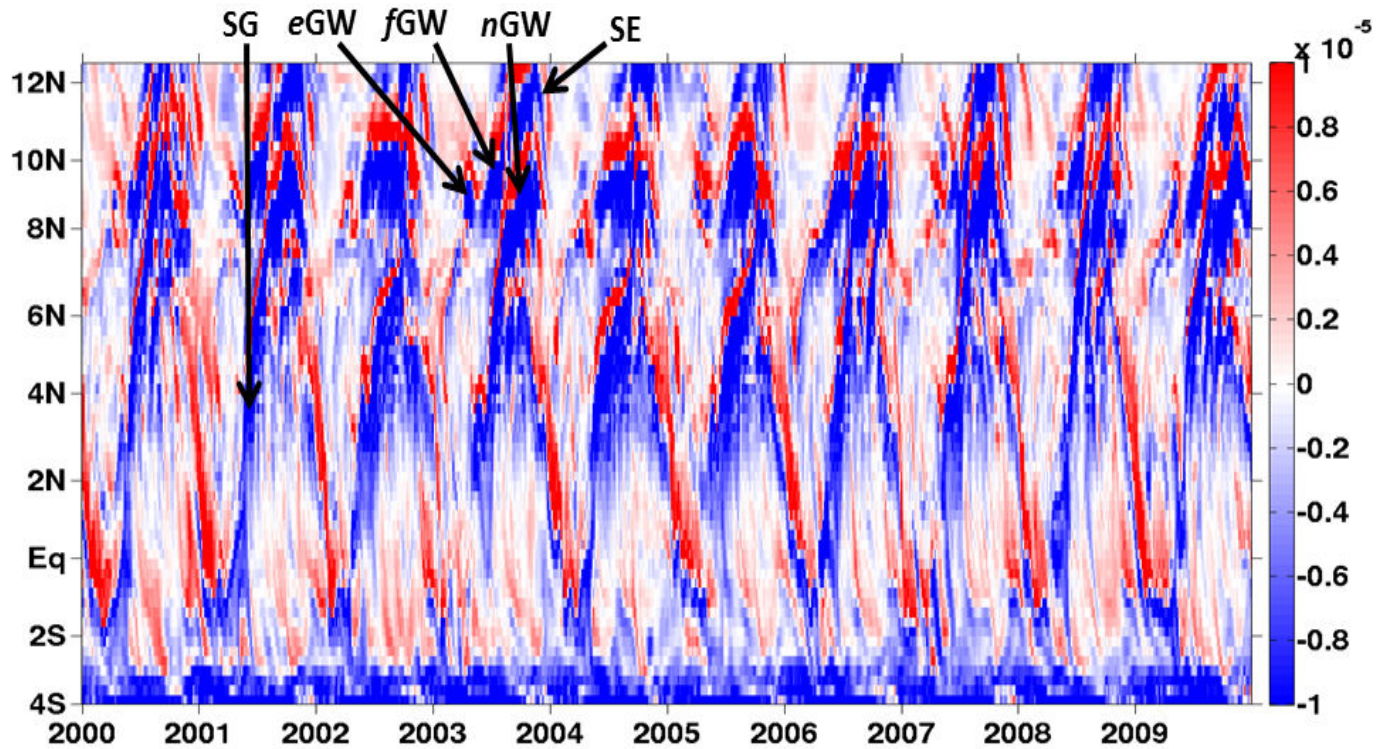Two scenarios are observed to occur during March – June:

Figure 7.8 – *Hovmöller diagram of relative vorticity (ζ; s^{-1}) along the along the Somali Coast (section S of Fig. 7.4) through the Somali eddies for ORCA025.L75-MJM95 experiment. Eddies (detected by the negative vorticity within the eddies) are early Great Whirl (eGW), fully developed Great Whirl (fGW), new Great Whirl (nGW), Socotra Eddy (SE) and Southern Gyre (SG).*

- (i) In the 1st scenario, the most frequently observed, is as follow. After the formation of the eGW in March/April, the intensification of the southwest Monsoon in June, reinforced the eGW which becomes the fGW. The SG is formed at the same time.
- (ii) In the 2nd scenario, less frequent, the eGW formed in March/April, translates through the Socotra Passage before the intensification of the southwest Monsoon, and translates slowly westward into the Gulf of Aden. This is corroborated by satellite observations in the eastern Gulf of Aden [Fratantoni et al. (2006)]. Following the intensification of the southwest Monsoon, the nSC retroflects to form the fGW. The SG is formed at the same time.

June − October

From June to August, the intensification of the southwest Monsoon strengthens the EACC, and causes the northward migration of the SG at a speed of $\sim$1m·s^{-1}. This migration ends in late July or early August when the SG encounters the fGW, then several scenarios can occur:

- (i) The SG collapses with the fGW to form a new fGW.
- (ii) The SG collides with the fGW but no merging occurs. The fGW is pushed through the Socotra Passage and becomes an anticyclonic vortex translating slowly westward into the Gulf of Aden. The SG takes its place to become a new fGW;
- (iii) The SG collides with the fGW. The fGW is then shifted northeastward with a reduction of its diameter. It becomes the smaller eddy located at the east (or southeast according to the experiment) of the Socotra Island, commonly called the Socotra Eddy (SE). The SG takes its place to become a new fGW (this type collision is discussed in detail in the following sub-section).

In addition, according to the inter-annual variability of the EACC, some years in the late phase of southwest Monsoon, a new weak SG may be created, but its behavior seems to be a coalescence with the fGW if the wind stress allows it.

The analysis of the three simulations shows that the formation and the behavior of the Somali eddies are a combination of these scenarios, which explains the chaotic dynamics of the Somali eddies.

7.2.2 Collision versus coalescence

A question that is still unresolved is, what is the nature of the interaction between the SG and the GW? Some observations have suggested that the two eddies may at times collapse. The suggestion is based on satellite SST images which indicated a rapid ($\sim$ 1m·s^{-1}) northward propagation of the southern cold wedge (just north of SG adjacent to the boundary) [Evans & Brown (1981)]. This interpretation has been supported by ship-survey measurements suggesting that low-salinity southern waters were present in the wake of the migrating southern cold wedge [Schott (1983); Swallow et al. (1983)]. The observational evidence for it is rather scant as it is only based on the coalescence of the two cold wedges. But a question subsists: does the coalescence of the two cold wedges, implies the coalescence of the two eddies? In an attempt to answer this question, I use the spiciness (π), a variable that quantifies whether water on a given isopycnal is warm

and salty or cold and fresh [Flament (2002)], as a tracer characterizing the eddies. Spicy waters (larger values of π) are relatively warm and salty, and minty waters (low values of π) are cold and fresh.

Spiciness is conservative on isopycnal surfaces in the absence of mixing and surface fluxes, so it is useful to assess mixing that occurs along a given current. I also compute the relative vorticity to characterize the dynamical aspect of the eddies. The 5-days averaged snapshots of the MAL84 experiment during the southwest Monsoon 1998 are shown in Fig. 7.9 to illustrate the formation process of the SE. At the beginning of June the cross-equatorial flow EACC transports spicy water retroflecting to form the SG between about 3°S – 2°N. On the northern flank of the SG, a minty cold wedge of upwelled water is formed, the southern wedge. It migrates northward with the SG. During the northward migration, the spiciness of the southern cold wedge decreases due to the intensification of southwest Monsoon which upwells sub-surface cold water-masses to the surface. At the same time the spiciness of the northern cold wedge also decreases. At about mid-July, begins the collapse of the two cold wedges which merge completely at the beginning of August. However no collapse is observed for the two eddies as shown by the relative vorticity (right panels of Fig. 7.9), but rather an elastic collision in which the GW is shifted northeastward to form the SE as can be seen in the spiciness/relative vorticity snapshots. The migrating SG takes the place of the GW, to become a new GW. This formation process of the new GW and the SE were not previously identified and it challenges the collapse interpretation based on the collapse of the two cold wedges. It appears clearly that the collision didn't produce the coalescence between the SG and the first GW as can be seen in Fig.7.9 in the difference of spiciness of the new GW and the SE. This is corroborated by the ship survey observations by Fischer et al. (1996) as is apparent from the difference in surface salinities between the GW and the SE shown in Fig. 5.7.

It appears clearly that in the models, the SE results from the collision without merging between the SG and the GW. This collision generally occurs at the end of July or early August.

7.2.3 Burst

During the northward migration of the SG, its collision (or coalescence) with the GW to form a new GW and the SE (or a new GW), intermittent detachments of positive vorticity from the WBC are observed in all the three experiments (Fig. 7.10). Similar intermittent detachments are also observed for the GW. These detachments are the most violent phenomena in these experiments with the strongest velocity and vorticity gradients. In the three experiments, the sheet of positive vorticity along the boundary (at the inner side of the nSC and EACC) breaks due to the action of the large anticyclones (SG/GW). The detached part is torn off the boundary by the anticyclone and accelerates away from the boundary (see Fig. 7.10). As said above in the sub-section 4.5.2, these events are called *bursts* in analogy with the bursts or ejections in the classical boundary-layer dynamics [Robinson (1991)]. The northward migration of the large anticyclones are constrained by the topography, so the bursts are also constrained to occur more locally
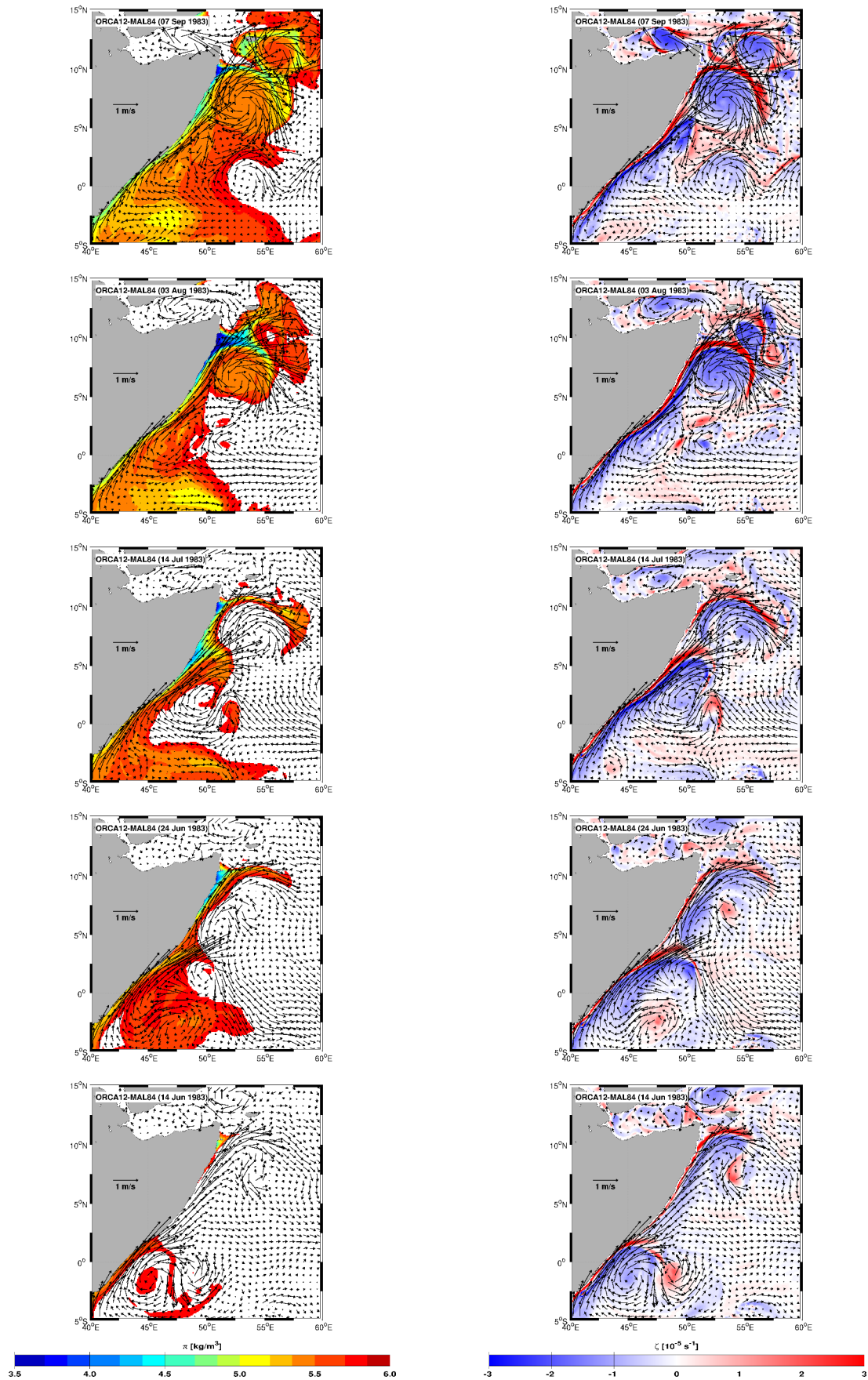
Figure 7.9 – *daily surface currents (vectors; m·s⁻¹), the spiciness (π; color shading; kg·m⁻³) and the relative vorticity (ζ; color shading; s⁻¹) from 0RCA12.L46-MAL84 experiments to illustrate the collapse of the two cold wedge and an elastic collision shock between the Great Whirl and Southern Gyre. Spiciness over 5.8 kg·m⁻³ are shaded white. Landmasses are shaded gray.*

at the north of the eddy center. After the occurrence of the bursts, their ejection off the boundary and their offshore transport are better resolved by the ORCA12 experiments than in the ORCA025 experiment. This confirms as said in sub-section 4.5.2 that the ejection of the boundary and the offshore transport of the bursts require fine numerical resolution and only appear for smaller viscosity coefficients. In the ORCA025 experiment, bursts occur but appear to be dissipated rapidly during the ejection process while in the ORCA12 experiments the ejection of the positive vorticity is transported offshore and persist.

7.2.4   Dipole

The positive vorticity anomalies ejected from the boundary during the bursts, spin cyclonicly and pair with negative vorticity of the anticyclones to form an asymmetric dipole. The behavior of the asymmetric dipole depends on the trajectory of the small cyclonic vortex. Several possible trajectories are observed for the small cyclonic vortex:

– (i) It remains attached to the large anticyclonic eddy, circles around it and returns to the western boundary, collides with the boundary current, before being sucked up into the large anticyclonic eddy and both merge. This process is responsible of the mixing of minty water masses of the cold wedge within the large Somali anticyclonic eddies as can be seen in the difference of spiciness of the same eddy at different dates in Fig. 7.9. The cyclonic vortices created by the GW most often follow this trajectory.

– (ii) It separates from the large anticyclonic eddy and drifts away offshore. This process is responsible for the offshore mixing of the upwelled-water masses detached by the bursts; the cyclonic vortices created by the SG most often follow this trajectory (Fig. 7.10).

– (iii) (No figure shown) It separates from the large anticyclonic eddy, pairs with a small negative anticyclonic detachment to form an almost symmetric dipole; the dipole travels ballisticaly (at almost constant velocity) over distances of several large eddy diameters. The SG of the MAL95 experiment exhibits this type of dipole which maybe amplified by the partial step boundary condition.

The behavior of the bursts shows that the SG has a dominant role over the GW in the offshore mixing of the coastal upwelled-water masses ejected away from the boundary.

The dynamics of the burst is damped in the lower resolution ORCA025 experiment and only a signature of a dipole is discernible. In the ORCA12 experiments the behavior of the bursts after ejection followed by the dipole formation is a very well marked phenomenon which clearly influences the circulation and the mixing (Fig. 7.10) at larger scales.

It is noteworthy to mention that bursts and dipoles are also formed along the western boundary of the north Arabian Sea (Yemen/Oman Coasts) and those of the Bay of Bengal, not only during the southwest Monsoon (northward flow), but also during the northeast Monsoon (southward flow).
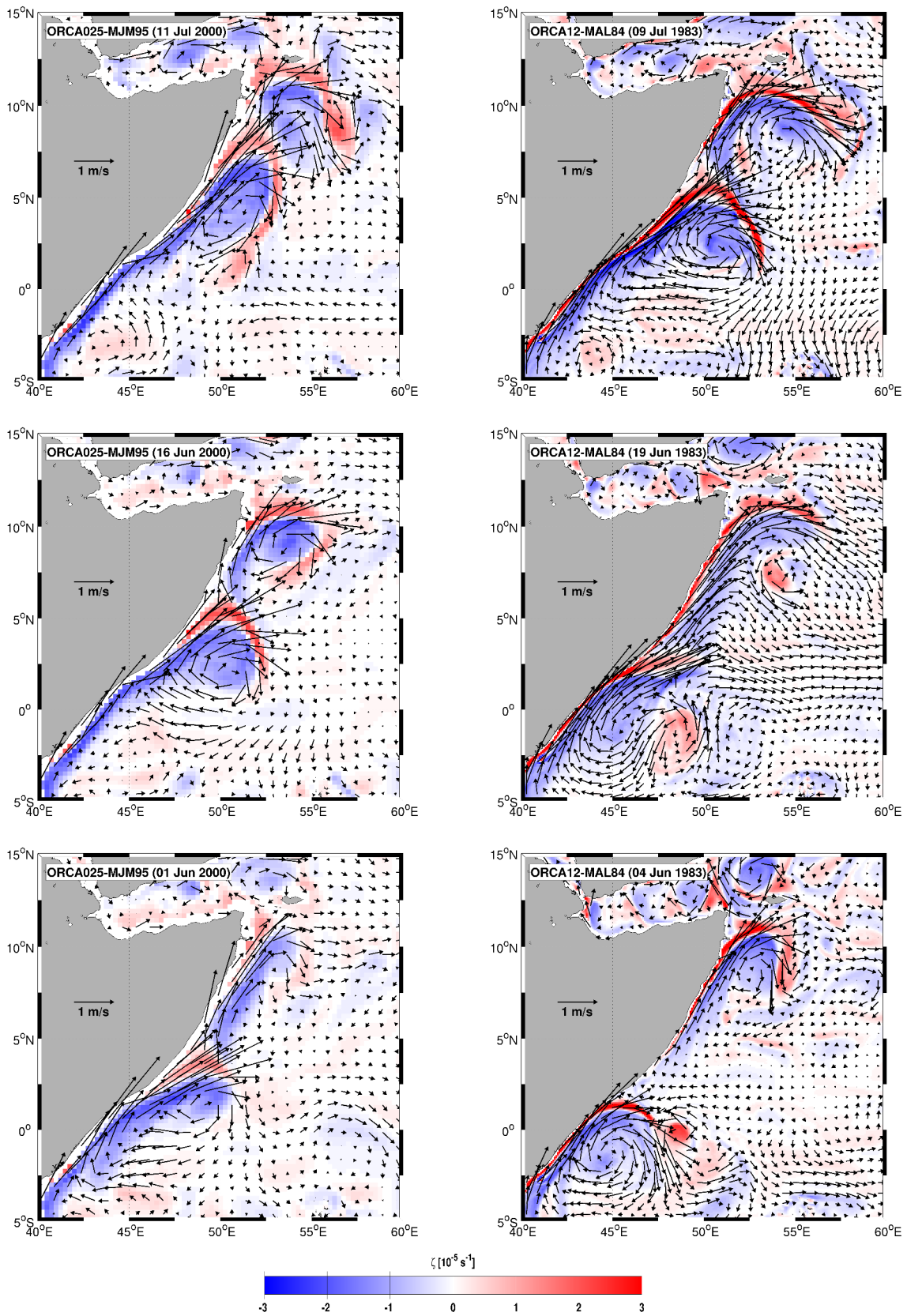
Figure 7.10 – *daily surface currents (vectors; m·s^{-1}) and the relative vorticity (ζ; color shading; s^{-1}) from ORCA025.L75-MJM95 and 0RCA12.L46-MAL84 experiments. Landmasses are shaded gray.*

7.3   Scales of motion

After discussing the formation processes of the Somali eddies, I shall now determine the spatial scales of their turbulent motion. For the three configurations the Taylor-scale and the viscous dissipation length-scale (see section 4.6) are calculated. The scales are calculated for the upper-layer, at 100m depth using, averages over 10 years. The scales are also calculated separately for the period of the southwest Monsoon (June - August, for 10 years) and for the period of the northeast Monsoon (December - February, for 10 years) when the nSC and the sSC, respectively, are well established.

I constructed the CDFTOOLS used for this calculation, they are *cdfeddyscale_pass1.f90* and *cdfteddyscale.f90* (see appendix 12 and for more information http://www-meom.legi.grenoble-inp.fr/Web/).

In the idealized reduced gravity shallow water model the grid size of 2.5km is sufficient to resolve the viscous dissipation length-scale in the experiment with a viscosity of $300\text{m}^2\cdot\text{s}^{-1}$ and the Monsoon Winds forcing (MW300); and a viscosity of $125\text{m}^2\cdot\text{s}^{-1}$ and the Trade Winds forcing (TW125). The grid size of $\sim$10km in the ORCA12 simulation (with a bi-harmonic viscosity of $-1.25\cdot10^{10}$ $\text{m}^4\cdot\text{s}^{-1}$) is not sufficient to resolve it and the same applies for the ORCA025 simulation (grid size of $\sim$25km and a bi-harmonic viscosity of $-1.8\cdot10^{11}$ $\text{m}^4\cdot\text{s}^{-1}$). The viscous dissipation scales obtained (not shown) are comparable to the grid size and they don't reflect interesting physical information. In the following, I only discuss the Taylor-scale defined in the Eq. 4.22 by the quantity λ_1. For the reason of simplicity I call it λ in this section:

$$\lambda = \sqrt{\frac{K(t)}{Q(t)}}, \tag{7.1}$$

where

$$K(t) = \frac{1}{2}\langle \mathbf{u}^2(x,t)\rangle \tag{7.2}$$

is the averaged kinetic energy of fluid motion and

$$Q(t) = \frac{1}{2}\langle \zeta^2(x,t)\rangle \tag{7.3}$$

is the averaged enstrophy (averages are calculated over 10 years of simulation).

This length scale characterizes the size of the velocity gradients and represents the large-scale coherent structures. This scale is instructive in a turbulent environment but near the boundary its significance is limited. At the boundary $\lambda = 0$ (see Figs. 7.11 and 7.12) as energy vanishes, which does not mean that there are infinitely small scales.

7.3.1   Annual scales of motion

Fig. 7.11 shows the annual Taylor-scale λ calculated over 10 years for the three configurations. Scales over 100km are shaded white. Small Taylor-scales are seen in the vicinity
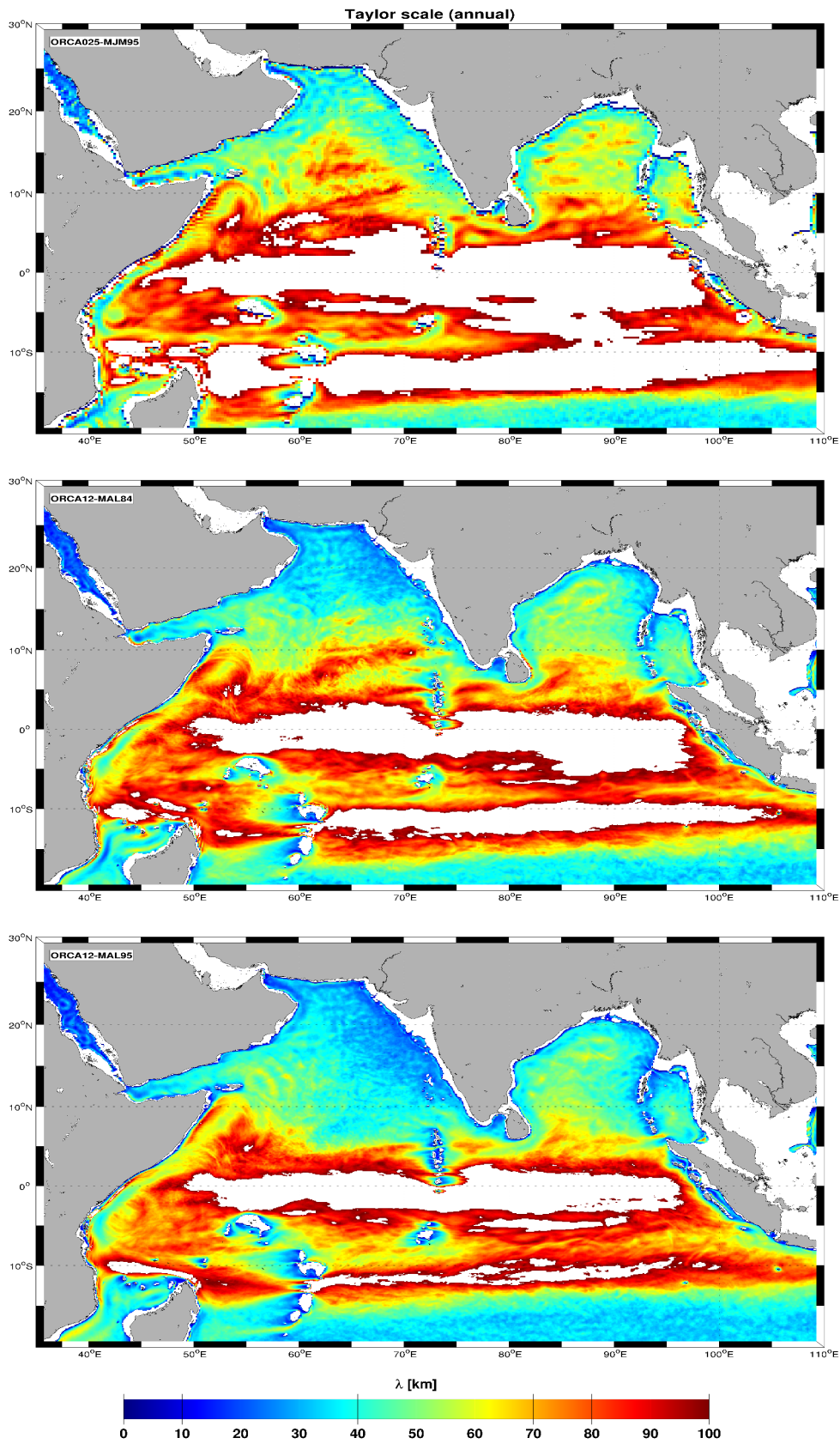
Figure 7.11 – Taylor-scale of the upper-layer (at 100m depth) calculated over 10 years for ORCA025.L75-MJM95, 0RCA12.L46-MAL84 and 0RCA12.L46-MAL95 experiments (top to bottom). Scales over 100km are shaded white, as are the islands and shallow topographic features (surrounded by small scale). Landmasses are shaded gray.

of islands and shallow topographic features. The annual Taylor scale shows roughly the same large scale patterns in all three experiments. Large scale circulations of $\lambda > 100$km (shaded white) are observed straddling the equator and between the latitudes 10 - 15ºS across the basin. The large scale circulations of $\lambda > 100$km appear to be more marked in the ORCA025 experiment (Fig. 7.11a) than in the ORCA12 (Fig. 7.11b,c) experiments. The MAL84 experiment shows larger regions with $\lambda > 100$km than MAL95 experiment. On either side of these two bands of large scale of $\lambda > 100$km, bands exist with $\lambda < 80$km.

Smaller scale circulations of $\lambda < 50$km are observed in the bay of Bengal and in the Arabian Sea. In the Bay of Bengal, the lower scale arises from the burst and dipole dynamics led by the vortex created by the EICC and the eastern boundary current in the bay. The same applies to the Arabian Sea, where the WICC and the WBC along the Oman and the Yemen coasts generate coherent structures as bursts and dipoles. According to the narrow width of the Bay of Bengal and the Bay of Arabia, the coherent structures created along the eastern and western boundaries may migrate during their evolution to the interior of the bays. These coherent structures are constrained to move within the bay, which leads to an intense turbulent circulation in the bays. In addition to that, the relative shallowness of the bays favors small scales. So intense turbulent motion added to the topographic effects are responsible to the small scales observed in the two bays.

The feeble values of $\lambda < 20$km observed around the islands are due to vortex sheets in the wake of topographic features.

Smaller scale circulations of $\lambda < 50$km are observed south of 15ºS, in the region of the SEC fed by the West Australian Current. These smaller scales come from eddies formed by the baroclinic instability of the West Australian Current which supplies this tropical zone with colder water masses from the subtropical south Indian gyre.

Along the Somali Coast, smaller scales of 50km $< \lambda < 80$km are observed. These are a signature of the sSC, the nSC and the associated eddy system namely the SG, GW and SE which create additional small scale coherent structures, namely bursts and dipoles. The relative small scales associated to the SC and the area of its extension to the interior is called as in the section 4.6 the *Somali extended boundary-layer* (SEBL hereater). The SEBL may partly overlap with the extended boundary-layer of the eastern boundary of the Arabian Sea which can be distinguished by the lower scale of $\lambda < 50$km, I called it *the Arabian extended boundary layer* (AEBL hereafter).

The analysis of the annual Taylor-scale of the boundary-layer proves to be intricated by the reversal of the SC, so it is appropriated to analyze the Taylor-scale separately for the seasons when the current has one direction, to entangle the impact of the nSC and sSC on the extended boundary. The next sub-sections focus on that.

7.3.2   Scales of motion during the southwest Monsoon

I recall that during the southwest Monsoon the SC flows northward and is called nSC. During this season the East African Coast Current (EACC) crosses the equator and flows along the Somali Coast. The Taylor-scale during the southwest Monsoon is calculated over the months of June to August (right panels of Fig. 7.12). Although the reversal of the
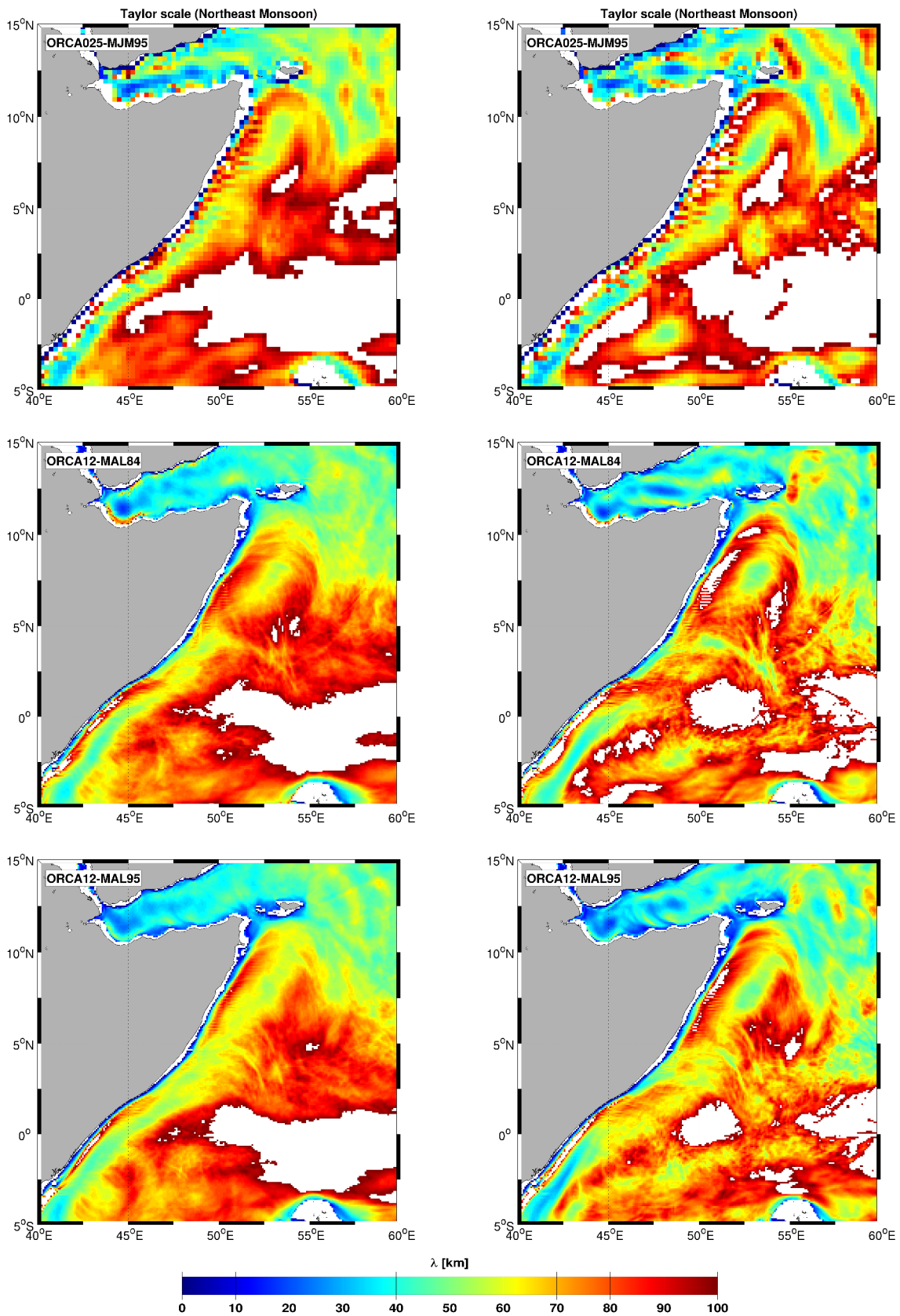
Figure 7.12 – *Taylor-scale of the upper layer (at 100m depth) calculated over 10 years for ORCA025.L75-MJM95, 0RCA12.L46-MAL84 and 0RCA12.L46-MAL95 experiments (top to bottom) during northeast Monsoon (left panels) and southwest Monsoon (right panels). Scales over 100km are shaded white, as are the islands and shallow topographic features (surrounded by small scale). Landmasses are shaded gray.*

sSC occurs before the month of June due to the arrival of the SSH high in March/April (see section 7.1). This choice is justified by the desire to calculate the average only over a period when the nSC is well established.

The Fig. 7.12 (right panels) shows the existence of relatively small scales of 40km $< \lambda <$ 70km in a 10º–15º wide band offshore, indicating that the SEBL is well developed into the Arabian Sea during this period. This band is a consequence of the detachment of turbulent features from the eddies formed along the Somali Coast throughout the Arabian sea. The appearance of this wide SEBL is caused by the intensification of the southwest Monsoon.

7.3.3 Scales of motion during the northeast Monsoon

I recall that during the northeast Monsoon the SC flows southward and is called sSC. The northeast Monsoon Taylor-scale is calculated for the months of December – February (left panels of Fig. 7.12). The interior Taylor-scales of $\lambda >$ 100km are more marked during the northeast Monsoon than during the southwest Monsoon. At about 5ºN–10ºN the signature of the cyclonic feature (previously observed by Beal et al. (2013) and identified in the model) remains in the Taylor-scale. This proves the robustness of this feature. Along the African coast, the sSC carries small scales of the same order than in the annual mean. Differently to the period of the southwest Monsoon, the band of small Taylor-scale of 40km $< \lambda <$ 70km is now not much wider than about 5º offshore. The SEBL is confined to this 5º band. Adjacent to the SEBL the scales are larger than 90km.

To summarize, during the southwest Monsoon, smaller scale features (bursts and dipoles) are created which are responsible for the creation SEBL. Both of the currents (nSC, sSC and EACC) carry small scales. The northeast Monsoon appears to be essentially responsible for the larger scale of $\lambda >$ 100km. This analysis reemphasize the unresolved small scales in the MJM95 experiment which are resolved in the MAL experiments as can be seen in the smallest SEBL in the MJM95 experiment.

Part III

Discussion and Conclusions

Chapter 8

Reduced Gravity Shallow Water Model

Contents

In the MW forcing case the boundary current crosses the equator. It is observed that the vanishing of the Coriolis parameter at the equator does not play a special direct role in the dynamics of western boundary currents. In the TW forcing case the equatorial current splits up and flows poleward in both hemispheres as a western boundary current. The importance of the equator is due to the larger latitudinal velocities (inertial effect) and the unstable wave dynamics at the equator, which increases the variability, also at the western boundary.

Without the stabilizing inertial effects, the transport of PV into the advective boundary-layer, the western boundary-layer does not exist for high Reynolds number flow. The western boundary area is rather a turbulent soup of eddies, bursts and dipoles. Its structure can only be recovered in an average sense. The turbulent dynamics leads to a split up of the boundary-layer into three layers: a viscous sub-layer, an advective boundary-layer and an extended boundary-layer. The thickness of the first and the third are, respectively, decreasing and increasing when the viscosity is decreased. The second shows no or only a weak dependence on viscosity, once it drops below values that allow for turbulent motion.

For the lower values of the viscosity, a sequence of stages in the evolution of the boundary-layer dynamics is identified: the anticyclones during their northward migration intermittently detach parts of the viscous sub-layer containing strong positive vorticity, these bursts pair with negative vorticity from within the anticyclones and form dipoles which then travel ballisticaly (at almost constant velocity) over distances up to several eddy diameters. Or then return boundary-ward, to collide with the boundary current, perturb it and sucked up by the boundary current or an another anticyclone.

When a flat boundary is used, the thickness of the Munk-layer goes to zero with viscosity. A rough boundary introduces a lower bound for the thickness of the boundary. Calculations with extensions of the Munk-layer smaller than the roughness of the boundary can be mathematically interesting but might not be useful to learn about the ocean dynamics.

8.1   Concerning numerical simulation of turbulent boundary-layers

It is the thickness of the viscous sub-layer that imposes the spatial resolution of a numerical model. The thickness of the turbulent viscous boundary-layer decreases faster with decreasing viscosity than the prominent $\frac{1}{3}$ scaling from Munk-theory in all the experiments performed and at all latitudes considered. The laminar Munk-layer theory is however used to determine the (hyper) viscosity for a given spatial resolution in todays simulations of the ocean dynamics. The here present results prove, that for the turbulent boundary-layer the thus obtained resolution is far from being sufficient.

The lower values for the viscous sub-layer in the MW calculations as compared to the TW calculations, for the same viscosity, explain also the result that simulations of the MW calculations were only possible down to $\nu = 300\text{m}^2\cdot\text{s}^{-1}$ while the simulations with the TW-forcing converged down to $\nu = 125\text{m}^2\cdot\text{s}^{-1}$.

From Fig. 4.25 it is clear that the gap between the thickness of the extended boundary-layer and the viscous boundary-layer widens with increasing Reynolds number. The gap is a measure of the complexity of the numerical calculations as the finest scale δ_ν has to be resolved throughout δ_{ext} in both horizontal directions. This shows that grid refinement near the boundary has no place in simulations of the turbulent boundary-layer as: (i) the structures are isotropic and (ii) the small scales extend far from the boundary. The ratio of $N = (\delta_{\text{ext}}/\delta_\nu)^2$ can be taken as a measure for the involved degrees of freedom in the calculations. Estimations based on the results in Tab. 4.3 clearly show a strongly increase with the Reynolds number, $N \propto Re^{2.4}$ in the low latitude MW forcing and up to $N \propto Re^{2.9}$ for the high latitude TW-forcing.

8.2   Concerning the parameterization of turbulent boundary-layers

In numerical simulations of the boundary-layer dynamics one can either simulate the turbulent dynamics or parameterize it.

One of the major challenges in the numerical simulation of the ocean dynamics is to parameterize the effect of the small scale dynamics not explicitly resolved on the explicitly resolved large scale flow.

Inertial theory and above presented results teach us that small westward velocities can stabilize the western boundary-layer. Velocity components in other directions have no such effect. A parameterization of the turbulence must therefore reflect this anisotropy. The instability of the boundary-layer is also strongly dependent of details of the velocity profile as noted by Ierley & Young (1991). Topographic features are also likely to play an important role in the stability and turbulent fluxes.

The determination of the eddy viscosity in section 4.11 is not a parameterization as the eddy viscosity is not obtained from large-scale properties of the flow, but from fine resolution simulations. These show that for the lowest viscosities δ_V saturates at a value corresponding to $\nu \approx 6000\text{m}^2{\cdot}\text{s}^{-1}$. Choosing viscosity values lower than $\nu \approx 6000\text{m}^2{\cdot}\text{s}^{-1}$ but above the threshold for fully turbulent boundary-layers $\nu \approx 300\text{m}^2{\cdot}\text{s}^{-1}$ leads to an irealistically thin average boundary-layer thickness, worsening the representation of the advective boundary-layer dynamics. In numerical simulations of the boundary-layer dynamics one can either simulate the turbulent dynamics or parameterize it. The findings discussed above suggest that one either uses fine resolutions and viscosities below $\nu \approx 300\text{m}^2{\cdot}\text{s}^{-1}$ or parameterizes it and uses larger viscosities $\nu \approx 6000\text{m}^2{\cdot}\text{s}^{-1}$.

Please not that the discussion did not focus on the more involved behavior of hyper dissipation operators (hyper-viscosity, powers of the Laplacian), which ask for boundary conditions for derivatives of the velocity field and which lead towards thermalization at small scales of the turbulent dynamics as explained by Frisch et al. (2008).

Chapter 9

Application to Somali Current via NEMO (Drakkar)

Contents

In the second part of the thesis, the NEMO model in the Drakkar configurations has been used. Three experiments ORCA025.L75-MJM95, 0RCA12.L46-MAL84 and 0RCA12.L46-MAL95 forced by different synoptic atmospheric data with different boundary conditions have been analyzed to get a better understanding of the monsoon circulation in the Indian Ocean, with a particular attention given to the Arabian Sea and its complex WBCs system.

9.1   Concerning the upper-layer circulation of the Arabian Sea

In this investigation, I presented model interpretations of the monsoon-related upper-layer circulations in the Indian Ocean with particular attention to the Arabian Sea. This particular attention is due firstly, because the dynamics of low latitude turbulent western boundary currents are the crux of my thesis (namely the Somali Current) and secondly because of the lack of observation, realistic models are a way to gain understanding of the ocean circulation. Indeed for the last ten or fifteen years, piracy has prevented ship measurements, but satellite and drifter data have come to maturity and have provided a robust seasonally evolving surface circulation as described in recent studies by Beal et al. (2013), which go beyond the static schematics of the Indian Ocean circulations previously drawn by Schott & McCreary Jr (2001). Both studies allow to converge to the seasonally evolving surface circulation described in section 5.3 for the Arabian Sea and in section 5.4 for the Indian Ocean WBCs.

The general circulation patterns of the three numerical experiments are consistent with observations described in sections 5.3 and 5.4. All currents and larger mesoscale features (diameter exceeding 100km) in the model domain have been well simulated in the three experiments for the both monsoon periods and appear in the right position at the right time. The model has skills in the way it reproduces the Monsoon driven ocean circulation characteristics, the reversal of currents, the interconnected currents, the smaller sub-grid structures in the observations (the observation data set has a half-degree resolution), and therefore the ability to entangle the dynamics of the effect of the annual Rossby wave and the eddy formation processes.

However some discrepancies exist between the model solutions and the observations as the latitudinal location of the SECC is shifted northward in the experiments. Another discrepancy resides in the reversal of the Oman and Yemen coastal flow which flows southward during the northeast Monsoon, shuts down in March for MJM95 experiment and in February for the MAL84/MAL95 experiments to flow northward the rest of the year whereas the recent observation analysis by Beal et al. (2013) doesn't carry this fact but suggests northward geostrophic flow year-round. However in their Fig. 3, the largest error in formal error speeds occur in the areas (west and along the equator) where reside the discordances between the experiments and the observation. Adding to that, Beal et al. (2013) observed hints of quasi-stationary cyclones and an inshore counter-current during the northeast monsoon, but their data resolution is insufficient at these latitudes to

confirm this. The present experiments confirm the reverse of the Yemen and Oman coastal current which flows northward in March/April, coinciding with the arrival and reflection of the Rossby waves at the western boundary (see Fig. 7.1, Fig. 7.2 and Fig. 7.3). This finding suggest that the annual Rossby waves have the reversal effect not only on the SC but also on the Yemen and Oman coastal current. Most of the differences in the validation between the observations and the experiments reflect the fact that the observational data set has a half-degree resolution while the model describes fine scale variations that are not present in the observations. Again, this general comparison of the observations and the three experiments permits to validate the general circulation of the three experiments and exposes small scale dynamics which are not seen in the observation.

In the later phase of the southwest Monsoon the distinction between the EACC and the nSC as suggest Beal et al. (2013) prove to be delicate because the two currents are merged.

9.2   Concerning the effect of annual Rossby waves

North of about the 4°N, during March/April 1979, Leetmaa et al. (1982) reported in the ship-drift observations that the SC was flowing northward (so called nSC) against the northeast monsoon which has weakened considerably during this period. Moreover, a similar nSC also developed in the Anderson et al. (1991) and McCreary et al. (1993) model solutions. Quadfasel & Schott (1983) suggested that the observed nSC was forced by local wind curl. However McCreary et al. (1993) suggested that remote forcing from the previous southwest Monsoon is an important driving mechanism of this early flowing nSC. Recent studies by Beal et al. (2013) attribute the initiation of the nSC to the arrival of the annual Rossby waves (associated with an anticyclonic circulation) at the Somali Coast where the energy is transfered to a northward boundary flow. Precursors of the nSC and a weak early GW appears. This is corroborated by the present experiments which demonstrate without doubt during 10 years of integration that the Rossby waves arrival at the boundary plays the dominant role in the forcing of the initiation of the early nSC precursor of the GW in March/April. The forcing originates during the previous southwest Monsoon, when a strong, negative wind stress curl (over the northern Arabian Sea) triggers a chain of planetary waves which feed back on the initiating region after about 300 days. As said in sub-section 7.1.2, this process begins with a westward, downwelling Rossby wave from the wind curl region to the Somali Coast, continues with coastal then equatorial Kelvin waves, and concludes with the propagation of Kelvin wave around the rim of the Bay of Bengal [Subrahmanyam et al. (2001); Shankar & Shetye (1997)] which radiates Rossby waves back into the Arabian Sea from the southern tip of India. The process carried on in a time scale of approximately 290 days, corroborated thus the predicted time scale of approximately 300 days by Shetye (1998). Beal et al. (2013) ask questions concerning predictability and feedbacks: "would the southwest Monsoon circulation look the same without the planetary wave feedback mechanism? It is possible that an ocean pathway exists through which one Monsoon can precondition the next? " The longitude-time section at 7°/7°30N (R_2) and

latitude/longitude-time sections (R_1K_1) of the SSH help to identity the rapid change in surface slope caused by the eastward propagating equatorial Kelvin waves (downwelling and upwelling), followed by the westward Rossby waves in the Arabian Sea. The semi-annual Kelvin waves are found to be propagating in April – May and October – November every year with considerable inter-annual variability. The Kelvin wave components were found to be strong along the equator. Strong annual Rossby waves centered at about 7º/7º30N are found to be precursor of the formation of the early GW in the Somali Coast.

9.3 Concerning the formation process of the Somali eddies

Previous efforts to understand the SC and the EACC retroflection have focused primarily on the large-scale dynamics governing the seasonal establishment rather than local Somali eddies processes. The SC eddies described herein appear to be quite similar in structure and behavior to eddies shed by low latitude WBCs elsewhere in the global ocean, even though they are among the lowest latitude and most topographically constrained eddies. For example, the generation mechanism and ultimate structure of the Somali eddies appears most similar to anticyclonic eddies formed in the western tropical Atlantic by the retroflecting NBC [see *e.g.* Johns et al. (1990); Barnier et al. (2001)]. Although the basic formation mechanism and physical characteristics of these low-latitude eddies are similar, their interactions with the general circulation and regional topography differ substantially. A weak basin-wide anticyclonic circulation associated to the Rossby wave, reaches the Somali Coast, a northward boundary flow is created, an early GW occurs in March/April, two months before the onset of the southwest Monsoon Winds. The intensification of the southwest Monsoon Winds in June, strengthens the early GW, prompts the equatorial overshoot of the EACC which retroflects to form the SG. In July/August the SG migrates northward to collide with the early GW. The outcome of this collision is twofold. The SG takes the place of the GW and becomes a new GW. The early GW, may translate through the Socotra Passage or be relocated east of the Socotra Island to form the SE. In a different scenario the SG may sometimes collapse with the early or the fully developed GW. These various scenarios are observed in the formation processes of the Somali eddies as described in the sub-section 7.2.1.

The model solutions pointed out a feature that was not pointed out by observations, the elastic collision between the SG and the GW to form a new GW and the SE, thus proposing a consistent mechanism for the formation process of the SE.

Strong spatially localized and temporally intermittent ejections of fluid with positive vorticity are observed, moving away from the boundary, initiated by the large anticyclonic eddies, called "burst". Bursts appear to have a dominant role in the mixing of the upwelled-water of the cold wedges through their interaction with the large coherent anticyclonic eddies, and their offshore drift (several eddy diameter away from the coast).

Detachments of bursts have speeds greater than $1\mathrm{m}{\cdot}\mathrm{s}^{-1}$. Bursts with positive vorticity

(negative vorticity) are also observed along the Yemen and Oman Coasts created by relative small anticyclonic (cyclonic) eddies when the current flows northward (southward). Most frequently, bursts with negative vorticity are observed for southward flowing Yemen and Oman coastal currents. The bursts created along the Yemen and Oman coast, travel ballistically offshore to the interior of the Arabian Sea and produce an offshore mixing of upwelled water masses.

It is noteworthy to mention that during some years a fleeting retroflection of the sSC is observed south of the equator, showing a signature of bursts with negative vorticity. This small eddy created by this burst is still cyclonic in the southern hemisphere.

The analysis of 10-years of model solutions show strong interannual variability of the intra-seasonal fluctuations, which are possibly related to the Somali eddy dynamics and in particular to their motion, their intermittent detachment of positive vorticity (bursts), their collapse or collision. A numerical study showed that besides the external forcing, the chaotic nature of the ocean dynamics contribute substantially to the interannual variability in the southwestern Arabian Sea [Wirth et al. (2002)].

Chapter 10

Synergies and Future Directions of Research

Contents

10.1 Some synergies between the idealized and the Realistic model used

The understanding of the dynamics of the low latitude turbulent western boundary currents through a fine resolution (2.5km) idealized reduced gravity shallow water model (RGSWM) and the application of the findings to 10-year realistic ocean general circulation model (OGCM) simulations of the Indian Ocean (with focus on the Arabian Sea and the Somali Current) brought out several synergies between the two types of simulation. they can be summarized as follows.

Non-importance of the equator

– **RGSWM**
  The retroflection of the WBC and the formation of eddy are not due to the *inertial overshoot* [mechanism proposed by Anderson & Moore (1979); Knox & Anderson (1985) and other authors], of the equator by the current but only due to the vorticity dynamics.

– **OGCM**
  The non-importance is confirmed in March/April when sSC and the early northward flowing nSC coexist. Although the early nSC does not originate from the southern hemisphere, it retroflects to form a weak early GW (*e.g.* the retroflection of the Yemen and Oman current).

Inertial effect

– **RGSWM**
  Small westward zonal velocities can stabilize the western boundary-layer, velocity component in other direction have no such effect.

– **OGCM**
  The inertial effect is discernible in the way that after reaching the Somali Coast at around 10ºS, the EACC overshoots several latitudes before it retroflects at the equator. This points out that a parameterization of turbulence must therefore reflect this anisotropy in the velocity component.

Retroflection and bursts

– **RGSWM**
  The large anticyclonic eddies shed in an idealized context have no constraint and can migrate northward with chaotic creation of bursts and dipoles which interact with the large anticyclonic eddies.

– **OGCM**
  The larger anticyclonic eddies are topographically constrained reducing their along-shore displacement. In spite of this their bursts and the further smaller cyclonic eddies reveal the chaotic aspect in which the SG and the GW may exchange water when they are very close before interacting with each other by coalescence or collision.

The burst dynamics discovered in the idealized simulations, and identified in the realistic simulations appear without any doubt vital for the fine scale processes as mixing and offshore transport of upwelled water-masses which are especially important for the biogeochemistry modelling and could also be relevant for coupled models. This asks for high spatial and time resolutions to resolve the burst dynamics.

10.2   Future directions of research

Clearly, many avenues remain to be explored for the continuation of the work started in this thesis.

Further investigation of Socotra Eddy formation

Nowadays the formation mechanism of the Socotra Eddy is still unresolved. The elastic collision between the SG and the GW found in the model solutions seem evident but needs dedicated high spacial and temporal resolution satellite measurements for confirmation. These measurements could also clarify the coalescence versus collision between the SG and the GW on one hand and the coalescence of the two cold wedges without coalescence of the two eddies on other hand.

After the collision of the SG and the GW, the reduction of the size may be caused by an erosion due to the Socotra Island, similar to the interaction between an eddy and a seamount as described Herbette et al. (2003, 2005) in idealized simulations. The authors found that the erosion by a seamount often results in a sub-division of the eddy, while the eroded original structure forms a dipole with the deep part of the eddy and is advected away. The filaments torn off from the original core aggregate into a new eddy above the seamount. Assuming that the size reduction of SE is due to this type of erosion, this suggests another mixing mechanism of upwelled water jailed in the SE and so deserves further study.

Bursts versus Open-ocean upwelling

The dynamical mixing of upwelled waters by the bursts may question the hypothesis of an open-ocean upwelling in the Arabian Sea, as proposed by Rixen et al. (2000). In their study of the role of coastal and open-ocean upwelling on the sedimentation in the western Arabian Sea, these authors suggest that the carbon fluxes are mainly governed

by the bloom due to the rapid onset of open-ocean upwelling in May/June. Indeed in their calculation the average velocity of around 0.6m·s^{-1} could transfer diatoms within two weeks from the coast to their sediment trap location in the western Arabian Sea, a time sufficient for the development of a diatom bloom [Brockmann et al. (1983); Goldman (1993)]. However in May/June the Somali eddies (except the SE) and the Yemen and Oman coastal eddies are fully developed; their bursts speed which is greater than 1m·s^{-1} could transfer diatoms within $\sim$ one week from the coast to their sediment trap location. This suggests that the carbon fluxes measured, may be due to coastal upwelled water-masses injected into the interior of the Arabian Sea by the burst dynamics.

Bursts, remote sensing?

It is tempting to explore the burst process via dedicated high spacial and temporal resolution satellite measurements because their evidence in numerical simulation is ubiquitous. Of course, such measurement could be possible in the future with the wide swath interferometric altimeter (SWOT[1] satellite), which will allow a fine resolution observation of sea level gradients over a swath of several tens of kilometers. But it is imperative to have more information about these fine scale processes. It is an interesting area and a revolution in the forecasting of biogeochemistry.

---

1. Surface Water and Ocean Topography

Bibliography

Anderson, D., Carrington, D., Corry, R., & Gordon, C. (1991). Modeling the variability of the somali current. Journal of marine research, 49(4), 659–696.

Anderson, D. L. T., & Moore, D. W. (1979). Cross-equatorial inertial jets with special relevance to very remote forcing of the somali current. Deep Sea Research, 26, 1–22.

Arnéodo, A., Benzi, R., Berg, J., Biferale, L., Bodenschatz, E., Busse, A., Calzavarini, E., Castaing, B., Cencini, M., Chevillard, L., et al. (2008). Universal intermittent properties of particle trajectories in highly turbulent flows. Physical review letters, 100(25), 254504.

Asselin, R. (1972). Frequency filter for time integrations. Monthly Weather Review, 100(6), 487–490.

Aumont, O., & Bopp, L. (2006). Globalizing results from ocean in situ iron fertilization studies. Global Biogeochemical Cycles, 20(2).

Barnier, B., Dussin, R., & Molines, J. (2011). Scientific validation report (scvr) for v1 reprocessed analysis and reanalysis: Glorys2v1. Tech. rep., MyOcean FP7-SPACE-2007-1 project, report MYO-WP04-ScCV-rea-CNRS Rep.

Barnier, B., Madec, G., Penduff, T., Molines, J.-M., Treguier, A.-M., Le Sommer, J., Beckmann, A., Biastoch, A., Böning, C., Dengg, J., et al. (2006). Impact of partial steps and momentum advection schemes in a global ocean circulation model at eddy-permitting resolution. Ocean Dynamics, 56(5-6), 543–567.

Barnier, B., Reynaud, T., Beckmann, A., Böning, C., Molines, J.-M., Barnard, S., & Jia, Y. (2001). On the seasonal variability and eddies in the north brazil current: insights from model intercomparison experiments. Progress in Oceanography, 48(2), 195–230.

Beal, L., & Donohue, K. (2013). The great whirl: Observations of its seasonal development and interannual variability. Journal of Geophysical Research: Oceans.

Beal, L., Hormann, V., Lumpkin, R., & Foltz, G. (2013). The response of the surface circulation of the arabian sea to monsoonal forcing. Journal of Physical Oceanography, 43(9), 2008–2022.

149

Beckmann, A., & Döscher, R. (1997). A method for improved representation of dense water spreading over topography in geopotential-coordinate models. Journal of Physical Oceanography, 27(4), 581–591.

Blanke, B., & Delecluse, P. (1993). Variability of the tropical atlantic ocean simulated by a general circulation model with two different mixed-layer physics. Journal of Physical Oceanography, 23(7), 1363–1388.

Boffetta, G., & Ecke, R. E. (2012). Two-dimensional turbulence. Annual Review of Fluid Mechanics, 44, 427–451.

Brandt, P., Stramma, L., Schott, F., Fischer, J., Dengler, M., & Quadfasel, D. (2002). Annual rossby waves in the arabian sea from topex/poseidon altimeter and in situ data. Deep Sea Research Part II: Topical Studies in Oceanography, 49(7), 1197–1210.

Brockmann, U., Ittekkot, V., Kattner, G., Eberlein, K., & Hammer, K. (1983). Release of dissolved organic substances in the course of phytoplankton blooms. In North Sea Dynamics, (pp. 530–548). Springer.

Bruce, J., Fieux, M., & Gonella, J. (1981). A note on the continuance of the somali eddy after the cessation of the southwest monsoon. Oceanologica Acta, 4(1), 7–9.

Bruce, J. G., Johnson, D. R., & Kindle, J. C. (1994). Evidence for eddy formation in the eastern arabian sea during the northeast monsoon. Journal of Geophysical Research, 99(C4), 7651–7664.

Cane, M. A., & Gent, P. R. (1984). Reflection of low-frequency equatorial waves at arbitrary western boundaries. Journal of Marine Research, 42(3), 487–502.

Charney, J. G. (1955). The gulf stream as an inertial boundary layer. Proceedings of the National Academy of Sciences of the United States of America, 41(10), 731.

Courant, R., Friedrichs, K., & Lewy, H. (1967). On the partial difference equations of mathematical physics. IBM journal of Research and Development, 11(2), 215–234.

Cox, M. (1981). A numerical study of surface cooling processes during summer in the arabian sea. Monsoon dynamics, (pp. 529–540).

Cox, M. D. (1979). A numerical study of somali current eddies. Journal of Physical Oceanography, 9(2), 311–326.

Cutler, A., & Swallow, J. (1984). Surface currents of the Indian Ocean (to 25 S, 100 E): Compiled from historical data archived by the Meteorological Office, Bracknell, UK. Institute of Oceanographic Sciences.

Deardorff, J. (1966). The counter-gradient heat flux in the lower atmosphere and in the laboratory. Journal of the Atmospheric Sciences, 23(5), 503–506.

Edwards, C. A., & Pedlosky, J. (1998a). Dynamics of nonlinear cross-equatorial flow. part i: Potential vorticity transformation. Journal of physical oceanography, 28(12), 2382–2406.

Edwards, C. A., & Pedlosky, J. (1998b). Dynamics of nonlinear cross-equatorial flow. part ii: The tropically enhanced instability of the western boundary current. Journal of physical oceanography, 28(12), 2407–2417.

Ertel, H. (1942). Der vertikale turbulenz-wärmestrom in der atmosphäre. Meteor. Z, 59, 250–253.

Evans, R. H., & Brown, O. B. (1981). Propagation of thermal fronts in the somali current system. Deep Sea Research Part A. Oceanographic Research Papers, 28(5), 521–527.

Fichefet, T., & Maqueda, M. M. (1997). Sensitivity of a global sea ice model to the treatment of ice thermodynamics and dynamics. Journal of Geophysical Research, 102(C6), 12609–12.

Fieux, M., & Stommel, H. (1977). Onset of the southwest monsoon over the arabian sea from marine reports of surface winds: structure and variability. Monthly Weather Review, 105(2), 231–236.

Findlater, J. (1971). Mean monthly airflow at low levels over the western Indian Ocean. HM Stationery Office.

Fischer, J., Schott, F., & Stramma, L. (1996). Currents and transports of the great whirl-socotra gyre system during the summer monsoon, august 1993. Journal of Geophysical Research, 101(C2), 3573–3587.

Flament, P. (2002). A state variable for characterizing water masses and their diffusive stability: spiciness. Progress in Oceanography, 54(1), 493–501.

Fox-Kemper, B., & Pedlosky, J. (2004). Wind-driven barotropic gyre i: Circulation control by eddy vorticity fluxes to an enhanced removal region. Journal of Marine Research, 62(2), 169–193.

Fratantoni, D. M., Bower, A. S., Johns, W. E., & Peters, H. (2006). Somali current rings in the eastern gulf of aden. Journal of Geophysical Research: Oceans (1978–2012), 111(C9).

Frisch, U. (1995). Turbulence: the legacy ofa. n. kolmogorov.

Frisch, U., Kurien, S., Pandit, R., Pauls, W., Ray, S. S., Wirth, A., & Zhu, J.-Z. (2008). Hyperviscosity, galerkin truncation, and bottlenecks in turbulence. Physical review letters, 101(14), 144501.

Goldman, J. C. (1993). Potential role of large oceanic diatoms in new primary production. Deep Sea Research Part I: Oceanographic Research Papers, 40(1), 159–168.

Herbette, S., Morel, Y., & Arhan, M. (2003). Erosion of a surface vortex by a seamount. Journal of Physical Oceanography, 33(8), 1664–1679.

Herbette, S., Morel, Y., & Arhan, M. (2005). Erosion of a surface vortex by a seamount on the β plane. Journal of physical oceanography, 35(11), 2012–2030.

Hervieux, G. (2007). Etude numerique des interactions courant/topographie: application au gyre subpolaire, aux seuils de Gibraltar et des mers Nordiques.. Ph.D. thesis, Université Joseph-Fourier-Grenoble I.

Hurlburt, H., & Thompson, J. D. (1976). A numerical model of the somali current. Journal of Physical Oceanography, 6(5), 646–664.

Ierley, G., & Young, W. (1991). Viscous instabilities in the western boundary layer. Journal of physical oceanography, 21(9), 1323–1332.

Jiang, S., Jin, F.-F., & Ghil, M. (1995). Multiple equilibria, periodic, and aperiodic solutions in a wind-driven, double-gyre, shallow-water model. Journal of physical oceanography, 25(5), 764–786.

Johns, W. E., Lee, T. N., Schott, F. A., Zantopp, R. J., & Evans, R. H. (1990). The north brazil current retroflection: Seasonal structure and eddy variability. Journal of Geophysical Research: Oceans (1978–2012), 95(C12), 22103–22120.

Kawamiya, M., & Oschlies, A. (2003). An eddy-permitting, coupled ecosystem-circulation model of the arabian sea: comparison with observations. Journal of Marine Systems, 38(3), 221–257.

Klein, P., Lapeyre, G., Roullet, G., Le Gentil, S., & Sasaki, H. (2011). Ocean turbulence at meso and submesoscales: connection between surface and interior dynamics. Geophysical & Astrophysical Fluid Dynamics, 105(4-5), 421–437.

Knox, R., & Anderson, D. (1985). Recent advances in the study of the low-latitude ocean circulation. Progress in oceanography, 14, 259–317.

Lecointre, A., Molines, J.-M., & Barnier, B. (2011a). Definition of the interannual experiment orca12. l46-mal95, 1989-2007.

Lecointre, A., Molines, J.-M., & Barnier, B. (2011b). Definition of the interannual experiments orca12.l75-mal83 (1978-1982) and orca12.l46-mal83/84/85 (1978-1982 and 1978-1992).

Lee, M.-M., Coward, A. C., & Nurser, A. G. (2002). Spurious diapycnal mixing of the deep waters in an eddy-permitting global ocean model. Journal of physical oceanography, 32(5), 1522–1535.

Leetmaa, A., Quadfasel, D., & Wilson, D. (1982). Development of the flow field during the onset of the somali current, 1979. J. Phys. Oceanogr.;(United States), 12(12).

Lichter, S., Flór, J., & van Heijst, G. (1992). Modelling the separation and eddy formation of coastal currents in a stratified tank. Experiments in fluids, 13(1), 11–16.

Lighthill, M. J. (1969). Dynamic response of the indian ocean to onset of the southwest monsoon. Philosophical Transactions for the Royal Society of London. Series A, Mathematical and Physical Sciences, (pp. 45–92).

Lin, L., & Hurlburt, H. (1981). Maximum simplification of nonlinear somali current dynamics. Monsoon dynamics, (pp. 541–555).

Luther, M. E., & O'Brien, J. J. (1985). A model of the seasonal circulation in the arabian sea forced by observed winds. Progress in Oceanography, 14, 353–385.

Madden, R. A., & Julian, P. R. (1972). Description of global-scale circulation cells in the tropics with a 40-50 day period. Journal of the Atmospheric Sciences, 29(6), 1109–1123.

Madec, G. (2008). Nemo ocean engine.

McCreary, J. P., & Kundu, P. K. (1988). A numerical investigation of the somali current during the southwest monsoon. Journal of marine research, 46(1), 25–58.

McCreary, J. P., Kundu, P. K., & Molinari, R. L. (1993). A numerical investigation of dynamics, thermodynamics and mixed-layer processes in the indian ocean. Progress in Oceanography, 31(3), 181–244.

Mesinger, F., Arakawa, A., & Kasahara, A. (1976). Numerical methods used in atmospheric models, vol. 1. World Meteorological Organization, International Council of Scientific Unions.

Molinari, R. L., Olson, D., & Reverdin, G. (1990). Surface current distributions in the tropical indian ocean derived from compilations of surface buoy trajectories. Journal of Geophysical Research: Oceans (1978–2012), 95(C5), 7217–7238.

Morel, Y., & McWilliams, J. (1997). Evolution of isolated interior vortices in the ocean. Journal of physical oceanography, 27(5), 727–748.

Morgan, G. (1956). On the wind-driven ocean circulation1. Tellus, 8(3), 301–320.

Munk, W. H. (1950). On the wind-driven ocean circulation. Journal of Meteorology, 7(2), 80–93.

Nof, D., & Pichevin, T. (1996). The retroflection paradox. Journal of physical oceanography, 26(11), 2344–2358.

Nof, D., & Pichevin, T. (1999). The establishment of the tsugaru and the alboran gyres. Journal of physical oceanography, 29(1), 39–54.

Nof, D., Van Gorder, S., & Pichevin, T. (2004). A different outflow length scale? Journal of physical oceanography, 34(4), 793–804.

Pedlosky, J. (1979). Geophysical fluid. Dynamics, Springer, New York, 21, 502–15.

Pedlosky, J. (1987). Geophysical fluid dynamics.

Philander, S., & Delecluse, P. (1983). Coastal currents in low latitudes (with application to the somali and el nino currents). Deep Sea Research Part A. Oceanographic Research Papers, 30(8), 887–902.

Philander, S., & Pacanowski, R. (1981). The oceanic response to cross-equatorial winds (with application to coastal upwelling in low latitudes). Tellus, 33(2), 201–210.

Pichevin, T., & Nof, D. (1996). The eddy cannon. Deep Sea Research Part I: Oceanographic Research Papers, 43(9), 1475–1507.

Pichevin, T., & Nof, D. (1997). The momentum imbalance paradox. Tellus A, 49(2), 298–319.

Pichevin, T., Nof, D., & Lutjeharms, J. (1999). Why are there agulhas rings? Journal of physical oceanography, 29(4), 693–707.

Prandtl, L. (1925). Bericht über untersuchungen zur ausgebildeten turbulenz. Z. Angew. Math. Mech, 5(2), 136–139.

Prandtl, L. (1944). Über flüssigkeitsbewegung bei sehr kleiner reibung (heidelberg, 1904). Vier Abhandlungen zur Hydrodynamik und Aerodynamik, Göttingen.

Quadfasel, D. R., & Schott, F. (1983). Southward subsurface flow below the somali current. Journal of Geophysical Research: Oceans (1978–2012), 88(C10), 5973–5979.

Rao, R., Kumar, G., Ravichandran, M., Rao, A., Gopalakrishna, V., & Thadathil, P. (2010). Interannual variability of kelvin wave propagation in the wave guides of the equatorial indian ocean, the coastal bay of bengal and the southeastern arabian sea during 1993–2006. Deep Sea Research Part I: Oceanographic Research Papers, 57(1), 1–13.

Rao, R. R., Molinari, R. L., & Festa, J. F. (1989). Evolution of the climatological near-surface thermal structure of the tropical indian ocean: 1. description of mean monthly mixed layer depth, and sea surface temperature, surface current, and surface meteorological fields. Journal of Geophysical Research: Oceans (1978–2012), 94(C8), 10801–10815.

Richardson, P., Hufford, G., Limeburner, R., & Brown, W. (1994). North brazil current retroflection eddies. Journal of Geophysical Research: Oceans (1978–2012), 99(C3), 5081–5093.

Rixen, T., Haake, B., & Ittekkot, V. (2000). Sedimentation in the western arabian sea the role of coastal and open-ocean upwelling. Deep Sea Research Part II: Topical Studies in Oceanography, 47(9), 2155–2178.

Robinson, S. K. (1991). Coherent motions in the turbulent boundary layer. Annual Review of Fluid Mechanics, 23(1), 601–639.

Roullet, G., & Madec, G. (2000). Salt conservation, free surface, and varying levels: a new formulation for ocean general circulation models. Journal of Geophysical Research: Oceans (1978–2012), 105(C10), 23927–23942.

Schlichting, H., & Gersten, K. (2000). Boundary-layer theory. Springer.

Schott, F. (1983). Monsoon response of the somali current and associated upwelling. Progress in Oceanography, 12(3), 357–381.

Schott, F., Fischer, J., Garternicht, U., & Quadfasel, D. (1997). Summer monsoon response of the northern somali current, 1995. Geophysical Research Letters, 24(21), 2565–2568.

Schott, F., & McCreary Jr, J. P. (2001). The monsoon circulation of the indian ocean. Progress in Oceanography, 51(1), 1–123.

Schott, F., & Quadfasel, D. (1982). Variability of the somali current and associated upwelling. Progress in Oceanography, 12, 357–381.

Schott, F., Swallow, J. C., & Fieux, M. (1990). The somali current at the equator: annual cycle of currents and transports in the upper 1000 m and connection to neighbouring latitudes. Deep Sea Research Part A. Oceanographic Research Papers, 37(12), 1825–1848.

Shankar, D., & Shetye, S. (1997). On the dynamics of the lakshadweep high and low in the southeastern arabian sea. Journal of Geophysical Research, 102(C6), 12551–12.

Shenoi, S., Saji, P., & Almeida, A. (1999). Near-surface circulation and kinetic energy in the tropical indian ocean derived from lagrangian drifters. Journal of Marine Research, 57(6), 885–907.

Shetye, S. R. (1998). West india coastal current and lakshadweep high/low. Sadhana, 23(5-6), 637–651.

Smagorinsky, J. (1993). Some historical remarks on the use of nonlinear viscosities. Large eddy simulation of complex engineering and geophysical flows, 1, 69–106.

Stern, M. E., & Whitehead, J. (1990). Separation of a boundary jet in a rotating fluid. Journal of Fluid Mechanics, 217(1), 41–69.

Stommel, H. (1948). The westward intensification of wind-driven ocean currents. Trans. Amer. Geophys. Union, 29(2), 202–206.

Subrahmanyam, B., Robinson, I., Blundell, J., & Challenor, P. (2001). Indian ocean rossby waves observed in topex/poseidon altimeter data and in model simulations. International Journal of Remote Sensing, 22(1), 141–167.

Sverdrup, H. U. (1947). Wind-driven currents in a baroclinic ocean; with application to the equatorial currents of the eastern pacific. Proceedings of the National Academy of Sciences of the United States of America, 33(11), 318.

Swallow, J., Fieux, M., & Schott, F. (1988). The boundary currents east and north of madagascar: 1. geostrophic currents and transports. Journal of Geophysical Research: Oceans (1978–2012), 93(C5), 4951–4962.

Swallow, J. C., & Bruce, J. (1966). Current measurements off the somali coast during the southwest monsoon of 1964. In Deep Sea Research and Oceanographic Abstracts, vol. 13, (pp. 861–888). Elsevier.

Swallow, J. C., Molinari, R. L., Bruce, J. G., Brown, O. B., & Evans, R. H. (1983). Development of near-surface flow pattern and water mass distribution in the somali basin in response to the southwest monsoon of 1979. Journal of Physical Oceanography, 13(8), 1398–1415.

Thierry, V., & Morel, Y. (1999). Influence of a strong bottom slope on the evolution of a surface-intensified vortex. Journal of physical oceanography, 29(5), 911–924.

Vallis, G. K. (2006). Atmospheric and oceanic fluid dynamics: fundamentals and large-scale circulation. Cambridge University Press.

Van Leeuwen, P. J., & de Ruijter, W. P. (2009). On the steadiness of separating meandering currents. Journal of physical oceanography, 39(2), 437–448.

Vandermeirsch, F., Morel, Y., & Sutyrin, G. (2001). The net advective effect of a vertically sheared current on a coherent vortex. Journal of physical oceanography, 31(8), 2210–2225.

Visbeck, M., & Schott, F. (1992). Analysis of seasonal current variations in the western equatorial indian ocean: Direct measurements and gfdl model comparison. Journal of physical oceanography, 22(10), 1112–1128.

Winton, M., Hallberg, R., & Gnanadesikan, A. (1998). Simulation of density-driven frictional downslope flow in z-coordinate ocean models. Journal of Physical Oceanography, 28(11), 2163–2174.

Wirth, A., Willebrand, J., & Schott, F. (2002). Variability of the great whirl from observations and models. Deep Sea Research Part II: Topical Studies in Oceanography, 49(7), 1279–1295.

Wyrtki, K. (1973). An equatorial jet in the indian ocean. Science, 181(4096), 262–264.

Zilitinkevich, S., Gryanik, V. M., Lykossov, V., & Mironov, D. (1999). Third-order transport and nonlocal turbulence closures for convective boundary layers*. Journal of the atmospheric sciences, 56(19), 3463–3477.

Part IV

Appendix

Chapter 11

Article

Ocean Science
Discussions

Open Access

Dynamics of turbulent western boundary currents at low latitude in a shallow water model

C. Q. C. Akuetevi[1,2] and A. Wirth[1]

[1]Univ. Grenoble Alpes, CNRS, LEGI UMR5519, Grenoble, France
[2]Univ. Grenoble Alpes, CNRS, LGGE UMR5183, Grenoble, France

Correspondence to: C. Q. C. Akuetevi (cyrille.akuetevi@legi.grenoble-inp.fr)

Discussion Paper | Discussion Paper | Discussion Paper | Discussion Paper |

OSD

11, 753–788, 2014

Dynamics of turbulent western boundary currents

C. Q. C. Akuetevi and A. Wirth

Title Page	
Abstract	Introduction
Conclusions	References
Tables	Figures
I◄	►I
◄	►
Back	Close

Full Screen / Esc

Printer-friendly Version

Interactive Discussion

Abstract

The dynamics of low latitude turbulent western boundary currents, subject to two different types of idealized wind forcing, Monsoon Wind and Trade Wind, is considered using numerical results from integrations of a reduced gravity shallow-water model. For viscosity values of $1000\,\mathrm{m^2\,s^{-1}}$ and above, the boundary layer dynamics compares well to the analytical solutions of the Munk-layer and the inertial-layer, derived from quasigeostrophic theory. Modifications due to variations in the layer thickness (vortex stretching) are only important close to the boundary. When the viscosity is reduced the boundary layer becomes turbulent and coherent structures in form of anticyclonic eddies, bursts (violent detachments of the viscous sub-layer) and dipoles appear. Three distinct boundary layers emerge, the viscous sub-layer, the advective boundary layer and the extended boundary layer. The first is characterized by a dominant vorticity balance between the viscous transport and the advective transport of vorticity. The second by a balance between the advection of planetary vorticity and the advective transport of relative vorticity. The extended boundary layer is the area to which turbulent motion from the boundary extends. The scaling of the three boundary layer thicknesses with viscosity is evaluated.

A pragmatic approach to determine the eddy viscosity diagnostically for coarse resolution numerical models is proposed.

1 Introduction

Strong western boundary currents are a dominant feature of the worlds oceans. They are also present at low latitudes in the Atlantic and the Indian ocean, where they are called the North Brazil current and the Somali Current, respectively. In both cases strong anticyclonic eddies are observed (Richardson et al., 1994; Schott and McCreary, 2001; Wirth et al., 2001). There are however substantial differences between the two cases. One is the forcing by the wind stress field. In the equatorial

Atlantic the trade winds are the major force. Whereas in the Indian Ocean the seasonally reversing Monsoon winds dominate. Another difference is the latitudinal inclination of the coast line, it is westward in the Atlantic Ocean and eastward in the Indian Ocean.

There is a large number of numerical work on the dynamics of the Somali current and the north Brazil current with a realistic coast line and topography. With the exception of the pioneering work by Edwards and Pedlosky (1998a, b) on the deep western boundary current and by Fox-Kemper (2005) on the dynamics of single and multiple gyres in a barotropic constant depth β-plane model, idealized low latitude western boundary currents have so far not been studied extensively. The above mentioned research was directed towards a detailed determination of the vorticity balances, fluxes and stability. Indeed, numerical evidence from idealized experiments on the subject with a turbulent boundary layer is scant. The present work is directed towards the determination of the turbulent structures, the fluxes and balances in low latitude western boundary currents, subject to two types of wind forcing, representing the trade wind and the Monsoon wind fields. The near western boundary region is the origin of a substantial part of turbulent kinetic energy production in the domain. It is an area of intense up-welling (Schott and McCreary, 2001; Wirth et al., 2001) and of biological production (Kawamiya and Oschlies, 2003).

To the best of our knowledge there is so far no description or theory of near wall turbulence in the western boundary current, that goes beyond the synoptic eddies. Even for oceanic western boundary currents in general the quantitative description is mainly based on laminar Munk-layer, inertial-layer theory and the analysis of their stability (see e.g. Edwards and Pedlosky, 1998b; Ierly and Young, 1991). This is in stark contrast to engineering fluid dynamics, where the turbulent boundary layer theory is the leading domain since its birth in the beginning of the 20th century (Prandtl, 1904). In the present work we focus on the dynamics of low latitude turbulent western boundary currents in a highly idealized configuration, to determine its structure, its dependence on the Reynolds number, by varying the viscosity between experiments, and its response to distinct wind forcing. The experimental set-up comprises essential

prerequisites such as a fine resolution throughout the domain and long-time integrations to obtain statistically converged results.

The physical situation considered, the mathematical model to study its dynamics and its numerical implementation are discussed in the next section. Results on the taxonomy of the coherent structures, the turbulent fluxes, their parameterization and the vorticity balance are given in Sect. 4 and discussed in Sect. 5.

2 The Model

2.1 The physical problem considered

To consider the dynamics of low latitude turbulent boundary currents, with an emphasis on the Atlantic and the Indian Ocean, we constructed a highly idealized version of them. The basin is a rectangular box spanning from 1000 km south of the equator to 3000 km north of it ($L_y = 4000$ km) and it extends $L_x = 6000$ km in the zonal direction. The Coriolis parameter varies linearly with latitude $f = \beta y$, with $\beta = 2 \times 10^{-11} \mathrm{m}^{-1}\mathrm{s}^{-1}$. This geometry is usually referred to as the equatorial β-plane. We further suppose that the dynamics considered is this of an homogeneous fluid layer of an average thickness of $H = 200$ m which superposes a constant density motion-less fluid layer of infinite depth. The density difference between the layers is expressed by the reduced gravity $g' = 3 \times 10^{-2} \mathrm{m}\mathrm{s}^{-2}$. These numbers are inspired by the water-mass properties in the Indian Ocean. The layer is forced by a wind shear at its surface. Two types of wind shear are considered, an equatorial easterly trade wind (TW) and a Monsoon wind (MW) which is southerly along the western boundary.

Title Page

Abstract | Introduction

Conclusions | References

Tables | Figures

|◄ | ►|

◄ | ►

Back | Close

Full Screen / Esc

Printer-friendly Version

Interactive Discussion

2.2 The mathematical model

The reduced-gravity shallow water equations are used in a rectangular basin on the equatorial β-plane:

$$\partial_t u + u\partial_x u + v\partial_y u - fv + g'\partial_x \eta = \nu\nabla^2 u + \frac{C_1\tau_x}{\rho(H+\eta)}, \tag{1}$$

$$\partial_t v + u\partial_x v + v\partial_y v + fu + g'\partial_y \eta = \nu\nabla^2 v + \frac{C_2\tau_y}{\rho(H+\eta)}, \tag{2}$$

$$\partial_t \eta + \partial_x[(H+\eta)u] + \partial_y[(H+\eta)v] = 0; \tag{3}$$

here u and v represent the zonal and meridional velocities, respectively. The system is subject to a zonal and meridional wind-stress forcing τ_x, τ_y and no-slip boundary conditions. A Laplacian lateral diffusion with a viscosity ν is used. It is necessary to insure the no-slip boundary condition and its role is also to prevent the accumulation of energy/enstrophy at the smallest scales that are resolved numerically. Please see Frisch et al. (2008), for a detailed discussion of this bottleneck phenomena.

The associated equation for vorticity is:

$$\partial_t \xi + u\partial_x \xi + v\partial_y \xi + \beta v + (\xi + f)(\partial_x u + \partial_y v) - \nu\nabla^2 \xi = F, \tag{4}$$

or in conservative form:

$$\partial_t \xi + \partial_x[u(\xi + f)] + \partial_y[v(\xi + f)] - \nu\nabla^2 \xi = F, \tag{5}$$

where F is the curl of the forcing.

2.3 The winds-tress forcing

The wind-stress implemented in Eqs. (1) and (2) is discriminated into a trade wind forcing $(C_1, C_2) = (4, 0)$ and a monsoon wind forcing $(C_1, C_2) = (0, 3.5)$ where we choose:

$$\tau_x = 0.1 \frac{\text{N}}{\text{m}^2} \left[1 - \exp\left(\frac{x}{L_x}\right) \right] \left[\exp\left(-4 \left(\frac{y}{L_y}\right)^2 \right) \right] \left[1 - \exp\left(\frac{-t}{t_c}\right) \right], \tag{6}$$

$$\tau_y = 0.1 \frac{\text{N}}{\text{m}^2} \left[\exp\left(-4 \left(\frac{x}{L_x}\right)^2 - 0.2 \right) \right] \left[1 - \exp\left(\frac{-t}{t_c}\right) \right]. \tag{7}$$

The values of the parameters are chosen, so that the transport in the boundary currents are similar at $y = +1500\,\text{km}$ for the TW and the MW forcing, for a viscosity $\nu = 1000\,\text{m}^2\,\text{s}^{-1}$. The spin-up time for the wind forcing is $t_c = 180$ days.

2.4 The numerical implementation

The numerical method used to solve the Eqs. (1)–(3) is a centered, second-order finite difference scheme in space and a second order Runge–Kutta scheme is used for time stepping. A fine numerical resolution of square geometry ($\Delta x = \Delta y = 2.5\,\text{km}$) is employed throughout the entire domain. This uncommon choice, of not using grid refinement at the boundary, is justified by the results presented in Sect. 4, where it is clearly seen that for high Reynolds number flow, parts of the viscous sub-layer are torn of the wall and transported away from it by the surrounding turbulent flow. This leads to small scale structures also far from the boundary. Such kind of process can only be represented when there is fine resolution in both horizontal directions throughout the extended boundary layer (to be defined in Sect. 4.4). Please note that the resolution is well below the Munk scale $\delta_M = (\nu/\beta)^{1/3}$, which is around $18\,\text{km}$ in the lowest viscosity experiment. We favor fine-resolution rather than high-order schemes. The time-step is $90\,\text{s}$, which is almost ten times shorter than the CFL time-step imposed by the speed

758

of the gravity waves. In the nonlinear boundary layer the high vorticity in the boundary layer is intermittently torn of the boundary. This process is the equivalent of bursts in 3-D boundary layers (see e.g. Robinson, 1991). It is this violent process and its nonlinear evolution that asks for a short time-step.

3 Experiments

For both types of wind forcing (TW and MW) experiments for different values of the viscosity were performed. Experiments are referred to by the forcing followed by the viscosity value: MW1000 is an experiment with MW forcing and a viscosity $\nu = 1000\,\mathrm{m}^2\,\mathrm{s}^{-1}$. The highest viscosity experiments with $\nu = 1000\,\mathrm{m}^2\,\mathrm{s}^{-1}$ converged towards a stationary dynamics, the corresponding Reynolds number based on the maximal average meridional velocity in the boundary current and the Munk-layer thickness at $y = +1500\,\mathrm{km}$ is $Re = \nu_0 \delta_\mathrm{M}/\nu = 31$ and 42 for TW1000 and MW1000, respectively. The numerical resolution and scheme allowed to perform calculations with viscosities down to $\nu = 125\,\mathrm{m}^2\,\mathrm{s}^{-1}$ for the TW forcing. For the MW forcing the lowest viscosity was $\nu = 300\,\mathrm{m}^2\,\mathrm{s}^{-1}$. The reason for the more stable TW experiments lies in the existence of inertial effects that play a stabilizing role, as discussed in Sect. 4.4.

In the high viscosity experiments the boundary layer dynamics converges towards a stationary state in about 3000 days of the dynamics. Lower viscosity experiments converge to a statistically stationary state. To increase the significance of the statistics, experiments were performed for 5000 days of the dynamics and averages were calculated over the last 2000 days.

4 Results

4.1 Large-scale circulation

For both types of wind forcing TW and MW strong western boundary currents with a recirculation in the rest of the domain were observed, as can be seen in Fig. 1.
With the TW forcing the boundary current is poleward in both hemispheres. The southward boundary current is less strong due to the domain extending only 1000 km to the south but 3000 km to the north. The MW forcing led to a single gyre extending over the entire domain with the western boundary current crossing the equator in the northward direction. Another important difference between the circulation resulting from MW and TW forcing, is that for the former the boundary current is in the northern direction and the zonal velocity vanishes almost completely except near the southern and northern boundaries of the domain. While in the latter the zonal velocity is westward at low latitudes up to about $y = +1300$ km and eastward above (see Fig. 2). We will see in the sequel that these relatively small zonal velocities have an important impact on the stability and nature of the boundary current system. For the largest viscosity values, the dynamics converge towards a stationary flow for both types of wind forcing. In experiments with lower viscosities, time dependence arises in the form of coherent anticyclones moving northward along the western boundary. For the lowest viscosity experiments the dynamics are fully turbulent, with chaotic motion over a range of spacial scales (see Sect. 4.4). The time averaged large-scale circulation of the low viscosity experiments is qualitatively similar to the stationary flow at high viscosity.

4.2 Laminar boundary layers

For the high values of the viscosity the stationary solutions of the boundary layer are, to leading order, given by a balance of the meridional transport of planetary vorticity (4th term in Eq. 4) and the viscous dissipation (last term on the l.h.s. of Eq. 4). This dynamic is described by the Munk-layer theory (Munk, 1950; Pedlosky, 1990) and the

Title Page

Abstract | Introduction

Conclusions | References

Tables | Figures

|◄ | ►|

◄ | ►

Back | Close

Full Screen / Esc

Printer-friendly Version

Interactive Discussion

solutions are:

$$v_M(x) = v_M^0 \exp\left(-\frac{x}{2\delta_M}\right) \sin\left(\frac{\sqrt{3}}{2}\frac{x}{\delta_M}\right) \qquad (8)$$

where $\delta_M = (v/\beta)^{1/3}$ is the characteristic boundary layer thickness of the Munk-layer and v_M^0 is a velocity scale. There is a fair agreement between Munk-layer theory and our numerical results for the MW and the TW forcing at higher latitude, where inertial effects vanish, as can be seen in Fig. 2. Munk-layer theory is base on quasi-geostrophy and neglects variations in the layer thickness, which are important in our reduced-gravity model (see Sect. 4.6) at low latitude. The vortex stretching is given by the fifth term in Eq. (4). We found the vortex stretching to be important very close to the boundary but decreases rapidly before the meridional velocity reaches its maximum (not shown), but does not lead to substantial deviations from the Munk-layer and inertial-layer solutions as can be verified in Fig. 2. This is in agreement with the results of Edwards and Pedlosky (1998a). At low latitudes in the TW circulation there is a significant westward velocity. This alters completely the boundary layer structure as the vorticity balance in the outer part of the boundary layer is now between the meridional transport of planetary vorticity (4th term in Eq. 4) and the westward transport of relative vorticity (second term in Eq. 4), leading to an inertial boundary layer (Charney, 1955, see also Pedlosky, 1990 and Vallis, 2006). The outer part of the boundary layer is now much better fitted (see Fig. 2) by the inertial boundary layer solution:

$$v_I(x) = v_I^0 \exp\left(-\frac{x}{\delta_I}\right), \qquad (9)$$

where $\delta_I = \sqrt{-u_I(y)/\beta}$ is the characteristic boundary layer thickness of the inertial layer and v_I^0 is a velocity scale. At the boundary the inertial solution is modified by viscous dissipation, which is necessary to satisfy the no-slip boundary condition. Such viscous dissipation is also necessary for the basin wide vorticity balance as discussed in

Title Page

Abstract | Introduction

Conclusions | References

Tables | Figures

|◄ | ►|

◄ | ►

Back | Close

Full Screen / Esc

Printer-friendly Version

Interactive Discussion

Sect. 4.6. Note, that the inertial scale δ_I, also called the Charney scale, is a result of the large-scale dynamics due to the wind forcing. It depends only weakly on the viscosity. Whereas, the Munk-layer scale δ_M depends only on external parameters, it can be calculated independently of the circulation. When $\delta_I > \delta_M$ inertial effects govern the outer part of the boundary layer, prevent it from becoming thinner and stabilize it (see also Ierly and Young, 1991). This explains the increased stability of the equatorward part of the boundary layer in the TW circulation. Please note, that an eastward velocity has no such stabilizing effect. Indeed in the TW experiment there is a eastward average velocity in the northern part of the domain, the Charney scale becomes complex valued and a tendency to spatial and temporal oscillations are observed (see Sect. 4.6).

4.3 Coherent structures

4.3.1 Anticyclones

The most conspicuous coherent structures are the anticyclonic eddies along the western boundary. In the MW experiments they start to appear at viscosity values of $\nu = 1000\,\mathrm{m^2\,s^{-1}}$ during the spin-up as poleward travelling waves in the boundary layer. They travel northward along the boundary at a speed of $V_{eddy} \approx 2.3 \times 10^{-1}\,\mathrm{m\,s^{-1}}$. This speed is faster than the fastest Rossby wave meaning that they do not radiate Rossby waves (Ierly and Young, 1991). Their size increases with a decreasing viscosity. At viscosities of $\nu \approx 500\,\mathrm{m^2\,s^{-1}}$, they are coherent regular vortices. Their diameter is then around the equatorial Rossby radius of deformation $L_\beta = \sqrt{\sqrt{g'H}/\beta} = 350\,\mathrm{km}$, a size that compares well to the size of the eddies in the Somali current (Schott and McCreary, 2001; Wirth et al., 2001) and to the eddies of the North Brazil current (Richardson and Schmitz, 1993). When inspecting the potential vorticity (PV) they appear as negative PV anomalies that move poleward with an average speed of $V_{eddy} \approx 1 \times 10^{-1}\,\mathrm{m\,s^{-1}}$, while the fluid velocity in their interior reaches a speed of $v_{eddy} = 2\,\mathrm{m\,s^{-1}}$. This demonstrates, that the eddies are advected water masses and not wave-like phenomena. A closer

inspection of the velocity field shows that they are eddies in almost perfect solid-body rotation and not vortex rings (not shown), with an almost motionless core (eye). One has to mention that in the literature eddy or ring are often used interchangeably to denote the same object. With decreasing viscosity their shape and poleward displacement exhibit a random-like behavior (Wirth et al., 2001) as can be verified analyzing Hovmöller diagrams (not shown) indicating a chaotic dynamics. For the lower viscosity values the eddy dynamics becomes more chaotic, some of the eddies migrate into the interior of the basin, merge with other eddies or are disintegrated by them in a 2-D turbulent eddy dynamics. At the lowest viscosity value of $v = 300\,\mathrm{m}^2\,\mathrm{s}^{-1}$, the average northward displacement velocity is around $V_{\mathrm{eddy}} \approx 6 \times 10^{-2}\,\mathrm{m}\,\mathrm{s}^{-1}$, while the fluid velocity in their interior reaches speed of $v_{\mathrm{eddy}} = 2\,\mathrm{m}\,\mathrm{s}^{-1}$.

With the TW forcing the boundary layer is stabilized by the inertial effect as discussed in Sect. 4.2 above. There are no eddies south of $y = +1000\,\mathrm{km}$, the latitudes at which the time averaged zonal velocity is negative. At higher latitudes and for a viscosity of $v = 1000\,\mathrm{m}^2\,\mathrm{s}^{-1}$ a single eddy is created that migrates northward to the northwest corner of the domain, where it stabilizes. A chaotic eddy dynamics appears for the viscosities of $v = 500\,\mathrm{m}^2\,\mathrm{s}^{-1}$ and below at latitudes higher than $y = +1000\,\mathrm{km}$. The eddies have an average tendency to migrate eastward and the fluid velocities reach locally up to $v_{\mathrm{eddy}} = 2.4\,\mathrm{m}\,\mathrm{s}^{-1}$.

4.3.2 Bursts

For the lowest values of the viscosity, intermittent detachments of the viscous sub-layer just northward of the eddy center are observed at the boundary (see Fig. 3). The viscous sub-layer is the thin layer of a few tenths of kilometers thickness, for the lower viscosity values, at the boundary where the vorticity has large positive values. It is discussed in detail in Sect. 4.6 of this section. The detachments are the most violent phenomena in the simulations with the strongest velocity and vorticity gradients. When the sheet of positive vorticity along the western boundary in the Munk-layer breaks due

to the action of an anticyclone, the southward part detaches, is torn of the boundary by the anticyclone and accelerates away from the boundary (see Fig. 3). North of the detachment the vorticity anomaly and the meridional velocity are negative. These events are the analog to bursts or ejections in the classical boundary layer (Robinson, 1991) and are thus given the same name here. They are strong spatially localized and temporally intermittent ejections of fluid and vorticity away from the wall, initiated by the large anticyclonic eddies. The separation of the boundary layer plays a key role in boundary layer dynamic since Prandtl (1904), see also Schlichting and Gertsen (2000).

The ejection of the boundary layer and its offshore transport, asks for fine resolution in both horizontal directions not only in the vicinity of the boundary layer but also in areas to which the boundary layer fragment is transported.

In our analysis we identify bursts as events when the meridional velocity in the viscous sub-layer is negative. Please note that the dynamics in the viscous sub-layer is not laminar, a feature that is also found in turbulent wall bounded flows in engineering applications (Robinson, 1991). To quantify the occurrence of burst, the percentage in time of the meridional velocity inversion at $y = +1000$ km is given by the T1 and the average over time and the interval $y \in [+125, +2250$ km$]$ by T2 in Table 1. In the MW experiments the percentage of the meridional velocity inversion is similar at $y = +1000$ km than those of the range of latitude between $y \in [+125, +2250$ km$]$ meaning that there is only a feeble dependence on latitude. In the TW experiments almost no bursts occur south of $y = +1000$ km in accord with the fact that there are no eddies south of $y = +1000$ km in the TW experiments as mentioned above (Sect. 4.3.1). For viscosities $v = 1000$ m^2 s^{-1} or larger there are no bursts in both type of wind forcing. Bursts are observed for $v = 500$ m^2 s^{-1} and lower in the MW experiments and for $v = 400$ m^2 s^{-1} and lower in the TW experiments. The percentage of bursts strictly increases with decreasing viscosity in all the experiments performed and reaches values of around 20 % for the lowest values of the viscosity, showing that they are a recurrent dominant feature of low viscosity boundary currents when inertial effects are absent.

4.3.3 Dipoles

In many instances the positive vorticity anomalies, ejected from the boundary during bursts, pair with negative vorticity anomalies from within the anticyclones and form dipoles (see Fig. 3) which then travel ballisticaly (at almost constant velocity) over distances of several eddy diameters. The size of the dipoles measured by the distance of the vorticity minima and maxima spans between the thickness of the viscous boundary layer δ_v (see below) and the size of the coherent anticyclones.

4.4 Scales of motion

For an understanding of the dynamics it is essential to determine the spatial scales of the turbulent motion. We consider two key quantities. The first is twice the time averaged kinetic energy (per unit mass) divided by the time averaged enstrophy (square of vorticity):

$$\lambda_1 = \sqrt{\frac{\langle u^2 + v^2 \rangle}{\langle \zeta^2 \rangle}}. \tag{10}$$

These quantity is shown in Figs. 4 and 5. In 3-D turbulence it is the Taylor-scale divided by $\sqrt{5}$ (see Frisch, 1995). This length scale characterizes the size of the velocity gradients. The second length scale is the time averaged enstrophy divided by the time averaged palinstrophy (square of the vorticity gradient):

$$\lambda_2 = \sqrt{\frac{\langle \zeta^2 \rangle}{\langle (\nabla \zeta)^2 \rangle}}. \tag{11}$$

These quantity is shown in Fig. 5. It is characteristic of the viscous dissipation length-scale in the enstrophy cascade (Bofetta and Ecke, 2012), the smallest scales in the vortical dynamics. The separation between the two scales gives an idea of the scale

Title Page

Abstract | Introduction

Conclusions | References

Tables | Figures

◄ | ►I

◄ | ►

Back | Close

Full Screen / Esc

Printer-friendly Version

Interactive Discussion

range over which turbulence is active. These scales are instructive in a turbulent environment but in the boundary layer dominated by viscosity their significance is limited. At the boundary $\lambda_1 = 0$ as energy vanishes, which does not mean that we have infinitely small scales there. At high viscosity the smallest scale is given by the Munk scale δ_M even when the analytic solutions for the laminar Munk-layer are (with $x' = \sqrt{3}x/(2\delta_M)$):

$$\lambda_1 = \delta_M \sqrt{\left(\frac{2\sin(x')}{\sin(x') - \sqrt{3}\cos(x')}\right)^2} \quad \text{and} \quad \lambda_2 = \delta_M \sqrt{\left(\frac{\sin(x') - \sqrt{3}\cos(x')}{\sin(x') + \sqrt{3}\cos(x')}\right)^2}, \quad (12)$$

which oscillate between zero and infinity. This shows that the above scales are not useful for analyzing time-independent flow. Note, that traces of these oscillations remain in the low viscosity experiments, as can be seen in Figs. 4 and 5.

Figure 4 shows the spatial distribution of the Taylor scale in the highest Reynolds number experiments for the MW and TW forcing, respectively. A striking feature is the wide extension of the low-size values into the interior of the domain in both cases, the feeble variation within this domain and the sudden jump to high values at its clearly defined boundary as seen in Figs. 4 and 5. A clear plateau at around a scale of 60 km is observed which extends of up to 2000 km into the interior of the domain. We call the area of the plateau, the extended boundary layer (EBL). The scale of 60 km is easily explained by the eddy size of 400 km $\approx 2\pi 60$ km. Figure 5 shows that the width of the extended boundary layer is increasing with decreasing viscosity. The dissipation length scale λ_2 is smallest near the boundary and increases slowly there after, approaching the Taylor scale. When λ_2 reaches the eddy scale λ_1, the velocity gradients are dissipated and turbulence disappears. The behavior of both scales, λ_1 being constant and λ_2 increasing by barely a factor of two through the extended boundary layer, shows that grid refinement near the boundary might be useful in laminar, low Reynolds number simulations, but is not adapted for the fully turbulent case where small scale structures dominate throughout the extended boundary layer. The zonal extension of the extended boundary layer increases with a decreasing viscosity as shown in Fig. 8 and quantified

in Sect. 4.6. Supposing a scaling behavior for the extension of the extended boundary layer with viscosity in the MW forcing experiments suggests an exponent close to $-2/3$ as shown in Table 2. An exponent that we can not explain. A striking feature is that, although the extension of the extended boundary layer depends on viscosity, the scales within it appear almost independent of it, once the viscosity is low enough to allow for turbulent motion. Turbulent motion in the extended boundary layer is likely to include the range of scales from λ_1 down to λ_2.

It is important to notice that in our calculations λ_2 is always more than 5 times the grid size showing that the dynamics is numerically well resolved in our calculations.

4.5 Moments of the velocity field

After having discussed the time averages of the velocity components, we will now focus on higher order moments of the fluctuations of these components. We suppose that the dynamics is in a statistically stationary state and we separate the variables into a time average and a perturbation that is: $a = \langle a \rangle + a'$. The higher order moments of the velocity components are given in Fig. 6, where they are also compared to the moments of a disc of radius R in anticylonic solid-body rotation. Taking the averages of moments of the velocity fluctuations in the y-direction over the disc, is equivalent to taking time averages at one y-location of a disc (or a succession of disks) transported by a mean flow in the y-direction at constant velocity. The comparison, presented in Fig. 6, shows that major aspects of the turbulent fluxes can be, to a good accuracy, explained by the anticyclonic discs in solid-body rotation. This confirms, that the anticyclones are the dominant coherent structures.

The positive value of $\langle u'^3 \rangle$, however, can not be explained by the disc model, which leads to a vanishing third order moment. It is a signature of the bursts and dipoles, with more intense and localized transport away from the boundary than the recirculation towards the boundary. This agrees with the findings of anisotropic burst and dipole dynamics in Sect. 4.3.

4.6 Vorticity fluxes

The vorticity balance in the laminar, time independent, boundary layer is described in Sect. 4.2. In the unstable boundary layer the vorticity balance changes. When time averaging is applied to Eq. (5) it transforms to:

$$\partial_x \left[\langle u \rangle \langle \xi \rangle \right] + \partial_y \left[\langle v \rangle \langle \xi \rangle \right] + \partial_x \langle u' \xi' \rangle + \partial_y \langle v' \xi' \rangle + \beta \langle v \rangle$$
$$+ f(\partial_x \langle u \rangle + \partial_y \langle v \rangle) - \nu \nabla^2 \langle \xi \rangle = \langle F \rangle. \tag{13}$$

In a statistically stationary state a time average of an integration of the advection of vorticity over a closed basin vanishes and the integral balance is between the forcing (r.h.s of Eq. 13) and the viscous vorticity flux through the boundary (last term on the l.h.s. of Eq. 13). Within the basin the advection of vorticity can connect the (basin-wide) source to the sink. The different terms in the l.h.s of Eq. (13) correspond to the relative vorticity advection (RVA, terms 1 and 2), turbulent relative vorticity advection (TRVA, terms 3 and 4), planetary vorticity advection (PVA, term 5), stretching (STR, term 6) and vorticity dissipation (FRIC, term 7). The stretching term is negligible and does not contribute significantly to the vorticity the balance (see Fig. 7). For high viscosities the local vorticity balance in the boundary layer is, to leading order, between the planetary vorticity advection (term 5) and the vorticity dissipation (term 7), leading to a Munk-layer as discussed in Sect. 4.2 of this section. When the viscosity is reduced the RVA and TRVA play an increasing role in the vorticity balance. The advection of relative vorticity spatially connects the transport of planetary vorticity and the viscous dissipation and both can exhibit a different zonal length scale. This is clearly visible in Fig. 7: the FRIC dominates in a narrow region near the boundary, whereas the PVA extends further from the boundary. We call the area of the viscous dissipation the viscous sub-layer (VSL) while we choose the expression "advective boundary layer" (ABL) for the wider area of large average meridional velocity. The thickness of the former is denoted by δ_v while the thickness of the latter is given by the symbol δ_V. In the Munk-layer theory they both coincide $\delta_v = \delta_V = \delta_M$. We estimate the thickness of the viscous sub-layer

768

Title Page

Abstract | Introduction

Conclusions | References

Tables | Figures

◄ | ►

◄ | ►

Back | Close

Full Screen / Esc

Printer-friendly Version

Interactive Discussion

by the distance from the boundary at which the absolute value of the Laplacian of the average vorticity has reduced to a third of its maximal value. The same criterion was applied to the average meridional velocity to obtain δ_V. Results for the corresponding boundary layer scales for the MW and TW cases and at different latitudes as a function of viscosity are assembled in Fig. 8. For the viscous sub-layer results show that its thickness drops well below the Munk-scale for the lower viscosities, while the thickness of the advective boundary layer is always above. The advection of relative vorticity can be decomposed into the advection of the average vorticity by the average velocity field (RVA), which we call inertial contribution, and the turbulent transport of vorticity (TRVA). The difference between the TW and the MW circulation at low latitude is that, for the former the inertial terms are important while for the later the turbulent terms transport the vorticity. This explains the laminar boundary layer of the TW circulation at low latitude and the turbulence of the MW boundary layer. Please note that the inertial boundary layer in the TW circulation stays laminar even for the smallest viscosity used, if it becomes turbulent at even lower viscosities, is an open question. This behavior is clearly depicted in Fig. 7, where at low latitudes of the TW circulation the inertial part connects the planetary vorticity advection to the viscous dissipation, whereas at higher latitudes and for the MW circulation it is the turbulent advection. Please note that Ierly and Young (1991) propose a scaling of $\delta_v \sim v^{1/6}$ for the boundary layer with an inertial component based on laminar boundary layer theory and an ansatz for the shape of the boundary layer. We analyzed the scalings of the turbulent boundary layer thickness by considering values obtained from turbulent boundary layers. Our results for the inertial boundary layer, see Table 2, show a much steeper scaling of 1/2 at low latitudes. This exponent suggests that the dominant vorticity advection near the boundary does not depend on the viscosity and has to be balanced at the boundary by viscous dissipation. At higher latitudes the scaling is higher for the TW forcing, showing that the boundary layer thickness decreases even faster with decreasing viscosity, when "inverse inertial" effects are present. In Fig. 7 the inertial part shows an oscillatory behavior at high

Dynamics of turbulent western boundary currents

C. Q. C. Akuetevi and A. Wirth

Title Page

Abstract | Introduction

Conclusions | References

Tables | Figures

|◄ | ►|

◄ | ►

Back | Close

Full Screen / Esc

Printer-friendly Version

Interactive Discussion

latitudes for the TW forcing, where the zonal velocity is positive, which leads to an inertial boundary layer scale that is complex valued, which explains the oscillations.

The scaling of the advective boundary layer thickness δ_V for the MW forcing shows a slight increase with decreasing viscosity (see Table 2) and a possible saturation around 200 km. For the TW forcing δ_V shows a slight decrease with decreasing viscosity at low latitude and a saturation at the value corresponding to the inertial boundary layer. At higher latitude, where an inverse inertial boundary layer is present, the thickness of the advective boundary layer still increases with decreasing viscosity.

4.7 Estimation of the eddy viscosity via the Munk formula

We have shown in Sect. 4.2 and Fig. 2 that the profile of the meridional velocity in the stationary boundary layer is close to the shape of the Munk-layer, when inertial effects are absent. When turbulence is present the shape of the time averaged meridional velocity still somehow resembles the Munk-layer solution with the meridional velocity vanishing at a distance x_0 from the boundary. For the Munk layer we have $x_0 = (2\pi/\sqrt{3})\delta_M$. The meridional gradient in layer thickness (s) imposed by the large-scale circulation adds a topographic $\beta_{topo} = -fs/H$ to the planetary value. Its value depends only weakly on the viscosity. When the effective β-term, composed of the planetary and topographic part, is constant, the Munk-layer scale is proportional to the cubic-root of the (eddy) viscosity and so is x_0. The idea is now to calculate an eddy viscosity ν_{eddy} based on x_0. To this end we measure the value x_0 in an experiment with high viscosity $\nu_{stat} = 1000\,\mathrm{m}^2\,\mathrm{s}^{-1}$ that has a time-independent dynamics and compare it to the value obtained from the average of a turbulent experiment at the same latitude. The eddy viscosity can then be obtained by using the proportionality:

$$\nu_{eddy} = \left(\frac{x_0}{x_0(\nu_{stat})}\right)^3 \nu_{stat}. \tag{14}$$

Such method can not be applied to the inertial boundary layer as, in this case the average meridional velocity decays exponentially away from the boundary and does not

vanish. The following analysis was not applied to the inertial boundary layer. A clear scaling for $v'_{eddy} = v_{eddy} - v$ as a function of the zonal maximum of the r.m.s. velocity fluctuations $u'_{r.m.s.}$ is observed in Fig. 9, for data from the MW and TW forcing at higher latitudes. The scatter plot is well fitted by an affine regression line of equation

$$v'_{eddy} = v_{eddy} - v = u'_{r.m.s.} \cdot 6283.3\,\text{m} - 639.3\frac{\text{m}^2}{\text{s}}, \tag{15}$$

which means that whatever the forcing and the viscosity, there is a correlation between the eddy viscosity and the fluctuating velocity. The correlation of the best fit linear regression is $R = 0.97$. The finding that for small values of $u'_{r.m.s.}$ there is no turbulent contribution to the eddy viscosity is explained by the fact, that the small perturbations have a wave-like structure which do not lead to turbulent fluxes.

The simplest way to estimate a eddy viscosity proposed by Prandtl (1925) Mischungsweg (mixing length) λ and the fluctuating velocity $u'_{r.m.s.}$ is:

$$v'_{eddy} = v_{eddy} - v = \alpha\lambda_1 u'_{r.m.s.} \tag{16}$$

The results of the nonlinear experiments confirm this proportionality. For our data and $\lambda_1 = L_{eddy}/(2\pi) = 60\,\text{km}$ calculate previously we obtain $\alpha \approx 0.1$. If we suppose, that the eddy viscosity is due to the anticyclones this value of α is within the range proposed by Smagorinsky (1993). The values of λ_1 and $u'_{r.m.s.}$ can not be obtained from external parameters but are a result from the numerical experiment. In concrete cases, they can often be obtained from observation or fine resolution numerical simulations.

Using $\alpha = 0.1$ and the typical values for the Somali current of $L_{eddy} = 400\,\text{km}$ and $u'_{r.m.s.} = 1\,\text{m s}^{-1}$ leads to $v_{eddy} \approx 6000\,\text{m}^2\,\text{s}^{-1}$ and a $\delta_{Munk} \approx 70\,\text{km}$. A consequence of this is that even a non-eddy permitting ocean model should have a grid size not exceeding 50 km to capture the boundary layer dynamics and the associated meridional heat transport at least in an average sense and no value of the eddy viscosity larger than $6000\,\text{m}^2\,\text{s}^{-1}$ should be used.

Title Page

Abstract | Introduction

Conclusions | References

Tables | Figures

|◀ | ▶|

◀ | ▶

Back | Close

Full Screen / Esc

Printer-friendly Version

Interactive Discussion

This pragmatic approach leads to a viscosity and a boundary layer thickness that compares well to average values in the turbulent boundary current. This approach is of course questionable as the eddy size is larger than the mean current, that is the scale separation is smaller than unity and the eddy viscosity approach asks for large scale-separations. This problematic was already noticed by Charney (1955) who states: "In order to account for the observed width of the current, Munk was forced to postulate an eddy viscosity so large that the eddy sizes were themselves comparable to the width."

We have estimated the eddy viscosity based on the average meridional velocity and have shown, that it can be connected via Prandtl's formula to the velocity fluctuations. This is however not a parameterization as the turbulent fluxes themselves are not obtained from the large-scale dynamics.

5 Discussion and conclusions

In the MW forcing case the boundary current crosses the equator and we have not observed that the vanishing of the Coriolis parameter at the equator plays a special direct role in the dynamics of western boundary currents. In the TW forcing case the equatorial current splits up and flows poleward in both hemispheres as a western boundary current. In our calculations the importance of the equator is due to the larger latitudinal velocities (inertial effect) and the unstable wave dynamics at the equator, which increases the variability, also at the western boundary.

Without the stabilizing inertial effects, the transport of PV towards the boundary area, the western boundary layer does not exist for high Reynolds number flow. The western boundary is a turbulent region with interacting eddies, bursts and dipoles and frequent velocity inversions. Its boundary layer structure can only be recovered in an average sense. The turbulent dynamics leads to a split up of the boundary layer into three layers: a viscous sub-layer, an advective boundary layer and an extended boundary layer. The thickness of the first and the third are, respectively, decreasing and increasing when the

viscosity is decreased. The second shows no or only a weak dependence on viscosity, once it drops below values that allow for turbulent motion.

We identified for the lower values of the viscosity a sequence in the evolution of the dynamics of the coherent structures: anticyclones are generated by instability, during their northward migration they intermittently detach parts of the viscous sub-layer containing strong positive vorticity, these bursts pair with negative vorticity from within the anticyclones and form dipoles which then travel ballisticaly (at almost constant velocity) over distances of several eddy diameters. In observations and a fine resolution Ocean General Circulation Models bursts are seen to lead to substantial upwelling of cold and nutrient rich water-masses from the deep. The dipole transports these water-masses offshore, leading to an increased biological production several hundreds of kilometers from the coast (Kawamiya and Oschlies, 2003; Wirth et al., 2001).

We showed that the turbulent eddy dynamics is the natural state of the high Reynolds number low latitude western boundary current. In this perspective, the question is not why eddies are present, but to the contrary, how inertial effects allow for the existence of a coherent western boundary current.

When a flat boundary is used, the thickness of the viscous sub-layer goes to zero with viscosity. A rough boundary introduces a lower bound for the thickness of the boundary.

5.1 Conclusions concerning numerical simulation of turbulent boundary layers

It is the thickness of the viscous sub-layer that imposes the spatial resolution of a numerical model. The thickness of the turbulent viscous sub-layer decreases faster with decreasing viscosity than the prominent $\frac{1}{3}$ scaling from Munk-layer theory, in all our experiments performed and at all latitudes considered. The laminar Munk-layer theory is however used to determine the (hyper) viscosity for a given spatial resolution in todays simulations of the ocean dynamics. The here presented results prove, that for the turbulent boundary layer the thus obtained resolution is far from being sufficient. The lower values for the viscous sub-layer in the MW forcing experiments as compared to the TW

forcing experiments, for the same viscosity, explain also the result that experiments of the MW forcing were only possible down to $v = 300\,\mathrm{m^2\,s^{-1}}$ while the experiments with the TW forcing converged down to $v = 125\,\mathrm{m^2\,s^{-1}}$.

From Fig. 8 it is clear that the gap between the thickness of the extended boundary layer and the viscous sub-layer widens with increasing Reynolds number. The gap is a measure of the complexity of the numerical calculations as the finest scale δ_v has to be resolved throughout δ_{ext} in both horizontal directions. This shows that grid refinement near the boundary has no place in simulations of the turbulent boundary layer as: (i) the structures are almost isotropic and (ii) the small scales extend far from the boundary. The ratio $N = (\delta_{\mathrm{ext}}/\delta_v)^2$ can be taken as a measure for the involved degrees of freedom in the calculations. Estimations based on our results in Table 2 clearly show a strongly increase with the Reynolds number, $N \propto Re^{2.4}$ in the low latitude MW forcing and up to $N \propto Re^{2.9}$ for the high latitude TW forcing. The scaling based on Munk-layer thickness leads to $N \propto Re^{2/3}$.

5.2 Conclusions concerning the parameterization of the turbulent boundary layers

One of the major challenges in the numerical simulation of the ocean dynamics is to parameterize the effect of the small scale dynamics not explicitly resolved on the explicitly resolved large-scale flow.

Inertial theory and the above presented results teach us that small westward velocities can stabilize the western boundary layer. Velocity components in other directions have no such effect. A parameterization of the turbulence must therefore reflect this anisotropy. The instability of the boundary layer is also strongly dependent on details of the velocity profile as noted by Ierly and Young (1991). Topographic features are also likely to play an important role in the stability and turbulent fluxes.

Our determination of the eddy viscosity in Sect. 4.7 are not a parameterization as the eddy viscosity is not obtained from large-scale properties of the flow, but from

Dynamics of turbulent western boundary currents

C. Q. C. Akuetevi and A. Wirth

fine resolution simulations. These show that for the lowest viscosities, δ_V saturates at a value corresponding to $v \approx 6000 \, \mathrm{m}^2 \, \mathrm{s}^{-1}$. Choosing viscosity values lower than $v \approx 6000 \, \mathrm{m}^2 \, \mathrm{s}^{-1}$ but above the threshold for fully turbulent boundary layers $v \approx 300 \, \mathrm{m}^2 \, \mathrm{s}^{-1}$ leads to an unreal thin average boundary layer thickness, worsening of the representation of the advective boundary layer dynamics. In numerical simulations of the boundary layer dynamics one should either simulate the turbulent dynamics or parameterize it. Our findings discussed above suggest to either use fine resolutions and viscosities below $v \approx 300 \, \mathrm{m}^2 \, \mathrm{s}^{-1}$ and perform large-eddy simulations or larger viscosity $v \approx 6000 \, \mathrm{m}^2 \, \mathrm{s}^{-1}$.

In our simulations we varied the eddy-viscosity parameter by roughly an order of magnitude. The corresponding necessary spatial resolutions vary from those of todays coarse resolution climate models down to those of fine resolution regional models. Even lower viscosity values lead to smaller boundary layer scales and higher velocities. At smaller scales the hydrostatic approximation, on which the shallow water equations are based is no longer valid as the dynamics becomes truly three-dimensional. Higher velocities lead to Froude numbers exceeding unity, hydraulic jumps occur and the flow becomes fully three dimensional such phenomena can not be explicitly resolved by the two-dimensional shallow water equations. In Fox-Kemper and Pedlosky (2004) and Fox-Kemper (2004) this problems are bypassed by using a constant depth model, where Froude number vanishes and by increasing the viscosity in the vicinity of the boundary. We propose here a numerical value, based on the Prandtl formula, for the eddy viscosity in the vicinity of the boundary that leads to a laminar boundary layer mimicking (on average) the dynamics of turbulent boundary layers at lower viscosity.

We did not consider the more involved behavior of hyper dissipation operators (hyper-viscosity, powers of the Laplacian), which ask for boundary conditions for derivatives of the velocity field and which lead towards thermalization at small scales of the turbulent dynamics as explained by Frisch et al. (2008).

References

Bofetta, G. and Ecke, R.: Two-dimensional turbulence, Annu. Rev. Fluid Mech., 44, 427–451, 2012. 765

Charney, J.: The Gulf stream as an inertial boundary layer, P. Natl. Acad. Sci. USA, 41, 731–740, 1955. 761, 772

Edwards, C. A. and Pedlosky, J.: Dynamics of nonlinear cross-equatorial flow. Part 1: The tropically enhanced instability of the western boundary current, J. Phys. Oceanogr., 28, 2382–2406, 1998a. 755, 761

Edwards, C. A. and Pedlosky, J.: Dynamics of nonlinear cross-equatorial flow. Part 2: The tropically enhanced instability of the western boundary current, J. Phys. Oceanogr., 28, 2407–2417, 1998b. 755

Fox-Kemper, B.: Wind-driven barotropic gyre II: effects of eddy and low interior viscosity, J. Mar. Res., 62, 195–232, 2004. 775

Fox-Kemper, B.: Reevaluting the roles of eddies in multiple barotropic wind-driven gyres, J. Phys. Oceanogr., 35, 1263–1278, 2005. 755

Fox-Kemper, B. and Pedlosky, J.: Wind-driven barotropic gyre I: circulation control by eddy vorticity fluxes to an enhanced removal region, J. Mar. Res., 62, 169–193, 2004. 775

Frisch, U.: Turbulence: the Legacy of A. N. Kolmogorov, Cambridge University Press, 1995. 765

Frisch, U., Kurien, S., Pandit, R., Pauls, W., Ray, S., Wirth, A., and Zhu, J.-Z.: Hyperviscosity, galerkin truncation, and bottelnecks in turbulence, Phys. Rev. Lett., 101, 144501, doi:10.1103/PhysRevLett.101.144501, 2008. 757, 775

Ierly, G. R. and Young, W. R.: Viscous instabilities in the western boundary layer, J. Phys. Oceanogr., 21, 1323–1332, 1991. 755, 762, 769, 774

Kawamiya, M. and Oschlies, A.: An eddy-permitting, coupled ecosystem-circulation model of the Arabian Sea: comparison with observations, J. Marine Syst., 38, 221–257, 2003. 755, 773

Munk, W. H.: On the wind-driven ocean circulation, J. Meteorol., 7, 79–93, 1950. 760

5 Pedlosky, J.: Geophysical Fluid Dynamics, 2nd Edn., Springer, 1990. 760, 761

Prandtl, L.: Über Flüssigkeitsbewegung bei sehr kleiner Reibung, Coll. Works, II, 575–584, 1904. 755, 764

Prandtl, L.: Bericht über Untersuchungen zur Ausgebildeten Turbulenz, Z. Angew. Math. Mech., No. 5, 136–169, 1925. 771

10 Richardson, P. L. and Schmitz, W. J.: Deep cross-equatorial flow in the Atlantic measured with SOFAR floats, J. Geophys. Res., 98, 8371–8387, 1993. 762

Richardson, P. L., Hufford, G. E., Limeburner, R., and Brown, W.: North Brazil current retroflection eddies, J. Geophys. Res., 99, 5081–5093, 1994. 754

Robinson, S. K.: Coherent motions in the turbulent boundary layer, Annu. Rev. Fluid Mech., 23, 15 601–663, doi:10.1146/annurev.fl.23.010191.003125, 1991. 759, 764

Schlichting, H. and Gertsen, K.: Boundary-Layer Theory, Springer Verlag, 2000. 764

Schott, F. and McCreary, J.: The monsoon circulation of the Indian Ocean, Prog. Oceanogr., 51, 1–123, 2001. 754, 755, 762

Smagorinsky, J.: Some historical remarks on the use of nonlinear viscosities, in: Large Eddy 20 Simulation of Complex Engineering and Geophysical Flows, edited by: Galperin, B. and Orszag, S. A., Cambridge University Press, 3–36, 1993. 771

Vallis, G.: Atmospheric and Oceanic Fluid Dynamics, Cambridge Univ. Press., 2006. 761

Wirth, A., Willebrand, J., and Schott, F.: Variability of the Great Whirl from observations and models, Deep-Sea Res.-Pt. II, 49, 1279–1295, 2001. 754, 755, 762, 763, 773

Dynamics of turbulent western boundary currents

C. Q. C. Akuetevi and A. Wirth

Title Page

Abstract	Introduction
Conclusions	References
Tables	Figures

|◀ | ▶|

◀ | ▶

Back | Close

Full Screen / Esc
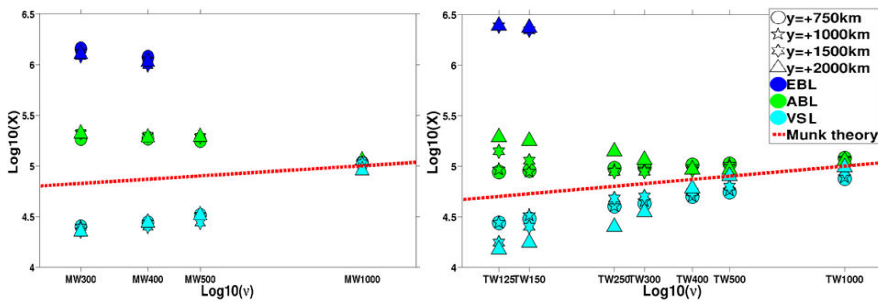
Printer-friendly Version

Interactive Discussion

Table 1. Percentage in time of the meridional velocity inversion in the viscous sub-layer at $y = +1000$ km (T1) and for $y \in [+125, +2250$ km] (T2).

Experiments	TW125	TW150	TW250	TW300	TW400	TW500	TW1000
T1 (%)	0.93	0.8	0	0	0	0	0
T2 (%)	15.57	11.62	4.81	2.63	0.52	0	0
Experiments				MW300	MW400	MW500	MW1000
T1 (%)				21.67	17.5	13.57	0
T2 (%)				19.07	14.36	10.38	0

Table 2. Scaling exponents for the zonal extension of the viscous sub-layer (VSL) thickness, the advective boundary layer (ABL) thickness and the extend boundary layer (EBL) thickness at different latitudes y for the MW forcing and the TW forcing.

y (km)	MW			TW		
	VSL	ABL	EBL	VSL	ABL	EBL
+750	0.50	−0.07	−0.68	0.50	0.13	–
+1000	0.50	−0.17	−0.63	0.50	0.08	–
+1500	0.39	−0.17	−0.71	0.89	−0.27	−0.48
+2000	0.71	−0.15	−0.62	1.20	−0.57	−0.25
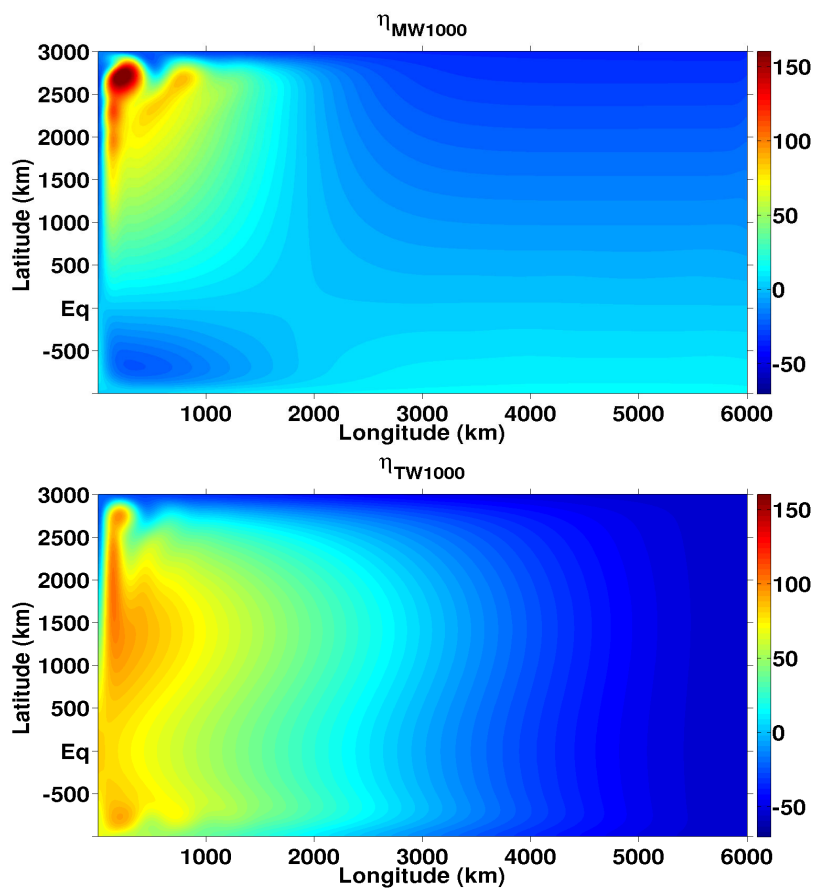
Fig. 1. Instantaneous contours of layer thickness variation at time $t = 2000$ days for MW1000 (above) and TW1000 (below).

Fig. 2. Zonal profiles of the u and v components for the experiments MW1000 and TW1000 at five latitudes, $y = +2000$, $y = +1500$, $y = +1250$, $y = +750$ and $y = +250$ km from top to bottom. Superposed are the zonal profiles of the analytic solutions of Munk-layer theory (red full line) and the analytic solution of inertial-layer theory (red dashed line). The amplitudes v_M^0 in Eq. (8) and v_I^0 in Eq. (9) are chosen to best fit the data.
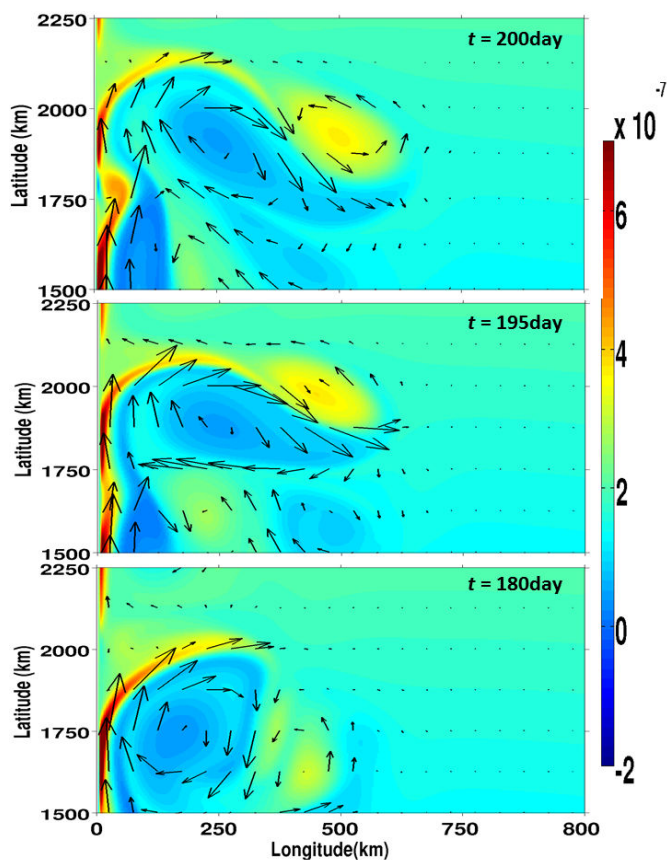
Fig. 3. Sequence of potential vorticity ($m^{-1} s^{-1}$) snapshots showing bursts and its subsequent development into a dipole for MW300 experiment. The snapshots were taken at $t = 180$, 195 and 200 days, from top to bottom.

Fig. 4. Taylor scale λ_1 (m) for MW300 (above) and TW125 (below). Note that the color-bar stops at 100 km to emphasize the behavior in the extended boundary layer.

Fig. 5. Zoom of zonal profiles of Taylor scale λ_1 and small-scale λ_2 at $y = +1500$ km for TW125, TW250, MW300 and MW400.

Title Page

Abstract | Introduction

Conclusions | References

Tables | Figures

|◄ | ►|

◄ | ►

Back | Close

Full Screen / Esc

Printer-friendly Version

Interactive Discussion

Fig. 6. Second and third order moments of the fluctuations of the velocity components from MW300 at $y = +1500\,\text{km}$ as a function of the distance from the boundary (left). And the analytic solutions of the same quantities for a disc in anticyclonic solid-body rotation (right).
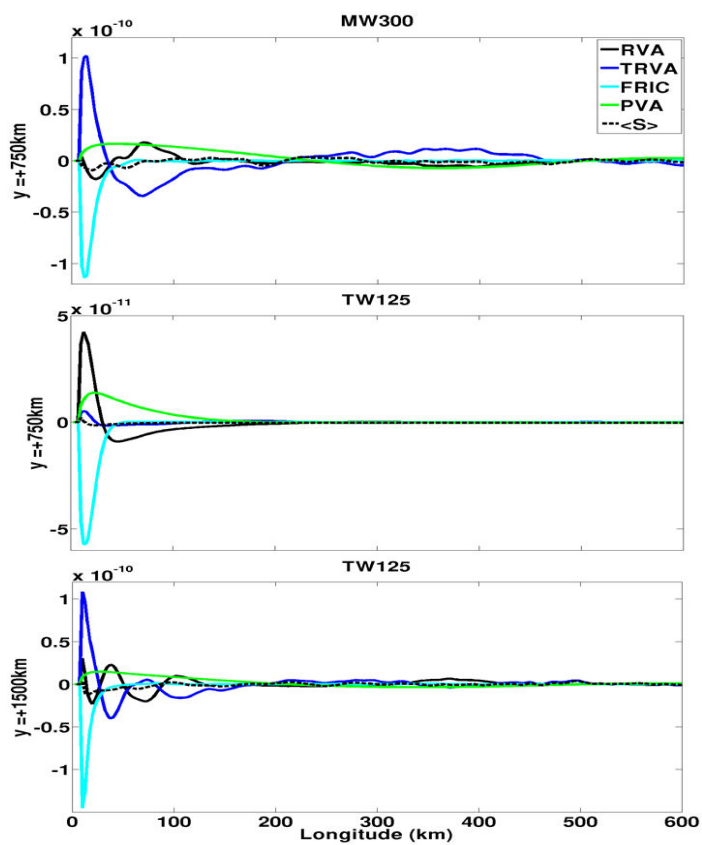
Fig. 7. Vorticity balance. Different terms of Eq. (13) are plotted for the MW300 experiment at $y = +750$ km (upper figure) and for the TW125 experiment at $y = +750$ km (middle figure) and $y = +1500$ km (bottom figure). $\langle S \rangle$ comprises forcing, stretching and residual time dependence.

Fig. 8. Thickness of the viscous sub-layer (VSL), the advective boundary layer (ABL) and the extended boundary layer (EBL) for MW forcing (left) and TW forcing (right) experiments at different latitudes y.
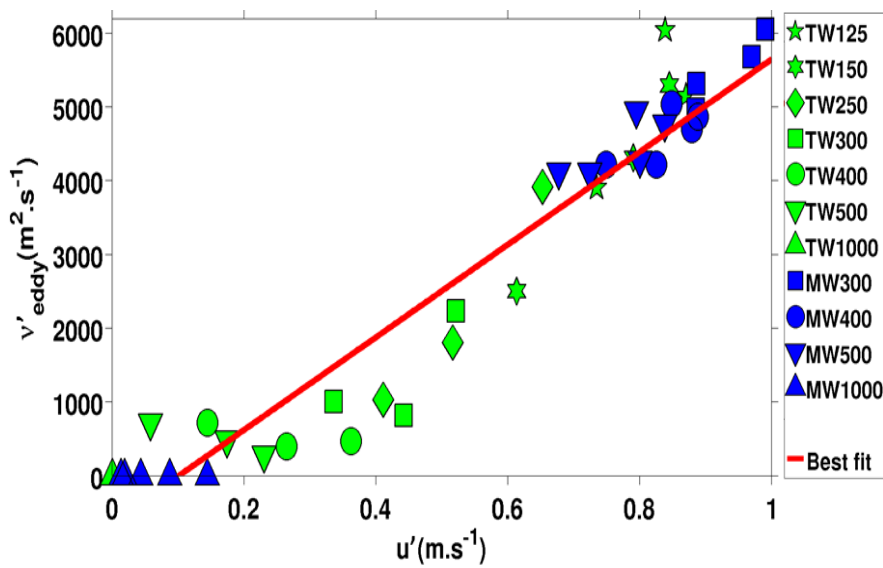
Fig. 9. Scatter plot diagram of eddy viscosity $\nu'_{eddy} = \nu_{eddy} - \nu$ computed from the data using the Munk formula approach of Eq. (14), as function of the maximum fluctuating velocity for all the nonlinear experiments at high latitudes $y = +1500$, $y = +1750$ and $y = +2000$ km. The green symbols represent the experiments with TW forcing and the blue ones those of MW forcing and the red line is the best fit affine regression line.

Chapter 12

CDFTOOLS

Contents

199

12.1 cdfeddyscale intermediate

```fortran
PROGRAM cdfeddyscale_pass1
   !!======================================================================
   !!                     ***  PROGRAM  cdfeddyscale_pass1  ***
   !!======================================================================
   !!  ** Purpose : Compute: - the curl and the square of curl on F-points,
   !!                        - the gradient components of the curl and the
   !!                          square of the gradient components on UV-points
   !!                        - the square of velocity components on UV-points
   !!             for given gridU gridV files and variables.
   !!             These terms will used to compute the Taylor scale or large
   !!             scale eddy (lambda1) and the small scale eddy (lambda2)
   !!             in the program cdflambda.f90.
   !!
   !!  ** Method  : Use the same algorithm than NEMO
   !!
   !!----------------------------------------------------------------------
   USE cdfio
   USE modcdfnames
   !!----------------------------------------------------------------------
   !! CDFTOOLS_3.0 , MEOM 2013
   !! $Id: cdfeddyscale_pass1.f90 718 2013-07-16 14:55:07Z molines $
   !! Copyright (c) 2013, C. Q. C. Akuetevi & J.-M. Molines
   !! Software governed by the CeCILL licence
   !! (Licence/CDFTOOLSCeCILL.txt)
   !!----------------------------------------------------------------------
   IMPLICIT NONE
   ! index of output variables
   INTEGER(KIND=4),                PARAMETER :: jp_nvar=8
   INTEGER(KIND=4),                PARAMETER :: jp_curl=1, jp_curl2=2, jp_dxcurl=3, jp_dycurl=4
   INTEGER(KIND=4),                PARAMETER :: jp_dxcurl2=5, jp_dycurl2=6, jp_u2=7, jp_v2=8

   INTEGER(KIND=4)                           :: ji, jj, jt        ! dummy loop index
   INTEGER(KIND=4)                           :: ilev              ! level to be processed
   INTEGER(KIND=4)                           :: npiglo, npjglo    ! size of the domain
   INTEGER(KIND=4)                           :: npk, npt          ! size of the domain
   INTEGER(KIND=4)                           :: narg, iargc       ! browse command line
   INTEGER(KIND=4)                           :: ncout, ierr       ! browse command line
   INTEGER(KIND=4), DIMENSION(jp_nvar)       :: ipk, id_varout    ! output variable properties

   REAL(KIND=4), DIMENSION(:),   ALLOCATABLE :: tim               ! time counter
   REAL(KIND=4), DIMENSION(:,:), ALLOCATABLE :: e1f, e2f          ! F-grid metrics
   REAL(KIND=4), DIMENSION(:,:), ALLOCATABLE :: e1u, e2u          ! zonal horizontal metrics
   REAL(KIND=4), DIMENSION(:,:), ALLOCATABLE :: e1v, e2v          ! meridional horizontal metrics
   REAL(KIND=4), DIMENSION(:,:), ALLOCATABLE :: un, vn            ! velocity field
   REAL(KIND=4), DIMENSION(:,:), ALLOCATABLE :: zun, zvn          ! working arrays
   REAL(KIND=4), DIMENSION(:,:), ALLOCATABLE :: fmask             ! fmask

   REAL(KIND=8), DIMENSION(:,:), ALLOCATABLE :: dl_rotn, dl_rotn2 ! curl and square curl
   REAL(KIND=8), DIMENSION(:,:), ALLOCATABLE :: dxrotn, dyrotn    ! curl gradient components
   REAL(KIND=8), DIMENSION(:,:), ALLOCATABLE :: dxrotn2, dyrotn2  ! square curl gradient components
   REAL(KIND=8), DIMENSION(:,:), ALLOCATABLE :: dl_vozocrtx2      ! square of velocity components
   REAL(KIND=8), DIMENSION(:,:), ALLOCATABLE :: dl_vomecrty2      ! square of velocity components

   CHARACTER(LEN=256)                        :: cf_ufil, cf_vfil  ! file names
   CHARACTER(LEN=256)                        :: cf_out = 'lambda_int.nc' ! output file name
   CHARACTER(LEN=256)                        :: cv_u, cv_v        ! variable names
   CHARACTER(LEN=256)                        :: cldum             ! dummy string

   TYPE (variable), DIMENSION(jp_nvar)       :: stypvar           ! structure for attibutes

   LOGICAL                                   :: lforcing = .FALSE. ! forcing flag
   LOGICAL                                   :: lchk     = .FALSE. ! flag for missing files
   LOGICAL                                   :: lperio   = .FALSE. ! flag for E-W periodicity
   !!----------------------------------------------------------------------
   CALL ReadCdfNames()

   narg = iargc()
   IF ( narg /= 5 ) THEN
      PRINT *,' usage : cdfeddyscale_pass1 U-file V-file U-var V-var lev'
      PRINT *,'      '
      PRINT *,'      PURPOSE :'
```

```fortran
     PRINT *,'     Compute: - the curl and the square of curl on F-points,'
     PRINT *,'               - the gradient components of the curl and the'
     PRINT *,'                  square of the gradient components on UV-points,'
     PRINT *,'               - the square of velocity components on UV-points,'
     PRINT *,'     for given gridU gridV files and variables. These variables are required'
     PRINT *,'     for computing eddy scales with cdfeddyscale. Therefore this program is'
     PRINT *,'     the first step in computing the eddy scales.'
     PRINT *,'        '
     PRINT *,'        These terms will used to compute the Taylor scale or large'
     PRINT *,'     scale eddy (lambda1) and the small scale eddy (lambda2) in'
     PRINT *,'     the program cdfeddyscale.'
     PRINT *,'        '
     PRINT *,'     ARGUMENTS :'
     PRINT *,'       U-file : zonal component of the vector field.'
     PRINT *,'       V-file : meridional component of the vector field.'
     PRINT *,'       U-var  : zonal component variable name'
     PRINT *,'       V-var  : meridional component variable name.'
     PRINT *,'       lev    : level to be processed. If set to 0, assume forcing file '
     PRINT *,'                in input.'
     PRINT *,'        '
     PRINT *,'     REQUIRED FILES :'
     PRINT *,'         ', TRIM(cn_fhgr)
     PRINT *,'        '
     PRINT *,'     OUTPUT : '
     PRINT *,'       netcdf file : ', TRIM(cf_out)
     PRINT *,'          variables : socurl (s^-1), socurl2 (s^-2)'
     PRINT *,'          variables : sodxcurl, sodycurl (s^-1.m^-1)'
     PRINT *,'          variables : sodxcurl2, sodycurl2 (s^-2.m^-2)'
     PRINT *,'          variables : vozocrtx2, vomecrty2 (m^2.s^-2)'
     PRINT *,'          WARNING : variables in the output file are not located at the same'
     PRINT *,'                   C-grid point.'
     PRINT *,'        '
     PRINT *,'     SEE ALSO : '
     PRINT *,'        cdfeddyscale'
     STOP
  ENDIF


  CALL getarg(1, cf_ufil)
  CALL getarg(2, cf_vfil)
  CALL getarg(3, cv_u   )
  CALL getarg(4, cv_v   )
  CALL getarg(5, cldum  ) ;  READ(cldum,*) ilev

  lchk = chkfile(cn_fhgr ) .OR. lchk
  lchk = chkfile(cf_ufil ) .OR. lchk
  lchk = chkfile(cf_vfil ) .OR. lchk
  IF ( lchk ) STOP ! missing files

  ! load the dimension
  npiglo = getdim(cf_ufil,cn_x)
  npjglo = getdim(cf_ufil,cn_y)
  npk    = getdim(cf_ufil,cn_z)
  npt    = getdim(cf_ufil,cn_t)

  PRINT *, 'npiglo = ',npiglo
  PRINT *, 'npjglo = ',npjglo
  PRINT *, 'npk    = ',npk
  PRINT *, 'npt    = ',npt
  PRINT *, 'ilev   = ',ilev

  !test if lev exists
  IF ( (npk==0) .AND. (ilev > 0) ) THEN
     PRINT *, 'Problem : npk = 0 and lev > 0 STOP'
     STOP
  END IF

  ! if forcing field
  IF ( ilev==0 .AND. npk==0 ) THEN
     lforcing=.TRUE.
     npk = 1 ; ilev=1
     PRINT *, 'npk =0, assume 1'
```

```fortran
END IF

IF ( npt==0 ) THEN
   PRINT *, 'npt=0, assume 1'
   npt=1
END IF
! check files and determines if the curl will be 2D of 3D

! Allocate the memory
ALLOCATE ( e1u(npiglo,npjglo)        , e2u(npiglo,npjglo)        )
ALLOCATE ( e1v(npiglo,npjglo)        , e2v(npiglo,npjglo)        )
ALLOCATE ( e1f(npiglo,npjglo)        , e2f(npiglo,npjglo)        )
ALLOCATE ( un(npiglo,npjglo)         , vn(npiglo,npjglo)         )
ALLOCATE ( zun(npiglo,npjglo)        , zvn(npiglo,npjglo)        )
ALLOCATE ( fmask(npiglo,npjglo)                                  )
ALLOCATE ( tim(npt)                                              )
ALLOCATE ( dl_rotn(npiglo,npjglo)    , dl_rotn2(npiglo,npjglo)   )
ALLOCATE ( dxrotn(npiglo,npjglo)     , dyrotn(npiglo,npjglo)     )
ALLOCATE ( dxrotn2(npiglo,npjglo)    , dyrotn2(npiglo,npjglo)    )
ALLOCATE ( dl_vozocrtx2(npiglo,npjglo)                           )
ALLOCATE ( dl_vomecrty2(npiglo,npjglo)                           )


! Read the metrics from the mesh_hgr file
e1u =  getvar(cn_fhgr, cn_ve1u, 1, npiglo, npjglo)
e2u =  getvar(cn_fhgr, cn_ve2u, 1, npiglo, npjglo)
e1v =  getvar(cn_fhgr, cn_ve1v, 1, npiglo, npjglo)
e2v =  getvar(cn_fhgr, cn_ve2v, 1, npiglo, npjglo)
e1f =  getvar(cn_fhgr, cn_ve1f, 1, npiglo, npjglo)
e2f =  getvar(cn_fhgr, cn_ve2f, 1, npiglo, npjglo)

CALL CreateOutputFile

DO jt=1,npt
   IF (MOD(jt,100)==0 ) PRINT *, jt,'/',npt
   ! if files are forcing fields
   zun(:,:) =  getvar(cf_ufil, cv_u, ilev ,npiglo,npjglo, ktime=jt)
   zvn(:,:) =  getvar(cf_vfil, cv_v, ilev ,npiglo,npjglo, ktime=jt)

   IF ( lforcing ) THEN ! for forcing file u and v are on the A grid
      DO ji=1, npiglo-1
         un(ji,:) = 0.5*(zun(ji,:) + zun(ji+1,:))
      END DO
      !
      DO jj=1, npjglo-1
         vn(:,jj) = 0.5*(zvn(:,jj) + zvn(:,jj+1))
      END DO
      ! end compute u and v on U and V point
   ELSE
      un(:,:) = zun(:,:)
      vn(:,:) = zvn(:,:)
   END IF

   ! compute the mask
   IF ( jt==1 ) THEN
      DO jj = 1, npjglo - 1
         DO ji = 1, npiglo - 1
            fmask(ji,jj)=0.
            fmask(ji,jj)= un(ji,jj)*un(ji,jj+1) * vn(ji,jj)*vn(ji+1,jj)
            IF (fmask(ji,jj) /= 0.) fmask(ji,jj)=1.
         ENDDO
      ENDDO
   END IF
   ! compute the curl
   dl_rotn(:,:) = 0.d0
   DO jj = 1, npjglo -1
      DO ji = 1, npiglo -1    ! vector opt.
         dl_rotn(ji,jj) = (   e2v(ji+1,jj  ) * vn(ji+1,jj  ) - e2v(ji,jj) *vn(ji,jj) &
               &             - e1u(ji  ,jj+1) * un(ji  ,jj+1) + e1u(ji,jj) *un(ji,jj)  ) &
               &           * fmask(ji,jj) / ( e1f(ji,jj) * e2f(ji,jj) )
      END DO
   END DO
```

```fortran
      IF ( lperio ) dl_rotn(npiglo,:) = dl_rotn(2, :)

      ! compute the square curl
      dl_rotn2(:,:) = dl_rotn(:,:) * dl_rotn(:,:)

      ! compute the gradient components
      dxrotn(:,:) = 0.d0
      dyrotn(:,:) = 0.d0
      DO jj = 2, npjglo
         DO ji = 2, npiglo    ! vector opt.
            dxrotn(ji,jj) = (dl_rotn(ji,jj) - dl_rotn(ji-1,jj))/e1v(ji,jj)
            dyrotn(ji,jj) = (dl_rotn(ji,jj) - dl_rotn(ji,jj-1))/e2u(ji,jj)
         END DO
      END DO

      IF ( lperio ) dxrotn(1,:) = dxrotn(npiglo-1, :)
      IF ( lperio ) dyrotn(1,:) = dyrotn(npiglo-1, :)

      ! compute the square module of the gradient
      dxrotn2(:,:) = dxrotn(:,:) * dxrotn(:,:)
      dyrotn2(:,:) = dyrotn(:,:) * dyrotn(:,:)

      ! compute the square of the velocity components
      dl_vozocrtx2(:,:) = zun(:,:) * zun(:,:)
      dl_vomecrty2(:,:) = zvn(:,:) * zvn(:,:)

      ! write dl_rotn on file at level k and at time jt
      ierr = putvar(ncout, id_varout(jp_curl),    REAL(dl_rotn),  1, npiglo, npjglo, ktime=jt)

      ! write dl_rotn2 on file at level k and at time jt
      ierr = putvar(ncout, id_varout(jp_curl2),   REAL(dl_rotn2), 1, npiglo, npjglo, ktime=jt)

      ! write dxrotn on file at level k and at time jt
      ierr = putvar(ncout, id_varout(jp_dxcurl),  REAL(dxrotn),   1, npiglo, npjglo, ktime=jt)

      ! write dyrotn on file at level k and at time jt
      ierr = putvar(ncout, id_varout(jp_dycurl),  REAL(dyrotn),   1, npiglo, npjglo, ktime=jt)

      ! write dxrotn2 on file at level k and at time jt
      ierr = putvar(ncout, id_varout(jp_dxcurl2), REAL(dxrotn2),  1, npiglo, npjglo, ktime=jt)

      ! write dyrotn2 on file at level k and at time jt
      ierr = putvar(ncout, id_varout(jp_dycurl2), REAL(dyrotn2),  1, npiglo, npjglo, ktime=jt)

      ! write dl_vozocrtx2 on file at level k and at time jt
      ierr = putvar(ncout, id_varout(jp_u2),  REAL(dl_vozocrtx2), 1, npiglo, npjglo, ktime=jt)

      ! write dl_vozocrtx2 on file at level k and at time jt
      ierr = putvar(ncout, id_varout(jp_v2),  REAL(dl_vomecrty2), 1, npiglo, npjglo, ktime=jt)

   END DO
   ierr = closeout(ncout)
CONTAINS

   SUBROUTINE CreateOutputFile
      !!---------------------------------------------------------------------
      !!                  ***  ROUTINE CreateOutputFile  ***
      !!
      !! ** Purpose :  Create output file
      !!
      !! ** Method  :   Use global program variables
      !!
      !!---------------------------------------------------------------------

      ! define new variables for output
      ! Relative Vorticity F point
      ipk(jp_curl)                  = 1    !2D
      stypvar(jp_curl)%cname        = 'socurl'
      stypvar(jp_curl)%cunits       = 's-1'
      stypvar(jp_curl)%rmissing_value = 0.
      stypvar(jp_curl)%valid_min    = -1000.
```

```fortran
      stypvar(jp_curl)%valid_max          =  1000.
      stypvar(jp_curl)%clong_name         = 'Relative_Vorticity (curl)'
      stypvar(jp_curl)%cshort_name        = 'socurl'
      stypvar(jp_curl)%conline_operation  = 'N/A'
      stypvar(jp_curl)%caxis              = 'TYX'

      ! Square of Relative Vorticity F point
      ipk(jp_curl2)                       = 1    !2D
      stypvar(jp_curl2)%cname             = 'socurl2'
      stypvar(jp_curl2)%cunits            = 's-2'
      stypvar(jp_curl2)%rmissing_value    = 0.
      stypvar(jp_curl2)%valid_min         = -1000.
      stypvar(jp_curl2)%valid_max         =  1000.
      stypvar(jp_curl2)%clong_name        = 'Square of Relative_Vorticity (curl2)'
      stypvar(jp_curl2)%cshort_name       = 'socurl2'
      stypvar(jp_curl2)%conline_operation = 'N/A'
      stypvar(jp_curl2)%caxis             = 'TYX'


      ! Relative Vorticity zonal gradient V point
      ipk(jp_dxcurl)                      = 1
      stypvar(jp_dxcurl)%cname            = 'sodxcurl'
      stypvar(jp_dxcurl)%cunits           = 'm-1*s-1'
      stypvar(jp_dxcurl)%rmissing_value   = 0.
      stypvar(jp_dxcurl)%valid_min        = -1000.
      stypvar(jp_dxcurl)%valid_max        =  1000.
      stypvar(jp_dxcurl)%clong_name       = 'Relative_Vorticity zonal gradient (dx_curl)'
      stypvar(jp_dxcurl)%cshort_name      = 'sodxcurl'
      stypvar(jp_dxcurl)%conline_operation = 'N/A'
      stypvar(jp_dxcurl)%caxis            = 'TYX'

      ! Relative Vorticity meridional gradient U point
      ipk(jp_dycurl)                      = 1
      stypvar(jp_dycurl)%cname            = 'sodycurl'
      stypvar(jp_dycurl)%cunits           = 'm-1*s-1'
      stypvar(jp_dycurl)%rmissing_value   = 0.
      stypvar(jp_dycurl)%valid_min        = -1000.
      stypvar(jp_dycurl)%valid_max        =  1000.
      stypvar(jp_dycurl)%clong_name       = 'Relative Vorticity meridional gradient (dy_curl)'
      stypvar(jp_dycurl)%cshort_name      = 'sodycurl'
      stypvar(jp_dycurl)%conline_operation = 'N/A'
      stypvar(jp_dycurl)%caxis            = 'TYX'

      ! Square of Relative Vorticity zonal gradient V point
      ipk(jp_dxcurl2)                     = 1
      stypvar(jp_dxcurl2)%cname           = 'sodxcurl2'
      stypvar(jp_dxcurl2)%cunits          = 'm-2*s-2'
      stypvar(jp_dxcurl2)%rmissing_value  = 0.
      stypvar(jp_dxcurl2)%valid_min       = -1000.
      stypvar(jp_dxcurl2)%valid_max       =  1000.
      stypvar(jp_dxcurl2)%clong_name      = 'Square Relative Vorticity zonal gradient (dx_curl2)'
      stypvar(jp_dxcurl2)%cshort_name     = 'sodxcurl2'
      stypvar(jp_dxcurl2)%conline_operation = 'N/A'
      stypvar(jp_dxcurl2)%caxis           = 'TYX'

      ! Square of Relative Vorticity meridional gradient U point
      ipk(jp_dycurl2)                     = 1
      stypvar(jp_dycurl2)%cname           = 'sodycurl2'
      stypvar(jp_dycurl2)%cunits          = 'm-2*s-2'
      stypvar(jp_dycurl2)%rmissing_value  = 0.
      stypvar(jp_dycurl2)%valid_min       = -1000.
      stypvar(jp_dycurl2)%valid_max       =  1000.
      stypvar(jp_dycurl2)%clong_name      = 'Square of Relative Vorticity meridional gradient
(dy_curl2)'
      stypvar(jp_dycurl2)%cshort_name     = 'sodycurl2'
      stypvar(jp_dycurl2)%conline_operation = 'N/A'
      stypvar(jp_dycurl2)%caxis           = 'TYX'

      ! Square of Zonal Velocity V point
      ipk(jp_u2)                          = 1
      stypvar(jp_u2)%cname                = 'vozocrtx2'
      stypvar(jp_u2)%cunits               = 'm^2/s^2'
```

```fortran
      stypvar(jp_u2)%rmissing_value    = 0.
      stypvar(jp_u2)%valid_min         = -10.
      stypvar(jp_u2)%valid_max         =  10.
      stypvar(jp_u2)%clong_name        = 'Square Zonal Velocity (vozocrtx2)'
      stypvar(jp_u2)%cshort_name       = 'vozocrtx2'
      stypvar(jp_u2)%conline_operation = 'N/A'
      stypvar(jp_u2)%caxis             = 'TYX'

      ! Square of Zonal Velocity V point
      ipk(jp_v2)                       = 1
      stypvar(jp_v2)%cname             = 'vomecrty2'
      stypvar(jp_v2)%cunits            = 'm^2/s^2'
      stypvar(jp_v2)%rmissing_value    = 0.
      stypvar(jp_v2)%valid_min         = -10.
      stypvar(jp_v2)%valid_max         =  10.
      stypvar(jp_v2)%clong_name        = 'Square Meridional Velocity (vomecrty2)'
      stypvar(jp_v2)%cshort_name       = 'vomecrty2'
      stypvar(jp_v2)%conline_operation = 'N/A'
      stypvar(jp_v2)%caxis             = 'TYX'

      ! use zun and zvn to store f latitude and longitude for output
      zun = getvar(cn_fhgr, cn_glamf, 1, npiglo, npjglo)
      zvn = getvar(cn_fhgr, cn_gphif, 1, npiglo, npjglo)

      ! look for  E-W periodicity
      IF ( zun(1,1) == zun(npiglo-1,1) ) lperio = .TRUE.

      ! create output fileset
      ncout = create     (cf_out, cf_ufil, npiglo,  npjglo, 0)
      ierr  = createvar  (ncout , stypvar, jp_nvar, ipk,    id_varout)
      ierr  = putheadervar(ncout,  cf_ufil, npiglo,  npjglo, 0, pnavlon=zun, pnavlat=zvn )

      tim  = getvar1d(cf_ufil, cn_vtimec, npt      )
      ierr = putvar1d(ncout,   tim,       npt,  'T')

   END SUBROUTINE CreateOutputFile
END PROGRAM cdfeddyscale_pass1
```

12.2 cdfeddyscale

```fortran
PROGRAM cdfeddyscale
  !!======================================================================
  !!                     ***  PROGRAM  cdfeddyscale  ***
  !!======================================================================
  !!  ** Purpose : Compute: -the Taylor scale or large scale eddy (lambda1)
  !!                        -the small scale eddy (lambda2)
  !!                        -and the inertial range (scar) on F-points
  !!               lambda1 = sqrt(mean Kinetic Energie / Enstrophy)
  !!               lambda2 = sqrt(Enstrophy / Palinstrophy)
  !!               scar    = lambda1 / lambda2
  !!
  !!               Enstrophy = 1/2 * ( mean((RV)^2) )
  !!               Palinstrophy = 1/2 * ( mean((dx(RV))^2 + (dy(RV))^2) )
  !!
  !!  ** Method  : Use the mean of the variables (vozocrtx2 + vomecrty2), socurl2,
  !!               (sodxcurl2 + sodycurl2) of the cdfeddyscale_pass1.f90
  !!
  !!  ** Warning : - the square of curl socurl2 is on F-points,
  !!               - vozocrtx2, vomecrty2, sodxcurl2 and sodycurl2 are on UV-points
  !!
  !!----------------------------------------------------------------------
  USE cdfio
  USE modcdfnames
  !!----------------------------------------------------------------------
  !! CDFTOOLS_3.0 , MEOM 2013
  !! $Id: cdfeddyscale.f90 718 2013-07-16 14:55:07Z molines $
  !! Copyright (c) 2013, C. Q. C. AKUETEVI & J.-M. Molines
  !! Software governed by the CeCILL licence
  !! (Licence/CDFTOOLSCeCILL.txt)
  !!----------------------------------------------------------------------
  IMPLICIT NONE

  INTEGER(KIND=4)                            :: ji, jj, jt        ! dummy loop index
  INTEGER(KIND=4)                            :: ilev              ! level to be processed
  INTEGER(KIND=4)                            :: npiglo, npjglo    ! size of the domain
  INTEGER(KIND=4)                            :: npk, npt          ! size of the domain
  INTEGER(KIND=4)                            :: narg, iargc       ! browse command line
  INTEGER(KIND=4)                            :: ncout, ierr       ! browse command line
  INTEGER(KIND=4), DIMENSION(3)              :: ipk, id_varout    ! output variable properties

  REAL(KIND=4), DIMENSION(1)                 :: tim               ! time counter in output file
  REAL(KIND=4), DIMENSION(:,:), ALLOCATABLE :: zun, zvn          ! working arrays
  REAL(KIND=4), DIMENSION(:,:), ALLOCATABLE :: rotn2             ! square curl
  REAL(KIND=4), DIMENSION(:,:), ALLOCATABLE :: zdxrotn2, zdyrotn2 ! square curl gradient components
  REAL(KIND=4), DIMENSION(:,:), ALLOCATABLE :: vozocrtx2         ! square of velocity components
  REAL(KIND=4), DIMENSION(:,:), ALLOCATABLE :: vomecrty2         ! square of velocity components
  REAL(KIND=4), DIMENSION(:,:), ALLOCATABLE :: zmke              ! mean kinetic energy
  REAL(KIND=4), DIMENSION(:,:), ALLOCATABLE :: ens               ! enstrophy
  REAL(KIND=4), DIMENSION(:,:), ALLOCATABLE :: zpal              ! palinstrophy
  REAL(KIND=4), DIMENSION(:,:), ALLOCATABLE :: zlambda1          ! Taylor or large scale eddy
  REAL(KIND=4), DIMENSION(:,:), ALLOCATABLE :: zlambda2          ! small scale eddy
  REAL(KIND=4), DIMENSION(:,:), ALLOCATABLE :: scar              ! inertial range

  CHARACTER(LEN=256)                         :: cf_meanfil   ! file names
  CHARACTER(LEN=256)                         :: cf_out = 'lambda.nc' ! output file name
  CHARACTER(LEN=256)                         :: cldum             ! dummy string

  TYPE (variable), DIMENSION(3)              :: stypvar           ! structure for attibutes

  LOGICAL                                    :: lforcing = .FALSE. ! forcing flag
  LOGICAL                                    :: lchk     = .FALSE. ! flag for missing files
  LOGICAL                                    :: lperio   = .FALSE. ! flag for E-W periodicity
  !!----------------------------------------------------------------------
  CALL ReadCdfNames()

  narg = iargc()
  IF ( narg /= 1 ) THEN
     PRINT *,' usage : cdfeddyscale mean-cdfeddyscale_pass1-file'
     PRINT *,'        '
     PRINT *,'     PURPOSE :'
     PRINT *,'     Compute: -the Taylor scale or large scale eddy (lambda1)'
     PRINT *,'              -the small scale eddy (lambda2)'
```

```fortran
    PRINT *,'                  -and the inertial range (scar) on F-points'
    PRINT *,'        '
    PRINT *,'     lambda1 = sqrt(mean Kinetic Energie / Enstrophy)'
    PRINT *,'     lambda2 = sqrt(Enstrophy / Palinstrophy)'
    PRINT *,'     Inertial Range    = lambda1 / lambda2'
    PRINT *,'        '
    PRINT *,'     Enstrophy = 1/2 * ( mean((RV)^2) )'
    PRINT *,'     Palinstrophy = 1/2 * ( mean((dx(RV))^2 + (dy(RV))^2) )'
    PRINT *,'        '
    PRINT *,'     ARGUMENTS :'
    PRINT *,'     mean-cdfeddyscale_pass1-file : mean of the terms compute by'
    PRINT *,'     the program cdfeddyscale_pass1'
    PRINT *,'        '
    PRINT *,'     OUTPUT : '
    PRINT *,'       netcdf file : ', TRIM(cf_out)
    PRINT *,'         variables : solambda1 (m), solambda2 (m), soscar'
    PRINT *,'        '
    PRINT *,'     SEE ALSO :'
    PRINT *,'       cdfeddyscale_pass1 '
    STOP
ENDIF

CALL getarg(1, cf_meanfil)

lchk = chkfile(cf_meanfil ) .OR. lchk
IF ( lchk ) STOP ! missing files

npiglo = getdim(cf_meanfil,cn_x)
npjglo = getdim(cf_meanfil,cn_y)

PRINT *, 'npiglo = ',npiglo
PRINT *, 'npjglo = ',npjglo

! Allocate the memory
ALLOCATE ( rotn2(npiglo,npjglo)                               )
ALLOCATE ( zdxrotn2(npiglo,npjglo)  , zdyrotn2(npiglo,npjglo)  )
ALLOCATE ( vozocrtx2(npiglo,npjglo) , vomecrty2(npiglo,npjglo) )
ALLOCATE ( zmke(npiglo,npjglo)                                )
ALLOCATE ( ens(npiglo,npjglo)                                 )
ALLOCATE ( zpal(npiglo,npjglo)                                )
ALLOCATE ( zlambda1(npiglo,npjglo)   , zlambda2(npiglo,npjglo) )
ALLOCATE ( scar(npiglo,npjglo)                                )

CALL CreateOutputFile

!load the mean variables
rotn2(:,:)     =  getvar(cf_meanfil, 'socurl2'  , 1,npiglo,npjglo )
zdxrotn2(:,:)  =  getvar(cf_meanfil, 'sodxcurl2', 1,npiglo,npjglo )
zdyrotn2(:,:)  =  getvar(cf_meanfil, 'sodycurl2', 1,npiglo,npjglo )
vozocrtx2(:,:) =  getvar(cf_meanfil, 'vozocrtx2', 1,npiglo,npjglo )
vomecrty2(:,:) =  getvar(cf_meanfil, 'vomecrty2', 1,npiglo,npjglo )

! Enstrophy
ens(:,:) = 0.5 * rotn2(:,:)

! compute the Kinetic Energy on F-points
zmke = -9999.
DO jj = 1, npjglo-1
   DO ji = 1, npiglo-1   ! vector opt.
      zmke(ji,jj) =  0.25 * (vozocrtx2(ji,jj+1) + vozocrtx2(ji,jj))   &
              & + 0.25 * (vomecrty2(ji+1,jj) + vomecrty2(ji,jj))
   END DO
END DO

! compute the Palinstrophy on  F-points
zpal = -9999.
DO jj = 1, npjglo-1
   DO ji = 1, npiglo-1   ! vector opt.
      zpal(ji,jj) =  0.25 * (zdxrotn2(ji+1,jj) + zdxrotn2(ji,jj))  &
              & + 0.25 * (zdyrotn2(ji,jj+1) + zdyrotn2(ji,jj))
   END DO
END DO
```

```fortran
  ! compute the Taylor and small scale eddy
  zlambda1(:,:) = 0.
  zlambda2(:,:) = 0.
  WHERE( ens > 0.  ) zlambda1(:,:) = SQRT ( zmke(:,:)/ens(:,:))
  WHERE( zpal > 0. ) zlambda2(:,:) = SQRT ( ens(:,:)/zpal(:,:))

  ! compute the Inertial Range
  scar(:,:) = 0.
  WHERE( zlambda2 > 0. ) scar(:,:) = zlambda1(:,:)/zlambda2(:,:)

  ! write zlambda1 on file
  ierr = putvar(ncout, id_varout(1), zlambda1, 1, npiglo, npjglo )

  ! write zlamdba2 on file
  ierr = putvar(ncout, id_varout(2), zlambda2, 1, npiglo, npjglo )

  ! write scar on file
  ierr = putvar(ncout, id_varout(3), scar,     1, npiglo, npjglo )

  ierr = closeout(ncout)

CONTAINS

SUBROUTINE CreateOutputFile
  !!---------------------------------------------------------------------
  !!                  ***  ROUTINE CreateOutputFile  ***
  !!
  !! ** Purpose :  Create Output file
  !!
  !! ** Method  :  Use global variable
  !!
  !!---------------------------------------------------------------------

  ! define new variables for output
  ! Taylor or large scale eddy F point
  ipk(1)                       = 1   !2D
  stypvar(1)%cname             = 'solambda1'
  stypvar(1)%cunits            = 'm'
  stypvar(1)%rmissing_value    = 0.
  stypvar(1)%valid_min         = 0.
  stypvar(1)%valid_max         =  100000.
  stypvar(1)%clong_name        = 'Taylor_large_eddy_scale (lambda1)'
  stypvar(1)%cshort_name       = 'solambda1'
  stypvar(1)%conline_operation = 'N/A'
  stypvar(1)%caxis             = 'TYX'

  ! Small scale eddy F point
  ipk(2)                       = 1   !2D
  stypvar(2)%cname             = 'solambda2'
  stypvar(2)%cunits            = 'm'
  stypvar(2)%rmissing_value    = 0.
  stypvar(2)%valid_min         = 0.
  stypvar(2)%valid_max         =  100000.
  stypvar(2)%clong_name        = 'Small scale eddy (lambda2)'
  stypvar(2)%cshort_name       = 'solambda2'
  stypvar(2)%conline_operation = 'N/A'
  stypvar(2)%caxis             = 'TYX'

  ! Inertial Range F point
  ipk(3)                       = 1   !2D
  stypvar(3)%cname             = 'soscar'
  stypvar(3)%cunits            = ''
  stypvar(3)%rmissing_value    = 0.
  stypvar(3)%valid_min         = 0.
  stypvar(3)%valid_max         =  20.
  stypvar(3)%clong_name        = 'Inertial range (scar)'
  stypvar(3)%cshort_name       = 'soscar'
  stypvar(3)%conline_operation = 'N/A'
  stypvar(3)%caxis             = 'TYX'

  ! create output fileset
```

```fortran
  ncout = create      (cf_out, cf_meanfil, npiglo, npjglo, 0)
  ierr  = createvar   (ncout , stypvar, 3,       ipk,    id_varout)
  ierr  = putheadervar(ncout,  cf_meanfil, npiglo, npjglo, 0 )

  tim  = getvar1d(cf_meanfil, cn_vtimec, 1      )
  ierr = putvar1d(ncout,      tim,       1,  'T')

  END SUBROUTINE CreateOutputFile

END PROGRAM cdfeddyscale
```

List of Tables

List of Figures

215

Part V

MINUTES

UNIVERSITÉ DE GRENOBLE

PROCES VERBAL DE SOUTENANCE

DOCTORAT DE L'UNIVERSITÉ DE GRENOBLE

Si cotutelle de thèse, nom de l'établissement étranger partenaire :

....

Nom ..AKUETEVI................................ Prénom ..Cataria Quam Cyrille..

Nom Epouse (s'il y a lieu) ....

N° Etudiant ..21061643..

Ecole Doctorale ..Terre Univers Environnement...................

Spécialité (**obligatoire**)..Ocean, atmosphere hydrologie.................

Laboratoire d'Accueil ..LEGI – UMR 5519...........................

Directeur de Laboratoire ..Achim WIRTH.........................

Directeur de Thèse ..Achim WIRTH.............................

Titre de la Thèse (**en français**) : ..La dynamique des courants turbulents de bord ouest, étude numérique...

....

Date de Soutenance ..20/02/2014..... à Grenoble heures ..11ᴴ30..

Lieu (adresse exacte) ..LEGI, Domaine Universitaire, salle K118 1209-1211 rue de la piscine 38400 Saint Martin d'Hères...............

....

Pour une soutenance hors des locaux universitaires du site Grenoblois, joindre une demande de dérogation signée par le Directeur de Thèse.

DEMANDE DE CONFIDENTIALITE du mémoire (Nombre de mois :...................... (renouvelable), soit date de fin de confidentialité prévue le ....

Soutenance (huis clos)   Oui   o   Non   o
La demande de confidentialité doit être accompagnée d'un courrier du Directeur de Thèse.

Avis du Directeur du Collège Doctoral

Favorable   Oui   o Non o   Signature :

COMPOSITION DU JURY POUR LA SOUTENANCE

Membres	Nom/Prénom	Grade	Université/Organisme
Rapporteur Mme/M	LANOTTE Alessandra, CR		ISAC (Italie)
Rapporteur Mme/M	MOREL Yves, DR		LEGOS/UPS (Toulouse)
Membre du jury - Mme/M	STAQUET Chantal, Pr		UJF (Grenoble)
Membre du jury - Mme/M	ROULLET Guillaume, MC		Univ. Brest
Membre du jury - Mme/M	HALL Nickolas, Pr		UPS (Toulouse)
Membre du jury - Mme/M	WIRTH Achim, CR1 HdR		LEGI (Grenoble) (dir th)
Membre du jury - Mme/M	BARNIER Bernard, DR1		LGGE (Grenoble) (dir th)
Membre du jury - Mme/M			

Le, 29/01/2014

Signature du Directeur de Thèse

Signature du Directeur de l'Ecole Doctorale
Le directeur de l'Ecole Doctorale
Terre - Univers - Environnement
de Grenoble
J. BRAUN

AUTORISATION DE SOUTENANCE

Devant un jury conforme à l'arrêté du 7 août 2006 et à la lecture des rapports de :

Mme/M Alessandra Sabina Lanotte

Mme/M Yves Morel

Mme/M Tatiana Aluetevi ....est autorisé(e) à présenter une thèse en vue de l'obtention du Doctorat de l'Université de Grenoble.

Grenoble le 3/01/2014

Le Président de l'UDG, par délégation, le Directeur du Collège Doctoral

2
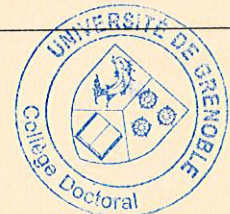
DOCTORAT DE L'UNIVERSITE DE GRENOBLE

Ecole doctorale de rattachement : ED105, Terre – Univers – Environnement

<div style="border:1px solid black">

RAPPORT

</div>

De M. : Yves MOREL

Qualité : Directeur de recherche CNRS

Lieu d'exercice : LEGOS, Toulouse

Rapport transmis à

Mr Jean BRAUN

Directeur de l'Ecole Doctorale ED105, Ecole doctorale Terre – Univers – Environnement

Adresse : Ecole Doctorale « Terre – Univers – Environnement »
Université de Grenoble- ISTERRE –OSUG C,
1381 rue de la Piscine,
BP 53,
38041 Grenoble - cedex 9

Sur la thèse présentée par

Mr : Cyrille AKUETEVI
Ayant pour sujet : Dynamics of turbulent western boundary currents at low latitude, a numerical study

Rapport sur la thèse de Cyrille AKUETEVI, "Dynamics of turbulent western boundary currents at low latitude, a numerical study"

Généralités et résultats :

Le document présente les résultats obtenus par modélisation numérique académique (modèle à une couche en gravité réduite dans un bassin rectangulaire avec forçage analytique simplifié), analyse théorique et modélisation numérique réaliste (extraction sur la mer d'Arabie des résultats des maquettes DRAKKAR) sur l'influence des processus de couche limite sur la dynamique des courants de bord Ouest.
Le manuscrit est rédigé entièrement en anglais, ce qui demande un travail supplémentaire non négligeable au doctorant mais facilite la diffusion du travail (dans sa forme actuelle ou sous forme d'articles).

Une introduction générale est faite sur l'état de l'art des connaissances sur le sujet. Celle-ci reste très succincte et quelques détails supplémentaires auraient été bienvenus dès ce stade sur certains résultats. Ces éléments sont toutefois donnés dans les chapitres suivants pour ce qui concerne les sujets au cœur de la thèse.

La partie principale est constituée de deux parties.
La première partie, qui représente la majeure partie des résultats aboutis, concerne la modélisation académique à l'aide d'un modèle shallow water. Le modèle, construit par le doctorant, est tout d'abord exposé en détail ainsi que les deux configurations étudiées (qui ne différent que par le forçage atmosphérique). Le chapitre 4, très fourni, présente l'ensemble des résultats obtenus sur la base de ces modèles simplifiés. Les résultats principaux sont repris dans un article soumis à Ocean Modelling, repris en annexe.
La seconde partie, présente les analyses des simulations DRAKKAR concernant le courant Somalien. Ces analyses sont en partie menées sur la base des résultats académiques obtenus dans la première partie, et mènent à une vision originale et de fort intérêt pour les simulations réalistes. Un peu moins aboutie que la première partie, les résultats sont d'un intérêt suffisant pour pouvoir mener à une autre publication à court terme.

Les résultats principaux obtenus au cours de cette thèse sont :

- la construction d'un modèle shallow water. Le modèle lui-même reste relativement simple et sans originalité numérique, mais il aura au moins permis au doctorant de maîtriser les principes de la modélisation numériques (maîtrise d'un outil de modélisation, choix des résolutions spatio temporelles, gestion des conditions aux limites en particulier), ce qui est une compétence importante ;
- la mise en place des expériences numériques académique et l'analyse des résultats des expériences. Il a été démontré notamment :
    o les limites des modèles théoriques de couche limite admise, en particulier aussi la sensibilité à la nature du courant (associé à la nature de son forçage) ;
    o la revisite des théories de couche limite et des équilibres principaux en terme de flux de vorticité, la démonstration de la complémentarité des approches de Munk et Charney et l'élargissement des théories pour la prise en compte des effets de stretching ;
    o l'importance des effets de la couche limite visqueuse sur la dynamique des anticyclones qui se forment au sein des courant de bord Ouest par faible viscosité. En particulier, leur détachement est clairement associé à la génération et appariement avec de « bursts » cycloniques issus de la couche limite visqueuse, étendant ainsi l'impact des termes frictionnels bien au-delà de la couche de Munk ou Charney ;
    o l'importance d'une haute résolution numérique pour la représentation des effets de couche limite dont les effets se font sentir bien au-delà du bord ;
    o des recommandations pour le choix des viscosités numériques pour les modèles de circulation ;

- l'analyse de résultats de modèles réalistes avec :
  - o l'analyse et la validation des résultats DRAKKAR sur le courant de Somalie et la mise en évidence des processus majeurs liés à la formation des tourbillons et gyres issues de ce courant ;
  - o l'influence de la résolution spatiale pour la représentation des effets de couche limite ;
  - o l'influence des conditions aux limites choisies pour la représentation des effets de couche limite.

Commentaires et avis :

Les outils numériques et le descriptif de l'ensemble des configurations utilisées sont clairement explicités. Comme mentionné plus haut, j'ai parfois regretté le manque de détail sur certaines études antérieures – notamment dans le chapitre introductif- mais cela concerne des travaux non pleinement connexes au sujet d'étude et n'est pas limitant pour la lecture et la compréhension des travaux effectués par Mr Akuetevi.

La rédaction en anglais est claire et le manuscrit se lit facilement (il reste des coquilles mais qui n'ont pas d'impact sur la compréhension), malgré la complexité des processus étudiés et le niveau de détail de certaines explications. Le manuscrit est donc rédigé dans les règles de l'art d'un manuscrit scientifique : clairement organisé et très argumenté quant aux descriptifs des processus. Il est aussi suffisamment concis et sans redondance. De mon point de vue le manuscrit satisfait donc parfaitement les normes attendues pour un doctorat.

L'originalité du travail réside dans plusieurs points qui sont bien mis en avant :

Pour commencer la démarche avec une première approche très dépouillée (académique) qui permet d'obtenir des outils théoriques d'analyse de modèles complets réalistes. Ce type de démarche n'est pas stricto sensu originale mais elle devient rare car il est difficile dans le cadre d'une thèse de trois ans d'aller au bout de la démarche, c'est-à-dire jusqu'à l'analyse des simulations réalistes. Comme mentionné plus haut, cette dernière partie n'est pas totalement aboutie en terme de publication, mais des résultats originaux sont obtenus et une bonne partie du travail a été réalisé. L'utilisation de modèles complexes devenant maintenant très facile, la tentation est grande d'en faire usage, parfois au détriment de la compréhension, la complexité des interactions entre la totalité des processus pris en compte dans ces modèles complets empêchant parfois l'identification de la mécanique principale. Le travail du scientifique consiste alors à trouver le cadre le plus simple possible permettant de pousser les analyses et la compréhension des processus le plus loin possible, ce qui est tout à fait la démarche des études présentées et me semble à souligner : c'est un vrai travail scientifique d'identifier l'outil et les configurations les plus simples possibles pour comprendre.

L'analyse détaillée de l'évolution de la vorticité au niveau des couches limites visqueuses est poussée très loin et constitue le résultat majeur du travail. Les résultats théoriques sur les complémentarités des modèles précédents et leur limitation, le rôle des processus de couche limite dans l'export de la turbulence vers le large ainsi que la sensibilité des résultats à la nature initiale (associée ici au forçage) et aux paramètres (viscosité) du modèle sont particulièrement bien documentés et argumentés.
Les processus d'interaction sont complexes et le détail des analyses montre une bonne maîtrise des mécanismes étudiés ici.
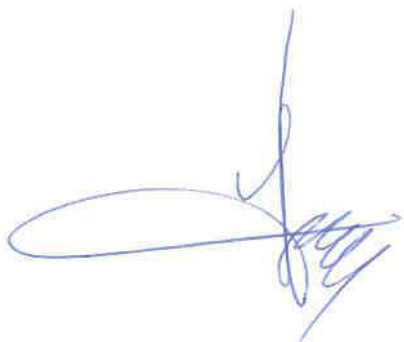
Un autre aspect original des travaux concerne l'utilisation d'indicateurs ou diagnostics habituellement utilisés par les mécaniciens des fluides (non géophysiques) pour l'étude de phénomènes océaniques. Les problématiques de descente d'échelle dans la modélisation des océans ou de l'atmosphère font que ces communautés s'intéressent à des échelles de plus en plus petites et les interactions avec la communauté « turbulence » de la mécanique des fluides vont naturellement s'accentuer en particulier au sein du LEGI, mais le présent travail est pionnier.

En conclusion, Mr Cyrille Akuetevi a fait la preuve, dans ce manuscrit, qu'il maîtrisait la dynamique des tourbillons géophysiques. Il a obtenu des résultats innovants et d'un grand intérêt pour la communauté des dynamiciens de l'océan.

En conséquence, Cyrille Akuetevi doit être autorisé à présenter son travail devant un jury afin d'obtenir le grade de docteur de l'Université Joseph Fourier.

A Toulouse, le 10 janvier 2014
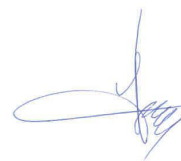
EVALUATION

Nom du rapporteur : Yves MOREL (DR, CNRS) ………….
(*Name of the referee*)

Nom du doctorant : Cyrille AKUETEVI.....................
(*Name of the candidate*)

Niveau scientifique : *Mark*	Satisfaisant *Satisfactory*	Bon *Good*	Très bon *Very good*	Exceptionnel *Exceptionnal*
	☐	☐	X	☐

C O N S I G L I O   N A Z I O N A L E   D E L L E   R I C E R C H E
Istituto di Scienze dell'Atmosfera e del Clima
Unità Organizzativa di Supporto di Lecce

École Doctorale "Terre - Univers - Environment"
Université Joseph Fourier, ISTerre – OSUG C
1381 rue de la Piscine, BP 53,
38041 Grenoble cedex 9- FRANCE

Report on PhD Thesis
Thesis author: Cataria Quam Cyrille AKUETEVI
Discipline: Physique appliquée á l'ocean
Thesis title: *Dynamics of turbulent western boundary currents at low latitude, a numerical study*

The PhD work of the candidate Cyrille Akuetevi focuses on the dynamics of oceanic western boundary currents at low latitudes, by adopting a turbulent boundary-layer theory approach.
The problem is important from the point of view of ocean sciences, since turbulent boundary layers are very active region of mixing of scalar quantities and of air-sea interaction. Moreover it is important also from the point of view of theoretical geophysical fluid dynamics, since it is an interesting playground for testing and developing new parameterisations on non-homogeneous and anisotropic non-linear flow systems in the presence of rotation, buoyancy and stratification. Western boundary currents are often associated to the formation of medium-size structures such as dipoles and (anticyclonic) eddies, and smaller structures, such as bursts. All these features deserve a detailed knowledge before being accurately modeled and parameterised.

The PhD work analyses the non-linear dynamics of low-latitude western boundary currents (WBC), focusing on the important instance of the Somaly Current. It is relevant to emphasize that a body of literature exists on the topic of low-latitude WBCs, of both analytical and numerical works. The former mostly deal with the problem of western boundary current retroflection and formation of anti-cyclonic eddies, while the latter generally deal with the response of the WBCs to local and remote forcings, within realistic but low resolution ocean models. All these works mostly focus on the synoptic features of the WBCs, while the small-scale turbulent dynamics has been so far neglected.
Due to the inherent chaotic nature of the WBC problem, it is however clear that idealised models which isolate processes and fully resolve their spatial and temporal variability are crucial to advance the knowledge, even at the price of loosing some features such as e.g., a realistic coastline and topography.

In his thesis, Cyrille Akuetevi has chosen to adopt such an approach to address an important and complex question. Namely, characterising the boundary-layer structure of low-latitude WBCs, determining their spatial and temporal variability by varying the applied wind forcing, and assessing the dependence on the Reynolds number, by varying the viscous dissipation of kinetic energy. This is done – in the first part of the thesis- within a simplified reduced-gravity shallow water model for the ocean dynamics.
In the second part, the detailed and quite-complete description of WBCs in response to external parameters changes is used to study the specific problem of the Somali current. This is done by performing a series of numerical experiments of 10-year realistic ocean general circulation model (OGCM) runs of the Indian Ocean, with model NEMO.

C O N S I G L I O   N A Z I O N A L E   D E L L E   R I C E R C H E
Istituto di Scienze dell'Atmosfera e del Clima
Unità Organizzativa di Supporto di Lecce

ISAC

The complex interactions taking place west of the Somalia coast, due to the action of reversing Monsoon winds, the presence of annual Rossby waves and Kelvin waves, in a basin that is constrained north by the Asian continent, make the region unique among the tropical ocean ones. Moreover, the choice of focusing on the Somali current is also timely, considering the fact that *in-situ* campaigns are difficult to realise, and remote-sensing data can be compared to numerical experiments only.

To cope with the problems under consideration, the candidate has appropriately combined different theoretical and numerical tools. In particular, the results of the space and time evolution of the simplified ideal model have been compared to laminar boundary-layer theories to characterise linear regimes; at the transition and in the fully non-linear regimes, statistical methods have been used to properly quantify the turbulent boundary-layer in terms of the characteristic scales of motion, velocity moments, and turbulent fluxes.

As a result, the work presented by the candidate is logically structured and denotes a good scientific maturity. Moreover it denotes a good capacity to identify a problem, approach it in a simplified but consistent way, and then study it in its full complexity.

One publication under revision in Ocean Modelling is joined to the thesis.

Let me detail my opinion by summarising the main parts of the manuscript and by discussing what I consider the important findings of the research done by the candidate.

In the first chapters (ch. 1, 2, 3 and 4) the problem of western boundary currents at low latitudes is put into the present context of knowledge in the field. Also, the equations of the adopted ideal reduced gravity shallow water model are introduced. Thanks to this choice, a fluid layer of average thickness (of H=200m) can be described accurately, while the underlying fluid layer of *infinite depth* is assumed to be at rest. From the fluid dynamics point of view, these are the equations of a bidimensional flow in the forward enstrophy cascade regime, coupled to an active scalar (the fluid layer heigh variation, η).

The numerical set-up of the physical problem is also briefly described, it is standard.

The choice of no-slip boundary conditions is less obvious and fewer details could be useful.

Chapter 4 contains the core of the first part of the thesis. First of all, key questions are pointed out: how do laminar Munk-layer and inertial theories compare with numerical simulations? Which is the range of parameters for which they apply? What are the different effects of Trade Winds and Monsoon Winds forcings? What is the role of latitude in both cases? How do coherent structures emerge in the WBC dynamics and what are their typical scales? The answers to these questions are all contained in chapter 4. In particularly, it is shown that the retroflection of the WBCs is directly linked to the vorticity dynamics, and not to the inertial crossing of the equator as suggested by previous works. This result, obtained within the idealised model, is then also confirmed by the OGCM numerical experiments focusing on the Somali current.

Still in chapter 4, two important points are discussed. The first concerns the scaling properties of the boundary-layer widths with the viscosity. It is shown that the viscous sub-layer is always thinner than what expected on the basis of Munk theory; moreover in the case of the Trade Wind forcing, it is shown that the viscous sub-layer thickness varies with viscosity with an exponent that is stepeer than that predicted by laminar theories ("1/2"), particularly at low latitudes.

The second important point made in Ch. 4 is the following: to which extent a turbulent

C O N S I G L I O   N A Z I O N A L E   D E L L E   R I C E R C H E
Istituto di Scienze dell'Atmosfera e del Clima
Unità Organizzativa di Supporto di Lecce

eddy viscosity closure can appropriately describe the turbulent dynamics in the considered cases of the WBCs?

To tackle the problem, C. Akuetevi has explored different strategies and collected a large amount of work by analysing data from all the numerical experiments performed by varying the forcing and the viscosity of the reduced gravity shallow water model.

It is shown that there is a linear correlation between the eddy viscosity (estimated by means of the Munk formula) and the maximum fluctuating zonal velocity. This is in agreement with Prandtl mixing length concept, and the proportionality constant is in the range proposed by Smagorinsky. This is an interesting result since it has a valuable practical consequence: two upper bounds for the ocean models grid size and viscosity values are proposed (50 km and 6000m^2/s, respectively) if one is willing to appropriately capture boundary-layer dynamics and the associated heat transport, crucial to estimate air-sea interaction. Finally, it is shown that eddy viscosity coefficients estimated via turbulent fluxes and counter-gradient corrections do not represent a satisfactory parameterisation for the turbulent WBCs.

In the second part of the thesis (chapters 5 to 9), the candidate goes further by applying this knowledge to the specific study of the Somali current, within the OGCM NEMO.

The description of the numerical experiments is preceded (chapt. 5) by a review of the Indian Ocean general circulation, the Arabian sea features as well as a schematic description of the main features of the Somali current annual variability. Chapter 6 intoduces NEMO model and the way the climatology study (10 year numerical experiment) is forced and initialised. Here some additional details on the use of ERA-interim data would improve the clarity of the manuscript.

An interesting point is made in chapter 7, where it is shown that as suggested by previous authors the elevation of the propagated sea-surface height anomaly could be a consequance of the retroflection of short, coastally trapped Rossby waves. This also confirms that the previous southwest Monsoon could have a large influence on the next norteast Monsoon, in the presence of strong negative wind stress curl.

Still in chapter 7 it is shown that small westward velocities can stabilize the boundary layer, as also predicted by inertial theory. This is in my opinion an important result since it calls for small-scale turbulent parameterisation that account for such anisotropy.

While further analysis is needed to better quantify this findings, I think that it clearly indicates that the use of simple statistically isotropic turbulent closures in not correct.

Let me also add that this is along the same line of a large amout of recent research in fluid dynamics, which has pointed out the statistical weight of anisotropic fluctuations in turbulent fields and the way these decay in space and time.

Finally, the main result of the OGCM climatology runs concerns the initiation of the northward Somali current by the arrival at the Somali coast of the annual Rossby waves. Here it is proven that indeed the Rossby waves play a dominat role on the early initiation of the northward Somali current, precursor of the formation of a large coherent structure, dubbed Great Whirl. This is a contribution to the important question of how a Monsoon can precondition the next one. More importantly grom the ocean modeling point of view, it is also shown the importance of the chaotic nature of coherent structures interactions in the non-linear dynamics of WBCs. This evidences the fact that high resolution data should be assimilated in the OGCM runs, to make the description of small scales phenomena meaningful.

C O N S I G L I O N A Z I O N A L E D E L L E R I C E R C H E
Istituto di Scienze dell'Atmosfera e del Clima
Unità Organizzativa di Supporto di Lecce

To summarise, my evaluation of the research work done by C. Akuetevi is good, as it is scientifically valid and contains some new and interesting ideas.

The scientific questions it investigates are definitely relevant for present and future research in geophysical fluid dynamics and oceanography, where the role of small scale dynamics is recognised to be more and more important.

The candidate shows a good formation, and ability to deal with both ideal and realistic modelisations of the ocean dynamics. The presentation is clear and complete. Fixing some typos in the editing, in the figure captions and in the review of current status of research can contribute to further improve the work.

To conclude, the work presented by C. Akuetevi is of good scientific quality and well organised. For these reasons, I suggest accepting the manuscript in the present form and without reservations I recommend that the PhD degree is worthy of a defence.

Alessandra S. Lanotte

Lecce, 21 January 2014

Alessandra S. Lanotte
CNR-ISAC
c/o Ecotekne, Str. Prov. Lecce – Monteroni, I-73100 Lecce, ITALY
e-mail: a.lanotte@isac.cnr.it
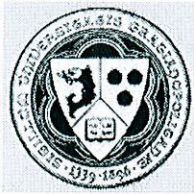Ph: +39 0832 298 814; Fax: +39 0832 298 716

EVALUATION

Nom du rapporteur : Alessandra Sabina Lanotte
(*Name of the referee*)

Nom du doctorant : Cataria Quam Cyrille Akuetevi
(*Name of the candidate*)

Niveau scientifique : *Mark*	Satisfaisant *Satisfactory*	Bon *Good*	Très bon *Very good*	Exceptionnel *Exceptionnal*
		X		

UNIVERSITÉ DE GRENOBLE

AVIS DU JURY SUR LA REPRODUCTION
DE LA THESE SOUTENUE

Nom : AKUETEVI .... Prénom : Cataria Quam Cyrille

Nom du Directeur de Thèse : Achim Wirth ....

Date de la soutenance : 20 Fevrier 2014 ....

Reproduction de la thèse soutenue :

A - ☒ Thèse pouvant être reproduite en l'état

B - ☐ Thèse ne pouvant être reproduite

C - ☐ Thèse pouvant être reproduite **APRES CORRECTIONS SUGGEREES** au cours de la soutenance.

Signature du Président du Jury

Nom et Prénom
STAQUET Chantal

CAS C : Télécharger sur l'ADUM à partir de votre compte personnel une attestation de correction qui devra être signée par le directeur de thèse et qui atteste que la version électronique déposée a été corrigée conformément aux exigences du jury.

L'attestation de correction est obligatoire.

Les corrections demandées par le jury doivent être effectuées dans un délai de trois mois maximum, conformément à la législation.

Les corrections doivent être absolument conformes aux corrections demandées par le jury.

RAPPORT DU PRESIDENT DE JURY
APRES LA SOUTENANCE

Il est demandé au jury d'indiquer clairement dans le rapport son jugement sur la qualité de la soutenance et sur le niveau de la thèse.

Mme/M ..... Chantal STAQUET Président(e) du jury
(C. STAQUET)

Le travail présenté par Mr Cataria Quam Cyrille AKUETEVI constitue la première étude numérique détaillée de la dynamique des structures cohérentes dans un courant océanique de bord ouest aux faibles latitudes. Une approche complémentaire est utilisée pour cela : d'une part un modèle numérique idéalisé d'un bassin océanique borné, que Mr AKUETEVI a mis en oeuvre, d'autre part l'analyse de simulations numériques réalistes basées sur le modèle NEMO dans le cadre du programme DRAKKAR, en configuration tropicale et sub-tropicale. Les prédictions du modèle idéalisé sont soigneusement comparées aux résultats du modèle réaliste tout au long du travail de thèse. Les principaux résultats obtenus concernent la caractérisation des différentes couches limites d'un courant de bord ouest aux faibles latitudes par l'étude idéalisée, une nouvelle vision des interactions turbulentes au sein du courant de Somalie et la proposition de recommandations pour la modélisation numérique réaliste. Le jury a apprécié l'exposé détaillé, clair et pédagogique présenté par Mr AKUETEVI, qui contenait de nouveaux résultats par rapport au mémoire de thèse sur la circulation au large de la côte somalienne. Mr AKUETEVI a bien répondu aux nombreuses questions du jury. En conséquence, le jury décerne à Mr AKUETEVI le titre de Docteur de l'Université de Grenoble.

....
....
....
....
....
....
....
....
....
....
....

ADMIS   Oui ✗   Non o

GRILLE D'EVALUATION

Les écoles doctorales (MSTII, ISCE, CSV, TUE, Physique) ne délivrent pas de mention mais le Jury complète la grille d'évaluation suivante :

Reporter ci-après les évaluations indiquées sur les Rapports préalables (niveau scientifique) :
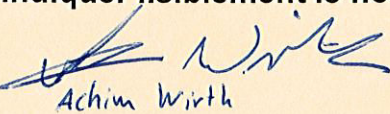
Rapporteurs :	Satisfaisant	Bon	Très bon	Exceptionnel
Mme/M ..LANNOTTE.....	[ ]	✗	[ ]	[ ]
Mme/M ....MOREL........	[ ]	[ ]	✗	[ ]
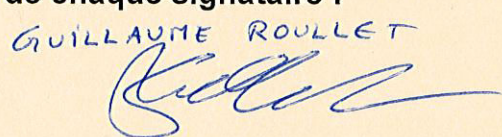
Évaluation générale de la présentation orale
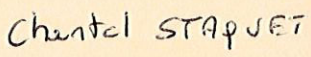
	Satisfaisant	Bon	Très bon	Exceptionnel
Qualité scientifique	[ ]	[ ]	✗	[ ]
Qualité pédagogique	[ ]	[ ]	✗	[ ]
Réponses aux questions	[ ]	✗	[ ]	[ ]

SIGNATURE DES MEMBRES DU JURY VALIDE PAR L'UNIVERSITE DE GRENOBLE AYANT ASSISTE A LA SOUTENANCE

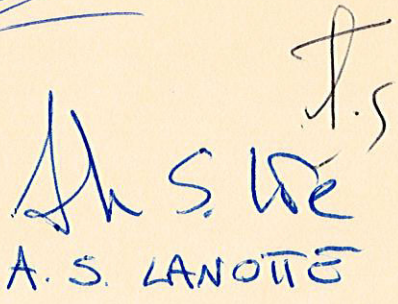**Indiquer lisiblement le nom et prénom de chaque signataire :**
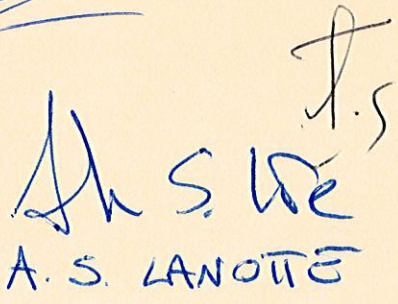
Achim Wirth

GUILLAUME ROULLET

Chantal STAQUET

Yves MOREL

N. HALL

B. BARNIER

A. S. LANOTTE